KERAF SHEAR ZONE, NE SUDAN: GEODYNAMIC CHARACTERISTICS OF THE NILE CRATON-NUBIAN SHIELD BOUNDARY

vorgelegt von
El Tahir Bailo Ahmed Suliman
(*M.Sc. Geology*)

vom Fachbereich 09
Bauingenieurwesen und Angewandte
Geowissenschaften der Technischen Universität Berlin
zur Erlangung des akademischen Grades

Doktor der Naturwissenschaften
- Dr. rer. nat. -

genehmigte Dissertation

Promotionsausschuß:

Vorsitzender: Prof. Dr. Burkhardt
Berichter: Prof. Dr. G. Franz
Berichter: PD Dr. H. Schandelmeier de Oliveira

Tag der wissenschaftlichen Aussprache: 28. November 2000

Berlin 2000
D83

ABSTRACT

This study integrates petrological, structural, geochemical, geochronological and isotopic investigations of the geodynamic evolution of the Neoproterozoic Keraf Shear Zone (KSZ) in NE Sudan. It is a ~500 km long, thrust-bounded and wedge-shaped belt, that is narrower (~30 km) in the S and wider (~150 km) in the N. The wedge-shape geometry reflects N-S variation in styles of the structures, distribution of the strain and grade of metamorphism. In the northern sector the structural style is ductile with folds of long amplitudes and the grade of metamorphism is green schist facies, whereas the southern sector of the belt is dominated by brittle deformation with folds characterised by short amplitudes and the rocks are in the upper amphibolite facies. Therefore metamorphism predates the shearing.

Lithologies in the KSZ are unique to the Keraf area and they were formed by the tectonic events of the KSZ. E-W geo-traverses in the Keraf area have revealed that the Keraf Petrotectonic Assemblage comprises: high- to medium grade gneiss, siliciclastic and carbonate-rich low-grade metasediments which intercalate with sills of meta-basalt and microdiorite, ophiolitic nappes, molasse-type sediments and post-tectonic granitoids. Mineral assemblages from the metasediments in the southern sector of the shear zone indicate metamorphic conditions of c. 700° C and 20 km crustal depth. In the northern part of the KSZ lithologies preserve most of their primary compositions, textures and structures. Sedimentary structures and textures (cross and graded bedding and oolitic textures) in the low grade metasediments indicate deposition in a shallow-passive marine environment. Keraf ophiolites occur as exotic N-S trending fault-bounded ridges and they have most of the lithological characteristics of Phanerozoic ophiolites. The Keraf Petrotectonic Assemblage is stratigraphically topped by molasse-type sediments which include non-metamorphosed polymict conglomerate, sandstones and volcanic tuffs. Collisional and post-collisional granitoids are widespread in the Keraf area. Geochemical investigations indicate existence of three layers in the Keraf ophiolites which show signatures of MORB and supra-subduction setting. The high-grade metasediments have geochemical signatures indicating low degree of sedimentary reworking and negligible values of secondary alteration. The low-grade metasediments are characterised by geochemical signatures which favour derivation from volcanic arc and deposition in a nearby shallow basin. The low grade-metavolcanics have both ocean floor and island arc geochemical characters. Geochemistry of the post-tectonic intrusions indicates that the older plutons are calc-alkaline, medium-K, metaluminous and collisional related I-type diorite and granodiorite. They have trace element signature of subduction zone emplacement. The younger plutons are high-K and post-collisional A-type granites. REE patterns favour derivation of the two types of plutons from a common magmatic source. Form, geometry and kinematics of evolution of the structural elements in the KSZ indicate a four-phased (D1-D4) transpressive deformation which is characterised by N-S sinistral faulting (simple shear). Shearing was associated with E-W horizontal compression (crustal shortening) and vertical extension (crustal thickening). The tectonic history of the shear zone manifests a scenario of ocean basin closure (the Mozambique Ocean) followed by collision of the Wadi Halfa-Bayuda Terrane (Nile craton) against the Gabgaba-Gerf Terrane (Nubian Shield). $^{207}Pb/^{206}Pb$ zircon single grain ages are ~730 Ma for the high-grade gneiss and ~710 Ma for the early post-tectonic intrusions. K/Ar ages are 660 Ma for hornblende from the post-tectonic intrusions and 560 Ma for biotite from the high-grade gneiss and the post-tectonic intrusions. This indicates that the tectonic and thermal history of the KSZ started ~750 Ma and ended at ~550 Ma. Pb isotopic ratios indicate an oceanic source for both the magmatic and metamorphic rocks in the KSZ. Sm/Nd model ages are 620-770 Ma for the post-tectonic plutons and 830-900 Ma for the gneiss, which indicate younger crustal residence and negligible involvement of a pre-pan African material in the evolution of the Keraf Petrotectonic Assemblage.

ZUSAMMENFASSUNG

Die vorliegende Arbeit zielt darauf ab anhand tektonisch-struktureller, petrologischer, geochemischer (Gesteins- und Mineralchemie), isotopengeochemischer und geochronologischer Untersuchungen einen umfassenden Überblick über die Entwicklung der neoproterozoischen Keraf Scherzone im Nordsudan zu erhalten. Die Keraf Scherzone ist ~500 km lang und wird seitlich von Überschiebungen begrenzt. In der Längserstreckung ist die Scherzone keilartig ausgebildet, d.h. im Norden wesentlich breiter (~150 km) als im Süden (~30 km). Diese Keilförmigkeit spiegelt sich auch in einem unterschiedlichen Stil der Deformationsstrukturen, der Strain-Verteilung und des Metamorphosegrades wieder. In der nördlichen Keraf herrscht duktile Deformation, weitständiger Faltenbau und grünschieferfazielle Metamorphose vor, während die südliche Keraf durch Spröddeformation, engständigen Faltenbau und amphibolitfazielle Metamorphosebedingungen gekennzeichnet ist. Dieser letztgenannte Umstand belegt daß die Scherbewegungen die Metamorphose überdauert haben.

Das lithologische Inventar der Keraf Scherzone wurde weitestgehend durch die tektonische Entwicklung geformt und wird deshalb als 'Keraf Petrotectonic Assemblage' (KPA) bezeichnet. Ost-West Geländetraversen haben ergeben daß die KPA aus folgenden Einheiten besteht: 1. mittel- bis hochgradig metamorphe Gneise, 2. siliziklastische und karbonatreiche geringgradige Metasedimente (mit Einschaltungen von Metabasalten und Mikrodioriten), 3. Ophiolit-Decken, 4. Molasse-Typ Sedimente, 5. diskordante Granit-Plutone. Mineralparagenesen aus metasedimentären Gneisen der südlichen Keraf Scherzone zeigen Metamorphosebedingungen um ca. 600 °C und 20 km Krustentiefe an. Im nördlichen Teil der Keraf Scherzone haben die nur geringgradig metamorphen Gesteine ihre primären Strukturen und Texturen erhalten können. Kreuzschichtung, 'graded bedding' und oolithische Texturen zeigen eine Ablagerung der Metasedimente in einem flachmarinen Ablagerungsraum an. Die ophiolithischen Gesteine kommen als 'exotische', N-S-streichende und von Störungen begrenzte, Rücken vor. Sie besitzen viele der Charakteristika phanerozoischer Ophiolithe. Den stratigraphischen Abschluss der KPA bilden molasseartige Sedimente die aus nicht-metamorphen polymiktischen Konglomeraten, Sandsteinen und Vulkanoklastiten bestehen. Kollisionale und post-kollisionale Granit-Plutone sind im Keraf-Gebiet weit verbreitet. Geochemische Untersuchungen belegen daß die Keraf Ophiolithe in drei Segmente unterteilt werden können: basale Tektonite, mafisch-ultramafische Kumulate, mafische Gesteine. Alle drei besitzen geochemische Signaturen die auf MORB- und Supra-Subduktionszonen-'Settings' hinweisen. Die Assoziation der Keraf Ophiolithe mit flachmarinen Sedimenten deutet auf eine Platznahme der Magmen im Spreading-Center eines Randbeckens hin. Die Geochemie der amphibolitfaziellen Metasedimente deutet auf nur geringfügige sedimentäre Aufarbeitung und Verwitterungsalteration hin, während die Geochemie der grünschieferfaziellen Metasedimente auf einen vulkanischen Inselbogen als Quelle schliessen läßt. Die in die Metasedimente eingeschalteten Metabasalte haben geochemische Signaturen von Ozeanboden- und Inselbogen-Basalten. Die Blei-Isotopenverhältnisse belegen eine ozeanische Herkunft für die magmatischen Gesteine der Keraf Scherzone, während die hoch-gradigen metasedimentären Gesteine geringfügige Zufuhren von präpanafrikanischem Krustenmaterial (8-10 Vol.%) erhalten haben.

Die granitoiden Plutonite können geochemisch in zwei Gruppen unterteilt werden. Die ältere Gruppe besteht aus kalk-alkalinen, metaluminösen, medium-K, I-Typ Dioriten und Granodioriten deren Spurenelement-Signaturen auf eine Subduktionszonen-Platznahme hinweist. Die jüngere Gruppe besteht aus high-K I-Typ Graniten und post-kollisionalen A-Typ Graniten. Die SEE-Muster beider Gruppen legen die Herkunft der Magmen aus einer gemeinsamen Quelle nahe.

Die tektonisch-strukturellen Untersuchungen der Keraf Scherzone belegen eine 4-phasige (D1 - D4) transpressive Deformation, die durch eine N-S gerichtete sinistrale Scherung (pure shear) charakterisiert wird. Die Scherbewegungen standen im Zusammenhang mit E-W gerichteter horizontaler Kompression (Krusteneinengung und Verdickung) während der Schliessung eines Ozeanbeckens (Mozambique Ocean) und anschliessender Kollision des Wadi Halfa-Bayuda Terranes (Nil-'Kraton') mit dem Gabgaba-Gerf Terane (Nubischer Schild). $^{207}Pb/^{206}Pb$ Isotopenbestimmungen an Einzelzirkonen haben für die hochgradigen Gneise ein Alter von ~730 Ma und für die älteren Granitplutone ein Alter von ~710 Ma ergeben. K/Ar Datierungen an Hornblende der älteren Intrusionen ergaben ein Alter von 660 Ma, während K/Ar Datierungen an Biotit der Gneise und der älteren Granite ein Alter von 560 Ma erbrachten. Die tektono-thermische Entwicklungsgeschichte der Keraf Scherzone begann daher um ca. 750 Ma und endete etwa um 550 Ma. Die Sm/Nd Modellalter von 620-770 Mio. Y. für die post-tektoniosche Pluton und von 830-900 Mio. Y. für die Gneise belegen einen kurzen krustalen Aufenthalt und eine geringe Beteiligung von prä-Pan-Afrikanischem Material an der Entwicklung der KPTA.

ACKNOWLEDGEMENTS

This study was conducted at the Institute of Engineering and Applied Geosciences (Bauingenieurwesen und Angewandte Geowissenschaften) of the Technical University of Berlin and was financially sponsored by the German Ackademic Exchange Service (DAAD) as scholarship which is sincerely appreciated.

I would like to express my deep thanks and gratitude to PD Dr. Heinz Schandelmeier for supervision, encouragement, advises and for his guidance and discussion in the fieldwork phase of the study. He is also thanked for the sacrifices he made to make the fieldwork less risky. These thanks are also extended to Prof. Dr. G. Franz for his partial supervision, his unlimited help in the laboratory work and for sharing me his knowledge of geology of NE Sudan. Thanks are extended to PD Dr G. Matheis for his administrative help and guidance in the geochemical laboratory work and in the fruitful discussion for interpreting the geochemical data. PD Dr U. Thorweihe is deeply thanked for providing me office and facilities in the GEOSYS building. He is also thanked for his unlimited help in solving the software problems that appeared from time to time. Dr. D. Küster is thanked for teaching me how to separate the zircon grains, reading the early manuscript of the thesis and for the constructive discussion and comments.

The Geological Research Authority of the Sudan and the University of Juba are highly thanked for providing logistics during the fieldwork. I am deeply indebted to Dr. O. Kheir, Dr. E. Abdelrahman, Dr. A. Kodi and Mr. Hassan El Tayeb and Prof. B. Khalil.

Geochemical analysis were conducted in the TU Berlin with the help of Mr. Domin, Mr. Becker and Mrs. Brown. My great thanks to them. The microprobe analysis was done in the ZELMI of the TU Berlin with the help of Mr. F. Galbert, to whom I am grateful. Petrology work was done in the TU Berlin, Dr. S. Büttner and Mrs. M. Krause are deeply thanked. Mrs. Suzin is thanked for drafting some of the diagrams in this thesis.

My colleagues in Ackerstrasse, Ack.9, and in Ernst Reuter Platz, Dr. R. Bussert, Dr. C. Werner, Mr. O. Reynolds and Mr. U. Fritz are thanked for their social and academic help.

Geochronological and isotopic analysis were conducted at the UT-Dallas, TU Bergakadmie Freiberg and Institut für Geologie und Dynamik der Lithosphere, Göttingen. Special thanks are due to Prof. Stern and Dr. M. Tichomirowa.

Satellite images were obtained from the Institute of Geology at the Free University in Berlin and from the French group of the BRGM in Sudan. Prof. F. K. List and Dr. J. Stein are deeply thanked for their co-operation.

My colleague Aleir Bullen is deeply thanked for the help he offered during the fieldwork.

My Sudanese colleagues in the TU, FU and HB University have provided social and emotional help for my family during the course of the study. In particular I would like to thank the families of Mr. A. Hussein, K. Abdun, H. Hussein and I. Babiker.

LIST OF CONTENTS

LIST OF FIGURES

LIST OF TABLES

LIST OF PLATES

1 INTRODUCTION

1.1 Location and accessibility

The area surveyed in this study is known as "Keraf Shear Zone" (KSZ). It covers an area of about 500 x 70 km. The KSZ is a N-S trending fault-bounded and wedge-shaped structural belt in northern Sudan and southern Egypt. The area affected by the shearing is confined by the co-ordinates 18°00` - 22°30` N. and 34°00`-35°00`E (Fig. 1). The width of the sheared area ranges from ~100 km in the north, where the KSZ truncates the Allagi suture, to 30 km in the south, at the junction of the KSZ with the Dam et Tor shear zone (Fig. 1).

The southern part of the KSZ could be reached from Khartoum by the asphalt road (Khartoum-Atbara highway). The central sector of the Keraf area is accessible by the Atbara-Abu Hamed motorable sandy road. The access to the northern sector of the study area is only by 4-wheel drive vehicles across the sand dunes of the Nubian Desert. The southern and the central sectors of the KSZ could also be reached by the Khartoum-Abu Hamed railway line. The Abu Hamed-Wadi Halfa railway line passes at about 50 km west of the Keraf area. It is not a helpful transportation device due to the thick sand dunes between the railway line and the Keraf area.

1.2 Physiography and climate

The northern and central domains of the KSZ are located in the western margin of the Nubian Desert, whereby more than 70% of the surface area is covered by sand dunes. The thickness of the sandy sheets varies from place to place, but in most localities reaches few meters above the surrounding. N-S trending ridges and basement inselbergs are scattered in this part of the study area. Low-lying basement outcrops are exposed as peneplains. The topography of the southern domain of the KSZ is characterised by the dominance of hills and peneplains. This part is topographically continuous with the outcrops of the Bayuda Desert.

The Keraf area is part of the Sahara Desert and thus the prevailing climate is dry with less than 50 mm per year rain fall in the period from July to September. The winter season is from November to February in which the daily mean temperature may drop to 10° C. Otherwise, the climate is very dry and hot and the daily mean temperature ranges from 45 to 50° C. Consequently, there is no vegetation cover. The drainage channels (Khors and Wadis) are very scarce. Wadi Gabgaba is an ancient channel flows in a N-S direction parallel to the trend of the KSZ (Fig. 2). In the southern domain of the KSZ, some water channels flow from the Red Sea Hills in the east to the River Nile in the west, the largest of which is Wadi Amur (Fig. 2).

The population density in the Keraf area is very low. The area north of Abu Hamed is unpopulated. The area to the south of Abu Hamed is populated only along the Nile banks.

1.3 Previous Studies

The Geology of the KSZ is poorly known due to the limited geological investigations conducted in the area. This can be attributed to the following two reasons: 1) the remote situation of the KSZ in the Nubian Desert, therefore it is not accessible with the local logistics of the Geological Research Authorities of the Sudan (GRAS). 2) the thick sandy cover obscures most of the surface features. Remote sensing tools are not very helpful to delineate and/or trace the geological features for long distances.

The KSZ was first identified and named by ALMOND and AHMED (1987). ABDEL-RAHMAN (1993) identified ophiolitic fragments in the Keraf area. The ophiolites were interpreted as remnants of a marginal

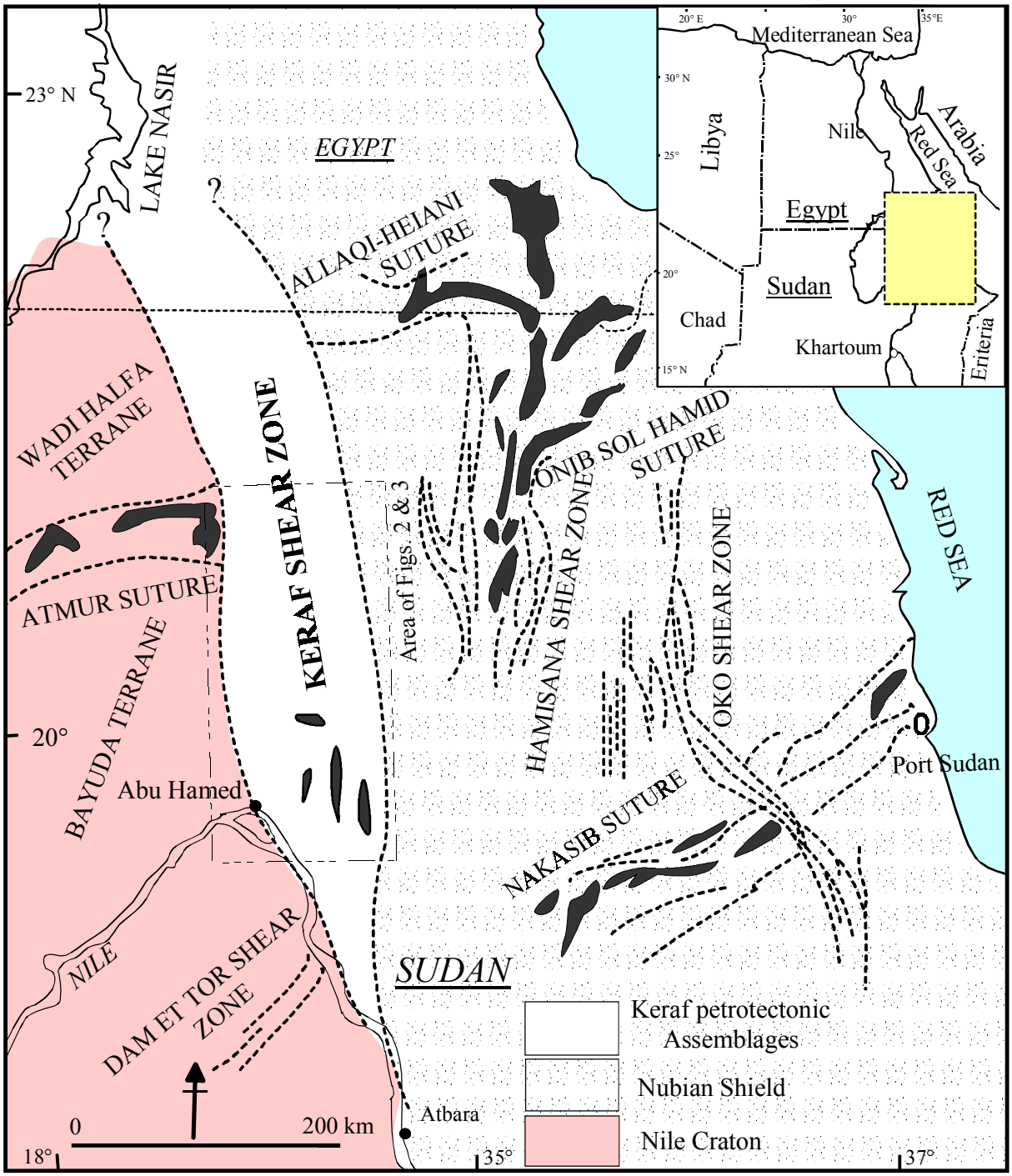

Fig. 1: Simplified tectonic map of NE Sudan and southern Egypt. The dominant features are the NE-SW trending ophiolite-decorated sutures offset and dislocated by the younger N-Strending shear zones. Keraf Shear Zone is a transitional domain between the enisalic Nile craton and the ensimatic Nubian Shield (modified after Abdelsalam and Stern 1996, Schandelmeier et al 1994).

oceanic basin which once existed between the composite arc terranes of the Nubian Shield in the east and the Nile craton in the west (ABDELRAHMAN, 1993). Carbonate-rich turbidites and pelagic sediments were identified in the Keraf area by STERN et al (1993). They were interpreted as passive margin related sediments deposited on the eastern foreland of the Nile craton (STERN et al, 1993). The structural setting and the tectonic evolution of the northern sector of the KSZ was studied by SCHANDELMEIER et al

(1994). They have concluded that the KSZ is a geo-suture formed due to the collision of the Nile craton with the Nubian Shield. Also they have reported that the KSZ structural styles are younger and overprint all the E-W trending structures in the high-grade gneiss in the west of the Nile. A deformational history of the KSZ was proposed by ABDELSALAM et al (1995, 1996, 1998). They have described the KSZ as a four-phased deformational belt formed above a NW-verging descending slab. Since 1998 the French BRGM (Bureau de Recherches Geologiques et Minieres) and GRAS are prospecting for gold in the quartz veins and across the palaeo-channels in the Keraf area. They have not published geological reports up to the moment of drafting this thesis.

The name Gabgaba Shear Zone (GSZ) was first introduced by ABDELRAHMAN (1993) for the whole area of the Keraf domain, but recently the name KSZ is established in the literature for the whole transitional zone between the Nile craton and the Nubian Shield (SCHANDELMEIER et al, 1995; STERN, 1994). In this study the name KSZ is adopted for the entire region which separates the Red Sea Hills from the Bayuda area. The name GSZ is proposed for the middle high strain and carbonate-rich part of the KSZ.

1.4 Aims of the study

The KSZ is the most prominent structural feature in northern Sudan. It is clear from the literature that only a few geological aspects are known from the Keraf area. In this study the following problems are addressed:

1. Detailed geological mapping of the northern sector of the KSZ (the area north of Abu Hamed to the Atumr suture – KSZ junction) (Figs. 1 and 2).
2. Lithological characterisation of the rock units existing in the KSZ, which are called hereafter the "Keraf Petrotectonic Assemblage" (KPTA).
3. Documentation of the structures which may provide a new perspective on the tectonic evolution of the KSZ.
4. Geochemical (rock and mineral chemistry), geochronological and isotopic characterisation of the major lithologies in the Keraf area.
5. Understanding of the nature of the Nile craton-Nubian Shield boundary in northern Sudan.

1.5 Methods

The methods of study applied in this research have included fieldwork and laboratory investigations.

1.5.1 Fieldwork

The field data were collected during the period from February to March 1998. The fieldwork was conducted in form of detailed E-W geo-traverses in the area between latitudes 18°45` - 21°00` N and longitudes 33°00 - 34°15`E. Regional E-W geo-traverses were conducted in the area south of Abu Hamed up to Dam et Tor shear zone (Fig. 2). For the detailed traverses TM satellite images (174-46; 173-46; 174-45 and 175-45) bands 1,4,5 with the scale of 1:200,000 were used as base maps. These maps were provided by the BRGM team who was prospecting for gold in the Keraf area during the 1998 field season. For the regional traverses MSS satellite imageries (187-45; 186-45; 187-46; 186-46 and 186-47) bands 4,5,7 with the scale 1:500,000 were used as base maps. The MSS images were provided by the Institute of Geology at the Free

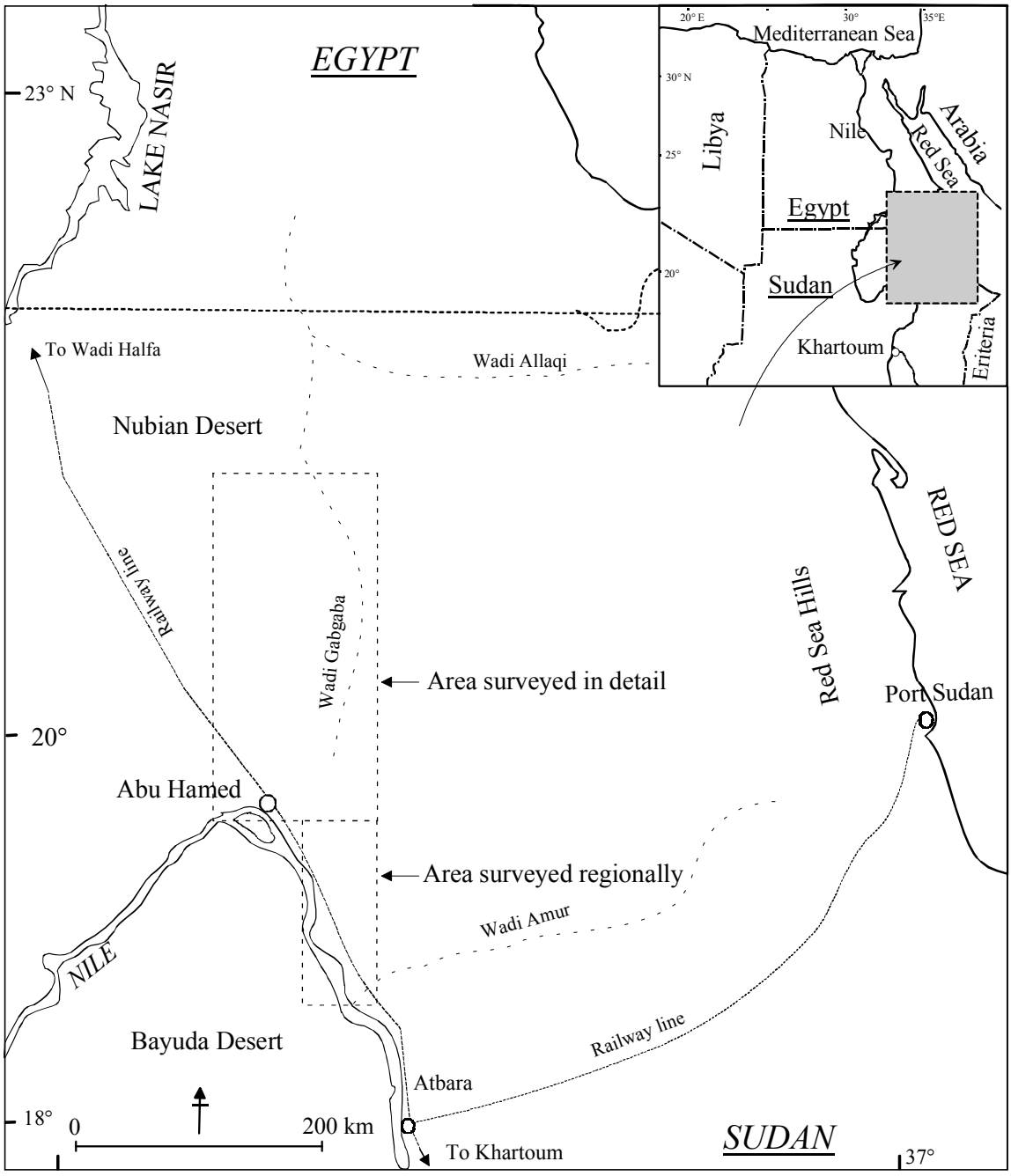

Fig. 2: Map shows location of the study areas and the major topographic features in N. Sudan.

University in Berlin. Topographic maps from the Sudan survey department at scale of 1:250 000 were used in checking navigation routes and names of localities.

During the fieldwork about 130 rock samples had been collected for petrographic studies. They represent varieties of the major lithologies encountered in the area. Large samples (20 kg each) were taken from the post-tectonic intrusions and the high-grade gneiss for the geochronological and isotopic investigations. 85 samples were selected for geochemical investigations (XRF and ICP). Oriented samples have been collected from the three sectors (northern, central and southern) of the KSZ for the strain analysis in each sector.

Systematic structural measurements and documentation of the planar and linear fabrics had been taken from the study area. The structural measurements are collected in such a way that the deformational history of

the KSZ and the field relation between the different lithological units can be revealed.

1.5.2 Microscopic investigations

Samples have been investigated under the petrographic microscope to reveal the mineralogical composition, textures and microstructures, degree of alteration and metasomatism. Consequently, some samples had been selected for the study of the whole rock and mineral chemistry. The thin sections were prepared in the laboratories of GRAS in Khartoum and in the department of Petrology in the TU Berlin.

Oriented thin sections were made from the oriented samples along the planes: XY; XZ and YZ of each sample.

1.5.3 Preparation of samples for geochemical analysis

The samples selected for the whole rock chemistry were characterised by minimum effects of alteration, metasomatism and veinlet intrusions. The weathering crust of the samples was removed with the geological hammer and/or with the rock-cutting machine in the TU Berlin, Department of the Geological Engineering. The fresh rock material was then broken into chips using the geological hammer. The chips were crushed by the mechanical jaw-crusher. The crushed material is quartered and a representative part of it is pulverised to sizes of less than 50µm in a Tema tungsten carbide disc mill. The powder is kept in dry closed plastic packs for the XRF (fused and powder pellets), ICP and LOI analysis.

1.5.4 Loss On Ignition (LOI)

By this technique the volatile part of the rock is removed by heating to high degrees of temperature. The chemically bound water, CO_2, OH and F will be expelled from the rock material at temperatures of 1000°C and above. LOI is defined as the decrease in the weight of the sample due to heating and it was determined by the following steps:

2 grams of the sample powder were weighted in a porcelain crucible and heated in an oven at 1000°C for one hour. After cooling in a desiccator for at least two hours the sample is weighted at room temperature and the loss in the weight is calculated as a percentage from the original weight of the sample.

1.5.5 X-Ray Fluorescence (XRF)

This method is applied to determine the major oxide and the trace element composition of the rocks. Both pressed powder pellet and fused glass discs are employed in this study. The analysis were conducted at the TU of Berlin.

In the pressed powder method (for analysis of trace elements) 6.0 g of the pulverised rock material is properly mixed with 1.5 g wax and placed in an aluminium container. The container is pressed under 20 ton in a steel liner. The pressed sample is then examined with the XRF machine. With this method the major oxides are not accurately determined due to the heavy matrix and the textural effects.

In the fused glass disc method (for analysis of major elements) 0.6 g of the pulverised sample is mixed with 3.6 g of lithium metaborate. The mixture is placed in a Pt-crucible and is ignited to form a melt in an induction furnace for 6 minutes at a temperature of ~1200°C. The melt is quenched to form a glass disc by pouring it into a Pt-mould. This method is more efficient in detecting the major elements compared to the pressed pellets, because the met is homogenous and there are no matrix or texture influences.

Detection limits and error values of the XRF machine in the TU Berlin are shown in tables 1 and 2.

1.5.6 Inductively Coupled Plasma (ICP) Emission Spectroscopy

This method is applied to determine the REE contents from the selected samples.

Table 1: Detection limits and analytical errors of the powder pelts of the XRF machine in the TU Berlin geochemical lab.

		Range of Calibration		absolute	No. of
Element	**Concn.**	**min.**	**max.**	**Stand.devi.**	**Standards**
SiO_2	Wt. %	0.2	90	2.4	77
Al_2O_3	Wt. %	0.2	60	1.1	88
Fe_2O_3	Wt. %	0.02	34	0.35	97
MgO	Wt. %	0.3	25	0.52	70
CaO	Wt. %	0.1	55	0.41	97
Na_2O	Wt. %	0.1	9	0.23	80
K_2O	Wt. %	0.05	13	0.10	90
TiO_2	Wt. %	0.03	3.8	0.03	79
P_2O_5	Wt. %	0.01	7.5	0.05	90
SO_3	Wt. %	0.05	6.2	0.08	42
Ba	ppm	30	4,000	22	80
Co	ppm	10	210	3.7	52
Cr	ppm	30	17,500	26	57
Cu	ppm	10	1,300	16	73
Ga	ppm	3	100	2.6	71
Mn	ppm	150	22,300	88	85
Ni	ppm	12	3,000	9.5	72
Pb	ppm	15	11,000	22	63
Rb	ppm	10	8,500	5.5	75
Sr	ppm	10	4,600	9.7	88
V	ppm	10	950	9.2	74
Zn	ppm	40	24,100	29	76
Zr	ppm	40	11,000	13	68
Ag	ppm	2.5	195	1.2	9
As	ppm	10	4,000	5.5	37
Bi	ppm	7	70	3.3	11
Br	ppm	4	300	2.4	19
Cd	ppm	5	470	2.7	7
Cl	ppm	300	40,000	78	15
Cs	ppm	8	640	4.2	20
F	ppm	800	85,000	1,000	26
Mo	ppm	5	310	2.5	16
Sb	ppm	7	410	3.0	16
Se	ppm	3	40	0.75	7
Sn	ppm	10	6,800	15	17
Th	ppm	10	380	2.4	32
Tl	ppm	3	35	1.5	8
U	ppm	5	650	3.2	27
W	ppm	15	450	6.0	19

The pulverised sample is converted to a solution which is pumped into a chamber with a flow of argon gas. A portion of the sample will be converted into an aerosol by the argon flow. The aerosol is sprayed into the centre of an argon plasma. The inductively coupled plasma is a stream of argon ions produced by inductive heating at very high temperatures. When the solution of the sample is sprayed into the argon flame the chemical bonds between the elements will dissociate and a large number of spectral lines will be produced. The spectral lines will be focused by a spectrometer on a photomultiplier. Signals from the photomultiplier will be directed onto a teletyper

Table 2: Detection limits and analytical errors of the fused pelts of the XRF machine in the TU Berlin geochemical lab.

		Range of Calibration		absolute	No. of
Element	Concn.	min.	max.	Stand.devi.	Standards
SiO_2	Wt.%	0.2	90	0.6	87
Al_2O_3	Wt.%	0.1	59	0.2	85
Fe_2O_3	Wt.%	0.06	75	0.1	92
MnO	Wt.%	0.02	1.25	0.005	82
MgO	Wt.%	0.1	45	0.1	81
CaO	Wt.%	0.1	66	0.1	88
Na_2O	Wt.%	0.2	11	0.1	68
K_2O	Wt.%	0.05	13	0.05	80
TiO_2	Wt.%	0.03	3.8	0.02	78
P_2O_5	Wt.%	0.05	34	0.07	68
Ba	ppm	50	5,000	27	68
Ce	ppm	40	2,200	14	51
Co	ppm	20	700	5.2	34
Cr	ppm	20	24,000	29	62
Cu	ppm	20	1,300	16	46
Ga	ppm	8	400	3.2	68
Hf	ppm	6	190	1.4	26
La	ppm	40	1,300	13	28
Nb	ppm	6	960	3.7	57
Nd	ppm	15	670	6.5	54
Ni	ppm	20	2,500	13	46
Pb	ppm	20	5,200	6	44
Rb	ppm	30	3,600	11	64
Sc	ppm	15	300	3.8	30
Sm	ppm	6	110	1.3	28
Sr	ppm	10	4,600	9.4	80
V	ppm	10	950	11	69
Y	ppm	10	720	3.6	60
Zn	ppm	20	3,600	8.8	80
Zr	ppm	50	11,000	13	62
As	ppm	10	410	3	21
Bi	ppm	10	1000	3.5	8
Mo	ppm	7	700	6.6	10
Pr	ppm	15	220	2.6	11
Th	ppm	20	1,000	6.2	19
U	ppm	9	650	2.9	15

to give intensities, which in turn be converted to concentrations. ICP detection limits and REE values of the standards used at the TU Berlin geochemical labs are list in table 3.

1.5.7 Electron microprobe analysis

This method is used to determine the chemical composition of some selected mineral phases. The method was carried at the ZELMI of the TU of Berlin. The samples are prepared in polished thin sections in which the minerals to be analysed are marked by circles. A beam of electrons is focused onto a small part of the mineral. The emitted X-ray is examined by wavelength dispersive spectrometers.

In this research the chemistry of minerals has been determined with a CAMEBAX Electron Beam microprobe equipped with four wavelength dispersive X-ray spectrometers. The operating parameters were 16 nA beam current and 15 kV accelerating voltage. The analysis was performed under automatic control using SAMX programme with PAP correction programme. The spot

Table 3: Detection limits of the ICP machine and REE values of standards in the TU Berlin geochemical lab (Chondritic value is after Evensen et al 1978).

Element	Min. detec. limit	Condrit.	Sample JGb-1 Geo	Sample JGb-1 TU	Sample JG- 1a Geo	Sample JG- 1a TU
Lu	0.10	0.025	0.16	0.13	0.53	0.43
Hf	0.10	n.d	0.84	1.40	3.70	2.80
Yb	0.10	0.165	1.00	1.00	3.00	3.20
Gd	0.10	0.204	1.50	1.50	n.d.	4.10
Ho	0.10	0.057	0.32	0.30	n.d.	1.00
Er	0.10	0.166	0.91	0.90	n.d.	2.30
Dy	0.10	0.254	1.40	1.80	n.d.	4.90
Sm	0.10	0.154	1.50	0.80	4.50	4.40
Eu	0.10	0.058	0.61	0.70	0.72	0.80
La	0.20	0.245	3.95	3.90	23.00	24.00
Ce	0.10	0.638	8.00	7.70	47.10	49.40
Pr	0.10	0.096	1.10	1.20	8.70	5.20
Nd	0.50	0.474	5.70	4.10	19.70	19.00

surface in most of the analysis is $4\mu m^2$. The standard formulas of the elements were obtained by using Minpet software and by setting the number of oxygen to 23, 32, 24, 6, 24 and 36 for amphibole, feldspar, garnet, pyroxene, biotite and chlorite respectively. The cation numbers used in the calculation of the garnet and pyroxene formulas are 8 and 4 respectively. Oh number used in the calculation of the biotite formula is 4 while that one used in the chlorite is 16 (DEER et al, 1992).

1.5.8 Isotopic Analysis

In this study Isotopic zircon single grain dating was conducted at the Bergakademie TU Freiberg, biotite and hornblende K/Ar dating was carried at Institut für Geologie und Dynamic der Lithosphere in Göttingen. Pb isotopic composition for the K-feldspar, Rb-Sr and Sm-Nd isotopic ratios were determined at the Centre for lithospheric studies University of Texas at Dallas.

Single zircon grains were separated from four samples at the TU Berlin using the conventional separation technique which comprises: rock crushing, sieving, heavy liquid separation, electromagnetic separation and hand picking of the zircon grains. The method used and the operating parameters are outlined in KOBER (1986, 1987).

Rb-Sr contents were determined for four samples by isotope dilution and were analysed for $^{87}Sr/^{86}Sr$ using a Finnigan MAT instrument. Accuracy on $^{87}Sr/^{86}Sr$ is ± 0.0004. Samples are normalised to $^{87}Sr/^{86}Sr = 0.70803 \pm 3$ for the E &A $SrCO_3$. standards.

Determination of Nd, Sm and $^{143}Nd/^{144}Nd$ were made using the University of Texas Finnigan-MAT261 Mass Spectrometer. Uncertainties on Sm/Nd measurements are about 1%. Calculations of $\varepsilon_{Nd(T)}$ were made assuming Bulk Earth $^{143}Nd/^{144}Nd = 0.1967$ and using the determination of ε_{Nd} for the UCSD standard (-15.2) and BCR (-0.16) reported by Bier et al (1989). For the calculation of the $^{143}Nd/^{144}Nd$ a total range of ± 0.00002 for the standards is taken as the analytical uncertainty.

K-feldspar was separated from three samples (two gneiss and a pluton) for the determination of their initial Pb isotopic compositions. The samples were rinsed in 6N HCl then leached overnight in 1% HF. Pb was isolated by an anion exchange column procedure followed by the single bed technique. The analysis were corrected for 0.15% per amu fractionation. Standard used in the analysis has the following lead isotopic ratios: $^{206}Pb/^{204}Pb = 16.946$, $^{207}Pb/^{204}Pb$ 15.501 and $^{208}Pb/^{204}Pb = 36.756$. Details of the procedure are outlined in STERN and KRÖNER (1993).

2 TECTONIC SETTING AND REGIONAL GEOLOGY OF THE KSZ

2.1 Introduction

The Precambrian geology in NE Africa comprises two distinct crustal domains: the Nile craton and the Arabian-Nubian Shield (STERN, 1994; KRÖNER et al, 1987a; VAIL, 1983; 1988; ROCCI, 1965) (Fig. 1). The Nile craton is dominated by heterogeneous gneisses and supra-crustal metasediments of pre-Neoproterozoic ages and ensialic geochemical affinities (KRÖNER et al, 1991; VAIL, 1988). The Nile craton has been pervasively remobilized during the Neoproterozoic Pan African Orogeny (STERN, 1994; KRÖNER et al, 1987b; VAIL 1988). The western and the southern extensions of the Nile craton are not precisely defined, therefore many names apart from "Nile craton" are (BLACK and LIEGEOIS, 1993; SCHANDELMEIER, et al 1988; BERTRAND and GABBY, 1978; KRÖNER, 1977). The identification of the Nile craton came mainly from the geochronological and isotopic composition of the gneisses. U/Pb zircon ages, Nd model ages, Pb, Sr and Nd isotopic composition point to the fact that the gneisses west of the Nile are mostly older than 900 Ma and have an old crustal history (STERN, 1994; HARMS et al, 1994 and 1990; SULTAN et al, 1994, 1992 and 1990; SCHANDELMEIER, et al 1988; DIXON and GOLOMBEK, 1988; WUST, et al 1987; KRÖNER et al, 1987b; HARRIS, et al 1984). In the study area such isotopically older gneisses are reported from Wadi Halfa and Bayuda Terranes (Figs. 1 and 3).

In contrast, the Arabian-Nubian Shield is dominated by Neoproterozoic arc terranes (STERN et al, 1994; KRÖNER et al, 1987a; VAIL, 1988; 1983). The arc terranes are believed to be intra-oceanic island arc/back-arc-basin complexes formed by the Pan African orogeny during ~900 - 550 Ma (KRÖNER et al, 1987a). The arc terranes are welded to each other along NE- to E-trending ophiolite-decorated sutures (Fig. 3) (BERHE, 1990; KRÖNER et al, 1987a). Structures along the sutures document subduction-related deformation in the period ~870-690 Ma (STERN, 1994). Geochemical and isotopic investigation of the magmatic rocks in the Arabian-Nubian Shield indicate derivation from a depleted mantle source with no or with very little contribution from a pre-existing continental crust (STERN AND KRÖNER, 1993). In the area of this study the Arabian Nubian Shield is represented by low-grade volcano-sedimentary sequences in the Gabgaba and Gerf Terranes (Fig. 3).

The Arabian-Nubian Shield collided against the Nile craton along a N-S trending boundary extending from S Kenya to S Egypt (STERN, 1994; ABDELSALAM and DAWOUD, 1991; VAIL, 1988) (Fig. 3). During the collisional processes, the eastern foreland of the Nile craton was remobilized and most of the cratonic signatures were overprinted by the juvenile Pan African features. The evolution of the Arabian-Nubian Shield and the remobilization of the eastern foreland of the Nile craton is termed the East African Orogen (STERN, 1994). In N Sudan and S Egypt the Nile craton-Arabian Nubian Shield boundary is represented by the KSZ (STERN, 1994; ABDELSALAM and DAWOUD, 1991; VAIL, 1988). Lithologies reported in the KSZ are very distinct and are particular to this zone, therefore the name Keraf Petrotectonic Assemblage (KPTA) is proposed and will be used in this study (chapter 3).

2.2 Geology of the Wadi Halfa-Bayuda-Gabgaba area

Wadi Halfa and Bayuda Terranes (SCHANDELMEIER et al, 1994) represent the reworked eastern foreland of the Nile craton, while Gabgaba Terrane (ABDELRAHMAN, 1993) represents the westernmost part of the Arabian-Nubian Shield (Fig. 3). The area covered by the Bayuda Desert is

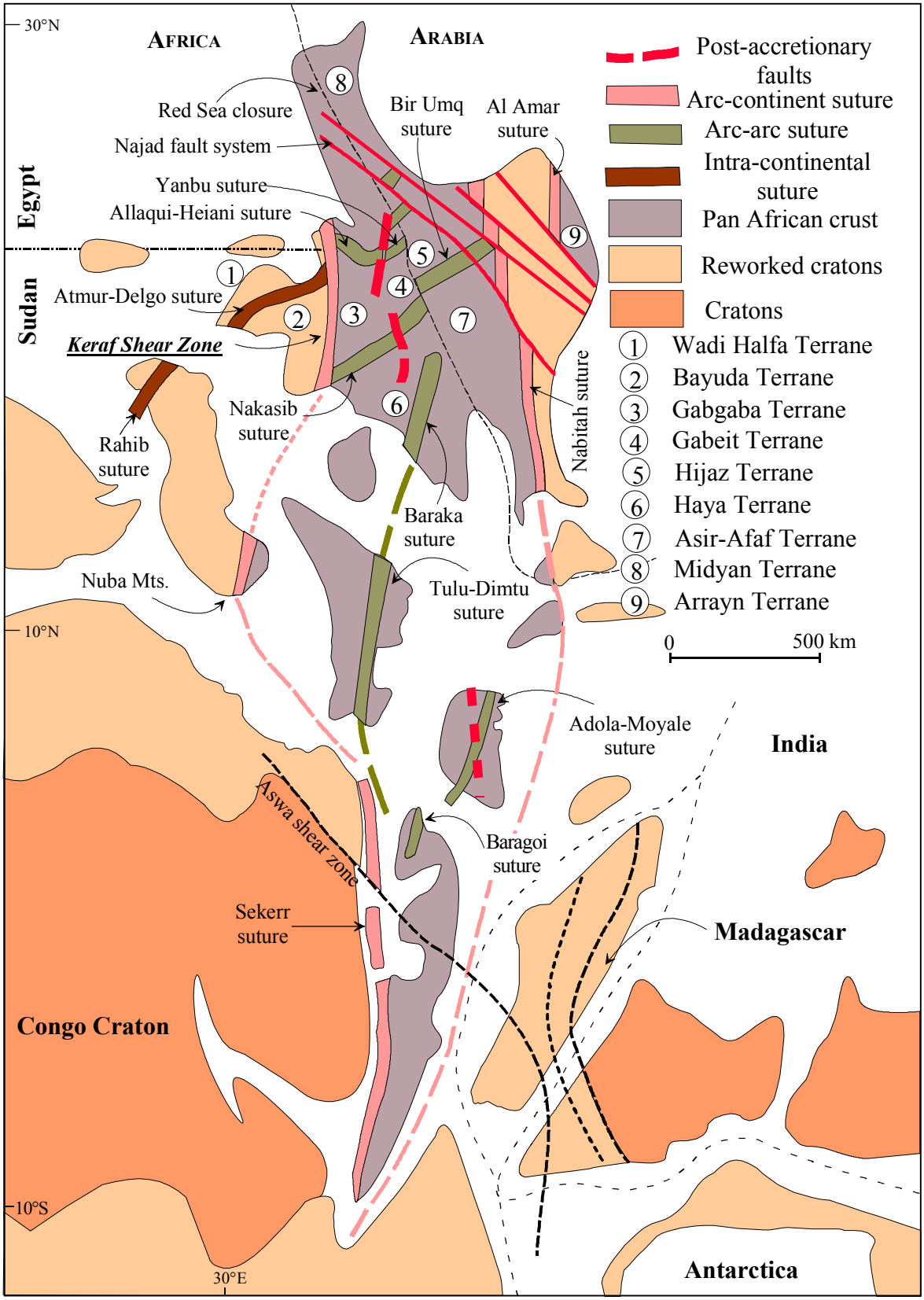

Fig. 3: Tectonic map showing the Precambrian structures and Terranes in NE Africa and Arabia. Sutures are connected by dotted lines. The area enclosed by the E and W arc-continent sutures is the Arabian-Nubian Shield (modified after Stern, 1994).

relatively well studied compared to other areas in northern Sudan (VAIL, 1971; BARTH and MEINHOLD, 1979; DAWOUD, 1980; RIES et al, 1985). Wadi Halfa area is poorly understood due to the limited studies conducted in the area (STERN et al, 1994, GRIFFITHS et al, 1987). The Gabgaba Terrane is the western extension of the Hijaz-Gebeit Terrane in Arabia and in the Red Sea Hills (CAMP, 1984; EMBELTON et al, 1983; FITCHES et al, 1983) (Fig. 3). Therefore, the geology, geochemistry and geochronology of the Gabgaba Terrane can be inferred by E-W correlation along the Hijaz-Gebeit-Gabgaba Terrane.

According to the previous studies in N and NE Sudan the lithostratigraphic units of the Wadi-Halfa-Bayuda-Gabgaba area are (DENKLER et al, 1994; ABDELRAHMAN, 1993; VAIL, 1988; BARTH and MEINHOLD, 1979):

1. High-grade gneisses (oldest)
2. High-grade supracrustal metasediments
3. Low-grade metasediments
4. Ophiolitic melange rocks
5. Volcano-sedimentary sequences
6. Molasse-type sediments
7. Magmatic rocks
8. Phanerozoic sediments (youngest)

2.2.1 Gneisses and migmatites

The high-grade gneisses occur in the central and the western sectors of the Bayuda Desert and in the area to the west of Wadi Halfa railway station (VAIL, 1988; STERN et al, 1994) (Fig. 4). They are poly-deformed, occupy the lowermost stratigraphic level and are in the upper amphibolite metamorphism. Similar lithologies are reported in the Wadi Hawar, to the west of the Nile, (SCHANDELMEIER et al, 1990) and in the Delgo area (DENKLER et al, 1994). The high-grade metamorphic rocks reported in J. Uweinat and J. Kamel (SCHANDELMEIER et al 1988) can be correlated with the gneisses in the Bayuda and Wadi Halfa Terranes on the basis of lithology and stratigraphy.

U/Pb zircon ages from the high-grade gneisses are in the range of 700 to 900 Ma (WUST et al, 1987; KRÖNER et al, 1987b; SULTAN et al, 1994). Nd model ages reported from the older granitic gneisses from Wadi Halfa-Bayuda Terrane and from the E. Desert of Egypt are generally greater than 1.2 Ga (HARMS et al 1990; 1994; STERN et al; 1994; SCHANDELMEIER, et al 1988; HARRIS et al 1984). $^{87}Sr/^{86}Sr$ ratio reported from the gneisses in the Nile craton ranges from 0.7060 to 0.7160 (STERN et al; 1994; HARMS et al 1990; DIXON and GOLOMBEK, 1988). These ages and isotopic ratios indicate the presence of older (Pre-pan African) material in the gneisses in the Bayuda and Wadi Halfa Terranes.

Lithologies with such isotopic characteristics were not reported from the Gabgaba Terrane.

2.2.2 High-grade metasediments & Keraf gneiss

These are amphibolites, calc-silicates, biotite-garnet schist, quartzo-feldspathic gneiss, metapelite, marbles and quartzite which overlie the high-grade gneisses. (RIES et al, 1985; DAWOUD, 1980; VAIL, 1979; BARTH and MEINHOLD, 1979) (Fig. 4). Mineral composition, textures and structures in these rocks indicate marine shelf depositional environment (STERN, 1994). High-grade metasediments near Abu Hamed has yielded Rb/Sr errochron age of ca. 761 and $^{87}Sr/^{86}Sr$ ratio of ca. 0.0703 (RIES et al, 1985). A quartzo-feldspathic gneiss from the Bayuda Desert has yielded a Nd model age of ca. 1000 Ma (HARRIS, et al 1984). These low ages and isotopic ratios exclude a long crustal history of the original rock material prior to the amphibolite facies metamorphism.

The high-grade metasediments and the Keraf gneiss are called by some authors the "supracrustal metasediments" due to their mode of formation (RIES et al, 1985; DAWOUD, 1980). Other authors, such as Vail (1988), believe that the high-grade metasediments belong to the high-grade gneisses and migmatites and they have been placed in their present stratigraphic level by younger tectonic activities.

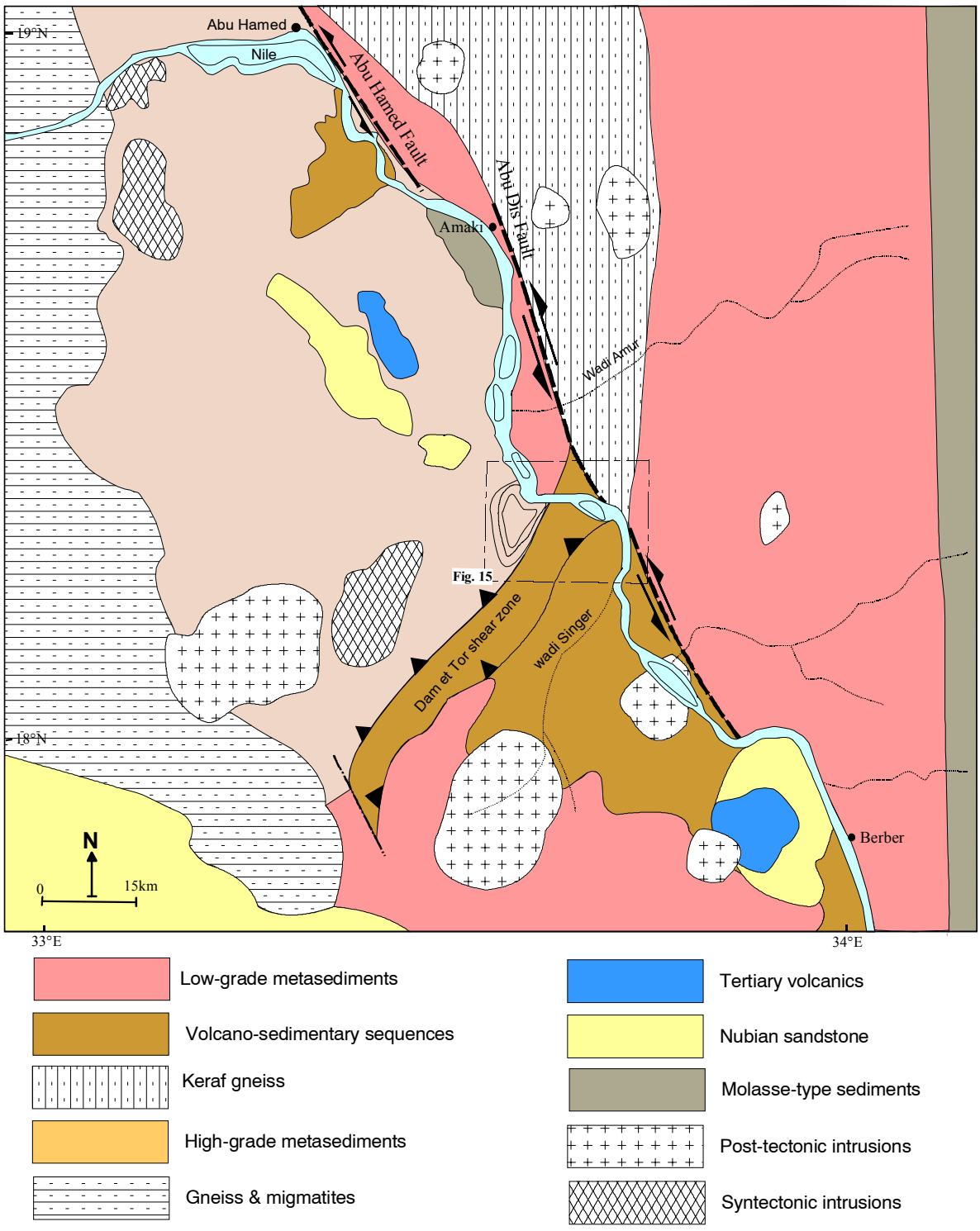

Fig.4: Geological map of the southern sector of the Keraf Shear Zone. Note the dominance of the high-grade metasediments west of the Nile and the low-grade ones in the east (modified after ABDELRAHMAN, 1993; RIES et al, 1985).

2.2.3 Low-grade metasediments

The low-grade metamorphic rocks form a N-S trending belt that covers more than 60% of the total surface area of the Nubian shield (ABDELRAHMAN, 1993; ALMOND and AHMED, 1987; RIES et al, 1985) (Fig. 4).

They are tectonically emplaced over the high-grade rocks (both the gneisses and metasediments) of the Wadi Halfa and Bayuda Terranes (ABDELRAHMAN, 1993; ALMOND AND AHMED, 1987). The sediments are locally divided into a proximal western portion which is coarse immature and a distal eastern portion with fine-grained textures (ABDELRAHMAN, 1993; STERN et al, 1993).

The low-grade metasediments and the high-grade supracrustal rocks are believed by some authors to have the same age and tectonic history but represent different levels within the Neoproterozoic crust in the area (Almond and Ahmed 1987, Ries et al 1985).

In the area mapped in this study the low-grade metasediments are divided into carbonate-rich and siliciclastic metasediments.

2.2.4 Ophiolitic melange rocks

These are highly tectonised and serpentinized mafic-ultramafic allochthonous sequences scattered in Wadi Halfa-Bayuda-Gabgaba domain (ABDELRAHMAN, 1993; ALMOND AND AHMED, 1987; DAWOUD, 1980; AHMED et al, 1980; BARTH and MEINHOLD, 1979). They occur along shear zones representing major tectonic features in the area, such as the KSZ, Atmur-Delgo suture and Dam Et Tor shear zone (Fig. 2). Geochemical signatures of these rocks favour a protolith derived from an oceanic crust back ground (ABDELRAHMAN, 1993).

2.2.5 Volcano-sedimentary sequences

These are volcanics and volcaniclastic rocks, which occur in the eastern margin of the Gabgaba Terrane, the E and SE Bayuda Desert and in the vicinity of Wadi Halfa area (ABDELRAHMAN, 1993; VAIL, 1988; RIES et al, 1985; DAWOUD, 1980) (Fig. 4). In E Bayuda Desert these rocks occur as intermediate volcanics in a sedimentary matrix of tuffaceous-silicious composition (RIES et al, 1985). In SE Bayuda Desert the volcano-sedimentary rocks include rhyolite, andesite and basalt intercalated with volcaniclastic sedimentary units. Limited occurrences of marbles, quartzites and Fe-rich cherts are associated with the volcanic material (MEINHOLD, 1983; BARTH and MEINHOLD, 1979; VAIL, 1979; EL RABAA, 1972). Rocks from this sequence have yielded Rb/Sr errochron ages of ~800-850 Ma and $^{87}Sr/^{86}Sr$ ratio of 0.70251-0.70299 (RIES et al, 1985). ABDELRAHMAN (1993) has argued that the volcano-sedimentary sequences in the SE Bayuda Desert could be correlated with the arc-related assemblages in the Haya Terrane of the Red Sea Hills. The argument is based on the structural trends, lithological and the petrological similarities. Limited occurrences of metavolcanics and volcaniclastic material were reported from the Delgo area west of the Nile (DENKLER et al, 1994).

In the Wadi Halfa area, successions of mafic metavolcanics intercalated with minor felsic volcanics and clastic sediments were reported by STERN et al (1994). The volcanic material has yielded Rb/Sr whole rock ages of ~650 – 580 Ma and $^{87}Sr/^{86}Sr$ ratio of 0.7025 - 0.7031 (STERN et al, 1994). This data support the conclusion that the volcanics and the associated volcaniclastic material represent a juvenile addition to the crust without contribution from the older gneisses (STERN and KRÖNER, 1993).

2.2.6 Molasse-type sediments

These are slightly metamorphosed and weakly deformed sedimentary units reported in the Amaki area by EL RABAA (1976) and DAWOUD (1980) (Fig. 4). The Amaki sedimentary sequences occupy the uppermost stratigraphic position among the basement units. Lithologies include conglomerate and sandstone with minor intercalations of chert, volcanic tuffs and limestone (DAWOUD, 1980). This sequence is considered to represent molasse-type sedimentation of the last orogenic phase in the Nubian Shield (RIES et al, 1985).

In this study similar lithologies were reported at the western margin of the Gabgaba Terrane (chapter 3 and Fig. 5).

2.2.7 Magmatic rocks

These are the plutonic emplacements and the Cainozoic volcanic extrusions (Fig. 4). The plutons have various dimensions, shapes and compositions. They are divided to syn- and post-orogenic intrusions on the basis of the emplacement time (HARMS et al, 1990, 1994; RIES et al, 1985; VAIL, 1983). The syn-orogenic intrusions are I-type foliated granitoids intruded during the period 800-550 Ma ago (HARMS et al, 1990; RIES et al, 1985). These rocks are mainly intruded in the high-grade gneisses. The post-orogenic intrusions are A-type pinkish granites scattered in Wadi Halfa-Bayuda-Gabgaba area as ring dykes, batholiths and small stocks (VAIL, 1983). The rocks are not foliated and composed predominantly of quartz and alkali feldspars (VAIL, 1983). They have emplacement ages less than 550 Ma (HARMS et al, 1994; 1990; RIES et al, 1985; HARRIS et al, 1984). Nd and Pb isotopic ratios of the Wadi Halfa post-orogenic A-type granite showed that the participation of older crust in the generation of the granite is very minor (STERN et al, 1994). Similar conclusions were reached by RIES et al (1985) for granites in the southern Bayuda Desert.

Cainozoic volcanics are reported in many localities within the Wadi Halfa and Bayuda area (DAWOUD, 1980; BARTH and MEINHOLD, 1979; EL RABAA, 1976) (Fig. 4). They occur as flows and plugs of trachyte, basalt, tephrite, phonotephrtie, latites and phonolites (BARTH and MEINHOLD, 1979).

N-S trending felsite dykes cutting the Nubian sandstone formations are frequent in the Bayuda area (BARTH and MEINHOLD, 1979).

Cainozoic volcanics were extruded during the post-Nubian fault system which is believed to be the NW extension of the great East African rift system (BARTH and MEINHOLD, 1979). Ages assigned to the Cainozoic volcanicity range from Pleistocene to Tertiary (BARTH and MEINHOLD, 1979).

2.2.8 Phanerozoic sediments

These are sedimentary outliers scattered in the Wadi Halfa-Bayuda area (Fig. 4). The rocks belong to the Nubian sandstone formation which is of Mesozoic age (VAIL, 1978; WHITEMAN, 1971). The major occurrences of the Phanerozoic sedimentary rocks are north of Wadi Halfa and SW Bayuda Desert (Fig. 4).

3 KERAF PETROTECTONIC ASSEMBLAGE (KPTA)

This chapter is concerned with the description of the field relations and the petrography of the different rocks occur in the KSZ. The discussion is based mainly on the data collected during the fieldwork phase of this study.

The lithologies that comprise the KPTA are characterised by an abundance of low and medium grade carbonate-rich metasediments. These rocks are interpreted to have been formed in a shallow passive continental margin setting associated with a limited igneous activity. The name Bailateb group, suggested by STERN et al (1993) for these rocks, does not describe all lithologies that occur in the area. Therefore, the term KPTA is introduced to include these rocks which have the same background and are affected by the Keraf tectonic processes. The term KPTA is recommended for the following reasons: 1) Lithologies in the Keraf area are unique and can easily be distinguished from those to the east in the Nubian Shield and those to the west in the Nile craton. 2) Deformational styles and tectonic history reported for these rocks are distinctively different from the other surrounding rocks. 3) The metamorphic history and thus the P-T-t path are different from those of the other rocks in the region.

In the central sector of the KSZ, i.e. between Lat. 18°45′ and 21°0′ N (Fig. 5) the KPTA has revealed the following lithostratigraphic units:

1 High- to medium- grade gneiss (oldest)

2 Keraf ophiolitic melange

3 Metavolcanic suites

4 Siliciclastic metasediments

5 Carbonate-rich metasediments

6 Volcaniclastic sedimentary sequences (youngest)

Syn- and post-tectonic plutons and dykes with varies compositions and sizes are frequent in the Keraf area.

3.1 High- to medium-grade gneiss

The gneiss occurs in low-lying scattered outcrops in the area NE and E of Abu Hamed occupying the core of the Abu Hamed antiform (Fig 5). Lithologies are biotite-muscovite gneiss, biotite-garnet gneiss and biotite-garnet-hornblende gneiss (appendix 1 samples 11.13, 11.14 and 11.15). Minor lenses of marble, biotite schist and quartzite are frequently intercalated. Rocks of this gneiss sequence are not reported in the northern sector of the KSZ (north of Lat. 19°30`N). To the south they continue up to Dam et Tor shear zone (Fig. 4). East of dam et Tor the gneiss intercalates with bands of marble, quartzite, paragneiss and amphibolite. The names "supracrustal metasediments and high-grade metasediments" are used by some authors for similar suites in Bayuda Desert (VAIL, 1979; MEINHOLD 1979; DAWOUD, 1980; ABDELRAHMAN, 1993).

Field relations and mode of occurrence suggest that the high-grade gneiss and the low-grade metasediments (both siliciclastic and carbonate-rich) are closely related to each other thus indicating similar age and similar geodynamic environment. Due to the intensive polyphase deformation and the extensive cover of sand sheets, the contact between the gneiss and the other rock units of the KPTA could not be located precisely. In the two limbs of the Abu Hamed antiform, the gneiss is partially flanked by nappes of the Keraf ophiolite emplaced during D1 thrusting (Fig 5). This indicates a tectonic contact between the high-grade rocks and the Keraf ophiolite. The gneiss occupies lower stratigraphical position in Keraf and Bayuda areas and therefore, it is believed by some authors such as VAIL, (1979); DAWOUD, (1980) and RIES et al, (1985) to be the oldest sequence in the area.

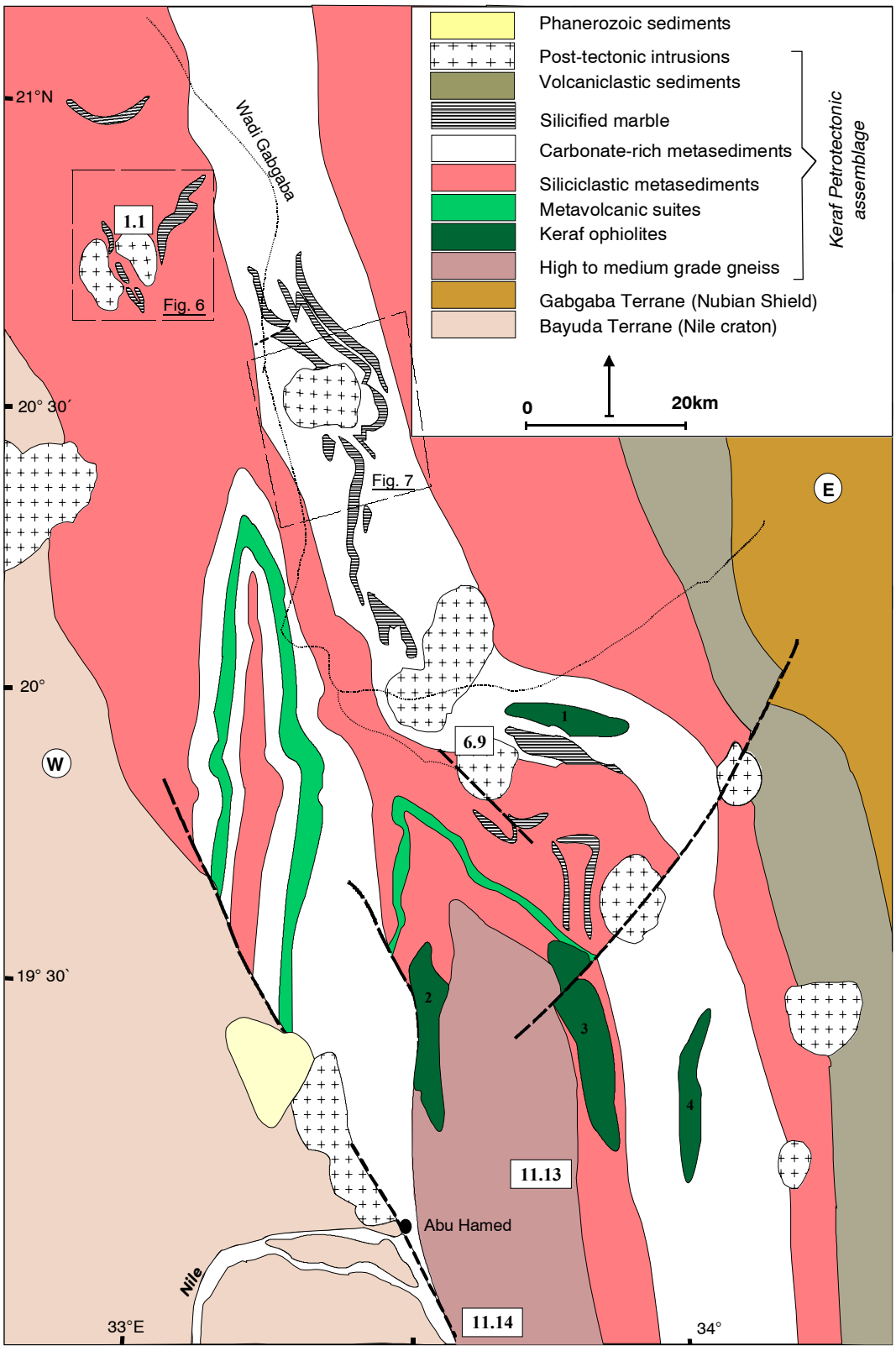

Fig. 5: Geological map of the northern and the central sectors of the Keraf Shear Zone (for location see Fig. 1). Note the N-S continuation of the strata and the dominance of the low-grade metasediments. Medium- to high-grade metamorphic rocks appear south of Lat. 19° 30`N. (the eastern and the western thrust boundaries are not indicated). Numbers in rectangles are the locations of the samples used in geochronology.

The mineralogical composition of these rocks is: quartz, microcline, plagioclase, biotite, muscovite, hornblende, calcite, gar net and opaque minerals. The crystals are medium to fine grained with anhedral outlines. Quartz is the most abundant mineral and occurs as porphyroblasts as well as in the matrix. Quartz crystals are highly strained and have cloudy appearance. The fine-grained quartz crystals are primary as well as secondary. Microcline is the second in abundance and occurs as large unhedral and as small equant crystals. Plagioclase is in the range of andesine-oligoclase and occurs as large to medium crystals. Biotite is reddish brown in colour (Fe-Ti rich) and forms medium to large laths aligned along the foliation planes. Muscovite is formed as fine-grained secondary crystals (sericite) after biotite. Hornblende is found in a limited number of samples and is sometimes retrograded to biotite, chlorite and/or epidote. Calcite occurs as accessory mineral formed after the primary plagioclases. Almandine garnet is found in some samples indicating amphibolite-facies metamorphism. Biotite and hornblende occur along S1 and S2 foliation planes indicating that the amphibolite facies metamorphism had taken place during D1 and D2 phases of deformations. Opaque minerals such as Fe-oxides, sphene, zircon and apatite are frequent in the gneiss.

The grade of metamorphism in the gneiss increases towards the south. At latitude 18°30′ N, east of the junction of the KSZ with the Dam et Tor shear zone (Fig. 4), grade of metamorphism in the gneiss is relatively higher (upper amphibolite facies) and the rocks develop very coarse (migmatitic) textures. Rocks available are amphibolite and almandine-hornblende-biotite gneiss (appendix 1 samples A55, A43, A52, A45, A26). Microprobe analysis of some hornblende crystals showed clionpyroxene cores indicating retrogression from granulite facies (see section 6.2). The gradual N-S increase in the grade of metamorphism of the gneiss may enable the division of the KSZ into three metamorphic sectors. The northern sector (north of latitude 19° 30`N) is characterised by lower green schist facies and all the primary structures and textures of the rocks are preserved. The middle sector (between latitudes 19° 30`and 19° N) is characterised by a mixture of green schist and amphibolite facies and the assemblage biotic-muscovite- chlorite with occasional garnet and hornblende. The southern sector (south of latitude 19°N) is dominated by rocks in the upper amphibolite facies. The gradual variation in the grade of metamorphism is attributed to a progressive increase in the P-T conditions from N to S due to variations in the crustal thickening and stacking accompanied D1 and D2 phases of deformation (see chapter 4).

Low-grade mineral assemblages were formed due to the retrogressive metamorphism which accompanied the D4 shearing deformation. Secondary chlorite, epidote, calcite and quartz were formed after biotic, amphibole and plagioclase.

The high- to medium-grade gneiss in the central and southern sectors of the KSZ are similar to the high grade metamorphic rocks to the west of the Nile in the Bayuda (Fig. 4) and the Wadi Halfa Terranes (VAIL, 1979; MEINHOLD, 1979; DAWOUD, 1980; STERN et al, 1994; DENKLER et al, 1994). Some authors (VAIL, 1979) believe that the gneiss in the KSZ was thrusted from the Bayuda area during the Keraf deformation. In this study field evidences for the transportation of the Keraf gneiss from the west of the Nile were not reported. There is insufficient isotopic investigations conducted in the area to determine genetic relationships between these lithologies. I suggest that the gneiss in the KSZ has acquired ist present mineralogical composition due to the higher pressure conditions resulting from the intensive crustal thickening and stacking that occurred in the southern and middle sectors of the Keraf.

3.2 Keraf ophiolitic melange

These are highly sheared, fault-bounded, carbonated and serpentinized mafic-

ultramafic rock assemblages in the Keraf and Bayuda areas (BARTH and MEINHOLD, 1979; MEINHOLD, 1979; DAWOUD, 1980; AHMED et al, 1980; ALMOND and AHMED 1987). The rocks were initially interpreted as mafic plutonic intrusions (MEINHOLD, 1979), or as ophiolitic nappes transported from other tectonic levels to the east in the Red Sea Hills (ALMOND and AHMED, 1980). ABDELRAHMAN (1993) concluded from geochemical investigations that these rocks consist of a basal ultramafic phase (basal tectonites), ultramafic cumulates and a mafic sequence of dismembered ophiolitic melange. STERN (1994), SCHANDELMEIER et al (1994) and ABDELSALAM et al (1995) have described these mafic-ultramafic sequences as remnants of a back arc basin (Mozambique Ocean) which once existed between the Nubian Shield to the east and the Nile Craton to the west.

In this study four major mafic-ultramafic occurrences were mapped in the area N and NE of Abu Hamed (Fig. 5). The outcrops occur as ridges which are named ridge 1 up to ridge 4 to make description easy (Fig. 5). The rocks in these ridges are serpentinized, carbonated, highly sheared, fault-bounded and metamorphosed in the green schist facies. Field relations indicate that the rocks are emplaced by D1 thrusting. In this study, the results of geochemical analysis is presented to confirm or disprove their oceanic origin and to postulate a tectonic and a geochemical environment for their emplacement (chapter 5).

In the mafic-ultramafic occurrences the following lithologies are reported: harzburgite, dunite, pyroxenite, massif chromite, layered and massif gabbro, plagiogranites, basalt and chert-jasper layers. The rocks, in many places, are converted to talc-schists, chlorite-tremolite schists and serpentinites. In spite of these transformations and the flaky nature of the secondary minerals, the rocks are densely packed and have coherent appearance. In some places large massif lenses and blocks of ultramafics surrounded by serpentine-talc schist are reported. They give a melange appearance for the outcrops (Plate 1). The lenses and blocks are the ones sampled for the geochemical investigations in this research.

The northernmost mafic-ultramafic outcrop (ridge 1) is located at about 90 km northeast of Abu Hamed within the carbonate-rich low-grade metasediments (Fig 5). The outcrop forms an E-W trending ridge (~ 5 x 1 km) surrounded by low-lying outcrops of the same composition but transformed to talc-serpentine-chlorite material. The present position and orientation of the ridge is controlled by the D4 shearing. Lithologies in ridge 1 include a serpentinite matrix in which unaltered lenses of pyroxenite and gabbro are embedded. Gabbro contains large crystals of pyroxenes which are in some samples altered to concretions of iron oxides. The pyroxenite occurs as bodiform enclosures within the serpentinite. The low-lying outcrops include serpentinite, chert and ferrigenous sedimentary material. This ophiolitic ridge represents a nappe of ultramafic tectonite which was emplaced during D1 thrusting over the Keraf metasediments. Primary contacts between the rocks are not observed. Petrographically, the rocks are reconstituted and not all of the primary mineral phases are existing. Mineral assemblages of selected samples from ridge 1 are shown in appendix I (samples: 5.7, 5.7c and 5.11).

The westernmost mafic-ultramafic occurrence, ridge 2, is located at about 20 km north of Abu Hamed (Fig. 5). The occurrence of the outcrop is controlled by the NW-trending left-lateral D4 shear faults (Ras Humar fault) which pass through the western limb of the Abu Hamed antiform (Figs. 5 and 6). The ridge is partially covered by sand dunes and the rocks are weathered to a grey serpentine-talc material with concretions of iron oxides. The W and the SW parts of the ridge are low-lying highly weathered outcrops. The N part of ridge 2 form a N-S trending (5-10 x 1-5 km) outcrop of massif dunite and pyroxenite with chromite occurrences. Chromite occurs as

euhedral grains within the dunite and the pyroxenite or as massif discontinuous lenses (podiform) within the dunite. The dunite and the pyroxenite were partially reconstituted to a massif serpentinite. In thin sections, the reconstituted samples show serpentine-talc-chlorite-epidote-calcite. Some samples have shown only serpentine and opaque minerals. Petrography of representative samples are shown in appendix I (samples: 8.8a, 9.4a, 9.5a, 9.5b, 9.5d and 9.7).

To the east of ridge 2 another NNW-trending mafic-ultramafic outcrop (ridge 3) is mapped (Fig. 5). Ridge 3 is located within the low-grade siliciclastic metasediments and it marks the eastern limb of the Abu Hamed antiform (Figs. 5 and 6). Lithologies in this ridge include layered and isotropic gabbro, plagiogranite, dolerite, basalt, and iron-rich chert. The rocks are in the green schist facies grade of metamorphism. The isotropic and the layered gabbro form the greater part of the ridge (about 60% of the outcrop). The layered gabbro shows alternation of black and grey bands of few cm thickness (Plate 1). The gabbro shows the mineral assemblage: chlorite-epidote-amphibole-plagioclase-pyroxene (altered). It is associated with a plagiogranite which has the mineralogical composition of calcic plagioclase, amphibole, biotite, quartz, chlorite, calcite and epidote. Dolerite occurs in the form of discontinuous patches overlying the gabbro. It is more metamorphosed than the other accompanying ophiolitic members and no distinct primary structures were observed. The basalt occurs as highly weathered scattered patches within the dolerite. Weathering, shearing and metamorphism have destroyed most of the igneous textures. The petrography of representative samples (10.1a, 10.8b, 10.8d, 10.9a, 10.9d and 10.11) is listed in appendix I.

The fourth locality in which mafic-ultramafic rocks are mapped is a N-S trending discontinuous outcrop (ridge 4) located at about 60 km NE of Abu Hamed (Fig. 5). Ridge 4 extends for more than 10 km and forms a prominent topographical high. The outcrop is located in the carbonate-rich low-grade metasedimentary belt of the KSZ (Fig. 5). Lithologies reported from ridge 4 include gabbro, microdiorite, pyroxenite, and massive serpentinite. These rocks occur as large exotic blocks enclosed in a serpentine-iron oxide-talc-carbonate rich matrix. They form sigma-structures and are rotated by the Keraf D4 shearing into N-S trending stretched blocks. D4 phase of shearing had obliterated the primary contacts between the rocks and a melange appearance is formed by the large-scale blocks. The small-scale competent rock fragments form boudin structures due to the difference in the rheological competence to the serpentinite matrix (Plate 1). To the north and to the east ridge 4 is associated with a reddish iron-rich alluvial cover which extends for more than 10 km in diameter. This alluvial cover resembles the laterites and the gossans associated with similar mafic-ultramafic sequences in the Red Sea Hills, Nuba mountains and Ingessana (ABELRAHMAN, 1993; BAKHIET, 1994; WIPFLER, 1994). The petrography of representative samples (11.1b, 11.1c, 11.2, 11.4b, 11.8a and 11.8c) is listed in appendix I.

Small scale (not to the map scale) mafic-ultramafic outcrops are reported in this study within the low-grade siliciclastic sediments in the eastern margin of the KSZ**.** Lithologies in these outcrops are serpentinite, gabbro and dolerite.

3.3 Metavolcanic suites

These are thin bands (100 - 200 m thick) found at two localities within the Atmur synform and in the outer layers of the Abu Hamed antiform (Figs. 5 and 6). They form continuous layers which are concordant with the different layers of the low-grade carbonate-rich and the siliciclastic metasediments. The metavolcanics and the low-grade metasediments preserve structural elements covering all phases of the Keraf deformation, thus they may have the same age and the same tectonic history. The metavolcanics form low-lying outcrops

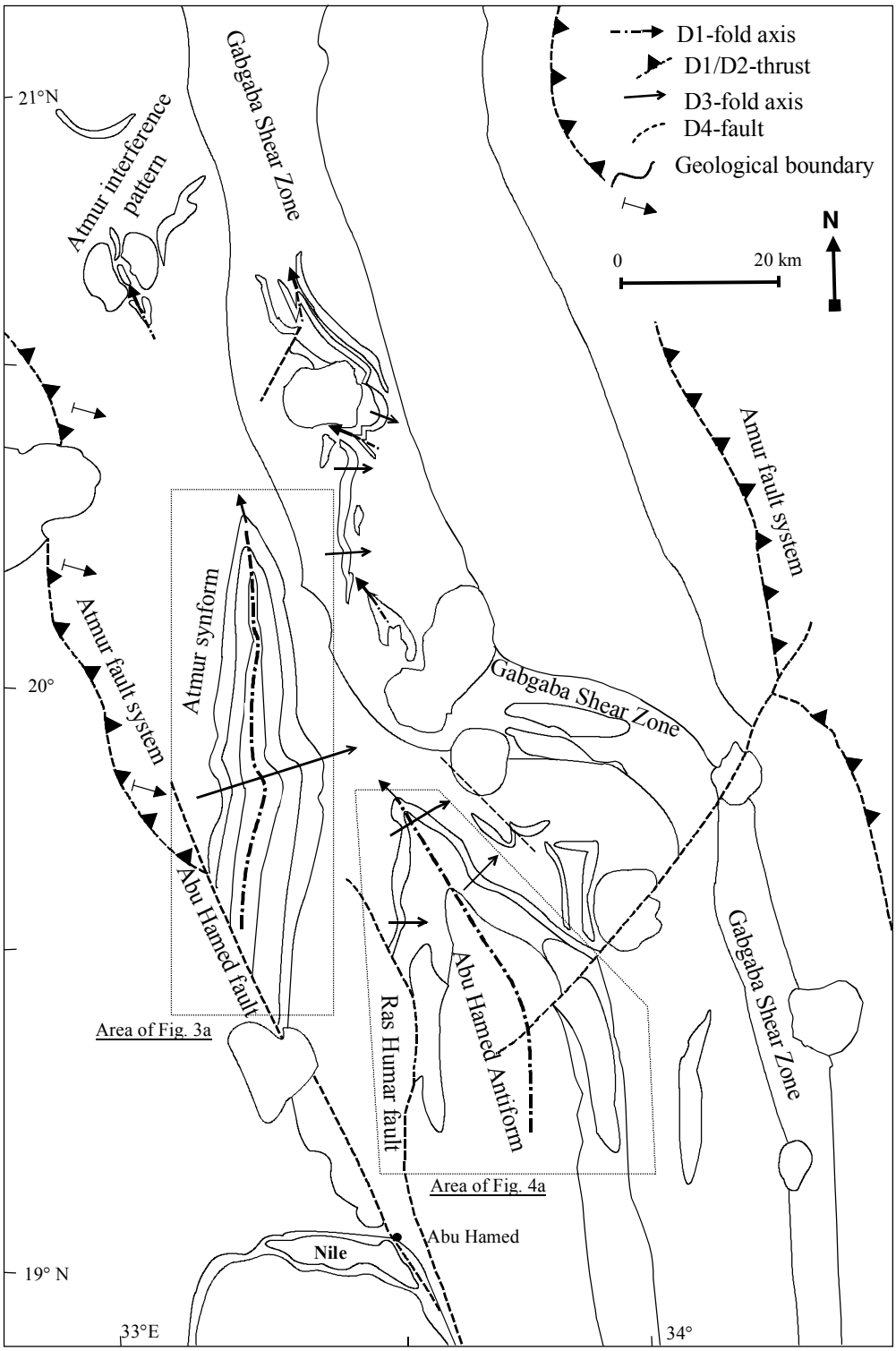

Fig. 6: Structural map of the northern and central sectors of the Keraf Shear Zone shows names of the major structures mapped in this study (for location see Fig. 1).

which are highly weathered and sheared. Lithologies are meta-basic and meta-intermediate volcanics which appear as dark and grey patches respectively. The meta-basic volcanics are mostly metabasalts which have the assemblage: pyroxene (relicts) plagioclase (kaolinitized), actiolite, biotite, chlorite, calcite, epidote and secondary silica. The intermediate metavolcanics are meta-andesite and meta-microdiorite. These rocks are limited in occurrence and form

alternate layers with the meta-basalt. Petrography of representative samples showed the assemblages: plagioclase (kaolinitized), hornblende, chlorite, calcite, epidote and opaque minerals.

The metavolcanics in the KSZ can be correlated with similar lithologies reported in Al Koro, south of Abu Hamed (DAWOUD, 1980; RIES et al, 1984), Dam et Tor (ABDELRAHMAN, 1995), north of Barber (MEINHOLD, 1979). (Fig. 4) and Wadi Halfa (STERN et al, 1994) Al Koro metavolcanics gave Rb/Sr ages of about 800 Ma (RIES et al, 1984). Geochemistry of the metavolcanics in Bayuda and Wadi Halfa Terranes is not well understood due to the limited studies so far conducted. The close association of these rocks with the pelagic and the volcaniclastic sediments and the limited geochemical investigations conducted by RIES et al (1985) and during this research (chapter 5) favour an aqueous environment of extrusion.

3.4 Siliciclastic metasediments

These are low-grade metasedimentary rocks which cover more than 60% of the surface area of the KSZ (Fig. 5). They occur as low-lying outcrops mostly covered by sand sheets or as silicified N-S trending ridges that mark the trend of the KSZ. This group of rocks occurs mainly in two wide bands separated by the layer of the carbonate-rich metasediments (Fig. 5). At the eastern margin these rocks are separated from the volcaniclastic metasediments by steep to vertical faults (Amur fault system), while in the west they are separated from the high-grade gneiss of the Bayuda Terrane by a low angle west verging thrust (Atmur fault system) (Fig. 6). Lithologies comprising this group include: sandstones (~50%); carbonate rocks (~25%); cherts and mudstones (~15%), conglomerates (~5%) and rare doleritic and granitic sills. These lithologies have been subjected to green-schist - amphibolite facies metamorphism and also to the Keraf shearing which produced highly silicified shear planes preserved as elevated ridges.

The sandstones vary in composition and texture. In composition they range from arkoses (in which quartz grains are the dominant constituent) to greywackes (in which the composition is quartz, clays and rock fragments). In both types calcite is an abundant constituent. In some localities the sandstones are highly silicified and are hard, while in other localities they are fragile and are poorly cemented. The sandstones preserve most of their primary structures such as bedding planes, graded bedding, and laminations (Plate 2). These structures indicate a passive margin depositional environment in which pelagic sediments and turbidites are the dominant constituents. The green schist facies metamorphism produced chlorite, epidote and calcite. Geochemical classification and affinities are discussed in chapter 5.

Carbonate rocks associated with these clastic sediments are marbles which have white, brown and black colours. White marble is predominantly composed of calcite with minor quartz, while coloured marble contains besides calcite and quartz other minerals such as dolomite, clay minerals chlorite and epidote. In some localities marble can be mapped as grey, banded and silicified (Figs. 7 and 8).

Chert and mudstone are recognised as small lenses intercalating with the sandstone in the western band of this series. Mudstone is reddish in colour with black inclusions. The low grade metamorphism produced chlorite, epidote, albite and secondary silica. Pyrite is a common accessory in these rocks. Some of the pyrite-rich chlorite schists can be mapped as independent rock units (Fig. 8).

The conglomerate member of this group of the clastic sediments is found in the west close to the boundary with the gneiss of the Bayuda Terrane. The pebbles vary in size, shape and composition. The dominant size ranges from 2 to 15 cm greatest dimension, and the domi

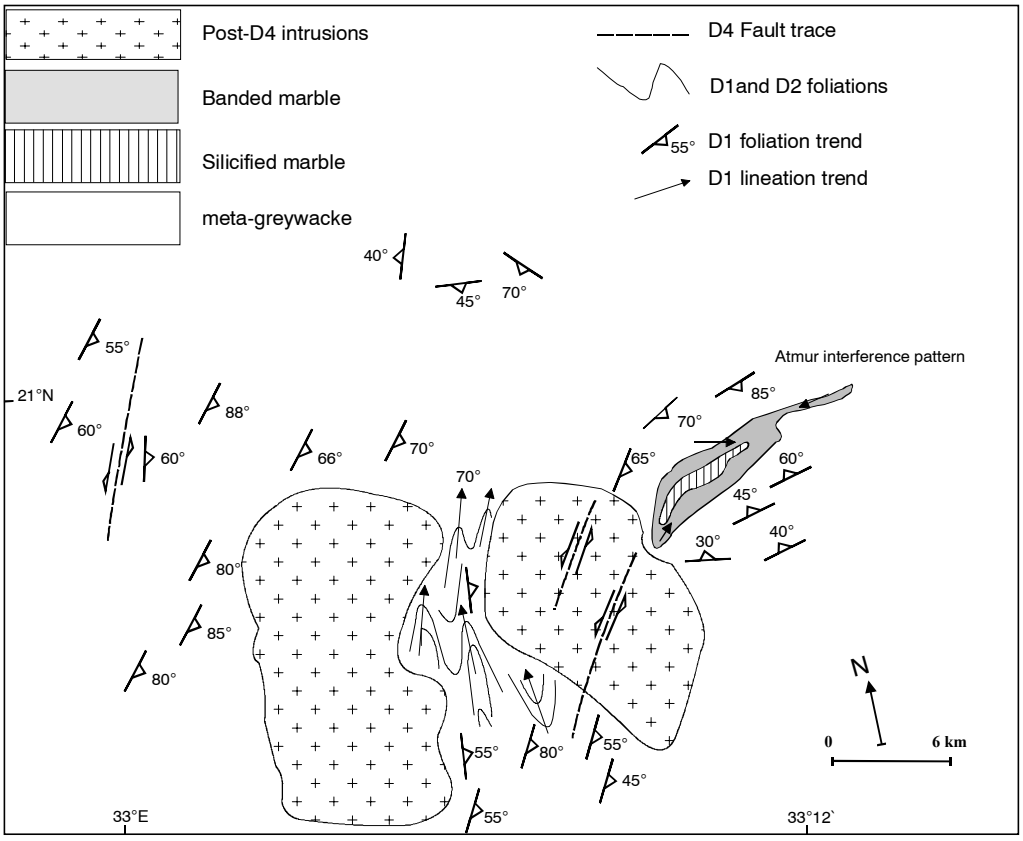

Fig. 7: Geological map of the intersectional area of the Keraf Shear Zone with the Atmur suture (for location see Fig. 5). D1 and D2 foliations are randomly oriented due to the influence of the pre-Keraf structures. Atmur dome-basin interference pattern is a NE-SW oriented doubly plunging synformal structure formed due to the superimposition of the D1 folds over the pre-Keraf NE-trending folds.

nant shape is rounded to sub-rounded. Conglomerate located close to the D4 shearing planes have elongated fragments with their greatest dimension oriented in a N-S trend. The composition of the pebbles is granitic, granodioritic, or their volcanic equivalents. The supporting matrix is composed of a fine-grained clastic material.

3.5 Carbonate-rich metasediments

This group comprises all metasediments which have more than 70% carbonate (marble and limestone). They occupy the central sector of the KSZ (Figs. 5 and 8). This sector of the KSZ has no sharp boundaries with the surrounding siliciclastic metasediments, thus indicating similar depositional processes but different deposition sites within the basin. The thickness of this carbonate-rich layer can not be estimated because it is not easy to identify its base. The aerial width of the layer is 15 - 20 km (Fig. 5). In this zone, the Keraf D4 shearing is very intense and the vertical to subvertical N-S trending D4 shear foliations are the dominant structures throughout the entire zone. Silicification planes are existing as resistant carbonate bands intercalating with the marble (Figs. 5 and 8). Marble ranges in colour from white, grey, brown and black among them the grey is the dominant. The white marble is composed of fine-grained calcite crystals with minor dolomite and ankerite. In the vicinity of the post-tectonic intrusions the calcite crystals have been recrystallised and thus give a sugary texture for the marble. White and silicified marble is composed of calcite and

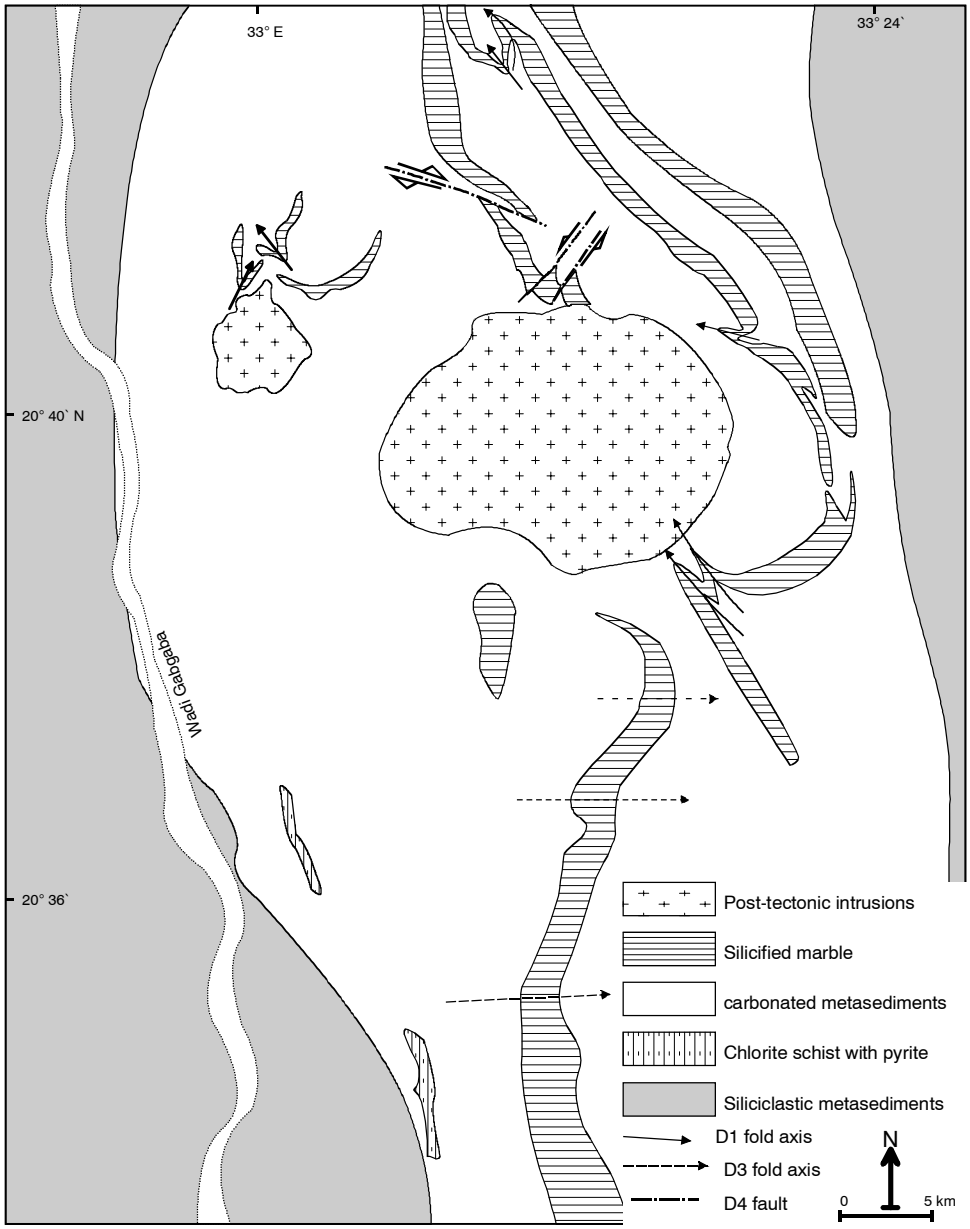

Fig. 8: A simplified geological map of the central part of the Gabgaba Shear Zone (for location see Fig. 5). Structures are preserved in the silicified marble. D1 and D3 folds are noticeable features in all scales.

quartz crystals. The brown marble is dolomitic in composition and some samples contain up to 20% MgO. The black marble is rich in clays and mud inclusions. Associated with the marble are minor clastic metasediments (sandstones, conglomerates and pelites), which are in some places metamorphosed to chlorite-epidote schists.

Primary textures and structures such as sedimentary layering and laminations and oolitic textures are common features among the marbles (Plate: 4). These are typical features of shallow marine depositional environment.

3.6 Volcaniclastic Sedimentary Sequences

This sequence represent a thin sedimentary layer occupying the easternmost margin of the Keraf assemblage (Fig. 5). The sedi-

ments have been deposited on the eastern margin of the Keraf basin and have received clastic material mainly form the east where arc volcanic and plutonic rocks of the Gabgaba Terrane predominate. This volcaniclastic layer has an average apparent width of 5-10 km with a reduction in width from north to south. It is separated from the volcanic rocks in the Gabgaba Terrane to the east by vertical and subvertical NE to N trending shear planes (the Aumr D4 fault system) (Fig. 6). The Amur fault planes represent the structural boundary between the KPTA and the arc assemblages of the Gabgaba Terrane. Lithologies are mainly polymict conglomerates (80%) and volcanogenic detrital fine material (20%). The volcaniclastic material comprises volcanic clasts of various size (from few mm to 30 cm length) and various composition (rhyolite, andesite and basalt). Rare clasts of dioritic composition are also seen. The shape of the clasts is, generally, elliptical to subrounded and their present orientation is controlled mainly by the Amur D4 fault system. The cementing material in the conglomerate is a mixture of volcanic fine-grained material and silica. Metamorphism and the intensity of the early phases of deformation (D1 and D2) are very low in the volcaniclastic sequence. This may indicate that this layer can represent a latest phase of sedimentation in the Keraf area. Similar lithologies, the Amaki series, were recognised in the eastern Bayuda Desert (EL RAABA, 1976; DAWOUD, 1980; RIES et al, 1985).

3.7 Plutonic and dyke intrusions

The study area was affected by post- and syn-D4 igneous activity which has resulted in the emplacement of numerous plutons and dykes (Figs. 5, 7 and 8). The plutons have various sizes, shapes (stocks, batholiths or ring dykes) and compositions (granitic, granodioritic or dioritic). The mafic and the intermediate intrusions occur mainly as dykes and stocks while the felsic intrusions occur as ring dykes and batholiths. Petrography of the granitic intrusions is quartz, microcline, albite and biotite with occasional perthitic and graphic textures. Mineralogy of the gabbroic stocks is mainly Ca - plagioclase and clinopyroxene with minor amphibole and biotite. The diorite is coarser in texture than the gabbro. Petrography of representative dykes and plutons are listed in appendix I.

The plutons are affected by the D4 shearing and they are concentrated in the areas which are characterised by high D4 strain. The dykes are a few 100 meters in length, have NE to NNE trend and they are neither affected by the green schist facies metamorphism nor by the D4 shearing. The possible genetical relation and the geochemical affinities of these rocks is discussed in chapter 5.

4 STRUCTURAL EVOLUTION OF THE KSZ

4.1 Introduction

A prolonged and a complex polyphased deformational history has been recognised in the Sudanese sector of the Nubian Shield by STERN (1994), VAIL (1988) KRÖNER et al (1987) and many other authors. Complicated structures have been reported from the crustal segment to the west of the Nile (SCHANDELMEIER et al, 1988; RIES et al, 1985; VAIL, 1975; etc.). On the other hand, a very limited structural work has been focused to decipher the structural nature of the boundary between the Nubian Shield and the Nile craton in northern Sudan (SCHANDELMEIER et al, 1994; ABDELSALAM et al, 1994 and 1995). The Nubian Shield in the study area is represented by the Gabgaba Terrane (ABDELRAHMAN, 1995) and the Nile craton (ROCCI, 1965) is represented by the Bayuda and Wadi Halfa Terranes (SCHANDELMEIER et al, 1995) (Fig. 3). As we have demonstrated earlier, this boundary is locally occupied by the KSZ in northern Sudan and southern Egypt (Figs. 1 and 3). In this section of the study the following structural objectives will be addressed:

1) Geometrical description of the structural elements formed during the different phases of the structural evolution of the KSZ.
2) Deformational history and tectonic implications of the Keraf shearing.
3) Kinematics of the transpressive deformation and localisation of strain in the KSZ.
4) Relationships between the pre-Keraf and Keraf structures.

The dominant structures in the studied sectors of the KSZ are N- to NW-trending and W-verging folds, thrusted nappes and other genetically-related structures. The structures were evolved through a poly-phased ductile deformational regime which was terminated by a brittle phase. The ductile deformation was resolved into three major phases (called hereafter D1, D2 and D3 phases). They have resulted in formation of folds, planar and linear fabrics in the area between Abu Hamed and the Sudanese-Egyptian border (Fig. 1). On the other hand, the brittle phase of deformation (D4 phase) resulted in conjugated sets of left-lateral and right-lateral wrench faults accompanied by subhorizontal E-W oriented shortening and vertical extension (thickening) components.

4.2 Geometry of the structural elements

Prior to a detailed discussion of the Keraf transpressional deformation, strain partitioning into E-W shortening and N-S elongation and strain localisation along the Nile craton-Nubian Shield tectonic boundary, a brief account of the structural elements associated with the main phases of deformation (D1, D2, D3 and D4) is presented below.

4.2.1 D1 Structures

Structures generated during D1 represent the main structural features in the KSZ. D1 folds are recognised in the entire domain of the KSZ and, even beyond, to the west of the Nile where they are superimposed on pre-Keraf structures producing complicated fold interference patterns. These interference patterns are reported at the junctions of the Keraf with the Atmur-Delgo suture in the north and with the Dam et Tor shear zone in the south (Fig. 1) (see section 4.6). D1 folds are recognised at various scales ranging from major, minor and mesoscopic structures. The major structures are mapped in two main locations: the Atmur synform and the Abu Hamed antiform (Figs. 6, 9 and 10). The Atmur synform is a NNE-trending tight fold with a long amplitude (25-30 km) and it governs the distribution of the rocks in the area north of Abu Hamed (Figs. 5 and 9b). The hinge zone of the structure is

preserved and can be mapped on the satellite image (MSS band 4,5,7 No. 186-46), whereas the limbs are partly covered by sand dunes and are truncated by the Abu Hamed D4 strike-slip fault (Figs. 6 and 9a). Distribution of the rock units within the structure from the core towards the limbs is: marble, siliciclastic metasediments, metabasalt and marble (Fig. 5). Fold axis lineations (L1) are steep or gently plunging towards the NNE or towards the NNW (Fig. 9e and 9d). The axial plane cleavages (S1) make small intersection angles (10-15°) with the bedding planes and the primary laminations.

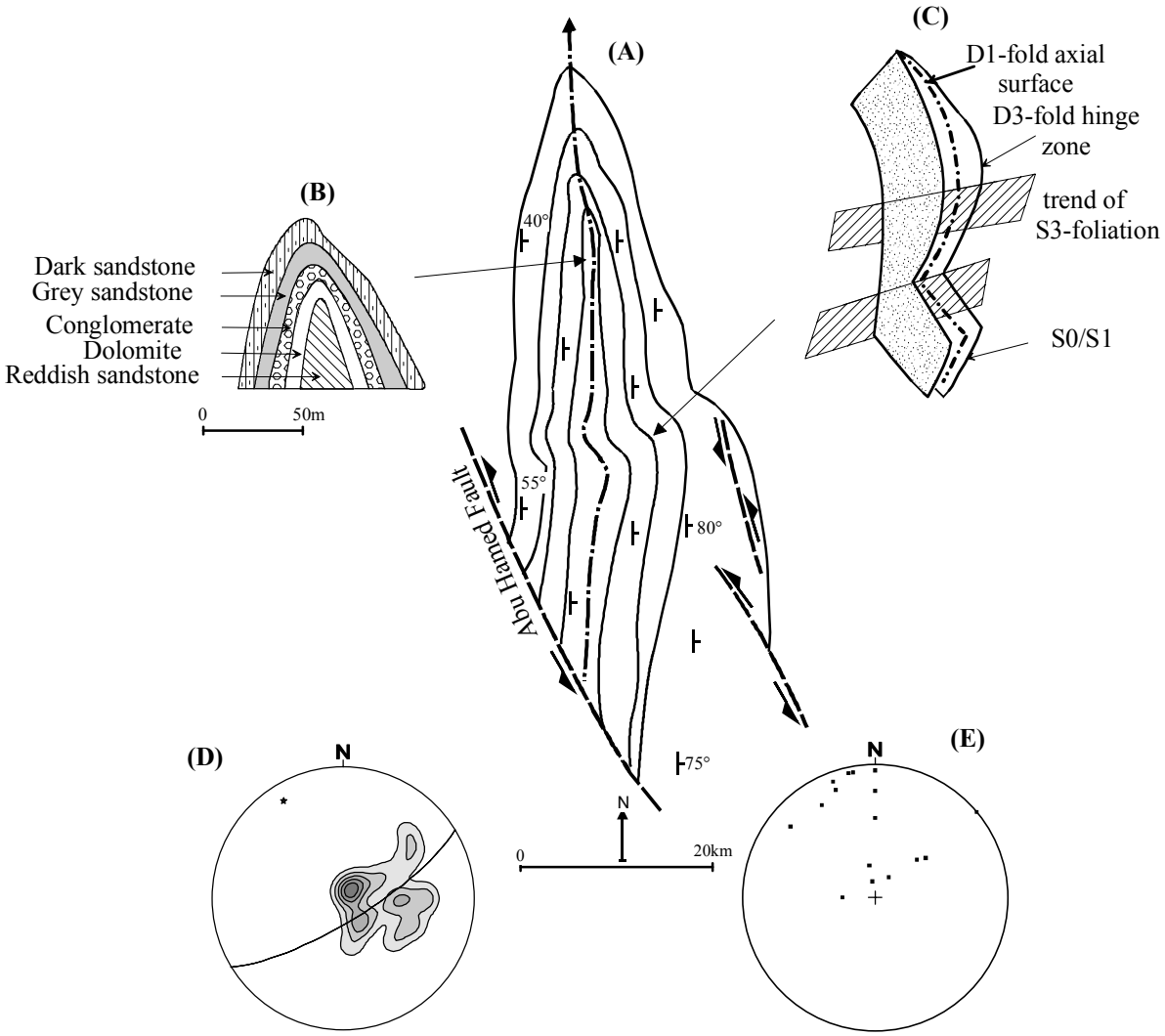

Fig. 9: A) Atmur synform with S0/S1 foliation trend (for location see Fig. 6). **B**) distribution of lithologies and how they are controlled by the Atmur synform. **C**) divergent- convergent interference pattern formed by refolding D1 folds around D3 fold axis. **D**) Pi plots of poles to planes (bedding & S1 foliations) from the hinge zone of the Atmur synform (N= 26). **E**) Orientation of D1 fold axis within the Atmur synform (N = 17). Note the axes vary in plunge from horizontal to subvertical with NE to NW bearing.

L1 and S1 are largely reoriented by the subsequent D2 and D3 structures. The Atmur synform is refolded by D3 folds producing a convergent-divergent (type-III) interference pattern (RAMSAY and HUBER, 1987) (Fig. 9c).

The Abu Hamed antiform, the second D1 major structure, is located to the SE of the

Atmur synform (Figs. 6 and 10). This structure is topographically defined by occurrence of the N-S trending ridges of the Keraf ophiolites in the limbs and the high-grade gneiss in the core (Fig. 5). The antiform is disturbed on both limbs by the D4 faults (Fig. 10a). The variation in lithology and thus in the rheological competence have made Abu Hamed antiform to have larger wave length and shorter amplitude compared to Atmur synform. The axial plane of the Abu Hamed antiform is folded around the NE plunging D3 fold axes forming type III interference pattern shape (RAMSAY and HUBER, 1987). Fold axes within the structure are moderately (40-50°) plunging towards the NNW (Fig. 10b).

Other D1 folds mapped in this study, smaller in scale than the above mentioned two structures, are reported in the silicified marble within the carbonate rich layer in the Gabgaba Shear Zone (GSZ) (Fig. 8). In the GSZ the D1 folds are rotated sinistrally by the D4 shearing. Fold axes are plunging towards the NW (Fig. 8). Type III interference patterns, of the map scale, are formed by the superimposition of the D3 folds over the D1 folds. Folds of similar scale are reported south of the Atmur interference pattern (Fig. 7).

Mesoscopic, not to the map scale, D1 folds are reported from the high-grade gneiss to the N of Abu Hamed (Fig. 10d and plate 4). These folds are upright to moderately plunging (15 - 30°) towards the N. Such orientation suggests location on the western limb of a D2 major synform where the planar structures are vertical and the linear ones are to horizontal (Fig. 10c). Other mesoscopic D1 folds are reported in the low-grade metasediments and the ophiolites (Plate 5).

Associated with the D1 folds are D1 thrusts. They are reported bordering the Keraf ophiolitic melanges. The thrusts have been reoriented by the younger D4 faults and they are not traceable for long distances. Movement across the thrust is characterised by westward vergence. This vergence is the same as that of the undisturbed D1 folds. A major D1 thrust is preserved at the western boundary of the KSZ, between the KPTA and the gneiss of the Nile craton. This marginal thrust is hereafter called Atmur fault system (Fig. 6). The Atmur thrust is partially affected by the Abu Hamed D4 strike-slip movements but the original westward vergence is preserved in most of the investigated localities. Another D1 thrust zone, which is called hereafter the Amur fault system, exists between the KPTA and the Gabgaba Terrane. This thrust was steepened by D2 folds and is partially over printed by the D4 faults (Fig. 11). Field relations and structural constructions suggest that D1 thrusts have caused:

1) emplacement of the ophiolitic melanges over the Keraf clastic metasediments
2) imprecation of the Keraf ophiolites and the formation of the ophiolitic melanges
3) emplacement of the KPTA over the western flank of the Nile craton
4) juxtaposition of the Gabgaba Terrane with the KPTA.

Foliations generated during D1 (S1 foliations) are axial planar cleavage and they represent the main planar fabrics observed in the entire area. They are defined by the grain shape and the aligned fabrics of chlorite, epidote, muscovite, biotite and calcite in the chlorite schist and are represented by fracture cleavages in the quartzite and the silicified marble. In the gneiss, S1 are defined by biotite and hornblende and in the ophiolites they are defined by serpentine and the platy flakes of talc and chlorite. S1 fabric has been significantly transposed and crenulated by the subsequent D2, D3 and D4 deformations (Fig. 10c and plate 5). S1 foliations, generally, have N-S trend and dips towards the E and the SE.

Developed within the S1 planes are mineral lineations (L1) which are defined by quartz, plagioclase, calcite and serpentine crystals. L1 have been disposed and reoriented by D2 and D3, thus range in plunge from 10° to 90° (Fig. 9e). This orientation is determined

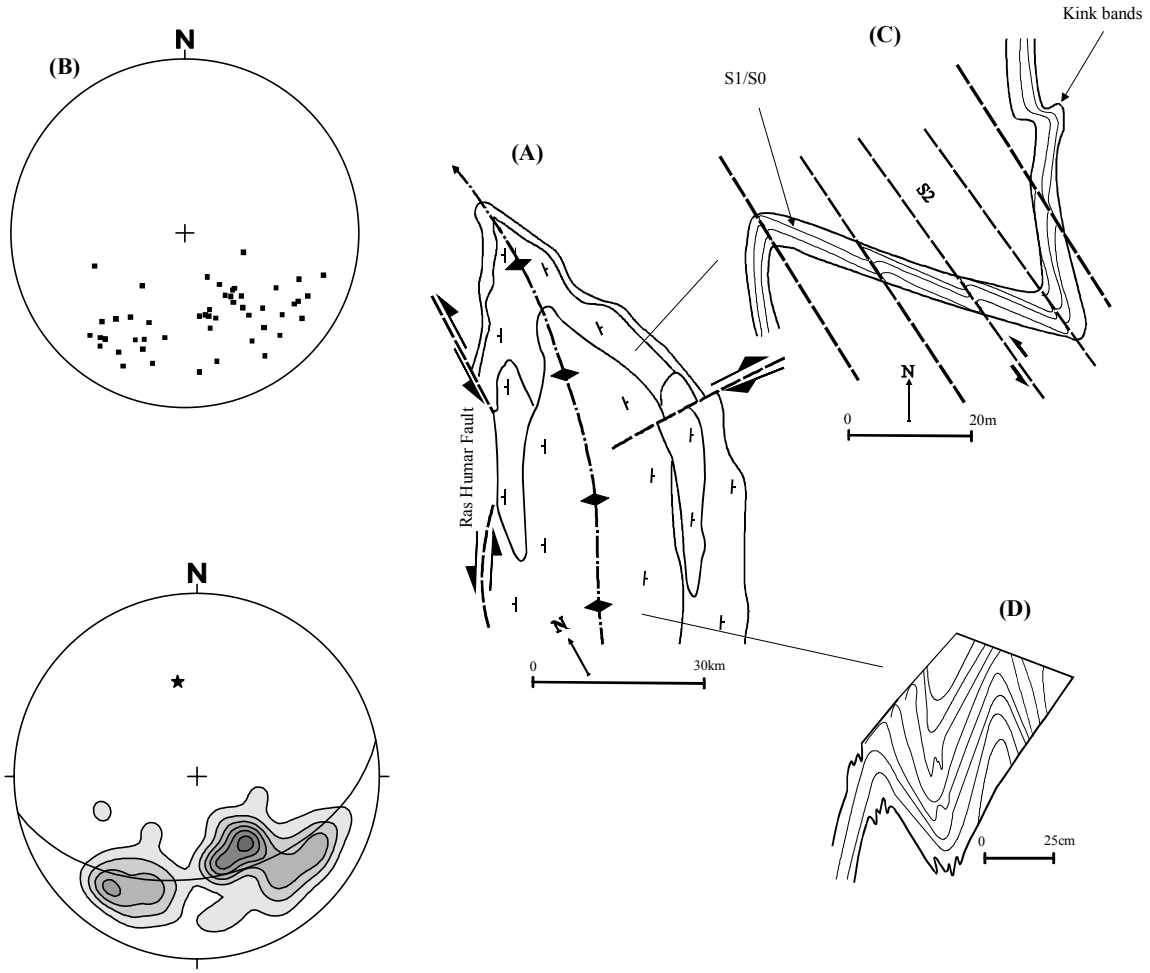

Fig. 10: A) Abu Hamed antiform with S0/S1 foliations and lineations readings (for location see Fig. 6). **B**) Pi plots of poles to planes (S0 and S1 foliations), the antiform is symmetrical about a NNW trending axis (N= 43). **C**) D2 minor fold preserved in the serpentinite with crenulation, dislocation and kinking of S0/S1 (sketch is based on a field photograph). **D**) Upright minor D1 fold in the gneiss NE of Abu Hamed (diagram is based on a field photograph).

by the position of L1 relative to D2 folds and D4 shear planes.

4.2.2 D2 Structures

Folds produced during D2 phase of deformation are preserved mainly as mesoscopic structures within the low-grade metasediments and the serpentinized ultramafic sequences (Plates 5). Major D2 folds are only inferred structures (Fig. 11). D2 folds are N-trending asymmetrical structures. They are upright with a subvertical eastern limb and the western limb is moderately dipping to the E. (Fig. 10c). D2 folds are tight to open with interlimb angle ranging from 75° in the serpentinized ultramafics to 30° in the silicified carbonates. The shape of the hinge zone of the D2 folds is rounded in the silicified lithologies and angular in the serpentinites (Plate 5). The subvertical limbs of the D2 folds in certain localities show kink bands with NE plunging axes (Fig. 10c and Plate 5). Fold axis of these kinks have orientation 30°/35°.

Planar axial foliations (S2) associated with D2 folds are closely spaced and are defined by the orientation of chlorite, amphibole, micas, serpentine and talc. S2 foliations crenulate and rotate S1 about sinistral planes

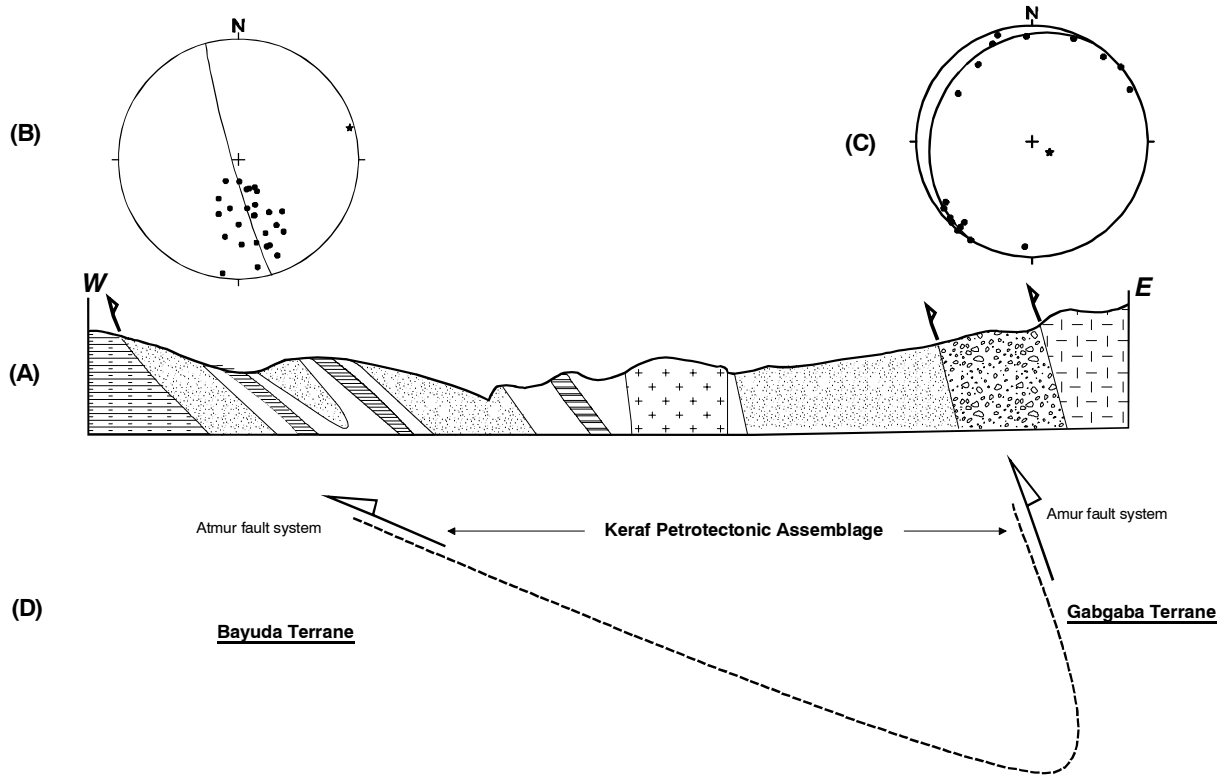

Fig. 11: **A)** Cross-section along the line joining the points W and E in Fig. 5. **B)** Pi plot of poles to thrust planes from the Atmur fault system (N = 27). **C)** Pi plot of poles to thrust planes from the Amur fault system (N = 18). **D)** W-E configuration of the planar fabric trajectories which mark a west verging D2 fold that governs the tectonic relation between the KPTA and the surrounding terranes.

of very minor discontinuities (Fig. 10c and Plate 5). S2 foliations are W to NW verging fabrics. L2 lineations are preserved as intersectional lineations formed by the intersection of S1 with S2 foliations.

The geometrical configuration of the various structures in an E-W cross section along the KSZ describes a major inferred D2 fold (Fig. 11). The western limb is moderately (40-50°) dipping towards the east and the eastern limb is subvertical. This configuration indicates that D2 folds are asymmetrical collisional structures formed as the result of the collision of Gabgaba and Bayuda Terranes.

4.2.3 D3 Structures

Structures associated with the latest ductile phase of deformation (D3) can be easily identified in the map as well as in mesoscopic scales as E-W trending open folds (Fig. 8 and Plate 7). D3 folds are symmetrical around steeply E plunging axes with rounded hinge zones. They are superimposed over D1 and D2 folds producing type III interference patterns (convergent-divergent patterns) (RAMSAY and HUBER, 1987). S3 are faint south-verging axial planar cleavages which intersect S1 and S2 foliations at right angles. L3 are intersectional lineations, where S3 are relatively pronounced or as fold axis lineations in the hinge zones of the D3 folds.

4.2.4 D4 Structures

The last phase of deformation in the evolutionary history of the KSZ is characterised by brittle structural styles (D4 faults). The D4 faults have started as conjugate NW- and NE-trending strike-slip faults offset and displace all the previously formed struc

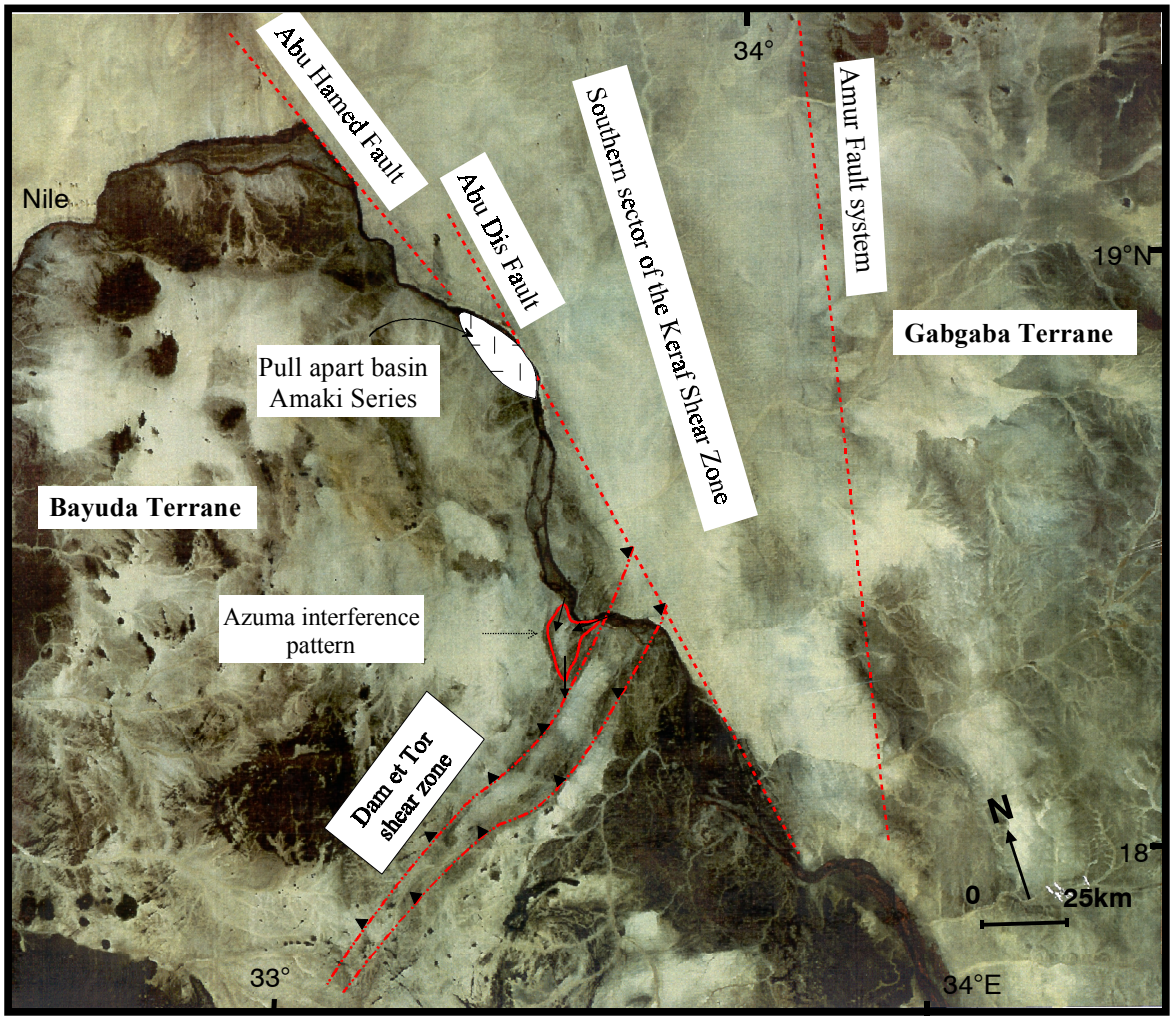

Fig. 12: MSS image band 4,5,7 for the southern sector of the KSZ. Most of the major structures can be traced for long distances and they control the course of the Nile. Note the wedge-shape of the KSZ.

tures and fabrics (Figs. 8, 9 and 10). The NW-trending faults are sinistral, while the NE-trending are dextral. The net movement along these faults is a N-S extension of the crust accompanied by an E-W shortening. D4 faults reduce in their intensity from S towards N in the KSZ. They have reversal relationship with the length of the amplitudes of D1 and D2 folds. That is, the southern part of the KSZ is characterised by dominance of the D4 faults, while D1 and D2 folds dominate in the northern sector. D1 and D2 folds in the northern area have longer amplitudes in comparison to similar folds in the southern sector of the Keraf. This distribution of structures enables the division of the KSZ into a southern brittle sector and a northern ductile one. The dividing boundary can be approximated by Lat. 19°N.

On the map scale, Abu Hamed, Abu Dis, Atmur and Amur faults are the major D4 structures in the area (Figs. 4, 6 and 12). The first two faults (Abu Hamed and Abu Dis) were mapped by Dawoud (1980), Ries et al (1985), and Abdelsalam et al (1997). They represent the western boundary of the KPTA with the high-grade rocks of the Bayuda Terrane. These two faults control the course of the Nile from Atbara to Abu Hamed (Figs. 4 and 12). Abu Dis is

a N-S trending sinistral fault which can be traced from the north of Berber in the south to the Amaki village in the north (Fig. 4). The fault plane is vertical to subvertical. Lineations along the fault plane indicate horizontal to subhorizontal left-lateral movement. Discontinuous mylonitic bands and brecciation zones are common features along the fault plane specially around the granitic intrusions. Vertical slickenslides of younger age are reported from a granitic outcrop to the SSE of Abu Hamed (Fig. 4) indicating rejuvenation of the Abu Dis fault. The vertical movements have elevated the topography of the Bayuda Desert relative to the area east of the Nile.

Abu Dis fault forms termination splays, around the Amaki village, and the movement was taken over by, relatively, small scale sinistral faults. Two faults of the termination splays are dominating, the Abu Hamed fault which strikes NNW and the Ras Humar fault which strikes towards the north (Fig. 6). Investigations of the movement kinematic indictors of the Abu Hamed fault have revealed mylonitic bands, NW-trending vertical shear planes, horizontal N-trending stretching lineations, and left-laterally rotated sigmoidal crystals (Plates 8 and 9). Slickenslides characterised by vertical movement directions are also reported in the same area. An outcrop of Nubian sandstone (Mesozoic in age) in the northern sector of the Abu Hamed fault system preserves brecciation, silicification and slickenslides of the vertical set of movement. This indicates that the vertical movement is post-Nubian and therefore, younger in age when compared to the sinistral movement. The sinistral movement is believed to have similar ages or older than the post-D4 intrusions which have been emplaced at around 550 Ma (HARMS et al ,1994, RIES et al, 1985; BARTH and Meinhold, 1979; VAIL, 1985).

The Ras Humar fault is NE trending and run parallel to the western limb of the Abu Hamed antiform (Fig. 10a). Movement along this fault is left-lateral and had formed narrow mylonitic bands within the metasediments and the serpentinized ultramafics. The fault disappear northward under the sand dunes.

Small scale D4 faults are recognised in the Keraf area within the low-grade metasedimentary assemblages and are marked by zones of high brecciation and silicification. The axial traces of these faults are preserved as quartzite ridges which have witnessed younger hydrothermal activities associated with the post-tectonic intrusions. The quartzite ridges have a N-S trend and extend for a few 100s of meters. Younger vertical slickenslides are recognised in these ridges.

The eastern margin of the Keraf Shear Zone is marked by a D4 fault, the Amur fault system (Figs. 6 and 12). On the satellite image the trace of the Amur fault could be followed for more than 150 km in a N-S trend (Fig. 12). The fault extends to the north where it separates the lithologies of the KPTA from the Gabgaba Terrane. Movement across the fault is left-lateral with subhorizontal stretching lineations. Movement in the Amur fault system was complicated by the D1 thrusting which was existing between the KPTA and the Gabgaba Terrane.

Most of the D4 faults have taken place along planes which were already occupied by D1 thrusts. This observation is supported by the fact that D4 faults are localised along the boundaries of the ophiolites and along the boundaries of the KPTA with the older surrounding lithologies to the east and to the west. In addition to the complicated kinematic indicators existing along the fault planes.

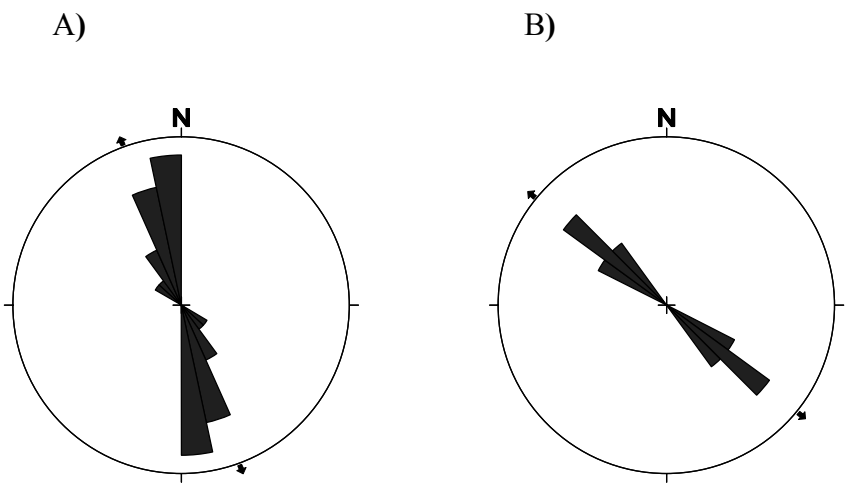

Fig. 13: Orientation of fold axes of the mesoscopic D1 folds. **A**) shows orientation of the fold axes outside Gabgaba Shear Zone. The average bearing of the fold axis is about 340° (arrow direction) (N = 18). **B**) shows the orientation of the fold axes within the greater bent of the Gabgaba shear zone. The average trend of the fold axis in this area is about 315° (arrow direction) (N = 22). The 25° anticlockwise rotation is due to the sinistral rotation of the D4 shearing.

4.3 Kinematics of deformation localisation

This section of the study displays the contrast in the response of the different rheological units to a single stress-field and establishes relations between the individual lithological units and the resulting strain. This will be achieved by inspecting the geometry of the structures and the intensity of deformation within the various sectors of the KSZ.

The geological boundaries between the various rock units of the KPTA are conformable. The marginal boundaries of the KPTA to the west with the Bayuda Terrane and to the east with the Gabgaba Terrane are tectonic and are marked by the D1 thrusts and D4 strike-slip faults. They have represented locus for the accumulation of the strain throughout the deformational history of the KSZ. On the other hand, rheological contrasts between the middle carbonate-rich layer and the surrounding siliciclastic metasediments are considered to have led to the accumulation of the strain within the middle marble band (GSZ). Therefore, GSZ is relatively more strained than the other sectors in the study area.

The architecture of the structures in the Atmur and Amur fault areas and in the GSZ is examined to characterise the strain localisation in the KSZ. The low-grade siliciclastic metasediments in the western boundary of the KSZ are separated from the high-grade gneiss by a tectonic boundary (the Atmur fault system) (Fig 6 and 11). In the northern part of the Atmur fault system (between latitudes 20° 16`- 20° 18` N) thrust plans are exposed with dips of 40 to 45° towards the E and the SE (Fig. 11). Nappe structures of the low-grade metasediments have been transported form the east and overthrusted on the high-grade gneiss to the west. Thrust planes, to the south of Lat. 20° 16` N, are obliterated by the younger D4 strike-slip faults (Abu Hamed fault) and no kinematic indicators of D1 thrusts are recorded. These faults (D1 thrusts and D4 faults) form narrow mylonitic zones in which shear bands, foliation swinging, and sigma-textures are recognised. The E-W trending pre-Keraf structures in the high-grade gneiss are signifi-

cantly reoriented and twisted by the N-S trending Keraf structures.

The eastern boundary of the KPTA with the Gabgaba Terrane is marked by D1 thrusts which are rejuvenated by D4 faults and formed complicated movement vectors (the Amur fault system). Thrusts in the Amur fault zone are steeper than those in the eastern margin of the Keraf, but still have S to SE dipping polarities (Fig. 11). They have emplaced rocks of the Gabgaba Terrane over the KPTA. Amur fault system is marked by mylonitic bands in which horizontal stretching lineations and shear bands are the dominant structural elements. Stretching lineations, sigma-structures and slickenslides indicate left-lateral strike-slip movements are reported. S1 foliations show sinistral crenulation and disposition along the D4 shear planes.

These two marginal boundaries of the KSZ (the eastern and the western) were originally characterised by an attenuated crust and thus had been ready to absorb higher quantities of stress than the other sectors within the shear zone. Thus, the rocks existing in these areas are characterised by higher degree of strain than the other rock units in the area.

The third zone in which localisation of strain is observed is the GSZ (Fig. 6). Lithology in the GSZ is dominated by banded marble (80%) associated with metagreywackes (20%). Contacts between the marble and the surrounding siliciclastic metasediments are stratigraphic and thrust indicators are not observed. Localisation of strain in the GSZ is demonstrated by the distinct geometries of D1 minor folds, S1 and S2 cleavage swinging, D4 shear bands, and the sinistral bend of the GSZ (Fig. 6). These structures are preserved by the silicified carbonates (Fig. 8). Geometry of D1 folds in GSZ is characterised by a relatively long-attenuated limb, while the other limb is short-buckled and the hinge is sheathed. The fold axes have been rotated by ~25° in an anti-clockwise sense (Fig. 13). The rotation made the bedding planes and the S1 foliations appear parallel to the shearing direction especially in the fold limbs. The hinge zones of the D1 folds in the GSZ are sheathed in a N-S orientation. Minor D4 sinistral shear bands have been reported within this area. They occur at acute angles (30°) to the main Keraf shear planes (Plate 9). A distinct feature of the S1 and S2 foliations in this area is the anti-clockwise swinging until they became parallel to the sheared bands. This feature is observed on a regional scale throughout the entire region of the GSZ. A major sinistral swing of the GSZ is at latitude 20° 25′ N (Fig. 6). This swing is a major anticlockwise rotation of S1 and S2 foliations as a result of the accumulation of the bulk strain within GSZ. D4 stretching lineations and boudinages are of frequent occurrence in this area. The orientation of the lineations indicates horizontal movement. Shear foliation (S4) are the dominant structures in the GSZ. They are characterised by a vertical N-S trend. They contain horizontal stretching lineations, an indicator to distinguish them from S1. The competent layers enclosed in the marbles and the serpentinized ultramafics form boudin structures (Plates 1 and 9).

GSZ**,** Amur and Atmur fault systems are field indicators for strain localisation within the KSZ. Similar high-strain zones within tectonic boundaries have been recognised elsewhere such as the Caledonian belts of Ireland, Greenland, California and central Arizona (CARRERAS and CASAS, 1987; ALSOP, 1994; HOLDSWORTH and STRACHAN, 1991; DOOLEY et al, 1996; MILLER, 1998; BERGH and KARLSTROM, 1992; Hudleston et al; 1988.).

4.4 Keraf transpressive deformation

Transpressional tectonics coupled with strain localisation and partitioning is proved to be a workable model to explain the orogenic evolution of tectonic boundaries (MILLER, 1998; BERGH and KARLSTROM, 1992; HOLDSWORTH and STRACHAN, 1991).

Transpressional zones represent strike-slip deformation associated with a component of shortening across them. They may simply be analysed in terms of pure shear

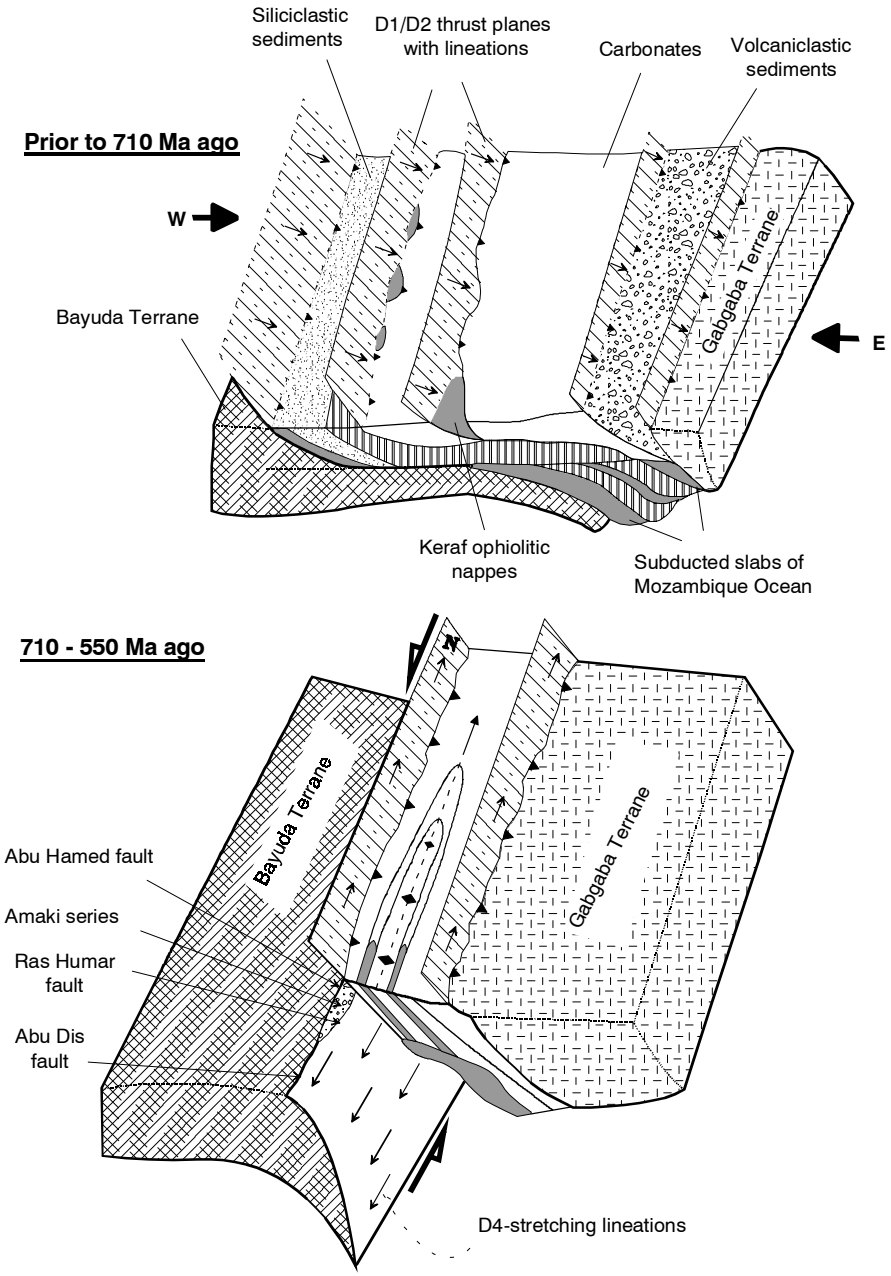

Fig. 14: Geodynamic model for the evolution of the Keraf Shear Zone. For the explanation see the text.

component involving subhorizontal compression (shortening) and vertical extension (thickening) across a wrench shear zone (WOODCOCK and SCHUBERT, 1994; SANDERSON and MARCHINI, 1984). Although originally recognised on plate tectonic scale (HARLAND, 1971), transpressional deformation has also been applied at regional and local scales (MILLER, 1998; HOLDSWORTH and STRACHAN, 1991). Tran-

spressional tectonics, the model proposed for the evolution of the KSZ, has been further complicated in the study area by:

1) focusing of strain (deformation) into narrow zones. These are, as described above, the Atmur and the Amur fault systems as well as the GSZ.
2) a considerable variation in the style of folding (de-amplification) and faulting intensity in a N-S orientation.
3) increase in the grade of metamorphism from the north to the south, which indicates variation in the vertical component (thickening) of the transpression.
4) involvement of the pre-Keraf structures, therefore complicated interference patterns were formed.

In spite of these limitations and after resolving the effect of the pre-Keraf deformation, a four-phase deformational history is proposed for the structural evolution of the KSZ. These phases as named above are D1 to D4. The W- and the NW- ward verging D1 folds are associated with development of a subduction zone. Subduction polarity was due to S and SE as indicated by the vergence of the D1 thrusts and the direction of transport of the Keraf ophiolite nappes. D1 structures are formed by E-W to NW-SE directed compressional stress, therefore the crust is assumed to have been shortened in this direction. Crustal stacking and thickening had occurred during D1 phase of deformation. The amphibolite-facies metamorphism had occurred as a consequence of this thickening. The green schist facies metamorphism is also assumed to have taken place during D1 in the upper crustal levels and in the northern sector of the KSZ. The areas of the low-grade metamorphic rocks are assumed to have been characterised by small vertical components of the transpression. D2 phase of deformation is a collisional stage because structures have been steepened at the eastern margin of the shear zone, in the area of the Amur fault system. Therefore, D2 folds have vertical eastern limbs and moderately dipping western ones (Fig. 11). D2 is a prolongation of D1 and thrusts initiated during D1 may had been active during D2. D1 and D2 folds were folded around similar fold axes but they differ in the orientation of the axial planes. The variation in the attitude of the axial plane have caused cross cutting relations between S1 and S2 therefore crenulation cleavages are formed, as demonstrated earlier. D2 deformation was culminated in the consumption of the oceanic lithosphere of the Mozambique ocean (which was separating Gabgaba from Bayuda Terrane), thrusting of the western flank of Gabgaba Terrane over the KPTA and thrusting of the latter over the eastern flank of the Bayuda-Wadi Halfa Terrane (Fig. 14).

D3 phase of deformation was formed by an anomalous N-S directed compressional stress, therefore the resulting D3 folds are E-W trending. That strain was weak, thus D3 structural elements are faint and could not be traced for longer distances. D3 folds have refolded D1 folds about E-W trending axes producing convergent-divergent patterns of folding (see section 4.6.3). In the model proposed for the evolution of the KSZ (Fig. 14), D3 plays no significant role and D3 folds do not fit with the orientation of the stress axes which had formed D1, D2 and D4 structures. Therefore D3 structures are assumed to be anomalous with respect to the orientation of the other structures.

D4 phase of deformation has reoriented the earlier (D1, D2 and D3) structures and is also associated with concentration of strain in the GSZ, Amur and Atmur faults (Fig. 8). Minor structures in these zones are dominated by the D4 faults which consistently transect and rotate the earlier structures in an anticlockwise sense. In a map view, the anticlockwise rotation of the axes of minor D1 folds inside and outside GSZ varies from 10 to 25° (Fig. 13), with the angle being greater in the proximity of the shear zone centre. This relationship demonstrates that, the intensity of D4 deformation fades out progressively away from the centre of the shear faults. The horizontal and subhori-

zontal L4 (stretching lineations) defines the trend of the D4 sinistral shear planes. L4 are located in areas characterised by high shear strain states and are enclosed within the shearing induced foliations (S4).

Folds and faults (D1 to D4) in the KSZ are the result of deformation across a zone that combines structural elements of E-W shortening and N-S extension. D1 and D2 structures favour SE-NW directed compressional strain which caused crustal shortening in the same direction. The strain was partially re solved into N-S directed shearing which is preserved as D4 faults.

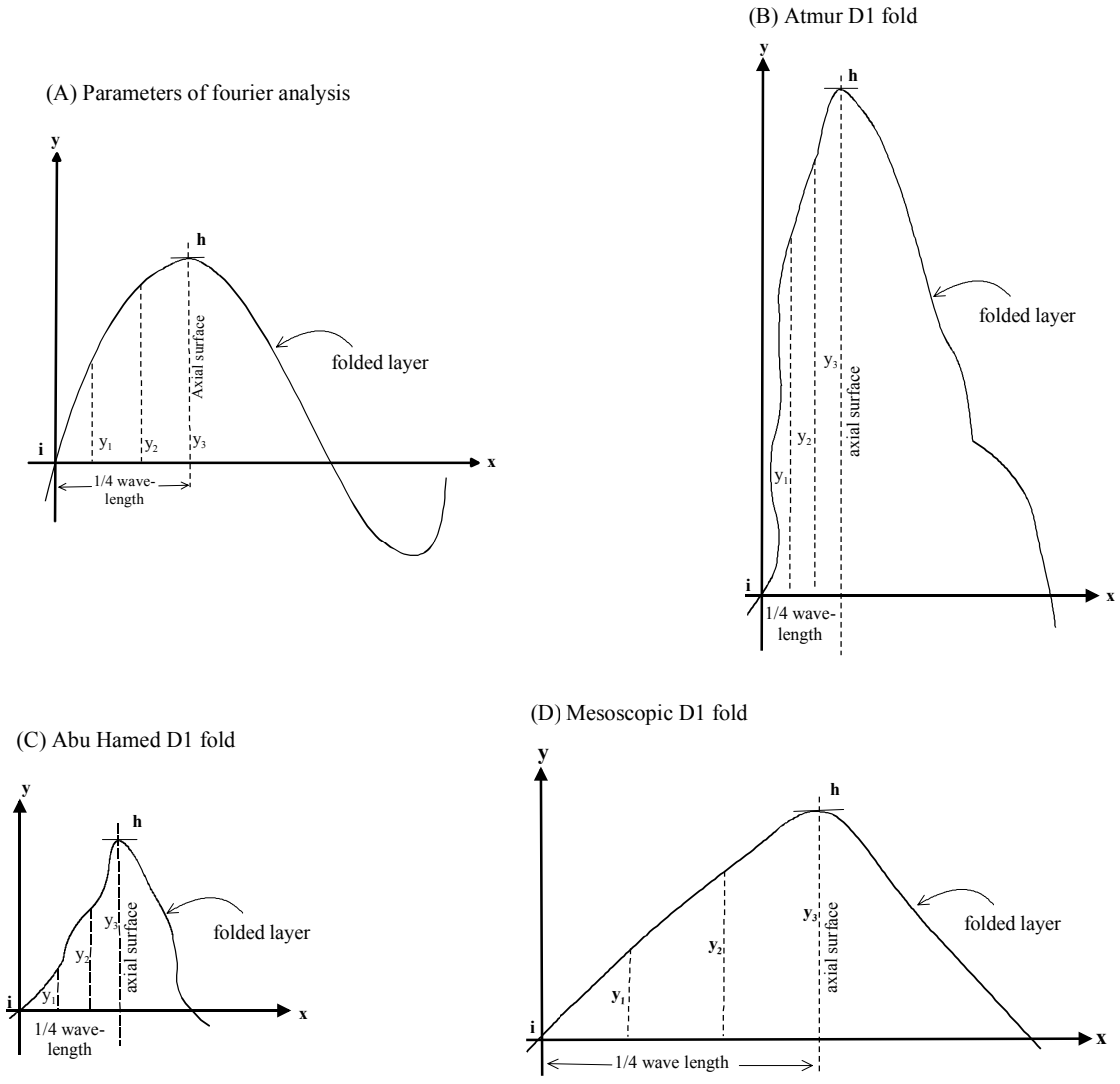

Fig. 15 : A) Method of selecting coordinates for a 1/4 wave of a folded layer. h is the hinge line (coinciding with the y-axis) and i is the point of inflexion (coinciding with the point of origin). **B)** Fourier parameters for Atmur synform. **C)** Fourier parameters for Abu Hamed antiform. **D)** Fourier parameters for a mesoscopic D1 fold.Trends of the folded layers are taken from the geological maps and the field photographs.

4.5 Fourier analysis of D1 folds

This section of the research synthesises the geometrical form of the folds which were formed during D1 phase of deformation. The curvatures of these folds are analysed mathematically and a series of simple X-Y functions were determined. The sum of

these functions gives a close fit to the more complex function of the original curves of the folds. The analytical techniques employed by RAMSAY and HUBER (1987), HUDLESTON and STEPHANSSON (1973) and HUDLESTON (1973) will be adopted in this section. This analysis is employed to satisfy the following two objectives:

1. Comparing forms of folds of the same genesis from one locality to another, mainly from the northern to the southern sector of the KSZ. This objective is to be satisfied because the style of the D1 folds is, visually, observed to be deamplifying in a N–S orientation.
2. Revealing features of folds which are not visually apparent. Abu Hamed antiform and Atmur synform are the major structures in the area and their geometrical characteristics could not be precisely determined by visual inspection, thus this method will help to reveal numerically some of the geometrical characteristics of these major structures.

4.5.1 Method

The fourier coefficients (*a* and *b*) which specify the curvature of the folded layers are calculated for the D1 folds. These coefficients are involved in a trigonometric function to express the shape of the folded layers. According to RAMSAY and HUBER (1987) these functions are:

$$\int(x,y) = a_0 + a_1\text{Cos}x + a_2\text{Cos}2x + a_3\text{Cos}3x$$

$$b_1\text{Sin}x + b_2\text{Sin}2x + b_3\text{Sin}3x \qquad (1)$$

If a small sector of the folded layer is selected the shape of the fold can be defined by a few number of coefficients. To do this, reference directions (X and Y axes) are selected to coincide with the special features of the fold such as the axial surface (hinge line) and the point of inflexion (Fig. 15a). With such co-ordinates frame all the *a*-type fourier coefficients tend to zero and only the b-type fourier coefficients can be presented in equation (1). Moreover, all the even-numbered b-type coefficients (b_2, b_4, b_6, etc) must be zero because they give rise to changes in the shape of the wave sector (RAMSAY, 1967). Due to the very small values of b_7, b_9, b_{11}, equation (1) will be reduced to:

$$\int(x,y) = b_1\text{Sin}x + b_3\text{Sin}3x + b_5\text{Sin}5x \qquad (2)$$

The fourier coefficients b_1, b_3 and b_5 are obtained by finding co-ordinate values of any three points (X_1,Y_1), (X_2,Y_2) and (X_3,Y_3) on the original folded layer. For the details of the computations see appendix II.

4.5.2 Fourier coefficients of D1 folds

In this section Atmur synform, Abu Hamed antiform and a mesoscopic fold in the GSZ will be analysed (Fig. 6). This set of folds is selected because they fall in different latitudes, i.e. cover the latitudes from 20° 30` N to 19° 00` N and hence can reveal the N-S ratio of D1 folds` deamplification. A sector between the hinge line and the point of inflexion is selected from each fold (Fig. 15b, c and d). The values of the three fourier coefficients (b_1, b_3 and b_5) for each folded sector are calculated (appendix III, IV and V). Atmur synform has value of b_3/b_1 equal to 0.035 which is within the range of the parabolic folds (RAMSAY and Huber, 1987). According to the HUDLESTON (1973) visual harmonic analysis of folds, the curvature of the Atmur synform is coinciding with type 4D folding.

Abu Hamed antiform has a value of b_3/b_1 in te range of 0.037 to 0.165 which is within the range of the parabolic to semi-ellipse folds (RAMSAY and HUBER, 1987). When this fold is introduced to the HUDLESTON (1973) visual harmonic analysis of folds, it will fit in the range of type 3D to 3C folds. This indicates that the curvature of the Abu Hamed antiform is rounded and the amplitude is short, while the Atmur synform is characterised by a relatively sharp hinge and a longer amplitude.

The mesoscopic fold in the GSZ has revealed a value of b_3/b_1 ranges from 0.165 to

0.333 which is equal to values calculated for the semi-elliptical - rounded folds (Ramsay and Huber 1987). When applying the visual harmonic analysis of Hudleston (1973) the fold could be classified as 2C to 2D. Therefore, this fold is more rounded than the above mentioned two folds and is characterised by a relatively shorter amplitude.

The Atmur fold is located to the north of the Abu Hamed fold and the mesoscopic fold is to the south of both of them, therefore the north to south deamplification of D1 folds in the KSZ is valid and could be attributed to the geometrical configuration of the sheared area, i.e. having a wedge shape (Fig. 12).

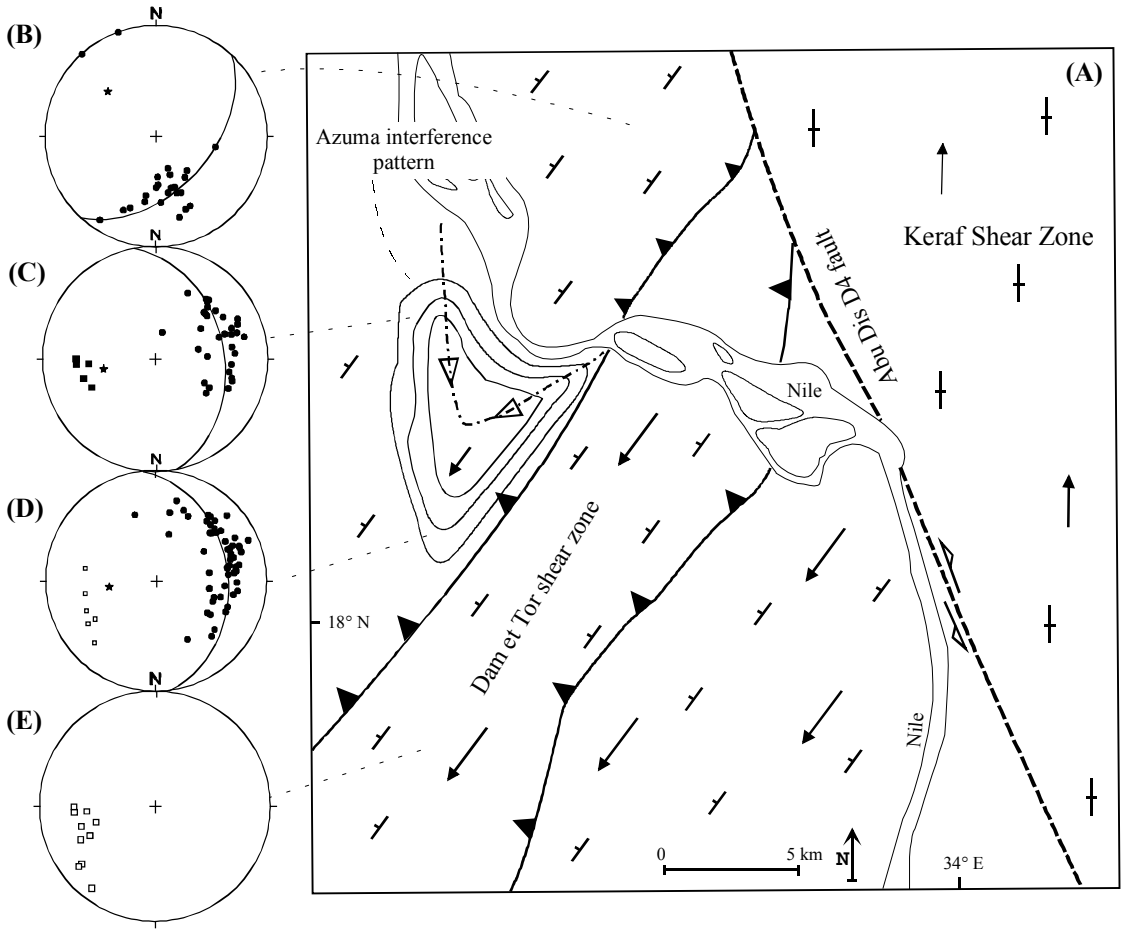

Fig. 16: A) Structural map of the Azuma interference structure and Dam et Tor shear zone (for location see Fig. 4). **B**) Pi plot of poles to S1 NE of Dam et Tor. They show NW plunging average pole which is the same orientation of L1 lineations (N = 24). **C**) Pi plots of poles to planes (circles, N = 33) and pre-Keraf lineations (squares, N = 6). **D**) Pi plots of poles to planes (circles, N = 58) and pre-Keraf lineations (squares, N = 6). **E**) Pi plot of pre-Keraf lineations in the Dam et Tor shear zone (N = 10). Azuma interference pattern was formed by the superimposition of the NW-trending Keraf structures over the SW- trending pre-Keraf structures.

4.6 Interference patterns in the KSZ

Two major E-W trending structural belts are recognised in the area to the west of the KSZ. These are the Dam et Tor shear zone and the Atmur suture (Figs. 1). The N-S trending Keraf structures were superimposed over the E-W trending structures of

the Dam et Tor belt and the Atmur suture. This superimposition has resulted in a complicated style of interference patterns. On another hand, Keraf D3 folds have refolded D1 and D2 folds forming different styles of interference patterns. This part of the study synthesis the geometrical characteristics of the interference structures in the KSZ and will establish a spatial relation between the Keraf and the pre- Keraf deformations.

4.6.1 Atmur interference structures

Deformation in the Atmur suture describes a SE verging subduction zone between the Wadi Halfa Terrane to the north and the Bayuda Terrane to the south (DENKLER et al, 1994; SCHANDELMEIER et al, 1994; ABDELSALAM and STERN, 1996). This view was substantiated by the occurrence of the Siniat and Atmur ophiolitic fragments which decorate the belt (SCHANDELMEIER et al, 1994). Structural styles in the Atmur suture are characterised by tight to isoclinal NE-trending and SE-verging folds (SCHANDELMEIER et al, 1994). The junction of the KSZ with the Atmur suture is characterised by complicated and interrelated interference patterns, which are called the Atmur interference patterns (Figs. 6 and 7). The structure coincides with the type II in

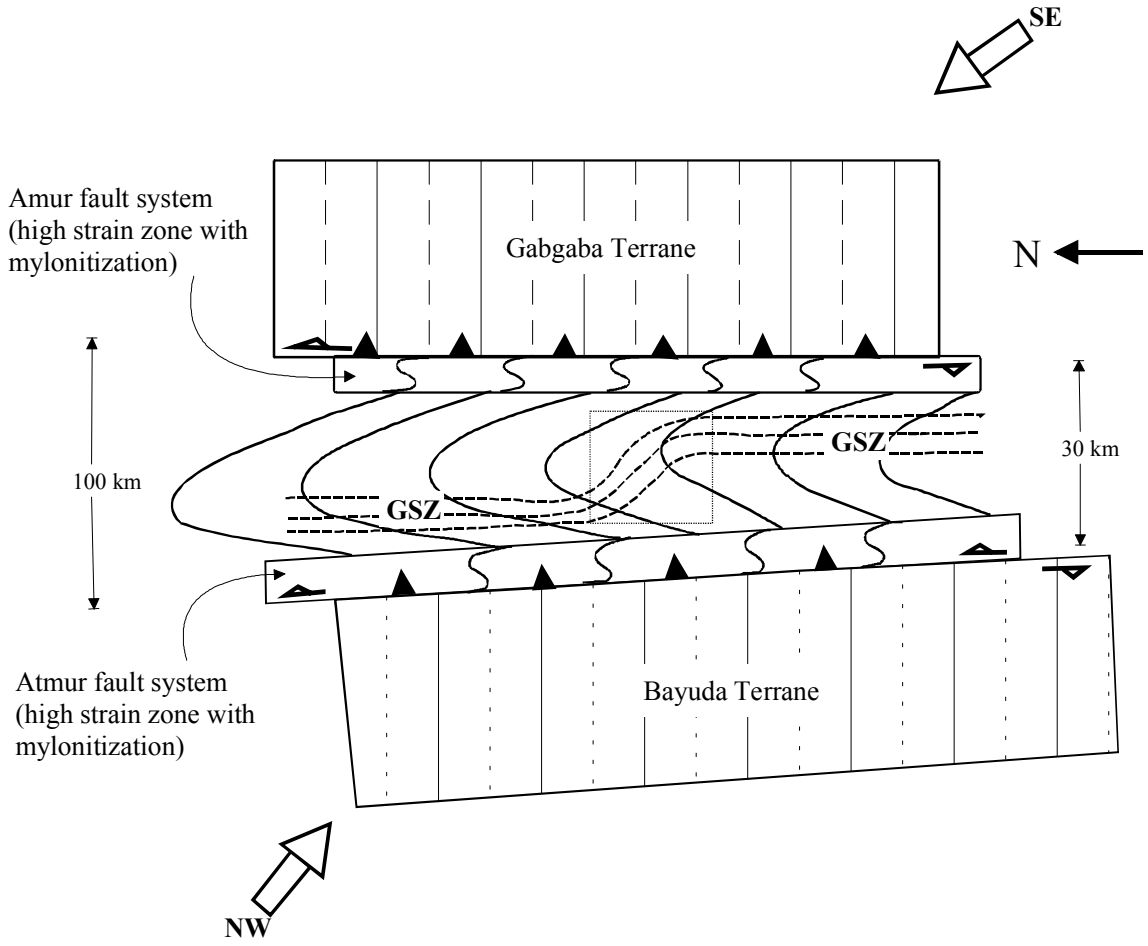

Fig. 17: The three high strain zones of the KSZ. Note the wedge shape of the sheared area and the swinging of the GSZ. The rectangle in the GSZ is the area of Fig. 18. Large arrows are the major compressional strain which was resolved into N-S shear strain and E-W shortening. The diagram is based on the trajectories of the S1 and S4 foliations.

terference pattern of RAMSAY and HUBER (1987). The interference pattern is preserved by metasedimentary sequences of marbles and clastic metasediments which have low lying topography and are partially covered by sand dunes. The structure is 5-7 km long and 1-2 km wide and has a NE trends. Lineations within the structure have moderate plunges towards the NNE and the SSW (Fig. 6).

Due to the difference in the level of the exposed surfaces the outer most layers of the Atmur interference structure show a long east- trending protuberance (Fig. 6). This protuberance is the intersection of the Atmur folds (earlier structures) with the horizontal surface. The western part of the structure is pointed to the SW with lineations plunging to NNE. The inner layers of the structure are alternating oval basins and domes with subvertical layers in the north and gentle ones in the south.

4.6.2 Azuma interference structure

This structure is formed at the intersection of the KSZ with the Dam et Tor shear belt (Figs. 12 and 16). The structure was first recognised by VAIL (1971) then mapped by DAWOUD (1980). The name Azuma is assigned by ABDELSALAM et al (1997). Structures in the Dam et Tor belt trend in the NE direction and have dips towards the NW (Fig. 16). During this study statistical measurements have been collected to characterise the geometry of the interference structure.
On the map scale, this structure is defined by medium- to high- grade metasediments (upper amphibolite facies) with a moderate topographic relief. The Azuma structure is a mushroom type II interference pattern (RAMSAY and HUBER, 1987). Foliations and other planar fabrics in the NE part of the structure are N-S trending with a moderate dip (45°) towards the W (Fig. 15c). In the SW part of the structure foliations are subhorizontal. Lineations are plunging toward the centre of the structure and then to the west (Fig. 16). The Azuma structure is explained as the resulted of the superimposition of the N- trending upright D2 Keraf folds over the E- trending NNW- dipping Dam et Tor folds.

4.6.3 Gabgaba refolded folds

These are a group of refolded structures located within the carbonate-rich layer of the GSZ and they are preserved by the silicified marbles (Fig. 7). These structures differ from the above mentioned interference patterns in two aspects: 1) they are formed by the Keraf structures only and no pre- Keraf structures are involved and 2) their final shape and position are largely modified by the Keraf D4 shearing because they are located in the high strain zone of the GSZ. The N-trending D1 and D2 folds are refolded by the E-trending D3 folds and they formed convergent-divergent, type III, interference pattern (RAMASY and HUBER, 1987). The original orientation and geometry of the structures are modified by the anticlockwise rotation which has taken place during D4 phase of deformation.

4.7 Strain distribution in the KSZ

The marginal walls of the KSZ are not parallel, they are separated by a distance of 30 km in the south while in the north the separating distance is more than 100 km (Figs. 12 and 17). Such geometry makes the sheared area to have a wedge-shape and consequently the distribution of the strain is significantly heterogeneous in a N-S orientation. The southern end (narrow) had experienced extensive shortening relative to the northern end (wider). This assumption is supported by the N-S deamplification of the D1 folds as well as by the dominance of the high-grade metamorphic rocks in the south.

The shear induced foliations (S4) in the GSZ are N-S trending parallel to the shear zone walls. At Lat. 20° N the shear foliations assume an E-W trend due to the high accumulation of the strain in this area. S4 foliations are planes characterised by N-S oriented flattening planes and E-W short

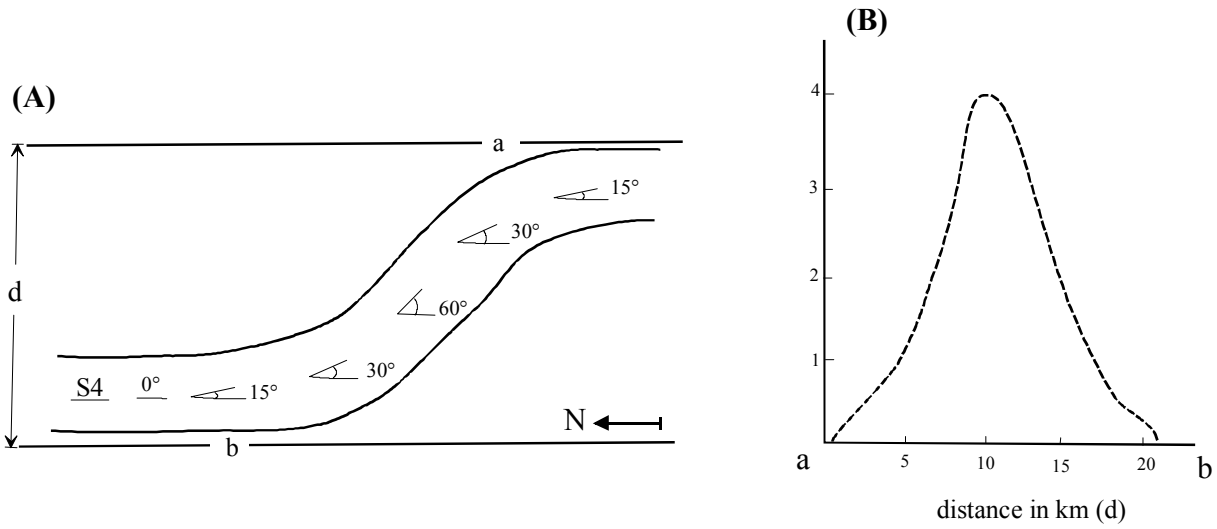

Fig. 18: A) Trajectories of the shear foliations (S4) in the greater swing of the GSZ. For location see Fig. 13. **B**) Shear strain profile across the line a-b. The distances (d) are approximated from the scale of the map in Fig. 2.

ening. Thus they can be used to calculated the shortening ratio and the reduction of the volume in the GSZ. The fabric trajectory isogons of S1 foliations are consider as the walls of the GSZ, because left-lateral movement across them is not reported. Therefore, they are used as a reference from which the trend of the GSZ (S4) is obtained (Fig. 18a). S1 isogonal lines are drawn at random intervals (θ°) to the shear foliations. The intervals 15°, 30°, 60°, 30°, 15 are selected (Fig. 18a). The shear strain (γ) at any interval is calculated using the equation defined by RAMSAY and HUBER (1987):

$$\gamma = \tan\theta$$

A shear strain profile across the GSZ is graphically represented by plotting γ versus the distance of S4 foliations from the shear zone walls (Fig. 18b). The total shear displacement (S) across the GSZ could be obtained by integrating the equation:

$$S = \int \gamma \, dx$$

Where x is the distance across the sheared area (RAMSAY and HUBER, 1987). The average trend of the S4 foliations in an ophiolite outcrop at the centre of the GSZ (20° 14` 43`` N and 33° 49` 47`` E) makes an angle of ~75° with the shear zone walls. The width of the sheared area is ~12 km. At this outcrop the shear stain is 3.7 and the total shear displacement i.e. reduction in volume is ~40 km. The magnitude of the displacement decreases towards the peripheries of the shear zone.

5 ROCK CHEMISTRY OF THE KERAF PETROTECTONIC ASSEMBLAGE

5.1 Introduction

Geochemical signatures and affinities of the major lithological units in the ANS are not fully understood particularly with respect to crustal evolution, assembly of Gondwana and inheritance of the pre-Pan African precursors. This can be mainly attributed to the vastly scattered geochemical data and the diversity of the large scale geodynamic and tectonic processes operated in the area during the Proterozoic (Pan African) thermotectonic episode. In the last decades many geochemical and geochronological investigations have been conducted in the Pan African sectors of Arabia (GREGORY, 1998; MILLSON et al, 1996; NASSEEF et al, 1984; STACEY and STOESER, 1983; etc) and in Egypt (EL SAYED et al, 1999; SULTAN et al, 1990; and 1992; STERN et al, 1991; etc). Comparatively, the work conducted in Sudan (RIES et al, 1984; HARMS et al, 1990; BAKHIET, 1991; STERN and KRÖNER, 1993; ABDELRAHMAN, 1993; DENKLER et al, 1993; WIPFLER, 1994), Somalia (Lenoir et al 1994), Ethiopia (TADESSE et al, 1990; GEORGE et al, 1998; AYALEW and PECCERILLO, 1998; WORKU and SCHANDELMEIER, 1995; BERHE, 1990) and Eritrea (DRURY and FIHO, 1998; BEYTH et al, 1997) is very limited and is still immature.

According to the geochemical data so far available, it is believed that the magmatic rocks of the ANS in Arabia, Egypt and Sudan are mainly calc-alkaline lithologies derived from a depleted mantle source with little or with no contributions from a pre-existing continental crust. The magmatic rocks have ages from 900 to 520 Ma with a climax of post-tectonic magmatic activities at ~700 Ma and a younger phase at ~550 Ma (STERN and KRÖNER, 1993).

The crustal segment to the west of the ANS, the Nile craton (ROCCI, 1965), is characterised by ensialic high-grade metamorphic rocks. Nd-, Sr- and Pb-isotopic compositions indicate significant contributions from pre-Pan African continental crust (HARRIS et al, 1984; HARMS et al, 1990). Inbetween the juvenile ensimatic rocks of the ANS and the older ensialic assemblages of the Nile craton is a transitional zone which is occupied by the KPTA in N. Sudan and S. Egypt.

In addition to the lithological, petrological and structural investigations described in the previous chapters, in this chapter the geochemical affinities and signatures of the major rock units in the KPTA will be discussed. These investigations are conducted to satisfy the following objectives:

i) to characterise the magmatic evolution of the Keraf igneous rocks,

ii) to determine the geochemical and geotectonic signatures of the Keraf ophiolites,

iii) to constrain the depositional environment of the Keraf metasediments, and

vi) to compare the geochemical and the geotectonic signatures of the Keraf lithologies with the surrounding rocks, i.e. to the east and to the west in the Gabgaba and the Bayuda Terranes respectively.

5.2 Alteration and general features

Major and trace element composition of representative samples of the Keraf ophiolites, the post-tectonic (post D4 phase of deformation) intrusions and the metasedimentary sequences (low- and high-grades) are listed in tables 1 to 8 in appendix IV. Loss on ignition (LOI), which is assumed as an index of alteration (weathering) and

metamorphism, is relatively high for the mafic and ultramafic units of the ophiolite assemblages. This is mainly due to the serpentinisation and carbonatisation of the ophiolites. The LOI values of the Keraf ophiolites are comparable to the values which have been reported from similar lithologies in the Red Sea Hills, Ingessana Mountains, Jebel Rahib and Delgo (WIPFLER, 1994; DENKLER et al, 1993; ABELRAHMAN, 1993; and BAKHIET, 1991). The post-tectonic intrusions have LOI between 0.35 and 2.25 wt %. The low-grade metasediments have very high LOI which may reach up to 40% in the marbles and in the carbonate-rich metasediments. The high-grade metamorphic rocks have low values of LOI, which is generally below 1 wt %.

The mobility of most of the major elements and some of the High Field Strength (HFS) elements is expected to be very high in the ophiolite suites, because the rocks have been affected by the Keraf metamorphism and deformation. Seawater interaction is believed to have introduced mineral rich in OH to the ophiolites in the early stages of their evolution (LECUYER et al, 1990). Thus, the present chemical composition of all the analysed samples might not tell the exact initial mineralogical composition of the oceanic lithosphere. But some of the HFS elements (used as petrologic indicators) such as Zr, Ti, P, Nb and Y as well as some of the transitional metals such as Co, Ni, V and Cr are believed to be relatively immobile up to medium grades of metamorphism (ROLLINSON, 1993). Accordingly, emphasis will be placed on the less mobile HFS and LIL elements and the REE for the tectonic discrimination and geochemical classification of the ophiolitic rocks.

The post-tectonic intrusions and the late-tectonic dykes are less altered and thus have LOI values in the range of 0.3 to 2.25 wt %. The major elements and of course the trace elements had not experienced mobility after the crystallisation of the plutons and the dykes. Major elements as well as trace elements are used for the rock classification and the tectonic discrimination of the intrusions.

The low grade-metasedimentary suites (meta-sandstones, meta-mudstones and meta-pelites, chlorite-biotite schists) are affected by the metamorphism and the D4 shearing of the Keraf. Their LOI is very high and may reach up to 25%. Ancient weathering (pre-metamorphic) is believed to have affected some of the low-grade metasediments. This is indicated by the existence of clay lenses (weathering end-members) enclosed in some of the samples and by the existence of Al-rich metasediments. This phenomenon of ancient weathering was reported in the Eastern Desert of Egypt and in Jebel Tawiga in NW Sudan (WIPKI, 1995; BWITZ and FISCHER, 1993). In these areas it is dated as Palaeozoic.

The major elements of the high-grade gneiss and the amphibolites were remobilized during metamorphism. The major elements of these rocks will be used to calculate the chemical index of weathering. Some major oxides will be used to constrain the possible background and the depositional environment of the sediments.

5.3 Whole-rock chemistry

5.3.1 Keraf ophiolites

More than 40 samples from the Keraf ophiolites have been analysed for major and trace elements by the powdered and fused pellet XRF techniques. Ten selected samples were analysed for Rare Earth Elements (REE) by Inductively coupled plasma (ICP-AES). The results of the analysis are listed in tables a1, a2 and a3.

According to the chemical data, the rocks of the Keraf ophiolites are divided into three geochemical groups (protoliths): basal tectonites, mafic-ultramafic cumulates and mafic non-cumulate units. The basal tectonites are significantly rich in MgO (17.6-39.2 wt %), Cr (1557-3582 ppm) and Ni (592-2130

ppm) (Table a.1). Their SiO_2 contents are low, between 35–43 wt % and they are markedly depleted in oxides of most of the major elements such as Al_2O_3, TiO_2, MnO, P_2O_5, Na_2O and K_2O (Table a.1). The values of Fe_2O_3 are in the range of 7.76 to 21.22 wt % which are conformable with the values reported by CARMICHAEL et al (1974) for the alpine-type orogenic peridotites. Mg-number (Mg# = Mg/Mg+Fe^{2+}) of the tectonites is in the range of 0.69-0.88. According to COLEMAN (1977) such values of Mg# are typical for metamorphosed peridotites from ophiolitic assemblages. Similar values were recognised by ABDELRAHMAN (1993) in the ophiolites of Onib, Ingessana and Jebel Rahib in the Sudanese sector of the Nubian Shield.

CaO values are relatively higher than what is reported from similar ultramafic tectonised rocks (ABDELRAHMAN, 1993). The enrichment in CaO can be attributed to the carbonatisation during the low-grade metamorphism which had taken place during the D1 and D2 phases of the Keraf deformation. Some of the tectonites are completely surrounded by marbles and carbonate-rich metasediments (Fig. 5). Such location is not encountered in the Red Sea Hills and in the Ingessana Mountains where the ophiolites are surrounded by arc-related volcaniclastic material (ABDELRAHMAN, 1993; ALMOND and AHMED, 1987). The highest values of CaO reported in this group are 4.40 and 10.08 wt % (samples 5.8a and 9.7 respectively) (Table a.1). CaO values reported by ABDELRAHMAN (1993) from analogous lithologies in Red Sea Hills, Ingessana Hills and Jebel Rahib are: 1.44%, 4.09% and 5.17% respectively. Such high values of CaO should not rule out the assumption that these rocks had a peridotite average composition, because the excess Ca is accommodated in the formation of secondary calcite which is easily identified in thin sections.

Elements which are considered to be incompatible within the peridotite composition, such as K, Rb, Ba, Pb, Zr and Th, have very little values in the basal tectonites (Table a.1). The limits of these elements are within the range of the dunites and peridotites reported from the modern (Phanerozoic) ophiolitic assemblages in Oman (EL SHAZLY and COLEMAN, 1990; COLEMAN, 1977).

According to this chemical composition, the basal ultramafic suite resembles the serpentinized harzburgites which represent the lower member of the ophiolitic sequences (LIPPARD et al, 1986; COLEMAN, 1977). Analogous lithologies with similar chemical signatures are reported within the ophiolitic rocks in Sudan as well as in the Arabian-Nubian Shield (ABDELRAHMAN, 1993; EL SHAZLY and COLEMAN, 1990; STACEY and STOESER, 1983; KRÖNER et al, 1987; CAMP, 1984; EMBELTON et al, 1983).

The composition of this group of rocks (tectonites) is close to a parental (peridotite) magma and is thus considered to be the least differentiated rocks among the Keraf ophiolitic suites. These rocks can be used to identify, or at least constrain, to which type of oceanic crust the Keraf ophiolites could have belonged. Combining the chemical composition of the tectonites with the other geological aspects (the structural setting, field relations and the associated lithologies), the tectonites could preferably be considered as mantle sequences of a back arc basin separating Bayuda-Wadi Halfa Terranes (continental flank) from Gabgaba-Gerf Terrane (volcanic arcs). Similar conclusions were reached for the mantle sequences reported in the ophiolitic melanges of Ingessana and Jebel Rahib in Sudan (ABDELRAHMAN, 1983). The ophiolites of the Keraf, Ingessana and, may be, Nuba Mountains lie on the western margin of the Nubian Shield and thus presumably have a similar geotectonic background, if not representing various segments of the same oceanic lithosphere of the former Mozambique Ocean (STERN, 1994).

Rocks of the second geochemical group of the Keraf ophiolites are the ultramafic-mafic cumulate rocks. They are characterised by wider variations in their chemistry and

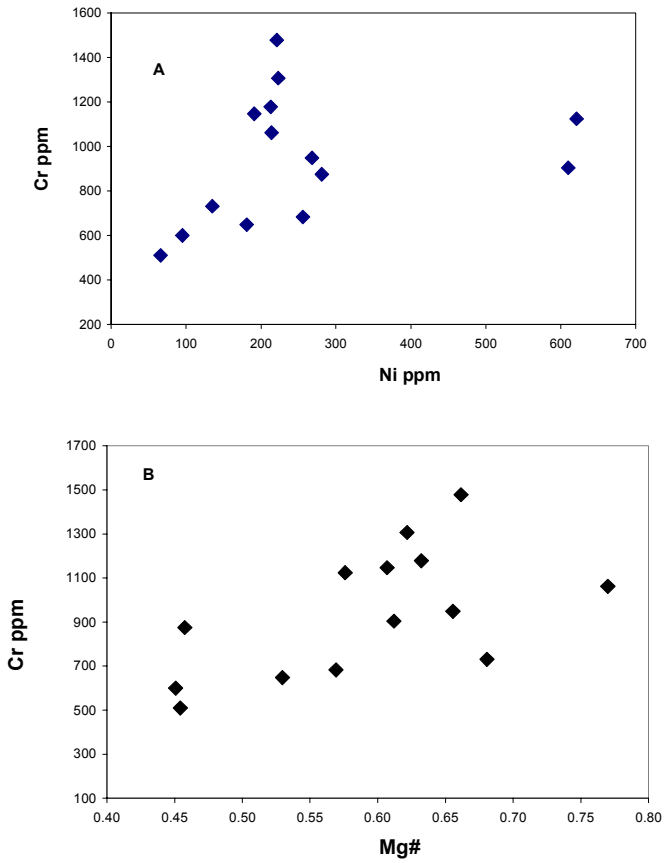

Fig. 19: A) Ni – Cr and B) Mg# - Cr variation diagrams of the cumulate rocks of the Keraf ophiolites.

mineralogy compared to the ultramafic tectonites (Table a.2). Their SiO_2 content is in the range of 35 - 53 wt %. They have higher contents of Al_2O_3 (10 - 18 wt %), Fe_2O_3 (3 - 12 wt %) and CaO (6 - 15 wt %) and relatively lower MgO compared to the basal tectonites (Table a.2). Their Mg# ranges from 0.45 to 0.77 which is similar to that of Rahib ophiolites (ABDELRAHMAN, 1993). TiO_2 content ranges from 0.05 wt % in sample 10.7b to 0.67 Wt % in sample 11.8c (Table a.2). TiO_2 contents are higher compared to the neighbouring Onib ophiolites (ABDELRAHMAN, 1993). CaO contents are higher than in the ultramafic basal tectonites. CaO values in this group are in the range of the values in gabbro-dunite rocks. The cumulate rocks contain relative higher values of total alkalis (K_2O+Na_2O), which reaches up to 4.8 wt % in sample 10.5 (Table a.2).

The rocks are enriched in some elements such as Ni and Cr which are compatible with the gabbro-dunite composition. Values of Cr are in the range of 510-1478 ppm and those of Ni are in the range of 66-621 ppm (Table a.2). Both of them are relatively lower than the ones of the basal tectonites. Cr and Ni are positively correlated with each other as well as the Mg# with the Cr (Fig. 19). The increase in Fe and Ti contents combined with the decrease in the Cr and Ni values may suggest crystallisation under progressively increasing fO_2 conditions (TSIKOURAS and HATZIPANAGIOTOU, 1998). Consequently, the progressive oxidation may have caused the formation of Fe and Ti oxides which are seen in the thin sections of these rocks. The relatively low values of MgO, Cr and Ni in

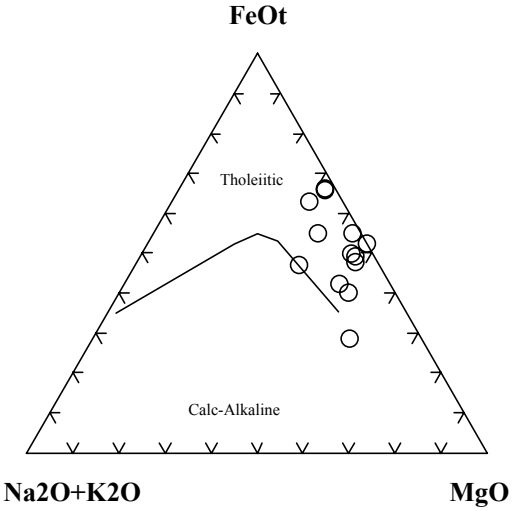

Fig. 20: AFM ternary plot of the cumulate rocks from the Keraf ophiolites. Trend is after Irvine and Baragar (1971).

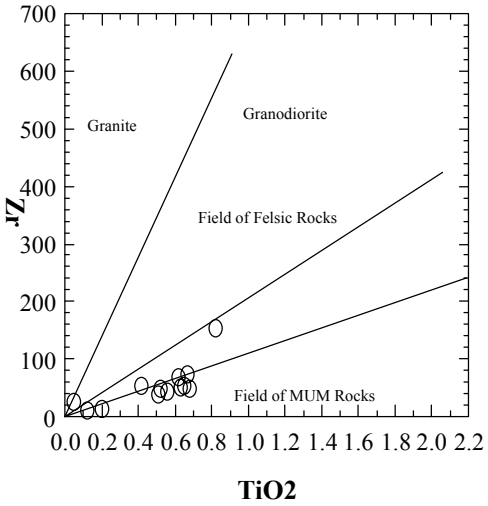

Fig. 21: TiO2-Zr classification of the cumulate rocks from the Keraf ophiolitic sequences. MUM is the Mg-rich ultramafic rocks (Rock et al, 1990).

this group, compared to the basal tectonites, suggest an advanced stage of magmatic differentiation.

On the AFM diagram (IRVINE and BARAGAR, 1971) the analysed cumulate samples show a tholeiitic trend (Fig. 20). On the TiO_2-Zr classification (HALLBERG, 1985) the cumulates are mainly plotted in the Mg-rich ultramafics with few points in the mafic field (Fig. 21). On the MgO-FeOt-Al_2O_3 discrimination diagram (PEARCE et al, 1977) the rocks are distributed among the ocean island and ocean ridge fields (Fig. 22). The distribution of the rocks in these two field may be attributed to the low-grade metamorphism. Any way, the plot of the rocks in oceanic island and oceanic rige fields might rule out any continental mode of emplacement of the ultramafic cumulate rocks.

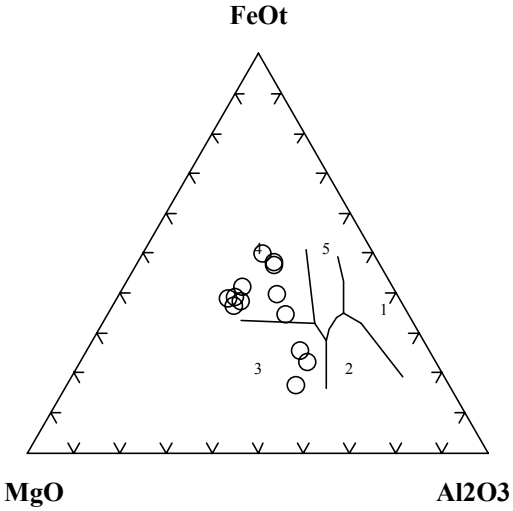

Fig. 22: MgO-Al2O3-FeOt ternary chemical classification of the cumulate rocks of the Keraf ophiolites. Field 1is spreading centre, 2 orogenic, 3 ocean ridge, 4 ocean island and 5 continental (PEARCE et al, 1977).

The third geochemical group of the Keraf ophiolites is the mafic-intermediate non cumulate suite. They range in composition from meta-basalt, meta-gabbro to meta-diorite. Their association with the other ophiolitic members is recognised mainly in two localities: i) in the ophiolitic ridge within the eastern limb of the Abu Hamed antiform (ridge 2) and ii) in the ophiolitic melange in the E-W trending bend of the Gabgaba Shear Zone (ridge 1) (Fig. 5). They have direct lithological contacts with the basal tectonites. Tectonically, they are possible candidates to represent the upper igneous part (gabbros, diorites, plagiogranites, sheeted dolerite dykes and pillow basalts) of the Keraf ophiolites. Thus, in spite of their lithological diversification, they are assumed to have similar geochemical signatures. The result of the chemical analysis are listed in Table a.3.

The rocks are characterised by an extended range of SiO_2 content, from ~ 33 to above 78 wt % (Table a.3). These values indicate that SiO_2 was mobilised (depleted or enriched) during D1 and D2 metamorphism. Al_2O_3, Fe_2O_3, CaO, Na_2O, TiO_2 contents are higher than in the above mentioned two groups. MgO, Cr and Ni values are low indicating an advanced stage of magmatic differentiation. The rocks are markedly depleted in K_2O and P_3O_5. Depletion in the former can be due to secondary processes while that of the latter is probably inherited from the original melt because P is stable up to medium metamorphic grades. The Na_2O enrichment might be attributed to the sea water metasomatism which is a common feature in old and recent ophiolitic suites (ABDELRAHMAN, 1993; ENGEL and ENGEL, 1964).

This group is more differentiated than the former two groups. Stable HFS elements (Ti, Zr, Nb, Y, P), which are not affected by the green schist facies metamorphism, will be used in geochemical discrimination and rock classification of these lithologies.

The geochemical rock classification of the analysed samples is revealed by using the

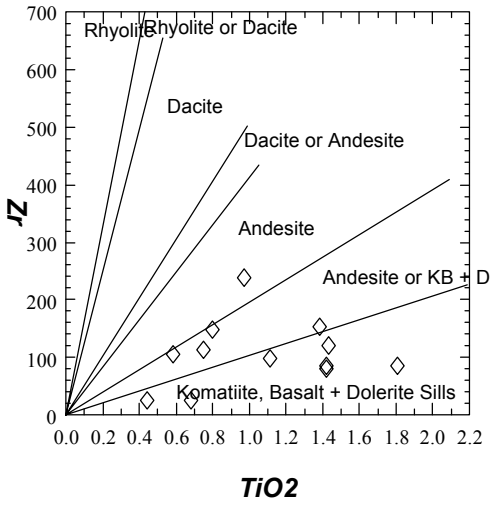

Fig. 23: TiO_2-Zr binary rock classification of the mafic rocks from the Keraf ophiolites. KB is komatiite & basalt and D is dolerite (HALLBERG, 1985).

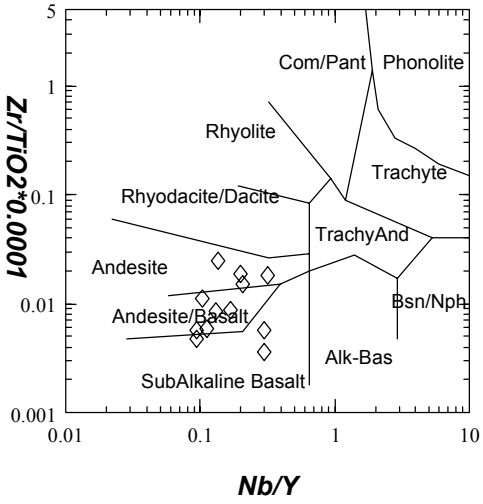

Fig. 24: Nb/Y-Zr/TiO2*0.0001 binary rock classification of the mafic rocks from the Keraf ophiolites. (WINCHESTER and FLOYD, 1977).

TiO_2-Zr diagram (Fig. 23) which can be applied to ancient rocks from green stone belts (HALLBERG, 1985). On this diagram, Keraf mafic rocks are distinguished as basalts, dolerite sills and andesite. Sample 10.8d is located in the andesite field due to its relatively higher Zr content. A more detailed geochemical rock classification of the mafic rocks from the Keraf ophiolites is obtained by the Nb/Y-Zr/TiO_2 plot (Fig. 24) (WINCHESTER and FLOYD, 1977). On that diagram, the rocks are plotted in the andesite and andesite/basalt fields, two samples appear in the field for subalkaline basalts. This classification is in agreement with field description and the petrographic results.

On the Zr/4-Y-2Nb ternary geotectonic discrimination diagram (MESCHEDE, 1986) the analysed samples plot in the volcanic arc basalt field and one sample (11.8a) is plotted in the P MORB field (Fig. 25). The

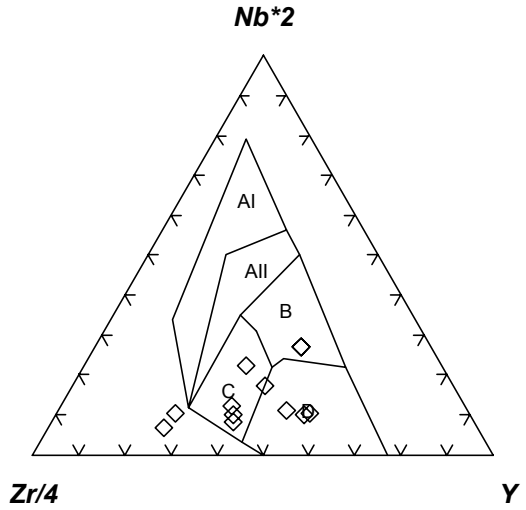

Fig. 25: Zr/4-Y-2Nb ternary tectonic discrimination diagram for the mafic rock sequence of the Keraf ophiolites. AI-AII within plate alkaline basalt, AII-C within plate tholeiite, B PMORB, D NMORB and C-D volcanic arc basalt (MESCHEDE, 1986).

relatively spreading plot of the samples can be attributed to the green-schist facies metamorphism, which is a common situation in the Precambrian ophiolites (ABDELRAHMAN, 1993). This plot can lead to the suggestion that, the mafic non cumulate sequence of the Keraf ophiolite is either part of the oceanic lithosphere of the Proterozoic Mozambique Ocean or they are belonging to the arc volcanics of the Gabgaba Terrane. This is also accompanied by the fact that most of the samples are relatively depleted in the big cations such as Rb, U, Th and Pb (Table a.3). Such geochemical signatures favour eruption in mid-ocean ridge of a back arc basin (WILSON, 1989).

This group of samples (mafic non cumulate) has Nb content in the range of about 3 ppm which might indicate oceanic crust origin (TAYLOR and MCLENNAN, 1985). Samples 11.8d and 10.9b have Nb contents of more than 6 ppm. Such values may indicate ocean ridge granites (PEARCE et al, 1984). Most of the samples have Y contents in the range of the oceanic crust and E-MORB i.e. from 32 to 22 ppm (TAYLOR and MCLENNAN; 1985, SUN and MCDONOUGH, 1989). Zr in most of the samples is in the range of MORB and Oceanic Crust (SUN and MCDONOUGH, 1989). Sample 10.8d has Zr value within the range of Ocean Island Basalt (Table a.3) (SUN and MCDONOUGH, 1989). Nb, Y and Zr values could indicate that Keraf ophiolites have oceanic crust signatures with slight ocean arc imprints.

In the MORB-normalised spider patterns of four selected samples from this group (mafic non cumulate), the values of Nb, Zr and Y are in the range of one (Fig. 26). All the plotted samples are enriched in Sr, Rb and Ba. The enrichment of the LIL elements (Sr, Rb and Ba) is due to the D1/D2 metamorphism. Since the metamorphism is varying across the KSZ, then the depletion and/or enrichment could also vary. Thus the MORB-normalised spider patterns of the plotted samples are not parallel to one another (Fig. 26). The depletion of Nb relative to Ce values (Fig. 26) is a geochemical signature of subduction zone emplacement (CONDIE, 1998).

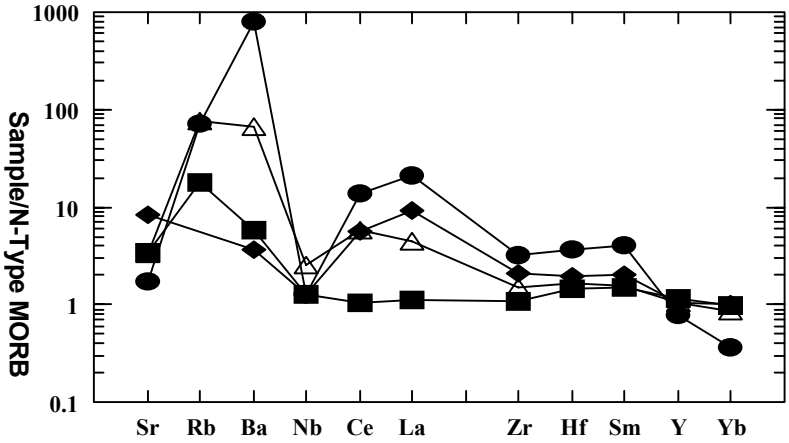

Fig. 26: MORB normalised spider diagram for four selected samples from the mafic non cumulate sequence of the Keraf ophiolites. Circle is 10.8d, diamond is 10.11a, triangle is 10.9b and rectangle is 5.7c. The SiO_2 contents (wt %) of the samples are: 33.30, 52.63, 57,24 and 50.82 respectively. The normalised values are after SAUNDERS and TARNEY (1984).

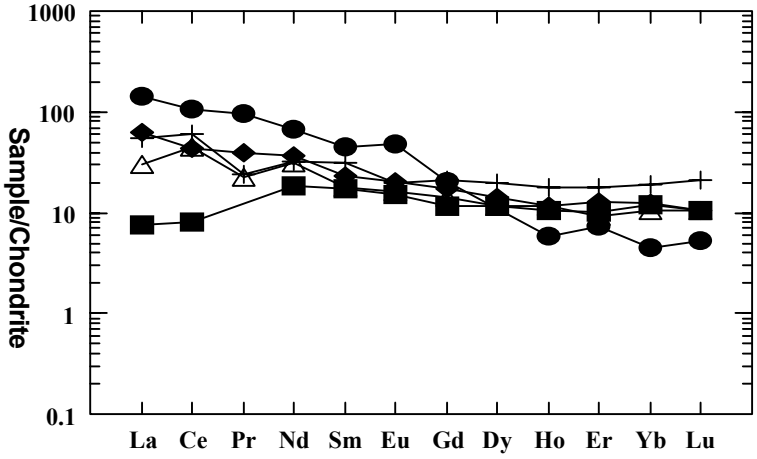

Fig. 27: Chondrite normalised REE patterns of four selected samples from the mafic non cumulate sequence of the Keraf ophiolites. Symbols of the samples are as in Fig. 26. Normalised values are after BOYNTON (1984). The sample indicated by plus sign is a diorite from ophiolites in Samothraki Island in Greece (TSIKOURAS and HATZIPANAGIOTOU, 1998). It is plotted for comparison.

The REE patterns, normalised to chondrites, of four representative samples from the mafic non cumulate rocks are shown in Fig. 27. Three of the plotted samples are obviously enriched in the (light) LREE and the (medium) MREE relative to the (heavy) HREE. The fourth one (sample 5.7c) is depleted in the LREE and the HREE relative to the MREE. Three samples have flat pattern in the region of the MREE and HREE while sample 10.8d shows a slightly positive Eu anomaly. The same sample is relatively enriched in the LREE and depleted in the HREE in comparison to the other three samples. The high value of La in all samples could be due to an effect of submarine

alteration (MASUDA and NAGASAWA, 1975). The relative enrichment of Nd, Sm and Eu in the pattern of all samples (i.e. values are above 1) is due to fractionation of pyroxenes into the rock phase (ROLLINSON, 1993). The relative enrichment of the LREE to the HREE can be caused by the progressive fractionation of the olivine and pyroxenes from the melt into the rock phase (ROLLINSON, 1993). The absence of Eu anomaly in samples 10.11a and 10.9b could not be attributed to lack of plagioclase in these rocks, because plagioclase crystals are present in the petrography of these rocks. The neutral values of Eu in these two samples could be explained by the prevalence of oxidation conditions during that stage of the magmatic differentiation and most of Eu became trivalent and could not enter the plagioclase phase (HESS, 1989). This assumption is supported by the presence of the opaque minerals (mainly of Fe and Ti oxides) in the samples which indicate high oxygen fugacity. Such environment occurs in the vicinity of a subduction zone (SAUNDERS et al, 1980). REE patterns of the non cumulate rocks of the Keraf ophiolites are comparable to patterns of similar rocks from ancient ophiolites (Fig. 27) (TSIKOURAS and HATZIPANAGIOTOU, 1998).

In conclusion, Keraf ophiolites demonstrate all the geochemical layers present in the Phanerozoic ophiolitic sequences (tectonites or basal ultramafics, cumulate mafic-ultramafic sequences and the mafic non cumulate assemblages). Geochemical characteristics favour that Keraf ophiolites can be transitional between the MORB and supra-subduction ophiolites. The association of the Keraf ophiolites with the passive margin-related sediments may indicate existence of a back arc basin with a spreading axis, initiation of a supra-subduction zone and extrusion of the Gabgaba arc. Gabgaba arc had collided with Bayuda Terrane and magmatic rocks were intruded. The geochemical signatures of the ophiolites have been imprinted with all these phases.

5.3.2 Post-tectonic intrusions

These are plutons and dykes intruded during or post to the D4 phase of deformation. They are scattered in the KSZ with a relative concentration in the areas affected by the D4 shearing (Fig. 5). About 15 samples from different outcrops were analysed for major and trace elements and five selected samples were analysed for the REE (Table a.4). Based on the mode of occurrence and the chronology of emplacement, the plutons were grouped in two categories: the syn-D4 (older) and the post-D4 (younger). The former are in most cases dioritic to granodioritic and are characterised by an extended range of SiO_2 (46-67 wt. %), while the latter are granitic in composition with SiO_2 wt. % above 70% (Table a.4). Petrographically, the diorites are rich in hornblende and Ca-plagioclase while the granodiorites are biotite and Na-plagioclase rich. The granites are pinkish in colour, rich in K-feldspar and they possess all the petrographic characteristics of the A-type intrusions scattered in NE Sudan (VAIL, 1985). The petrography of selected samples is displayed in appendix I. The wt % of Na_2O, CaO, TiO2, Fe_2O_3 and MgO is high throughout the range of composition. Sr and Ba contents are also high in most of the samples (Table a.4).

On HARKER (1909) variation diagrams, the rocks show clear trends for most of the major and trace elements when plotted against SiO_2 (Fig. 28). On the SiO_2-TiO_2 variation diagram two lines of correlation trends could be observed (Fig. 28a). One trend is for the samples characterised by SiO_2 content less than 70 wt % which are the older. The other variation trend is for the younger samples which have SiO_2

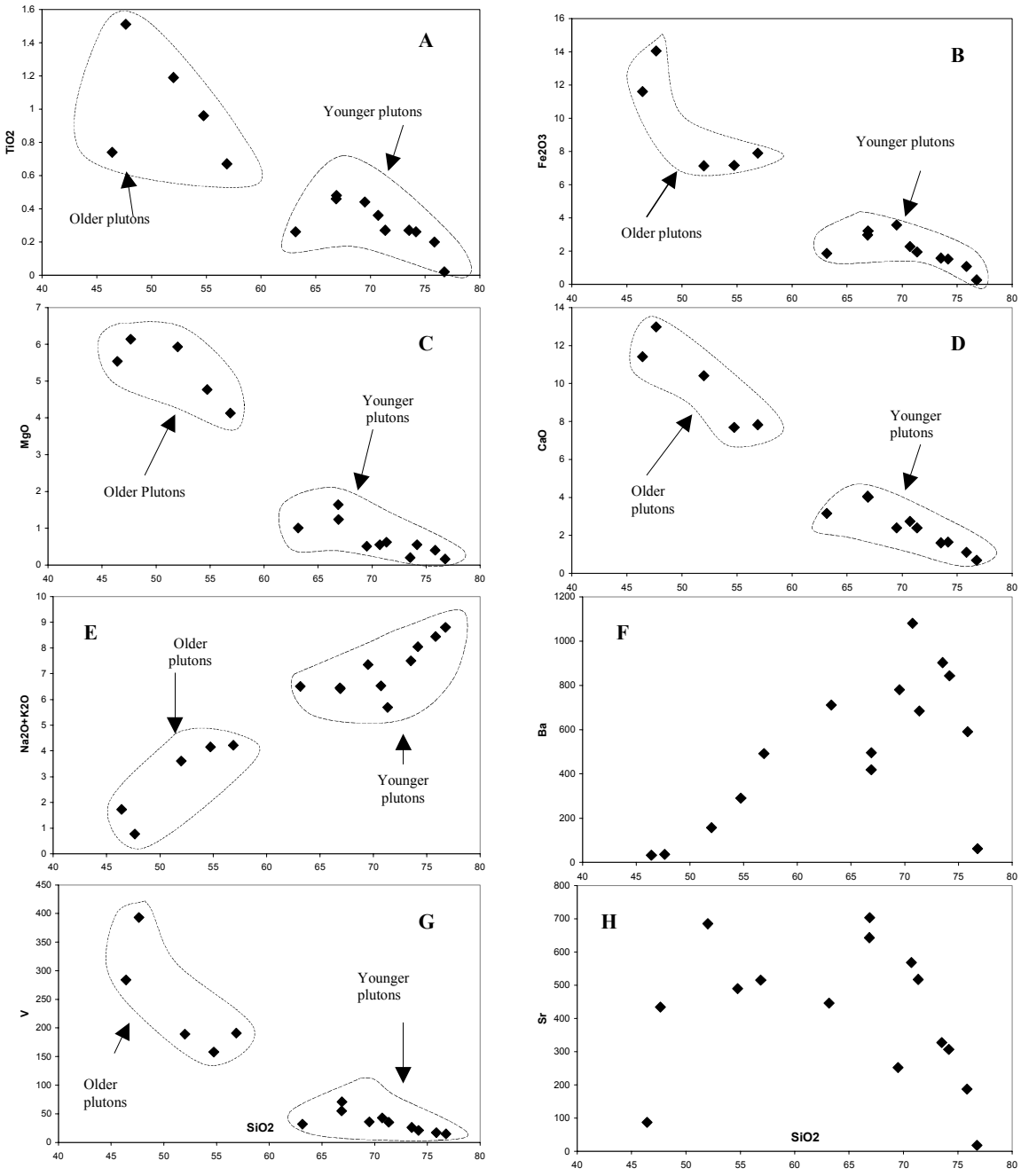

Fig. 28: Harker variation diagrams of SiO_2 against some of the major oxides and trace elements of the granitoids from the Keraf Shear Zone. Note that in most cases a remarkable coherent linear correlation could be revealed.

contents between 70 and 80 wt %. The same pattern is observed in the SiO_2-Fe_2O_3 plot (Fig. 28b). On the SiO_2-MgO variation diagram all the samples fall on a single coherent line (Fig. 28c). SiO_2-CaO variation plot shows a coherent straight line for all the samples (Fig. 28d). SiO_2-(Na_2O+K_2O) plot shows a positive trend for all the samples (Fig. 28e). In this plot the samples of the younger plutons are more coherent than the older ones. Most of trace elements show linear correlation with SiO_2, but less coherent as in the major oxides (Figs. 28f and g). Other trace elements revealed scattered distribution with SiO_2 (Fig. 28h). The argument that variation trend of oxides of the

older plutons differ from that of the younger ones is to be substantiated by more analysis.

Samples 1.1 and 11.11 are characterised by relatively higher values of Cr, Ni and TiO_2 than the other samples (Table a.4). These values are higher than the average concentrations for a normal continental crust (TAYLOR and MCLENNAN, 1985). Thus a contamination from a mafic material could be possible.

Chemical data indicate that Keraf plutons plot mainly in the medium- and high-K fields, with the older rocks being less potassic and less felsic than the younger ones (Fig. 29). The samples are characterised by Alumina Saturation Index, ASI (ASI = molar $Al_2O_3/CaO+Na_2O+K_2O$) less than 1.1, with the exception of one sample, and most of them are plotted in the meta-aluminous field of Fig. 30. On the geochemical rock classification diagram of SiO_2 Vs (Na_2O+K_2O) (Le Maitre et al 1989, Cox et al 1979), the older plutons are plotted in the gabbroic-diorite field, whereas the younger ones appear in the granite-granodiorite fields (Fig. 31). This classification is in agreement with the petrographic characteristics of the rocks. Mafic dykes are plotted in the gabbro field. It is observed that all the plotted samples lie in the sub-alkaline field (Fig. 31). On the AFM diagram (IRVINE and BARAGAR 1971) the plutons are characterised by calc-alkaline trend of differentiation while the mafic dykes show tholeiitic trend of differentiation (Fig. 32).

On the tectonic discrimination diagram using major elements, Keraf plutons are scattered mainly in the fields of syn-collision and pre-late collision granitoids when plotted in the R1-R2 diagram (Fig. 33) (BATCHELOR and BOWDEN, 1985). One sample (11.11) is located in the mantle fractionated fields. This sample is among the relatively old group and is characterised by higher values of Cr, Ni, TiO_2, and V in comparison to the other plutons (Table a.4). On the SiO_2-Al_2O_3 discrimination diagram (MANIAR and PICCOLI, 1989) the plutons which have SiO_2 more than 70 wt % plot in the field of post-orogenic granitoids (POG) or in the field of the island arc + continental arc + continental collision granitoids (IAG+CAG+CCG) (Fig. 34). In this case a continental collision tectonic environment is favoured in accordance with the structural and lithological data. On the MgO-FeOt discrimination diagram (MANIAR and PICCOLI, 1989), Keraf plutons are also distributed among the POG and CCG (Fig. 35).

On the trace elements tectonic discrimination diagram (PEARCE et al, 1984) the samples analysed for Y and Nb fall in the volcanic arc + syn-collision granitoids (VAC+SCG) (Fig. 36).

The patterns displayed by the REE of five selected samples from the Keraf post-tectonic intrusions normalised to chondrites are seen in Fig. 37**.** It is observed that the patterns for the plotted five samples are enriched in all the REE relative to chondrite, i.e. they are plotted above 1. The REE patterns are relatively flat and remain mostly sub-parallel which may indicate that they are product of the same crystal fractionation process (ROLLINSON, 1983). The only exception is the pattern of sample 6.9 (granodiorite) in the LREE segment (Fig. 37). The LREE are relatively enriched than the HREE. Three samples (3.10, 7.15 and 1.1) coincide in their La, Ce and Pr contents but their patterns split apart in the MREE and the HREE segments. The only significant Eu-positive anomaly is the one displayed by sample 1.1 (diorite). This is attributed to the phenocrysts of Ca-rich plagioclase which is a major mineralogical phase in the thin section of the rock. A relatively weak positive Eu-anomaly is displayed by the pattern of sample 7.15 (granodiorite). Both of these (1.1 and 7.15)

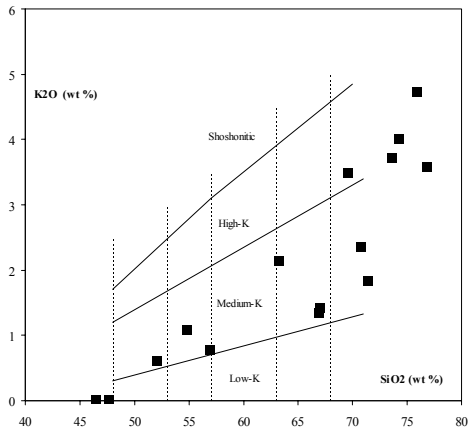

Fig. 29: SiO_2 Vs. K_2O binary plot of the Keraf post-tectonic intrusions. The relatively older plutons plot in the low-K and medium-K fields, while the younger ones plot in the high-K field. Boundaries are after PECCERLIO and TAYLOR (1976).

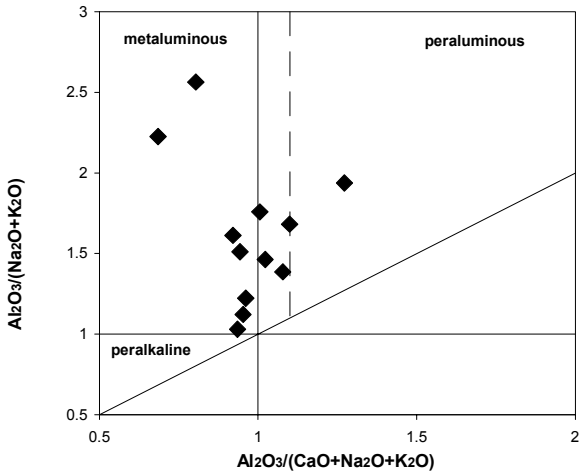

Fig. 30: Molar A/CNK Vs. molar A/NK binary plot for the Keraf granitoids. The majority of the samples plot in the metaluminous field because they have alumium saturation index of less than 1.1. Dashed line is the 1.1 A/CNK boundary (boundaries are after MANIAR and PICCOLI, 1989).

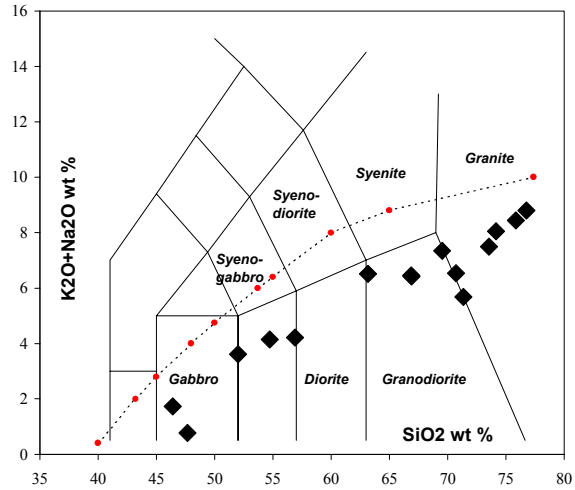

Fig. 31: Total alkali-silica classification of the plutons from the Keraf Shear Zone. The dotted line is the alkaline-subalkaline series boundary. The original names of the volcanic rocks are replaced by the plutonic equivalents to make comparison easier (COX et al, 1979; LE MAITRE et al, 1989).

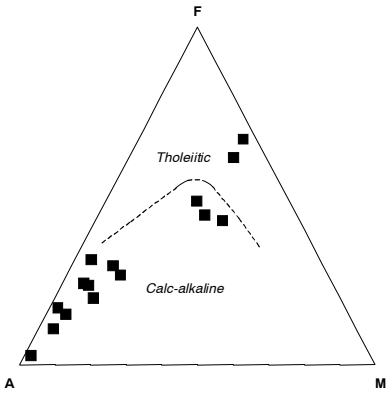

Fig. 32: AFM ternary plot shows the predominant calc alkaline trend of the Keraf post-tectonic intrusions. The two mafic dyke samples plot in the tholeiitic field (trend is after IRVINE and BARAGAR, 1971).

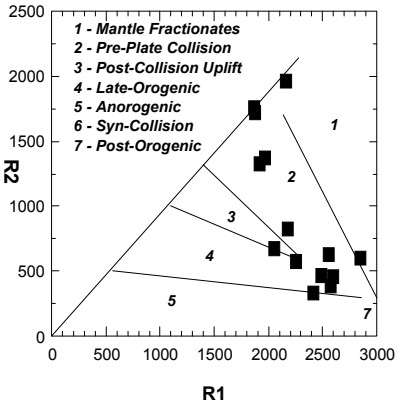

Fig. 33: R1 {4Si-11(Na+K)-2(Fe+Ti)} vs. R2 {6Ca+2Mg+Al} classification for the Keraf post-tectonic intrusions. Most of the samples are concentrated in the syn-collision and pre-late collision fields (BATCHELOR and BOWDEN, 1985).

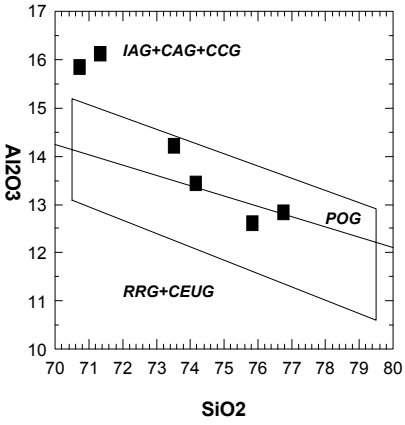

Fig. 34: Silica-Alumina binary discrimination plot for the Keraf plutons which have SiO_2 content more than 70 wt %. POG: post orogenic granitoids, RRG: rift-related granitoids, CEUG: continental epeirogenic uplift granitoids, IAG: island arc granitoids, CAG: continental arc granitoids and CCG: continental collision granitoids (MANIAR and PICCOLI, 1989).

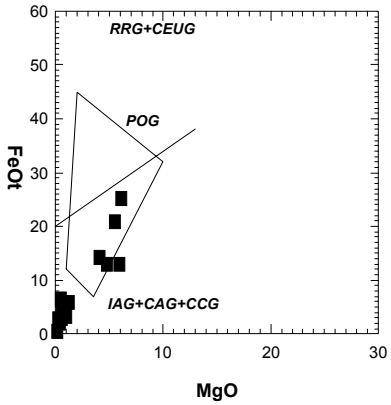

Fig. 35: MgO-FeOt binary tectonic discrimination plot for the Keraf granitoids. Names of fields are similar to those of Fig. 35. The line divides RRG+CEUG from IAG+CAG+CCG fields, while the closed field is POG (MANIAR and PICCOLI, 1989).

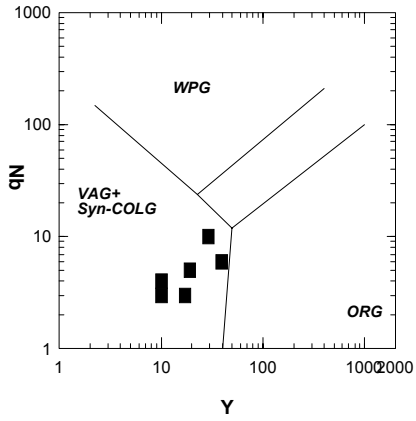

Fig. 36: Y-Nb binary discrimination plot for the Keraf plutons which were analysed for Nb and Y. VAG: volcanic arc granitoids, WPG: within plate granitoids, ORG: oceanic ridge granitoids (PEARCE et al, 1984).

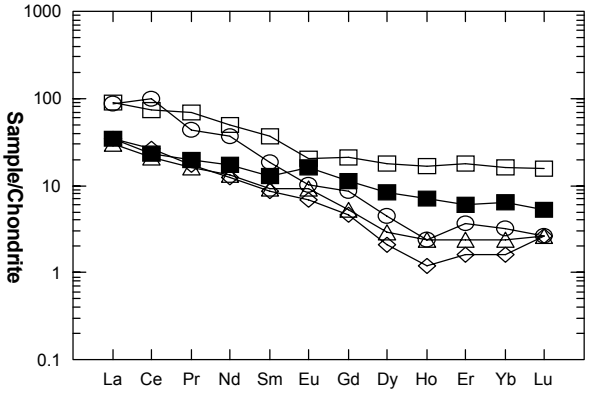

Fig. 37: Chondrite-normalised REE patterns of five selected samples from the Keraf plutons. Open rectangle: sample 11.10 (granodiorite), filled rectangle: 1.1 (diorite), diamond: 3.10 (granite), circle: 6.9 (granodiorite) and triangle: 7.15 (granodiorite). Chondrite normalisation value is after BOYNTON (1984).

samples belong to the low SiO_2 older group. A negative Eu-anomaly is revealed by the pattern of sample 11.10 (granite). This sample is classified among the high-SiO_2 younger plutons. The negative Eu anomaly could be attributed to the fractionation of the Eu into the plagioclase phase of the early formed rock phase.

Patterns displayed by spider diagram normalised to primitive mantle are seen in Fig. 38. The patterns have shown a negative Nb anomaly compared to the LREE and Th. This character is observed in the subduction related granitoids (CONDIE, 1998).

To conclude, Keraf plutons embrace two lithological as well as geochemical groups. The first group is the relatively older and dioritic-granodiorite in composition, medium to low K and depleted in Nb (relative to Th, La and Ce). Mineralogically, they are rich in plagioclase, hornblende and biotite. This group has all the characteristics of the I-type granitoids (CONDIE, 1998; KÜSTER and HARMS, 1998). The second group is relatively younger, granitic in composition, and has a high-K character. Their petrography is mainly quartz, K-feldspars (microcline and perthite) and biotite. This group has the characteristics of the (post-collisional plutons) A-type granitoids (CONDIE, 1998; KÜSTER and HARMS, 1998). The older plutons have been emplaced around the period 700 Ma ago (chapter 7). No zircon geochronological data is available from the presumably younger plutons to draw age correlation between the two groups. Therefore, magmatic activities in the Keraf area could have started by fractional crystallisation of a primitive mantle or partial melting of the lower crust. The older group (I-type) of the intrusions was formed in earlier stages of the magmatic differentiation. The younger (A-type) granitoids were later crystallised from the residue of the magma. It could also be possible that the two groups have no genetical relation. However, the sub-parallel patterns exhibited by the REE of the granitoids favour a common back ground of the two groups.

5.3.3 High- to medium- grade gneiss

The high-grade metamorphic rocks in the KSZ are metasedimentary sequences in the upper amphibolite-facies metamorphism and they occupy the lowermost stratigraphic level within the KPTA (chapter 3). Lithologies encountered include: leucocratic gneiss and migmatites, high-grade calc-silicates, amphibolites and garnet-bearing schists. Rock chemistry is investigated to substantiate the field and the petrological evidences that the high-grade rocks in the Keraf area have a sedimentary precursor. This will help in the reconstruction of the geodynamic evolution of the Bayuda-Wadi Halfa Terranes which represent the possible eastern foreland of the Nile Craton (ROCCI, 1965).

Eight samples from the high-grade gneiss were analysed for the major and trace elements (Table a.5). Most of the high-grade metamorphic rocks are moderately siliceous with SiO_2 content above 70 wt %. Only two samples (11.15 and 12.2b) have SiO_2 contents less than 70 wt %. All the analysed samples have LOI values in the range of 0.4 - 0.8 wt % and chemical index of alteration (CIA) within the range of the granite-granodiorite (Table a.5) (NESBITT and YOUNG, 1984; 1982). Sample 12.2b (amphibolite) has CIA of 32 which is in the range of unaltered basalt (NESBITT and YOUNG, 1982). The two parameters, CIA and LOI, indicate low degree of sedimentary reworking in the source rock and negligible values of secondary alteration.

On the molar $(CaO+Na_2O)$-Al_2O_3-K_2O diagram (Fig. 39) (NESBIT and YOUNG, 1989) the samples plot within the trend of normal weathering irrespective of their composition. This may indicate that, beside the lack of palaeo-weathering, the rocks have not experienced noticeable metasomatic changes, i.e. addition or removal of K_2O, Na_2O or Al_2O_3 (NESBITT and YOUNG,

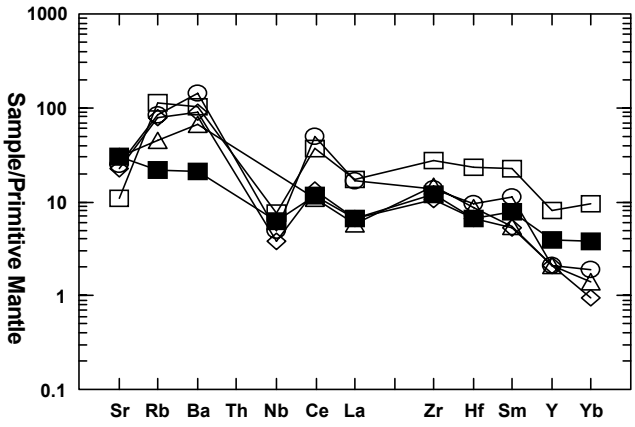

Fig. 38: Primitive mantle-normalised spider patterns of selected samples from the post-tectonic intrusions. Symbols of the plotted samples as in Fig. 37. Normalisation values are after SUN and MCDONOGH (1989).

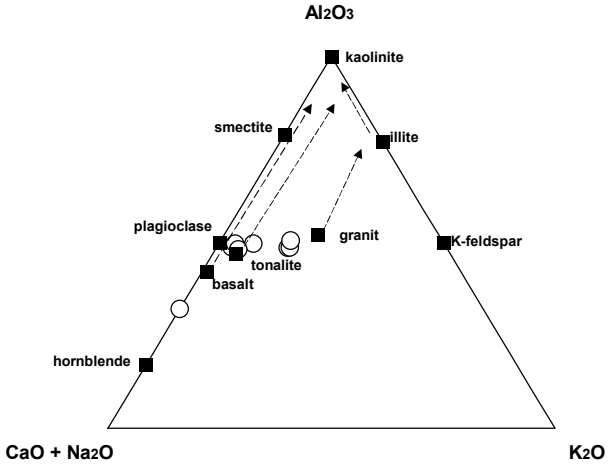

Fig. 39: Molar $(CaO+Na_2O)$-Al_2O_3-K_2O weathering trend diagram for the high- to medium- grade gneiss from the KPTA. Arrows point to the average weathering trend (NESBIT and YOUNG, 1989).

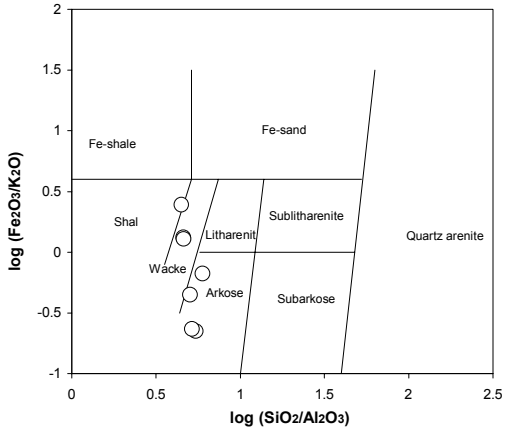

Fig. 40: Log SiO_2/Al_2O_3 vs. log Fe_2O_3/K_2O binary plot for the classification of high- to medium-grade gneiss of the KPTA. For explanation see the text (HERRON, 1988).

1982). Sample 12.2b (amphibolite) plots on the ($CaO+Na_2O$)-Al_2O_3 axis due to its depletion in K_2O (which is only 0.03 wt %).

Unlike the majority of the high-grade metasediments, the amphibolites (samples 11.15 and 12.2b) show high values of Fe_2O_3, MgO, CaO, TiO_2 and V (Table a.5). These elements are accommodated in the amphiboles and epidotes, which are the dominant mafic constituent of these rocks.

On the major element geochemical classification diagram of HERRON (1988), all the samples with the exception of 11.15 and 12.2b plot in the fields of arkose and greywacke (Fig. 40). Sample 11.15 (amphibolite) plots on the shale-greywacke boundary, while sample 12.2b (amphibolite) does not appear on the diagram because of its low K_2O content. The sedimentary origin of the felsic high-grade metamorphic rocks in the Keraf area can be a mature continental source or an acidic volcanic material. The amphibolites may have been derived from a sedimentary source (i.e. marls). Gabgaba-Gebeit-Gerf volcanic arcs are possible sources for the sedimentary material. Similar conclusions have been reached for the high-grade metasediments from Bayuda Dessert (KÜSTER and LIEGEOIS, 2000). These findings are to be further substantiated by REE and isotopic investigations (Nd and Sr).

5.3.4 Metavolcanic suites

Nine samples from the low-grade metavolcanics have been analysed for major and trace elements (Table a.6**)**. The rocks are metamorphosed at greenschist facies and have higher degree of alteration and carbonatisation. The LOI is relatively high, between 2.9 and 7.2 and therefore, the major oxides and the mobile trace elements can not be used for the geochemical rock classification and the geotectonic discrimination of this suite. In this study, only the HFS and the stable transitional elements which have higher degree of petrogenetic stability such as Ti, P, Zr, Y, Th, Co, Ni, V, and Cr are used (PEARCE, 1975).

On the TiO_2-Zr chemical classification binary diagram (HALLBERG, 1985) the Keraf metavolcanics are scattered in the basalt, basaltic andesite and the andesite fields (Fig. 41).

On the Ti-V geotectonic discrimination diagram (SHERVAIS, 1982) the metavolcanics have Ti/V in range of 20 - 50, thus are characterised by ocean floor basalt affinities with little imprints from island arc basalts (Fig. 42). It is observed that the geochemical signatures of the metavolcanics are different from that of the post-tectonic intrusions. This may rule out any genetical relation between the two suites. Our data indicate that the post-tectonic intrusions are calc-alkaline collisional related I-type and post-collisional A-type granitoids, while the metavolcanics are of ocean floor or island arc geochemical affinities. The Keraf metavolcanics can be correlated with similar assemblages in the NE of Bayuda and to the N. of Berber (RIES et al, 1985). If such a correlation is valid the Keraf metavolcanics could have an age of ~ 800 Ma (RIES et al, 1985), while the post-tectonic intrusions are in the range of 710-700 Ma old. In the Keraf area it is structurally evident that the volcanics are relatively older than the granitoids because the metavolcanics have witnessed all the deformational history whereas the granitoids bear only structural elements associated with D4-phase (latest) of deformation. The metavolcanics could not be part of the Keraf ophiolitic sequences because of their mode of occurrence as thin layers conformably intercalated within the low-grade metasediments, while the ophiolitic sequences are recognised as thrusted massif ridges.

5.3.5 Siliciclastic and carbonate-rich metasediments

Low-grade metasediments both silica-rich clastic and carbonate-rich rocks have been analysed for major and traced elements

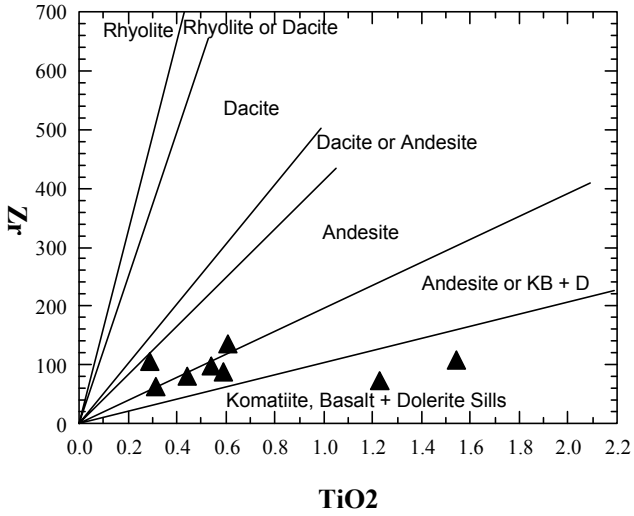

Fig. 41: TiO2-Zr classification for the metavolcanics from the KPTA (HALLBERG, 1985)

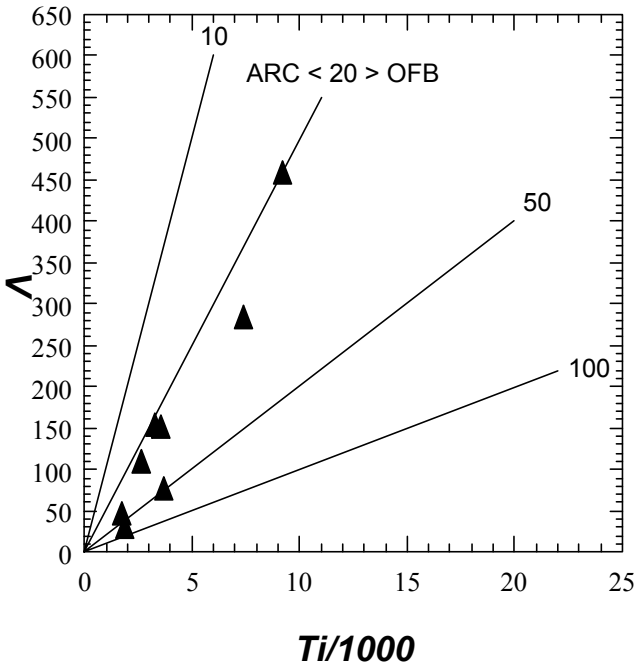

Fig. 42: Ti-V discrimination plot for the metavolcanics from the KPTA. OFP: ocean floor basalt and ARC: island arc basalt (SHERVAIS, 1982).

(Table a.7). The original composition of the low-grade metasediments can only be inferred by the HFS elements. The major oxides are expected to be highly mobilised due to the sediment transport, deposition in marine environment and the low-grade metamorphism. Unfortunately, the REE content of the sediments were not determined, thus the data displayed on table a.7 is not sufficient to construct a conclusive tectonic environment for the deposition of the sediments. Nevertheless, the following geochemical trends could be good contributions to understand the background and

the sedimentary environment of the Keraf low-grade metasediments.

In this study, the low-grade metasediments of the KSZ have already been divided into siliciclastic and carbonated sequences (chapter 3). The siliciclastic metasediments represent the most abundant rocks in the northern sector of the KSZ (Fig. 5). In some localities the rocks are not much affected by the low-grade metamorphism and most of sedimentary textures and structures are preserved (Plate 3). Chemically, the rocks have SiO_2 content in the range of 50-80 wt %. Al_2O_3 content is more than 10 wt % and may reach up to 20 wt % in the rocks containing clays and/or muscovite. The existence of clays indicate chemical weathering of the feldspars. The chemical index of alteration (CIA) of the rocks is within the range of the altered granite and granodiorite, i. e. not very high. Fe_2O_3 content is variable and may reach up to 15 wt % in the samples containing Fe-oxides. This may indicate deposition in an oxidising environment. TiO_2 content of the samples are above the average level of the upper crust (SUN and MAC DONOUGH, 1989). This could favour an igneous rock as a source of the sediments. CaO content is up to 20 wt % in some of the samples. This may lead to the fact that sedimentation had taken place in a shallow basin where the compensation depth of the carbonates was not reached.

Combing these chemical facts with the field relation, structural elements and the petrography of the Keraf metasediments, I conclude that the sediments were derived from a volcanic arc and deposited in a nearby shallow basin.

The carbonate-rich metasediments could be grouped in two chemical categories depending on the MgO contents: the marbles and the dolomites. The marbles are rich in CaO and are depleted in all other major oxides (Table a.8). The black and the brown marbles are relatively enriched in V, Ni, Mn, Fe_2O_3 and Cr than the white and grey marbles (Table a.8). Some marble samples are SiO_2 enriched. These are mainly located close to the D4-shear zones. Dolomites have MgO content up to 20 wt % and, in comparison to marbles, they are relatively depleted in CaO, Al_2O_3, V and Sr (Table a.8). Variation diagrams of major and trace elements show scattered patterns.

The carbonate-rich metasediments preserve most of their primary textures and structures, such as laminations, bedding and oolitic textures (Plate 4). Such features favour deposition in a shallow passive margin. These conclusions need to be confirmed by further trace elements studies and isotopic investigations.

6 MINERAL CHEMISTRY

6.1 Introduction

Petrographic examination of 7 polished thin sections from the medium- to high-grade gneiss (sample 11.13), the high-grade metasediments (A26, A45 and A55), the post-tectonic intrusions (samples 1.1 and 6.9) and a volcanic rock of the low-grade metamorphic rocks (sample A57) was carried out. Mineral assemblages with appropriate equilibrium textures (relatively low post-magmatic and post-metamorphic alterations) were selected for the microprobe analysis to satisfy mainly the following two objectives:

1) To characterise the chemical composition of the selected minerals, especially for those not identifiable microscopically.

2) To constrain the peak metamorphic temperature and pressure conditions wherever it is possible.

3) To reveal a relation between composition and age of minerals.

6.2 Amphiboles

Amphibole crystals from three samples (1.1, A45 and A55) have been analysed. The results of the analysis are displayed in table a.9.

Sample 1.1 is a dioritic pluton, thus the primary amphiboles are igneous. They are large euhedral phenocrysts, cracked and contain inclusions of secondary mica, chlorite and epidote (Fig. 43a). The amphibole phenocrysts are embedded in a coarse grained matrix of plagioclase and quartz. Three different amphibole phenocrysts were analysed. They have a composition of Ca-Mg rich hornblende and actinolite (Table a.9). The hornblende is relatively rich in TiO_2 and Na_2O. Both Ti and Na increase from rim to core where they reach maximum values of 3.6 and 1.9 oxide wt % respectively (Fig. 44a). CaO has a reverse relation with Na_2O and TiO_2, i. e. CaO is relatively higher at the rims compared to the cores (Fig. 44b). Si decreases from rim to core (Fig. 44c), while Al shows slight increase from rim to core (Fig. 44d). Under microscope the rims are yellowish and the cores are green in colour in between them is a mixed coloured area.

The points which have actinolite composition have a relative lower Al_2O_3 content (from 1.7 to 6.4 wt % Al_2O_3) than the Ca-Mg amphiboles (Table a.9). It is most likely that the original igneous hornblende was rich in Na_2O, TiO_2 and Al_2O_3 and depleted in CaO. Therefore, the actinolite is more likely to be a secondary phase, because it is close to the rims. A late phase of mineral reactions had occurred during D4 shearing and had caused the formation of epidote, chlorite and mica inclusions within the primary mineral phases.

On the Si-Mg/(Mg+Fe^2) binary plot a clear positive relation is seen for the igneous amphiboles which indicates enrichment of X_{Mg} {Mg/(Mg+Fe2)} with Si enrichment (Fig. 45a). The X_{Mg} for the igneous amphiboles ranges from 0.57 to 0.74. On the Si-(Na+K) plot, a coherent negative relation is revealed by the igneous amphiboles (Fig. 45b). The high CaO values at rims of the amphiboles could be attributed to a local equilibrium with the matrix which is predominantly composed of Ca-rich plagioclase.

The igneous amphiboles are calcic amphiboles ((Ca+Na)-Na diagram), (Fig. 46a) (DEER et al, 1992). On the Si-Mg/(Mg+Fe^{2+}) lassification diagram (HAWTHORNE, 1981), they are mainly actinolite hornblende and magnesio-hornblende, while few points are on the actinolite and Tschermakeite hornblende (Fig. 46b).

The metamorphic amphiboles of the gneiss and the high-grade metasediment occur either as large porphyroblasts or as inclusions within the large garnet porphyroblasts (Fig.

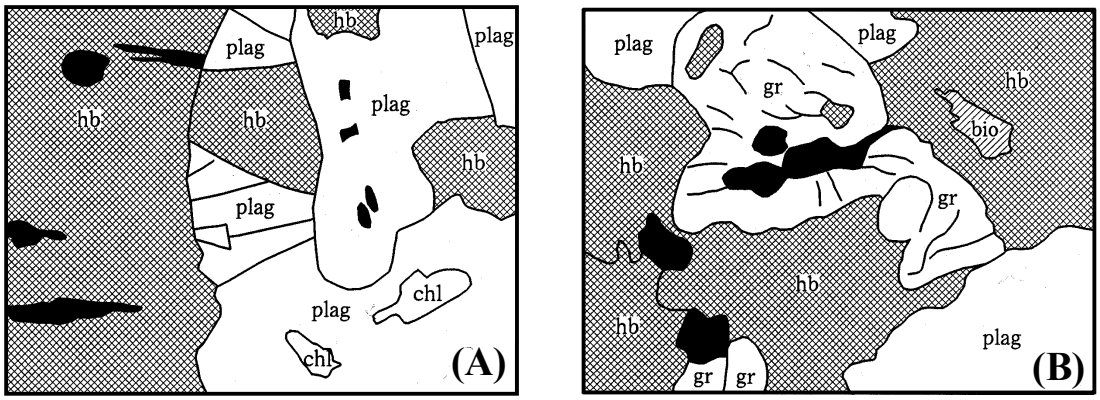

Fig. 43: Sketch of a photomicrograph of **A)** sample 1.1 (diorite) shows the mineral assemblage and the igneous texture. Dark areas: epidote, chl: chlorite, hb: hornblende and plg: plagioclase. **B)** sample A45 (metasediment) shows the mineral para-genesis of the garnet and the hornblende. Dark areas: ilmenite, hb: hornblende, gr: garnet, bio: biotite and plg: plagioclase.

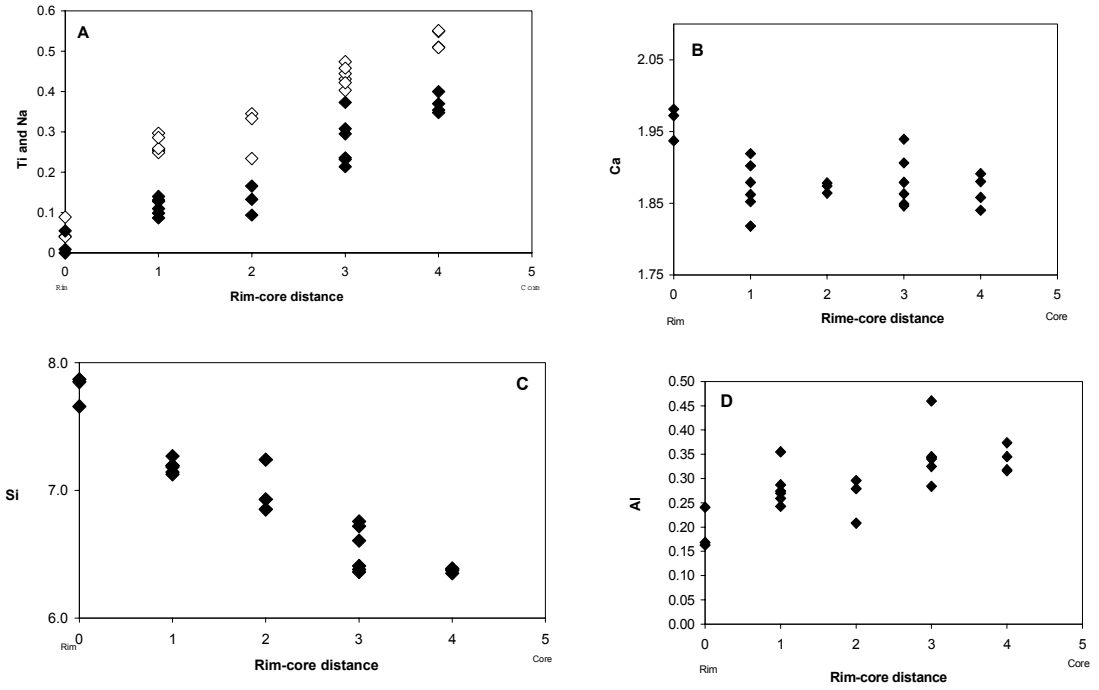

Fig. 44: Rim – core zoning in igneous hornblende from a dioritic intrusion, sample 1.1. **A**) distribution of the Ti (filled diamonds) and the Na (open diamonds). They both increase systematically from rim to core. **B**) Ca decreases slightly towards the core. **C**) Si decreases drastically towards the core. **D**) Al increases towards the core. Measurements are taken from five points at 100 μm interval.

43b). Three analysis from the amphibole inclusions (points 46, 47 and 48 in table a.9) are reported from an assemblage of garnet-biotite-plagioclase-hornblende (Fig. 43b). They have a composition very close to that of the Tschermakite (Fig. 46) (DEER, et al 1992). The composition is characterised by a relatively high Al_2O_3 and K_2O content and low MgO and Na_2O contents from that of the porphyroblasts (Table a.9). The compositional variations within the amphibole inclusions is not clear due to their small size.

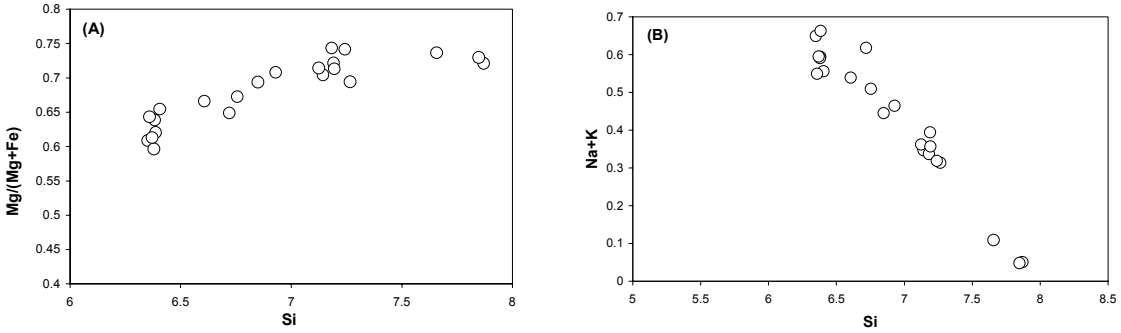

Fig. 45: (A) Si-Mg/(Mg+Fe) plot of the igneous amphiboles (sample 1.1). X_{Mg} increases progressively with increase in Si up to Si=7.5, then the values of X_{Mg} remain constant for values of Si more than 7.5. **(B)** Si-(Na+K) plot revealing a clear negative relation. The Amphiboles are also characterised by an extended value of Na+K.

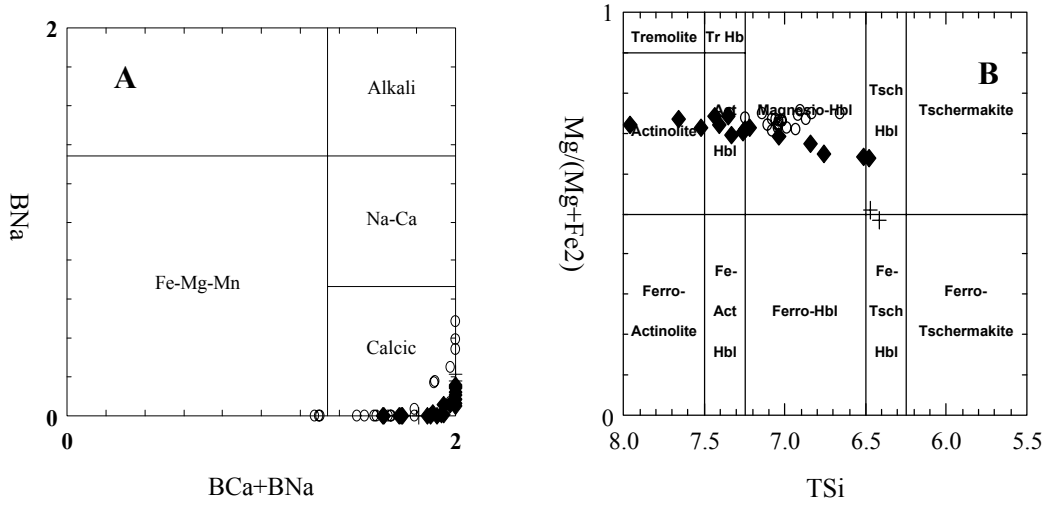

Fig. 46: Classification of the igneous and metamorphic amphiboles according to their Na and Ca contents **(A)**.and according to the Si and X_{Mg} ratio **(B)** (DEER et al, 1992). Circles are the metamorphic (porphyroblasts, samples A55 and A45), crosses are inclusions (sample 26) and diamonds are the igneous amphibole (sample 1.1) (HAWTHORNE, 1981).

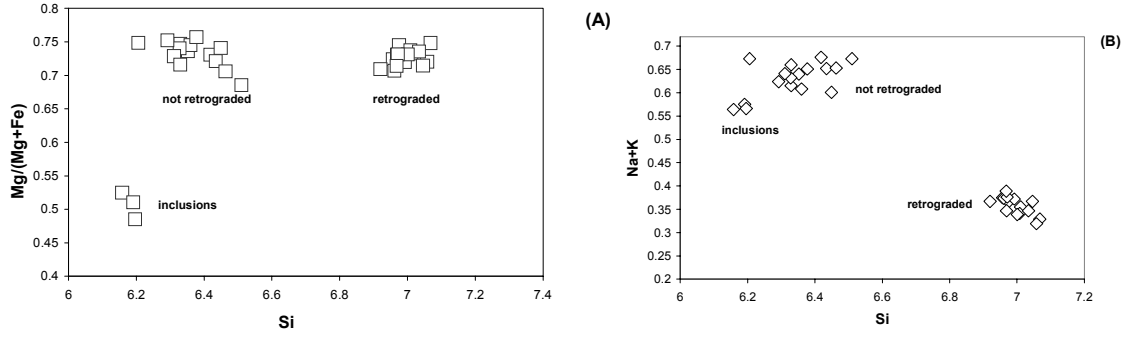

Fig. 47: (A) Binary plot of Si vs. X_{Mg} for the metamorphic amphiboles. The three chemically different varieties are clustered around three points of Si = 7, 6.4 and 6.2. **(B)** Variation of Si with alkalis in the metamorphic amphiboles. The amphiboles which were retrograded from pyroxene have low alkalis content than the other amphiboles. Inclusions are from sample A26, retrograded are from sample A55 and the not retrograded are from sample A45.

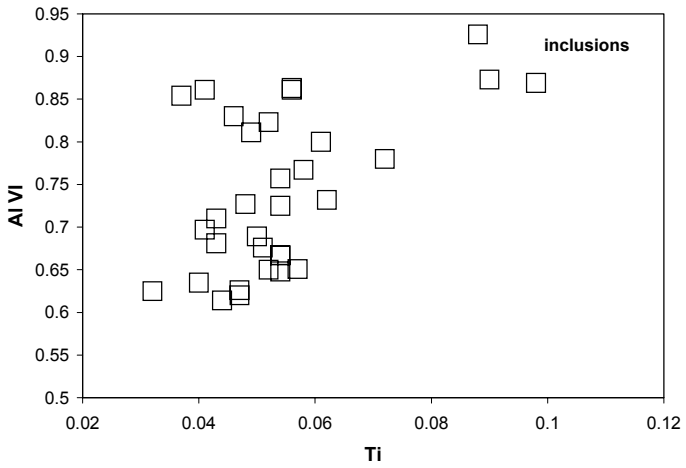

Fig. 48: Variation of Ti vs. Al for the metamorphic amphiboles (samples A55, A45 and A26). The retrograded and the not retrograded amphiboles plot in one area and have a weak positive Ti-Al relation. The inclusions have higher Ti values.

The amphiboles which occur as large porphyroblasts have a composition of Ca-Mg rich hornblende (DEER et al, 1992) (Table a.9). Some of the large calcic amphibole porphyroblasts have cores with a composition very close to calcic-pyroxene (Table a.12 points 142, 144 and 145). This indicates that the development of the hornblende crystals had taken place during retrogressive metamorphic conditions. The analysed metamorphic hornblende can be divided into two groups. The first group is in the assemblage: hornblende-biotite–plagioclase-clinopyroxene-titanite, while the second group is in the assemblage: hornblende-garnet-plagioclase-quartz-epidote-titanite. These assemblages indicate crystallisation under two different T-P conditions. Both of them are within the gneiss and the high-grade metasediments which occur in the southern sector of the KSZ. The first hornblende group is characterised by a relatively higher SiO_2 (~49%) lower Al_2O_3 (~10%), lower Na_2O (~1.2%), higher MgO (~14%) and higher CaO (~12%). On the other hand, the second group has revealed a relatively lower SiO_2 (~43%) higher Al_2O_3 (~14%), higher Na_2O (~2.1%), lower MgO (~10%) and lower CaO (~10%) (Table a.9). The composition in both groups is different from that of the magmatic hornblende reported in sample 1.1. The later is characterised by relatively high contents of TiO_2 and Na_2O (Table a.9).

Thus, the composition of the amphiboles depend mainly upon the mineral paragenesis. This fact is reflected by the values displayed by X_{Mg} {Mg_{Fe} = Mg/(Mg+Fe)}. The Tschemakite (inclusions in the garnet) has reported the lowest values of $X_{Fe,}$ which range from 0.49 to 0.52. The amphiboles which have low silica contents have a wide range of X_{Mg} which extends from 0.69 to 0.76. The amphiboles with pyroxene cores are characterised by a X_{Mg} in the range of 0.71 to 0.75 (Table a.9). On the Si-Mg/(Mg+Fe) variation diagram, for the metamorphic amphiboles, the majority of the points are clustered on two points, i.e. at about Si = 7.0 and Si = 6.4, whereas the area in between is occupied by a few scattered points. Nearly all points are confined in the X_{Mg} value of 0.75 (Fig. 47a). The high Si-content (7.0) amphiboles show a negative relation of Si with X_{Mg} (Fig. 47a), while the low Si-content (6.4) amphiboles show a weak positive Si-X_{Mg} relationship (Fig. 47a). Most of the amphiboles which have retrogressive signatures (have cores of Ca-pyroxene) are among the ones of the high Si content.

On the Si-(Na+K) variation diagram, the samples with higher Si-content (~ 7) are

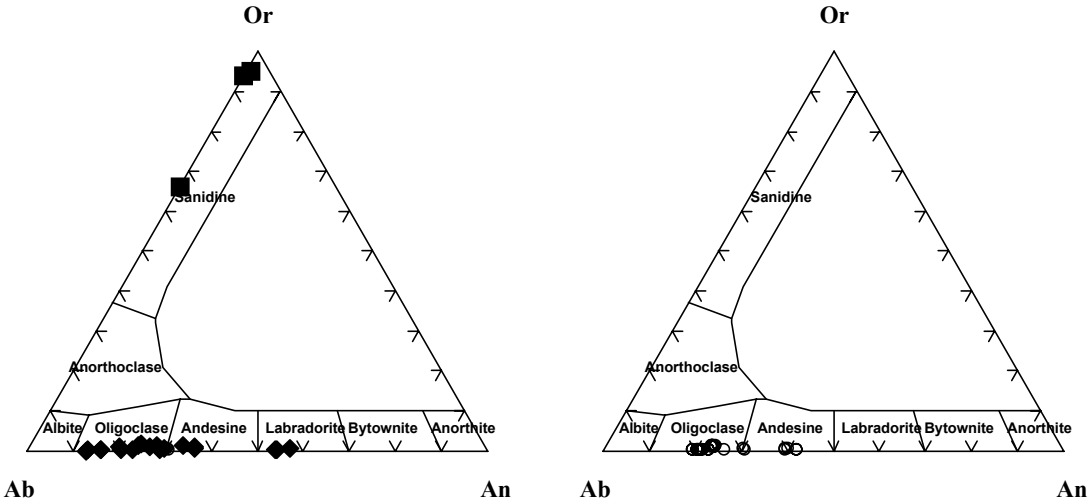

Fig. 49: Ab-An-Or Ternary classification plot of the feldspars from the KPTA. **A**) Igneous feldspars from samples 1.1, 6.9 (filled diamonds) and A57 (filled squares). The volcanic feldspars (sample A57) plot in the andesine-orthoclase field and the plutonic feldspars (samples 1.1 and 6.9) are oligoclase - labradorite. **B**) Metamorphic feldspars from samples A26, A45 (high-grade metasediment) and 11.13 (gneiss) (DEER et al, 1992).

plotted around (Na+K) = 0.35 and show a coherent negative relation, while the samples with lower Si-content (~ 6.4) are clustered around the 0.65 (Na+K) value (Fig. 47b). On the Ti-Al variation plot, the metamorphic amphiboles show a weak positive linear relation (Fig. 48).

On the amphibole classification diagrams (HAWTHORNE, 1981), the metamorphic amphiboles plot in the calcic amphibole field (fig. 46a). The majority of the analysis are classified as Mg-hornblende and a few are actinolitic hornblende, while the inclusions plot in the Fe-Tschmerkite-hornblende field (Figs**.** 46b).

6.3 Feldspars

The feldspars analysed in this study are reported from the post tectonic plutons (samples 1.1 and 6.9), the high-grade metamorphic rocks (samples A26, 11.13 and A45) and the volcanics of the low-grade metamorphic assemblages (sample A57). The chemical composition of the feldspars in 58 points from 9 different paragenesis are determined. The results are displayed in table a.10.

Feldspars in the plutonic intrusions occur as euhedral phenocrysts in a matrix of hornblende-quartz-biotite-secondary epidote and chlorite. They have common boundaries with phenocrysts of quartz, hornblende and micas. The phenocrysts of the igneous plagioclase are zoned, turbid and cracked with secondary mineral phases as inclusions and as crack-fillings (Fig. 43a). The composition of the plagioclase ranges from An_{13} at the rim to An_{53} at the core in the diorite (sample 1.1). In the granodiorite (sample 6.9) the plagioclase composition ranges from An_{20} at the rims to An_{36} at the cores. On the Ab-An-Or triangular classification plot of the feldspars (DEER et al, 1992) all the plutonic plgioclase are plotted in the fields of oligoclase, andesine and labradorite (Fig. 49a). Cores of phenocrysts are labradorite whereas the rims are oligoclase and the points between the core and the rims are in the andesine field.

The feldspar crystal in a volcanic rock (sample A57), which is associated with the Keraf low-grade metasediments, are elon-

gated laths warped around sub-circular Na- and Al-rich pseudomorphic crystals (Fig. 50). The pseudomorphic crystals are assumed to be nepheline which were transformed to a mixture of clays. X-ray mapping of the polished thin section has shown that the feldspar laths are alternating albite and K-rich alkali feldspars (sanidine and orthoclase) which define the trend of the relict primary igneous foliation. The sub-circular pseudomorphic crystals are enriched in Al and Na and have moderate Si content with respect to the matrix (Figs. 50b and d). They show zoning with respect to the distribution of K and Na (Fig. 50c). Such texture indicate that the volcanics associated with the low-grade metasediments in the southern sector of the KSZ may have been originated from a trachytic volcanic material.

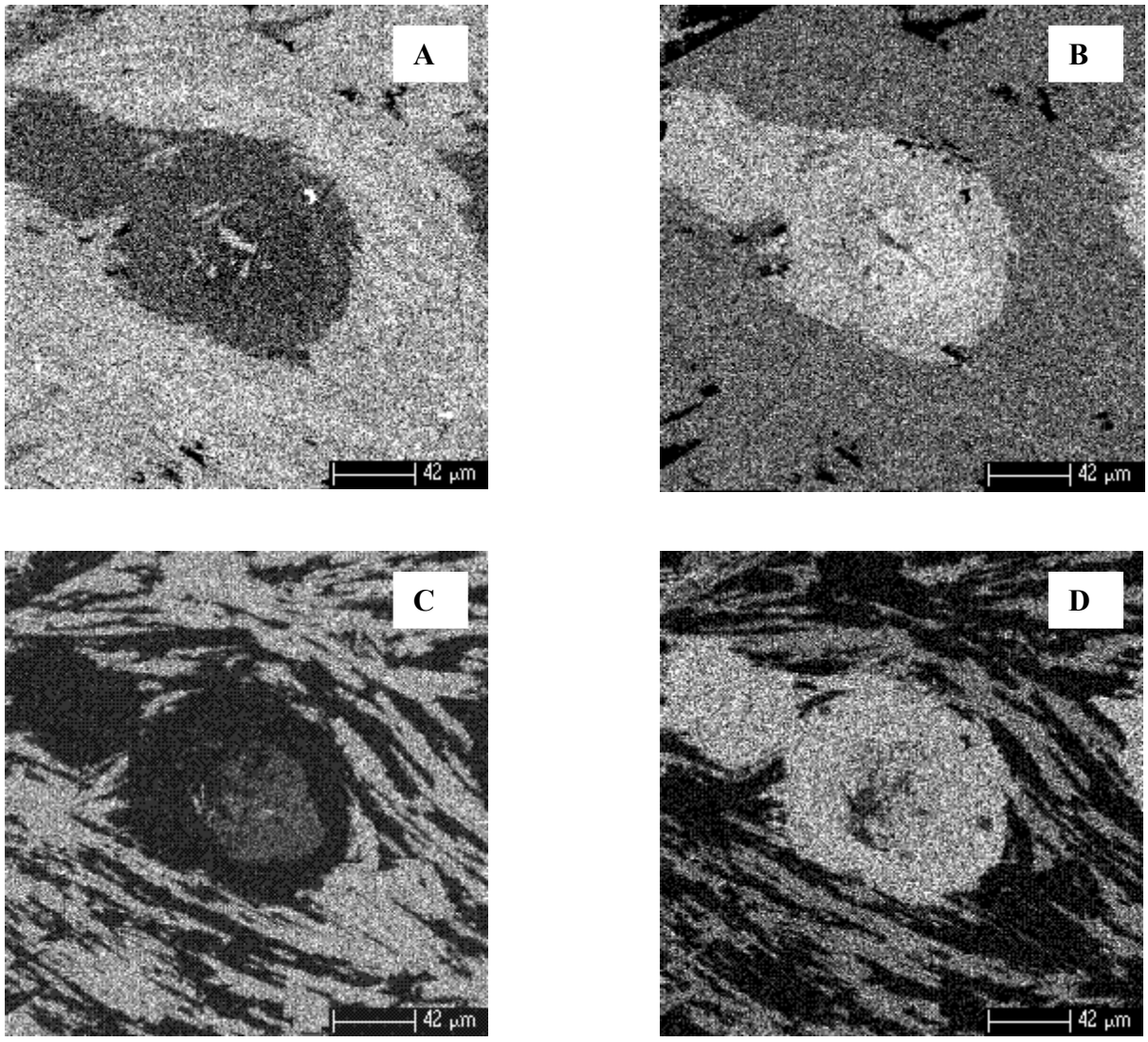

Fig. 50: X-ray mapping of a metavolcanic polished thin section (sample A57) showing the distribution of elements in the trachytic matrix and within the relicts of the nepheline phenocrysts. **A)** shows a matrix more rich in Si than the phenocryst which has some Si rich inclusions. **B)** shows that Al is rich in the phenocrysts than in the matrix. **C)** reveals the distribution of K in the crystals. K-feldspars appear as elongated laths in the matrix (white areas) alternating with albite (dark areas). The phenocryst relicts are zoned with cores richer in K and rims rich in Na. **D)** shows the distribution of Na. The phenocrysts are richer in Na and the white areas in the matrix are albite laths.

Three points from the feldspars in the metavolcanics were analysed (Table a.10**,** sample A57). They are very rich in K_2O corresponding to more than 70% Or (Table a.10) (Fig. 49a). It is believed that the K-enrichment is an original feature of the volcanic rock because the alkali feldspars are coexisting with a primary Na-rich pyroxene and albite.

Feldspars associated with the high-grade gneiss and metasediments (samples 11.13, A26 and A45) occur as inclusions within the garnet and the amphiboles, as large subhedral phenocrysts or as small crystals in the ground mass of the rocks. The mineral paragenesis and textures favour a metamorphic origin. They are Na-rich plagioclase (Table a.10, Fig. 49b) which occur in the following assemblages: 1) plagioclase-hornblende-biotite-quartz-chlorite-epidote, 2) plagioclase-garnet-biotite-quartz-alkali feldspar, 3) plagioclase-biotite-muscovite-quartz-chlorite.

The An-content is similar irrespective of the mode of occurrence or the mineral paragenesis which is in the range of An 20 to 40 mole %. Zoning in the plagioclase is weak and observed only in few crystals.

6.4 Garnet

Microprobe analysis of about 40 points were conducted to determine the average composition of the garnet from the gneiss (sample 11.13) and from the high-grade metasediments (samples A26 and A45). The results are displayed in Table a.11.

Garnet from the gneiss occurs in the mineral assemblage: plagioclase-hornblende-biotite-garnet-quartz-epidote-chlorite. It occurs as large subhedral porphyroblasts with inclusions of quartz and chlorite. The crystals are weakly zoned, with Fe^{2+} and Mg slightly increase from rim to core, while Mn and Ca decrease in the opposite direction. The garnet end members are: almandine ranges from 60 to 61, spessartine from 20.6 to 24.3, pyrope from 10.4 to 11.5 and grossular from 6.0 to 7.1 (Table a.11). On the Grs-Alm-Pyp ternary plot, garnets associated with the high–grade gneiss plot close to the Alm apex indicating more Fe contents and less Mg and Ca contents than the garnets associated with the high-grade metasediments (Fig. 51). On the Grs-Sps-Pyp ternary diagram the garnets from the gneiss show higher Mn content than the garnets from the metasediments (Fig. 51).

Garnet in sample A26 is associated with the mineral assemblage: plagioclase-quartz-hornblende-biotite-garnet-opaque minerals, while in sample A45 it is associated with the assemblage: hornblende-garnet-plagioclase-quartz-epidote-titanite (Fig. 43b). In both samples, the garnets are large euhedral to subhedral porphyroblasts with fractures filled with secondary minerals.

The crystals are not zoned and the distribution of the Ca, Fe^{2+}, Mn and Mg from rim to the core is random. The distribution of Fe, Mg, and Ca does not show any pattern.

On the Gross-Alm-Pyp ternary plot the garnets associated with the metasediments are plotted close to the Alm apex (Fig. 51). Garnets from sample A45 are closer to the Alm-Pyp axis than the garnets of sample A26. On the Grss-Spess-Pyp ternary plot the garnets associated with sample A26 are closer to the Gross apex (Fig. 51). Generally speaking, garnets associated with the gneiss in the northern sector of the KSZ are characterised by high Fe and Mn than those occur in the high-grade metasediments in the southern KSZ. On the other hand, the garnets in the metasediments are more calcic and Mg rich than those in the gneiss. The Fe:Mg ratio ranges from 5.4 in the garnet of the gneiss to 4.5 in those of the metasediments. This may indicate increase in the crystallisation temperature in a range of more than 100°C from the north towards the south (SPEAR and CHENEY, 1989).

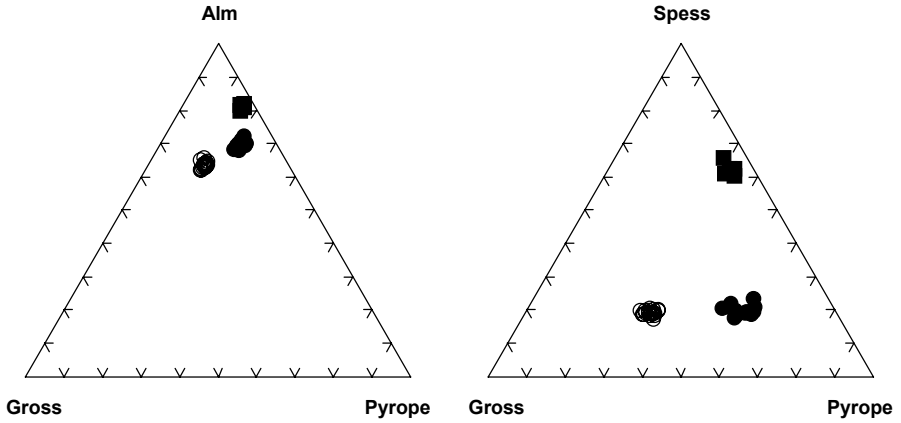

Fig. 51: Ternary classification of garnet from the KPTA. Squares are the garnet from high-grade gneiss (sample 11.13), open circles and filled circles are the garnets from metasediment samples A26 and A45 respectively.

6.5 Pyroxenes

Chemical composition of pyroxenes, from two different localities (samples A55 and AA57) in the southern sector of the KSZ, was determined using the microprobe techniques. Analysis were obtained from 13 measuring points and the results are displayed on table a.12.

The pyroxenes can be classified into two groups: the Na-rich and the Ca-rich pyroxene (Table a.12). The Na-rich pyroxenes are reported from metavolcanics (sample A57) and they occur as euhedral to subhedral greenish crystals in a matrix of alkali feldspars (albite + sanidine). The pyroxene crystals are fractured with serpentine filling the fractures. The rock suite is a volcanic material enclosed within the metasediments close to the junction of the KSZ with the Dam El Tor Shear Zone (Fig. 4). Distribution of the elements within the Na-rich pyroxene crystals do not reveal any particular pattern. Generally, the crystals are rich in Na_2O (up to 13.24 wt %) and Fe_2O_3 (up to 28.9 wt %). On the other hand they are poor in CaO (max. 2.7 wt %) and MgO (0.02 wt %) (Table a.12). On the Q-J binary classification plot (MORIMONTO, 1989) these pyroxenes are plotted in the Na field indicating their enrichment in Na and depletion in Ca, Mg and Fe^{2+} (Fig. 52). On the Jd-Ae-WEF ternary plot (MORIMONTO, 1989) they appear in the aegirine field (Fig. 53). This is in agreement with petrographic optical properties.

The Ca-rich pyroxenes were found only by the microprobe chemical analysis in the cores of the some large hornblende porphyroblasts. They occur in a hornblendite suite in the paragenesis: hornblende (two generations)-biotite-plagioclase-clinopyroxene-titanite. The distribution of the elements do not show significant variation because the dimensions of the areas having pyroxene composition are very small. On the Q-J binary plot (MORIMONTO, 1989) the Ca-rich pyroxenes are plotted in the Quad field (Fig. 52). The same results are revealed by the Jd-Ae-WEF ternary plot (Fig. 53) (MORIMONTO, 1989). On the En-Fs-Wo ternary nomenclature plot (MORIMONTO, 1989) the Ca-rich pyroxenes are plotted in the diopside - augite field (Fig. 54).

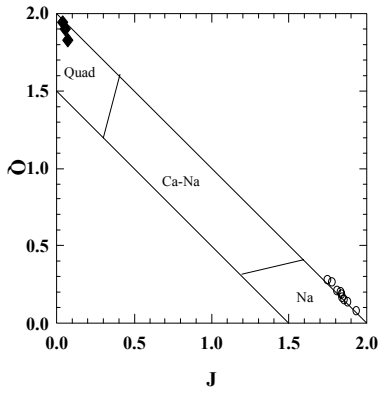

Fig. 52: J-Q binary plot of the pyroxenes. J = 2Na and Q = Ca+Mg+Fe^2. Open circles are the Na-rich pyroxenes from sample A57 and the filled circles are the Ca-pyroxene from sample A55 (MORIMONTO, 1989).

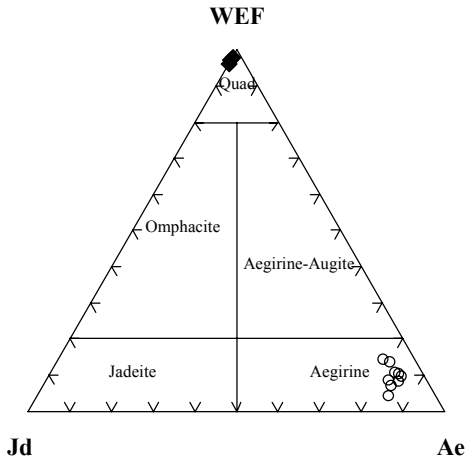

Fig. 53: Jadeite-aegirine-(Wo, En, Fs) plot for the pyroxenes. The Na-rich group has appeared in the aegirine field while the Ca-rich members are plotted in the Ca-Mg-Fe pyroxene field (Quad). Symbols as in Fig. 55. (MORIMONTO, 1989).

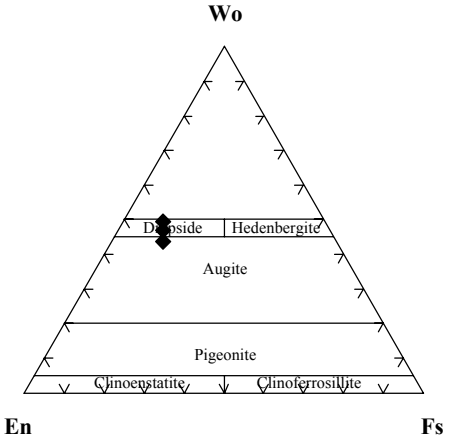

Fig. 54: En-Fs-Wo ternary plot for the pyroxenes. The Ca-pyroxenes are distinguished as diopsidic augite while the Na-pyroxenes are plotted close to the Fe-rich pyroxene apex. Symbols as in Fig. 55 (MORIMONTO, 1989).

6.6 Biotite

Igneous biotite from a granodioritic pluton (sample 6.9) and metamorphic biotite from a high-grade gneiss (sample 11.13) were analysed. The results of the analysis are displayed in table a.13.

Igneous biotite are small to medium sized flakes scattered in a matrix of plagioclase-alkali feldspar-biotite-quartz-muscovite. Rim to core variations are not reported, this may be due to nature of the points selected for the measurements, which are governed by the small size of the crystals and the goodness of the polishing. It is observed that the igneous biotite is richer in K and F than the metamorphic ones (Fig. 55). Their values of the Mg/(Mg+Fe) is around 0.43 and does not reflect significant variation with respect to F, K, and Si (Figs. 55 and 56). Ti values have reflected a positive relation with Al values for the igneous biotite (Fig. 56b). In the (Al+Ti)-(Mn+Fe)-Mg ternary classification diagram the igneous mica show slight enrichment in Fe relative to Mg and thus tend to fall in the Fe-biotite field (Fig. 57). In the Fe/(Fe+Mg)-Al binary classification diagram (DEER, et al 1992) the igneous biotite are plotted in the biotites field (Fig. 58).

The metamorphic biotite (sample 11.13) occurs as porphyroblasts with various sizes defining the trends of S1 and S2 foliations in the mineral paragenesis: biotite-plagioclase-hornblende-garnet-epidote-chlorite-quartz. In comparison with the igneous biotite, the metamorphic biotite is relatively low in its K, F, Ti and Si contents (Figs. 55 and 56). Its value of the Mg/(Mg+Fe) ranges from 0.47 to 0.52, which is relatively higher than the one of the igneous biotite. Both igneous and metamorphic biotites have nearly similar contents of Al^{VI}, which ranges from 0.6 to 1.0 (Fig. 56b). In the Al-(Mn+Fe)-Mg ternary classification diagram the biotite from the gneiss shows a relative enrichment in Mg and thus plot on the boundary between the Mg-biotite and the Fe-biotite (Fig. 57). On the Al-Fe/(Fe+Mg) binary classification plot the biotite from the gneiss appears in the biotite field, but more closer to the biotite-phologpite boundary than the igneous biotite (Fig. 58).

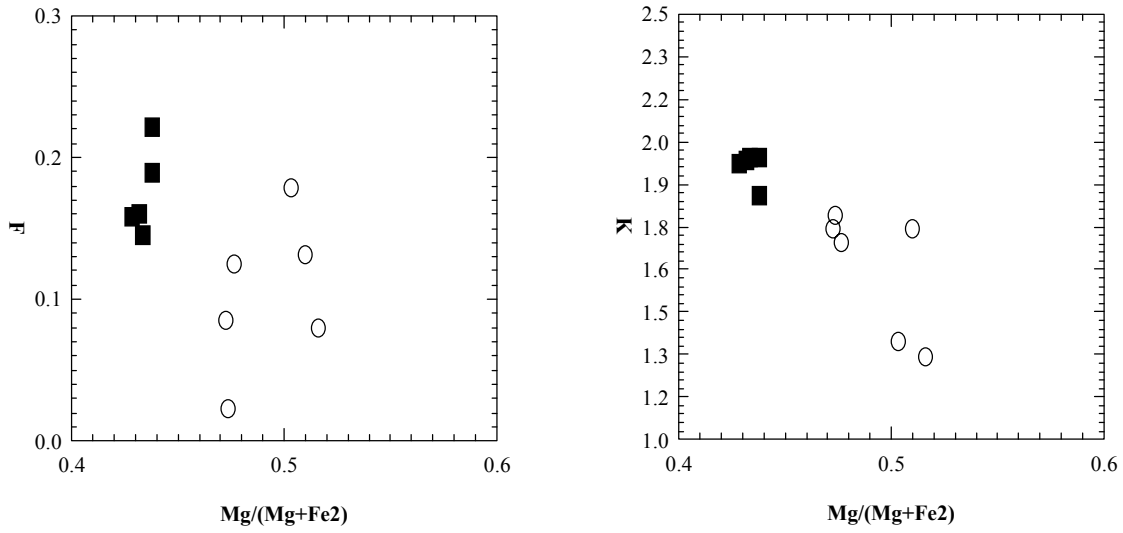

Fig. 55: X_{Mg} Vs. F and K binary plot of the biotite from the metamorphic and plutonic rocks from the KPTA. Squares are igneous mica from the granodiorite (6.9) and the circles are metamorphic biotite from the gneiss. Igneous biotite does not show an extended range of X_{Mg} values and are relatively rich in F and K from the metamorphic ones.

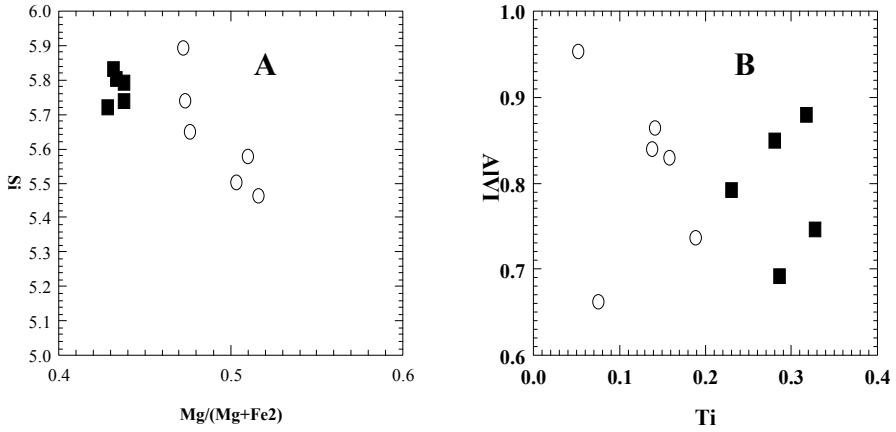

Fig. 56: A) X_{Mg}-Si binary plot of the biotites from the KPTA. The metamorphic biotites (open circles) show a reversal relation of Si with respect to X_{Mg}. **B)** Ti-Al binary plot for the biotites from the KPTA. Igneous biotites (squares) are rich in Ti relative to the metamorphic ones.

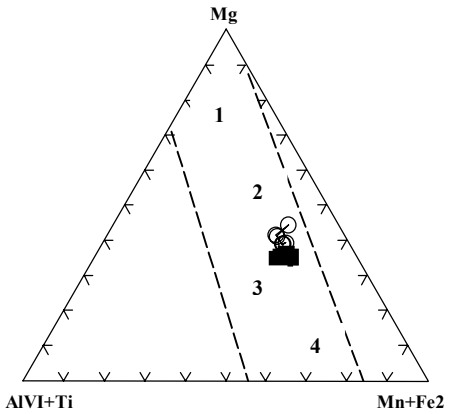

Fig. 57: (Al+Ti)-Mg-(Mn+Fe) ternary classification diagram for biotite from the KPTA. Field **1** is phlogopite, **2** Mg-biotite, **3** Fe-biotite and **4** siderophyllite and lepidomelane. Symbols as in Fig. 55.

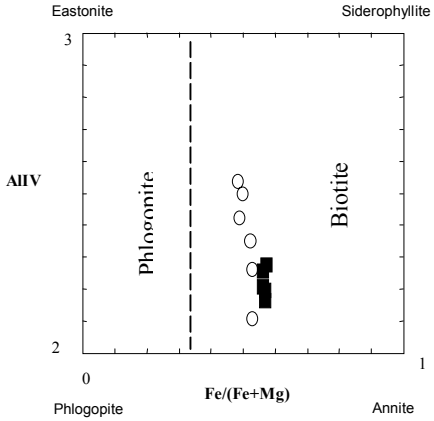

Fig. 58: X_{Fe}-Al classification of the biotite from the KPTA. Symbols as in Fig. 55

6.7 Chlorite and Epidote

Chlorites and epidotes are recognised in most of the rocks within the KPTA. They occur either as secondary mineral phases formed after biotite, amphibole, pyroxene or olivine in the high-grade metamorphic rocks, the post-tectonic plutons and in the mafic-ultramafic assemblages of the Keraf ophiolites, or they occur as primary mineral phases associated with biotite, plagioclase, calcite, and alkali feldspars in the low-grade metasediments. In this study chlorite associated with the garnet bearing high-grade metamorphic suites (sample A26) and the epidote associated with post-tectonic intrusion (sample 1.1) were analysed (Table a.14).

The chlorite occurs as small flakes within a matrix of plagioclase-quartz-hornblende-biotite-chlorite-garnet-ilmenite. Not much emphasis is placed on the small changes of the composition of the chlorite because of the small size of the individual crystals and the improper polishing of the sheet minerals. Thus good measuring points were selected and small raster beams were employed (4µm). The chlorite has X_{Mg} {Mg/(Mg+Fe)} ranges from 0.54 to 0.56 and Si ranges from 5.3 to 5.5 per formula unit (Fig. 59). In the Si-(Fe2+Fe3) binary classification diagram (DEER et al, 1992) the chlorite fall in the ripidolite field (Fig. 60).

The analysed epidotes are secondary mineral phases enclosed within the igneous plagioclase of a dioritic post-tectonic pluton (sample 1.1). They are in the form of small inclusions within the plagioclase phenocrysts (Fig. 43). Elemental variations are not recognised among the measured points (Table a.14).

The Fs contents {$Fs=100*Fe^3/(Fe^3+Al)$} of the epidote ranges from 12.5 to 20.0, which is within the epidote-clinozoisite composition (DEER et al, 1992). Fs shows a negative correlation with the Al (Fig. 61).

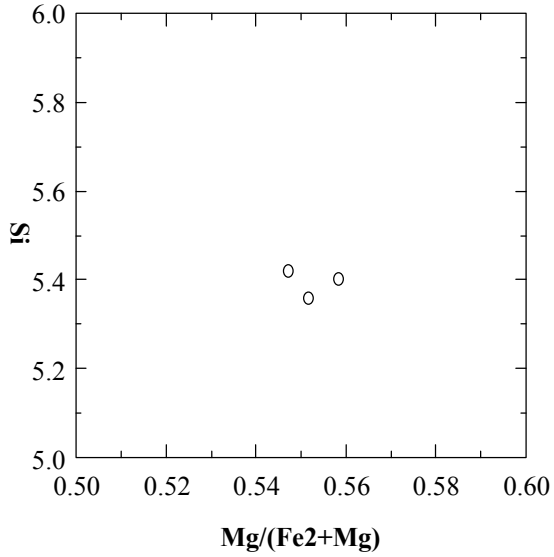

Fig. 59: X_{Mg}-Si variation diagram for the chlorite from sample A26. For explanation see the text.

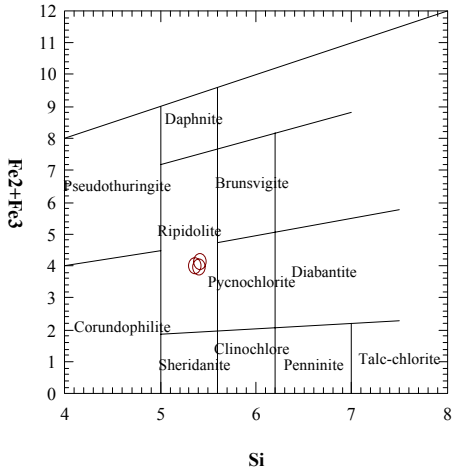

Fig. 60: Si-Fe classification diagram for the chlorite (sample A26). The analysed three points are located in the ripidolite field.

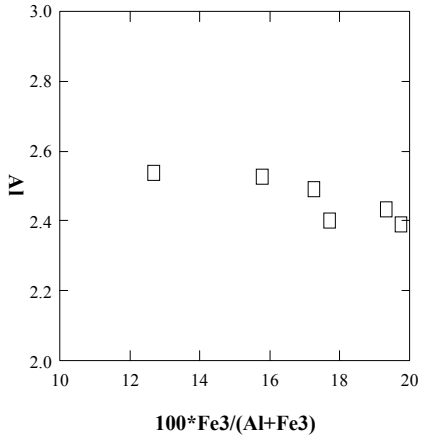

Fig. 61: Fs-Al binary plot of the epidote from sample 1.1. A negative correlation trend is observed.

6.8 Ilmenite

Representative ilmenite crystals were analysed by the microprobe techniques to determine the compositional range of the opaque mineral phases within the samples studied. The result of the analysis of the opaque minerals is displayed in table a.14. The calculated formula for the analysed opaque minerals have revealed the following mean ratios per unit formula: 86% ilmenite, 9% pyrophanite and 5% hematite. Trace geikielite are also reported (Table a.14).

6.9 Metamorphic history

Mineral paragenesis, textural relations and mineral chemistry suggest three metamorphic phases (M1, M2 and M3) witnessed by the rocks of the KPTA. M1 is a granulite facies metamorphism which had the assemblage: pyroxene (diopside - augite)-garnet-plagioclase. Pyroxene was detected by the microprobe as relicts in the cores of the hornblende (sample A55). Possible P-T conditions for M1 are in the range of 7 KP and 750 °C (FERRY and SPEAR , 1978). Zircon geochronological data indicate that M1 occurred at or before 730 Ma, the age of the metamorphic zircon in the high-grade

gneiss (chapter 7). High-grade metamorphic conditions are also evident by the chemical composition of the garnet which shows no zoning (section 6.4). M2 is characterised by rocks in the amphibolite facies metamorphism. Mineral assemblage is: hornblende-garnet-plagioclase-biotite. M2 is a retrogression phase of M1 and it had taken place in the interval 730 to 700 Ma. P-T conditions of M2 are 4 Kb and 600°C T (FERRY and SPEAR , 1978). M3 is characterised by the assemblage: biotite-actinolite-chlorite-epidote. These minerals are mostly formed as secondary minerals after the mineral phases of M2. K/Ar age determination indicate that biotite were crystallised at an age of 560 Ma (chapter 7). This age is considered as the age of M3 which represents the last thermal activity in the area.

Fe:Mg ratio in the garnet indicates that the garnet crystallisation conditions in the southern KSZ were higher than those in the north by 100°C (section 6.4). This indicates that the metamorphic conditions were not similar throughout the KSZ. Our structural data revealed higher crustal thickening in the south of the KSZ than in the north.

7 GEOCHRONOLOGY AND ISOTOPE GEOCHEMISTRY

Isotope studies of the post-orogenic intrusions and the high-grade gneiss of the KPTA have been investigated to constrain the ages of the magmatic, metamorphic and tectonic events in the KSZ. They are also used to determine the crustal and cooling history of the magmatic rocks and the gneiss. This will pave the way to reveal the inheritance of the older (pre-Pan African) crustal material in the magmatic rocks and the gneiss of the KPTA.

The age determination involved $^{207}Pb/^{206}Pb$ single zircon grain evaporation, Nd model ages and K/Ar age determination of biotite and hornblende from the gneiss and the post-tectonic plutons. The isotope analysis included the initial Pb-isotopic ratios from the K-feldspar of these samples, Rb/Sr and Sm/Nd ratios.

7.1 $^{207}Pb/^{206}Pb$ zircon ages

Zircons are among the most important minerals used for the geochronological investigations of rocks of all geological times. Their crystal lattice is extremely stable and resistant to alteration, metamorphic events and magmatic episodes (e.g. KOBER, 1986; 1987). Therefore, the isotopic information of the radiogenic Pb and U are preserved in zircon from the time of crystallisation up to now, irrespective of the evolutionary path of the rock material. The exception of this rule is zircon which has higher contents of U and Th. High concentration of radioactive elements may cause radiation damage and thus resetting of the isotopic clock. This phenomenon could be observed within the zircon crystals of the same population or within different domains of the same zircon crystal. The method of whole zircon grain evaporation for $^{207}Pb/^{206}Pb$ age determination proved to be a successful tool in decoding the geochronological information carried by the Pb-isotopes (KOBER, 1987; 1986). In the course of this research, four samples from the KPTA were selected for $^{207}Pb/^{206}Pb$ age investigations by single zircon grainsand the results are displayed in table 4. The four samples have been collected in such a way that the age of the KPTA could be bracketed, i.e. two samples are from the post-tectonic intrusions (1.1 and 6.9) which are assumed to be the youngest rocks and the other two samples are from the high-grade gneiss (11.13 and 11.14) which are believed to be the oldest lithologies in the Keraf area. For the location of the samples see Fig. 5.

7.1.1 Post tectonic plutons (samples 1.1 and 6.9)

Sample 1.1 is collected from an area at ~15 km east of the junction of the KSZ with the Atmur suture (Fig. 5). The outcrop is low-lying semicircular dioritic pluton intruding the low-grade siliciclastic metasediments. Petrographic variations within the outcrop are not noticed. For the petrographic description of the rock see appendix 1. The sample collected for the geochronological investigation was selected from the insitu-boulders at the centre of the outcrop. The rocks do not contain S1 and S2 foliations, but effects of D4 shearing are preserved. Thermal aureoles are not noticed around the outcrop. Four zircon grains were selected for the $^{207}Pb/^{206}Pb$ age investigations, the analytical data are displayed in table 3. Zircons are clear and yellowish with long prismatic shapes. Ages yielded by the four zircon grains range from 704.5 ± 5 to 721.8 ± 9.6 Ma with a mean age of 714 ± 7 Ma (Table 4 and Fig. 62). This age is interpreted as the intrusive age of the pluton.

Sample 6.9 was collected from an outcrop very close to the sinistral bent of the GSZ (Fig. 5). The rock is granodioritic in composition and is affected by the Gabgaba shearing. S1 and S2 (older) foliations are not recognised in the outcrop. The petrog

Table 4: Geochronological data of the single zircon grain evaporation. Scan is the number of $^{207}Pb/^{206}Pb$ ratio evaluated for age assessment.

	Zircon grain	$^{207}Pb/^{206}Pb$	$^{204}Pb/^{206}Pb$	$^{204}Pb/^{206}Pb$ corr.	Scan	Age / Ma	Mean age/ Ma
Sample: 1.1							
	1	$0.07453 \pm 2.87*10^{-4}$	$8.3*10^{-4} \pm 1.97*10^{-5}$	$0.062892 \pm 1.47*10^{-4}$	90	704.5 ± 5	
	2	$0.070816 \pm 2.0*10^{-4}$	$5.57*10^{-4} \pm 1.46*10^{-5}$	$0.063074 \pm 1.31*10^{-4}$	90	710.7 ± 4.4	
	3	$0.063888 \pm 2.87*10^{-4}$	$4.96*10^{-5} \pm 8.15*10^{-6}$	$0.063407 \pm 2.88*10^{-4}$	90	721.8 ± 9.6	
	4	$0.063978 \pm 8.04*10^{-5}$	$6.07*10^{-5} \pm 3.27*10^{-6}$	$0.063338 \pm 8.23*10^{-5}$	90	719 ± 2.8	**714 ± 7**
Sample 6.9							
	1	$0.064374 \pm 1.64*10^{-4}$	$1.09*10^{-4} \pm 5.42*10^{-6}$	$0.063038 \pm 1.86*10^{-4}$	90	709.5 ± 5.7	
	2 _ 4	$0.0658121 \pm 7.30107*10^{-5}$	$2.163*10^{-4} \pm 3.19758*10^{-6}$	$0.06295 \pm 4.41075*10^{-5}$	90	706.4 ± 2.6	
	3 & 6	$0.064891 \pm 8.36*10^{-5}$	$1.43*10^{-4} \pm 2.91*10^{-6}$	$0.063079 \pm 8.41*10^{-5}$	90	710.9 ± 2.8	
	7 _ 13	$0.0648173 \pm 5.67811*10^{-5}$	$1.212*10^{-4} \pm 1.75163*10^{-6}$	$0.06332 \pm 5.76853*10^{-5}$	90	718.7 ± 1.4	**711 ± 5**
Sample 11.13							
	1	$0.071912 \pm 3.25*10^{-4}$	$5.88*10^{-4} \pm 2.4*10^{-5}$	$0.063746 \pm 3.06*10^{-4}$	90	733.1 ± 10.1	
	2	$0.071066 \pm 3.95*10^{-4}$	$5.26*10^{-4} \pm 2.13*10^{-5}$	$0.063779 \pm 2.62*10^{-4}$	90	734.3 ± 8.7	
	3 & 4	$0.067429 \pm 1.27*10^{-4}$	2.5*10-4 ± $1.09*10^{-5}$	$0.064094 \pm 1.35*10^{-4}$	90	744.7 ± 4.5	
	5 & 6	$0.066025 \pm 1.51*10^{-4}$	$1.72*10^{-4} \pm 6.79*10^{-6}$	$0.063804 \pm 1.3*10^{-4}$	90	735 ± 4.3	**737 ± 5**
Sample 11.14							
	1	$0.066241 \pm 2.39*10^{-4}$	$1.36*10^{-4} \pm 1.03*10^{-5}$	$0.064534 \pm 2.38*10^{-4}$	90	759.1 ± 7.8	
	2	$0.071125 \pm 2.43*10^{-4}$	$4.96*10^{-4} \pm 1.75*10^{-5}$	$0.064279 \pm 2.45*10^{-4}$	90	750.8 ± 8.1	
	3	$0.070207 \pm 4.95*10^{-4}$	$4.88*10^{-4} \pm 2.54*10^{-5}$	$0.063456 \pm 3.63*10^{-4}$	18	723.5 ± 12.2	
	4 & 5	$0.067235 \pm 2.43*10^{-4}$	$3.17*10^{-4} \pm 1.43*10^{-5}$	$0.062924 \pm 1.42*10^{-4}$	42	705.6 ± 4.8	
	6 _ 8	$0.0645268 \pm 1.23127*10^{-4}$	$8.723*10^{-5} \pm 5.50522*10^{-6}$	$0.06351 \pm 1.23482*10^{-4}$	90	725.3 ± 4.2	**733 ± 18**

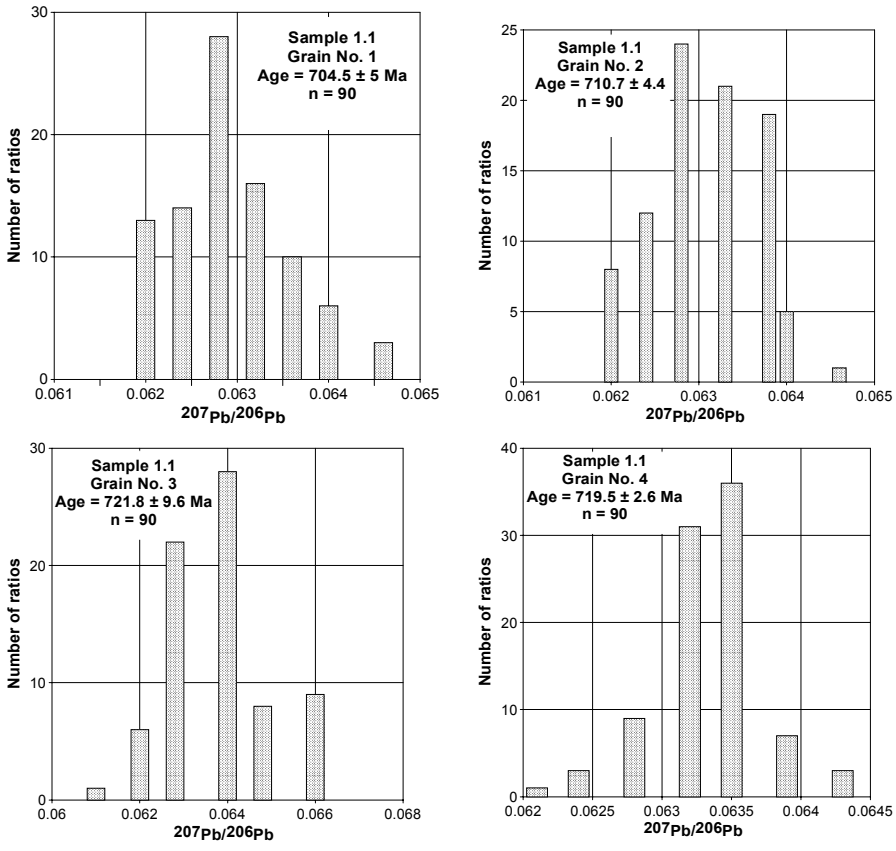

Fig. 62: Histograms showing the distribution of lead isotope ratios derived from evaporation of zircon grains separated from sample 1.1. Analytical data is displayed in table 1. The number of ratios are the values of $^{207}Pb/^{206}Pb$ verified for the apparent age whereas n is the scan number

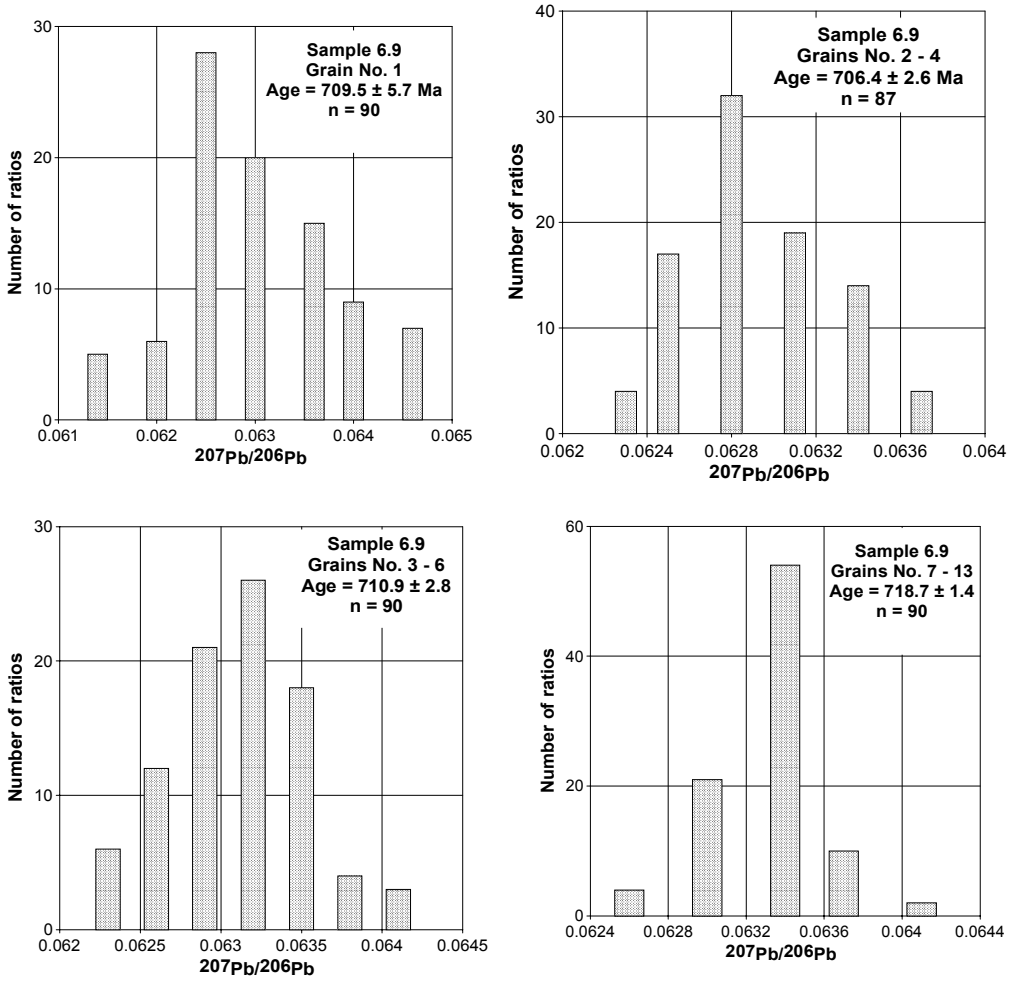

Fig. 63: Histograms showing the distribution of lead isotopic ratios derived from evaporation of zircon grains separated from sample 6.9. Analytical data is displayed in table 1. The number of ratios are the values of $^{207}Pb/^{206}Pb$ verified for the apparent age whereas n is the scan number.

raphy of the rock is described in appendix 1. The rock is intruded in the low-grade metasediments.

Thirteen zircon grains were investigated for the $^{207}Pb/^{206}Pb$ age determination. Zircon morphology is like the ones of sample 1.1. The results are listed in table 4. Ages range from 706.4 ± 2.6 to 718.7 ± 1.4 Ma with a mean age of 711 ± 5 Ma (Fig. 63). This age is considered as the intrusion age. The low-grade metasediments which occupy more than 60% of the Keraf surface area are older than 700 Ma, because they are intruded by the post-tectonic plutons. That means the source of the sediments can be Gabgaba or Gerf Terrane (~750 Ma old) or the continental block to the west of the Nile (>800Ma). (STERN and KRÖNER, 1993; KRÖNER et al 1987; RIES et al, 1985). The ~700 Ma age is considered as period of peak magmatic activity in the Arabian-Nubian Shield and Mozambique belt (LENOIR et al, 1994; STERN and KRÖNER, 1993; HARMS et al, 1990; ALMOND et al, 1989). The plutons of that time are characterised by calc alkaline geochemical affinity and are basic to intermediate in composition (STERN and KRÖNER, 1993). Younger generation of granitoids emplaced in the Arabian-Nubian Shield during the period 500 - 550 Ma (RIES et al, 1985; ALMOND et al, 1989). This generation of granitoids is described as A-type intrusions (HARMS et al, 1990).

7.1.2 High-grade gneiss (samples 11.13 and 11.14)

The gneiss samples were collected from the high-grade metamorphic rocks which occupy the core of the Abu Hamed antiform (Fig. 5). They are of upper amphibolite metamorphic facies and bear all the structural elements characterising the earliest deformational events of the KSZ. The outcrops are low-lying scattered boulders separated by sand sheets. All zircon grains separated from the gneiss are euhedral and small to medium in size with no obvious overgrowth. Six zircon grains from sample 11.13 were analysed for the $^{207}Pb/^{206}Pb$ age determination. The ages range from 733.1 ± 10.1 to 744.7 ± 4.5 Ma with a mean age of 737 ± 5 Ma (Table 4 and Fig. 64). Sample 11.14 is located at about 1 to 1.5 km SE of sample 11.13 (Fig. 5). Eight zircon grains from this sample were evaporated for the $^{207}Pb/^{206}Pb$ age determination. Their morphology is like that ones of sample 11.13. The dating results are in the range of 705.6 ± 4.8 to 759.1 ± 7.8 (Table 4 and Fig. 65). The morphology of the zircon grains indicate metamorphic origin. Therefore, the zircon ages are considered as the ages of the high-grade metamorphism (upper amphibolite-granulite facies) in the Keraf area because zircon grains are assumed to be stable throughout the evolutionary history of the rock. It is obvious that the age span of the zircon grains in sample 11.13 is very narrow compared to that of sample 11.14 (Table 4). The wider range of sample 11.14 may indicate heterogeneity in the source rock.

Gneiss in Wadi Halfa area, which can be correlated with the Keraf gneiss, have yielded $^{207}Pb/^{206}Pb$ ages covering the whole Proterozoic era, i. e from 720 to 2400 Ma (STERN et al, 1994). Zircons older than 750 Ma are described as detrital, which indicates derivation from an older rock material to the west of KSZ.

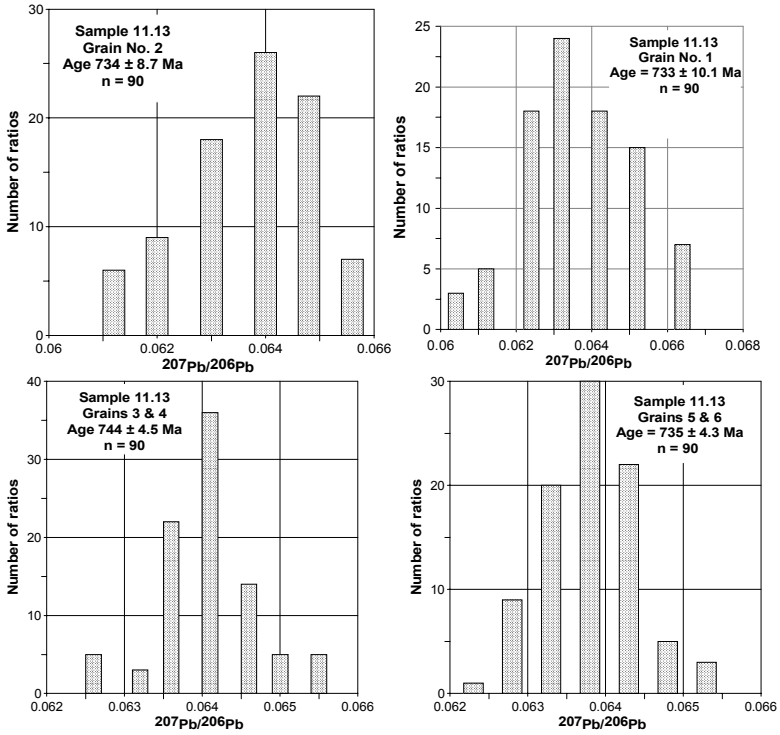

Fig. 64: Histograms showing the distribution of lead isotopic ratios derived from evaporation of zircon grains separated from sample 11.13. Analytical data is displayed in table 1. The number of ratios are the values of $^{207}Pb/^{206}Pb$ verified for the apparent age whereas n is the scan number.

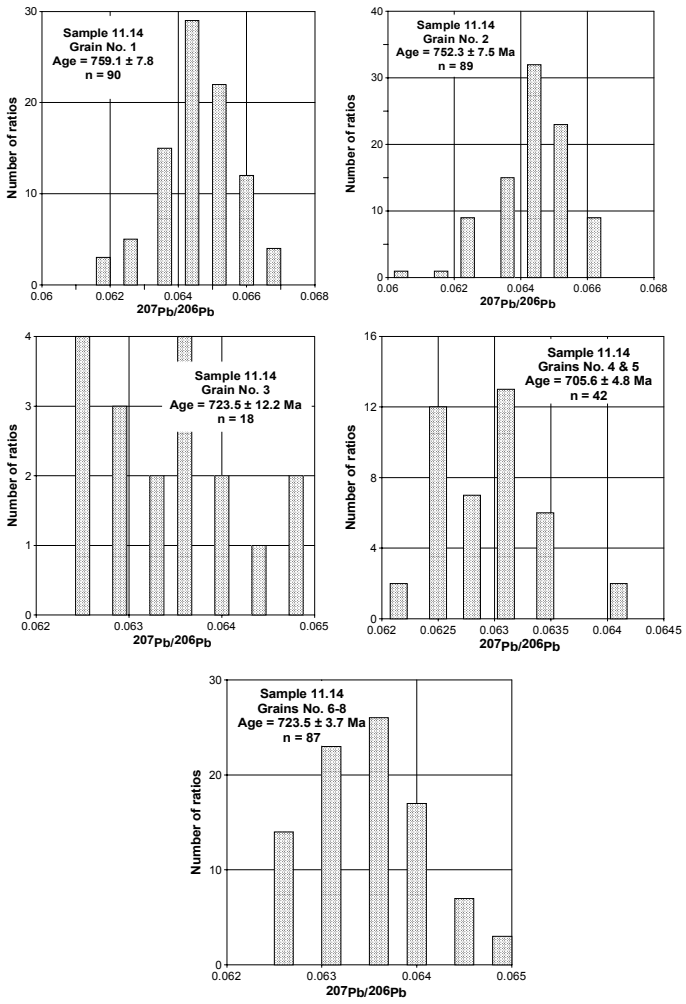

Fig. 65: Histograms showing the distribution of lead isotopic ratios derived from evaporation of zircon grains separated from sample 11.14. Analytical data is displayed in table 1. The number of ratios are the values of $^{207}Pb/^{206}Pb$ verified for the apparent age whereas n is the scan number.

Table 5: K/Ar geochronology data for four samples from the KPTA.

Sample	Mineral	Spike No.	K_2O wt. %	40 Ar nl/g	40 Ar %	Age Ma	2s-error Ma	2s-error %
1.1	Hornblende	2574	0.46	11.77	87.71	658.0	24.0	3.6
6.9	Biotite	2586	9.52	202.95	99.65	563.5	11.5	2.0
11.13	Biotite	2583	9.57	204.69	99.10	565.1	11.7	2-1
11.14	Biotite	2582	9.35	200.21	99.62	565.6	12.9	2.3

7.2 K/Ar ages

K/Ar analytical data for hornblende and biotite separated from four rock samples are listed in table 5. K/Ar age of hornblende separated from a dioritic pluton (sample 1.1) is ~ 660 Ma. Zircon age of the same pluton is ~ 710 Ma, therefore all the primary minerals must have ages close to the crystallisation age of the zircon. Microprobe analysis data indicate that the hornblende has rims and inclusions of secondary minerals such as epidote and actinolite. Thus ages obtained by hornblende are mixture between the crystallisation age of the hornblende and the metamorphic overprint which had formed the secondary minerals.

Ages of biotite from both the plutons and the high-grade gneiss are ~ 560 Ma (Table 5). This indicates that the KSZ was cooled to 350 °C by 560 Ma after the regional metamorphism (amphibolite-to granulite facies) which had occurred at ~ 730 Ma.

Considering ages obtained for similar rocks (gneiss and post-tectonic plutons) in the Keraf and Bayuda area, deformation, magmatism and metamorphism in the NE Sudan can be bracketed by 750-550 Ma.

7.3 Rb-Sr Isotopes:

Rb-Sr isotopic ratio of a rock is given by the equation (ROLLINSON, 1993):

$[^{87}Sr/^{86}Sr]_m = [^{87}Sr/^{86}Sr]_i + [^{87}Rb/^{86}Sr]_m (e^{\lambda t}-1)$

where:

m = measured isotopic ratio, i = initial isotopic ratio, λ = decay constant (1.42×10^{-11} yr^{-1}) and t = rock age in years which in turn is expressed by:

$t = 1/\lambda \ln\{[(^{87}Sr/^{86}Sr)_m - (^{87}Sr/^{86}Sr)_i]/(^{87}Rb/^{86}Sr)_m + 1\}$

The Rb-Sr system of a rock can be disturbed by influx of fluids or by thermal events, therefore in most cases it is not useful in determining the age of formation of rocks. Generally, Rb-Sr ages are successfully used in dating the post-magmatic events, such as metamorphism and thermal alterations (ROLLINSON, 1993). The $(^{87}Sr/^{86}Sr)_i$ is important in distinguishing the crustal residence time of a rock material.

$(^{87}Sr/^{86}Sr)_i$ values are reported for four samples form the KPTA (two gneiss and two plutonic intrusions) (Table 6). The $(^{87}Sr/^{86}Sr)_i$ values are plotted in Fig. 66 to compare them with the values obtained from the Eastern Desert of Egypt, Red Sea Hills (NE Sudan), Arabia and the Nile craton (the continental sector west of the Nile). The suites used in this comparison have zircon ages in the range of 700 – 850 Ma (STERN and KRÖNER, 1993; HARMS et al, 1990; Stern and Hedges, 1985; HENJES-KUNST et al, 1990). The $(^{87}Sr/^{86}Sr)_i$ values reported from the KPTA fall in the interval 0.7026 – 0.7046 with a mean value of 0.7034. These values are indistinguishable from the initial ratios reported from the juvenile crust of the Arabian Nubian Shield and are lower than the ones reported from the Nile craton (Fig. 66). Therefore the $(^{87}Sr/^{86}Sr)_i$ values indicate a very short crustal residence time for both magmatic and metamorphic rocks from the KPTA. The magmatic rocks (samples 1.1 and 6.9) are likely to have been formed by fractionation of mantle-derived melts, whereas the gneiss (samples 11.13 and 11.14) were formed by melting of mantle-derived rocks. This situation is typical for island arcs (the Arabian Nubian Shield) (STERN and KRÖNER, 1993). The relatively higher $(^{87}Sr/^{86}Sr)_i$ value (0.7046) of sample 6.9 can be attributed to a younger Sr isotopic disturbance which may have accompanied the ~ 550 Ma magmatic activity in NE Africa.

Table 6: Sm-Nd and Rb-Sr isotopic data of four samples from the KPTA.

Sample No.	Sm (ppm)	Nd (ppm)	$^{147}Sm/^{144}Nd$	$^{143}Nd/^{144}Nd$	$\varepsilon_{Nd(t)}$	T_{DM}(Ga)	Sr (ppm)	$(^{87}Sr/^{86}Sr)_m$	$(^{87}Sr/^{86}Sr)_i$
1.1	4.80	19.6	0.1481	0.512781	+7.3	0.62	645	0.703038	0.70275
6.9	4.48	30.4	0.0891	0.512418	+5.6	0.77	639	0.705493	0.70459
11.13	0.62	3.10	0.1213	0.512497	+4.5	0.90	477	0.704374	0.70322
11.14	0.36	2.43	0.0896	0.512369	+4.9	0.83	538	0.703426	0.70298

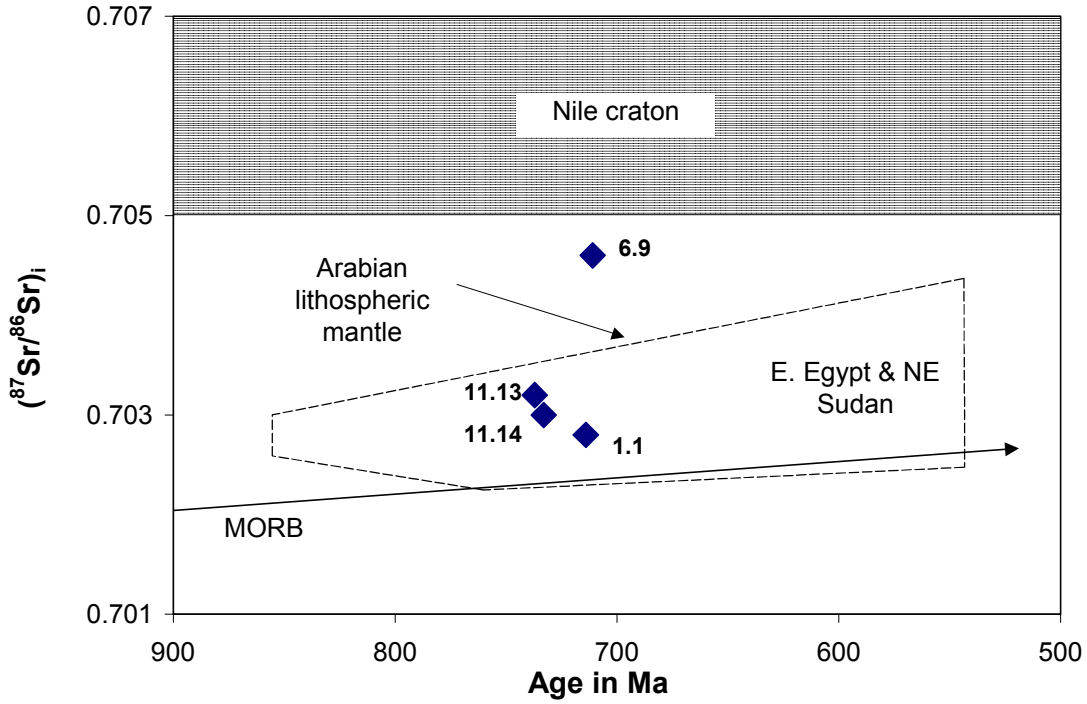

Fig. 66: Initial $^{87}Sr/^{86}Sr$ vs. age for four samples from the KPTA. Samples 1.1 and 6.9 are post-tectonic plutons while 11.13 and 11.14 are high-grade gneiss. Fields labelled E. Egypt & N. Sudan and Nile craton are from Stern and Kröner (1993); Arabian lithospheric mantle from Henjes-Kunst et al (1990); the inferred trajectory of MORB type depleted mantle is after Stern and Hedges (1985).

7.4 Sm–Nd isotopes and model ages

Sm-Nd isotopic ratio of a rock is given by the equation (ROLLINSON, 1993):

$$[^{143}Nd/^{144}Nd]_{sample} = [^{143}Nd/^{144}Nd]_t + [^{147}Sm/^{144}Nd]_{sample}(e^{\lambda t}-1)$$

where sample stands for the present day measured ratio, λ is the decay constant of ^{147}Sm to ^{143}Nd ($6.54 \times 10^{-12} yr^{-1}$) and t is time (age). The Nd depleted mantle model age (T_{DM}) of a rock is given by the equation (ROLLINSON, 1993):

$$T_{DM} = 1/\lambda \ln\{[(^{143}Nd/^{144}Nd)_{sample,today} - (^{143}Nd/^{144}Nd)_{DM,today}]/[(^{147}Sm/^{144}Nd)_{sample,today} - (^{147}Sm/^{144}Nd)_{DM,today}] + 1\}$$

Sm-Nd isotopic studies are used to evaluate the history of crustal growth and they reflect the time of differentiation of the crust from the mantle. Because Sm and Nd are

rather immobile under hydrothermal conditions, their isotopes are used to reflect the actual proportion of rock or magma that involved in a petrological process (ROLLINSON, 1993).

Sm-Nd isotopic ratios and model ages of four samples from the KPTA are reported in table 6. Initial Nd data are reported as $\varepsilon_{Nd(t)}$, where t refers to the crystallisation age of the rock and T_{DM} is model age calculated from the intersection of the sample's radiogenic growth and that of hypothetical depleted mantle (NELSON AND DEPAOLO, 1985). Keraf samples have a narrow range of $\varepsilon_{Nd(t)}$, between +4.5 and +7.3 with a mean of +5.6. The magmatic rocks (samples 1.1 and 6.9) are characterised by relatively higher values of $\varepsilon_{Nd(t)}$ than those of the metamorphic rocks (samples 11.13 and 11.14). The concentration of the Nd and Sm in the magmatic rocks is higher than in the gneissic rock (Table 6). The $^{147}Sm/^{144}Nd$ values allow calculation of T_{DM} age for all four samples. The magmatic rocks have a T_{DM} in the range of 620-770 Ma with a mean of ~700 Ma, which is indistinguishable from the mean crystallisation age (710 Ma). Therefore the Keraf magmatic rocks can represent a juvenile crustal addition to the continental crust of NE Sudan. On the other hand, the Keraf gneiss has model ages of 830-900 Ma (Table 6) which are older than the mean crystallisation age (~730 Ma). The model ages indicate that the Keraf gneiss has crustal residence longer than the magmatic rocks. Nd model ages of the Keraf rocks are similar to the ages obtain for rocks from NE Sudan and west of the Nile (Fig. 67).

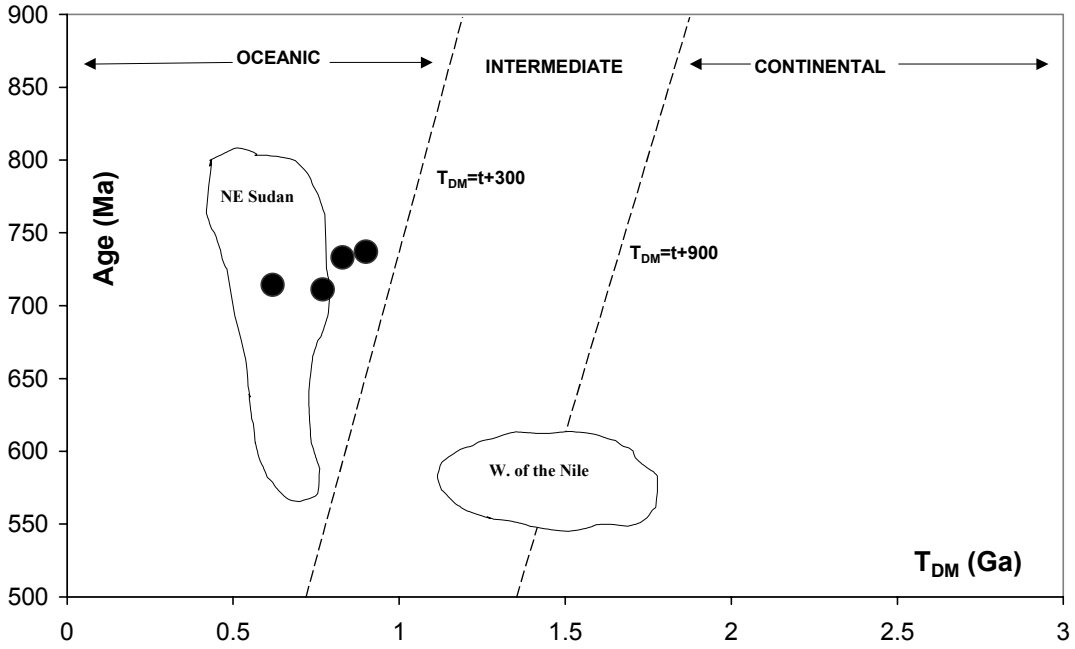

Fig. 67: Crystallisation age vs. T_{DM} diagram for the magmatic and gneiss rocks from the KPTA. All samples plot inside or close to field for NE Sudan and they show oceanic origin without involvement from older continental crust. Diagram is modified after HARRIS et al (1990). Data for NE Sudan from STERN and KRÖNER (1993) and data for W. of the Nile from HARMS et al (1990).

7.5 Initial Pb-isotopes

Studies of the Pb-isotopic compositions in K-feldspar and ores have been motivated by the fact that the Pb-isotopes of the mantle-derived rocks are very sensitive to crustal contamination. It could even be possible to determine whether the contamination source is the lower or the upper crust

(STERN and KRÖNER, 1993; ZARTMAN and HAINES, 1988; STACEY and STOESER, 1983; STACEY et al, 1980; ZARTMAN and DOE, 1981). Many Pb isotopic studies had been conducted in the Arabian-Nubian Shield and the Nile craton to draw a genetical relation between the various lithologies in NE Africa (WORKU and SCHANDELMEIER, 1996; LENOIR et al, 1994; WIPFLER, 1994; STERN and KRÖNER, 1993; SULTAN et al, 1992; GILLESPIE and DIXON, 1983; BOKHARI and KRAMERS, 1982).

K-feldspar has been isolated from the gneiss (samples 11.13 and 11.14) and a post-tectonic pluton (sample 6.9) to determine their initial Pb isotopic composition (Table 7).

The Pb-isotopic composition data are plotted in the three conventional diagrams for the classification of the Pb isotopes (STACEY and STOESER, 1983; BOHKARI and KRAMERS, 1982; STACEY et al, 1980) (Fig. 68). Data from NE Sudan (STERN and KRÖNER 1993) are included in the diagrams for comparison. The $^{206}Pb/^{204}Pb$ vs. $^{208}Pb/^{204}Pb$ the Pb-isotope ratios from the three samples of the Keraf area plot in the oceanic field (Fig. 68a). According to STACEY et al (1980), the oceanic field includes Pb of mantle origin, i.e. Pb which has little or no contamination from the older continental crust into the melt source. The Pb isotopes from the Keraf gneiss are less radiogenic than the Pb isotopes of NE Sudan obtained by STERN and KRÖNER (1993) (Fig. 68a). The latter lie in-between the oceanic and the continental fields with few points in the oceanic field (Fig. 68a). The Keraf gneiss is the oldest suite within the KPTA on the basis of the field relations and structural data. This longer crustal history may favour high Pb-isotopic ratios. However, in the $^{206}Pb/^{204}Pb$ vs. $^{208}Pb/^{204}Pb$ plot the two feldspars from the gneiss (samples 11.13 and 11.14) appear in the oceanic field (Fig. 68a). The low Pb isotopic ratios of the gneiss in the Keraf area could be attributed to the fact that a substantial material from the neighbouring ensimatic juvenile volcanic arcs in the Red Sea Hills had played a major role as a sedimentary source for the high-grade metasediments (paragneiss) in the Keraf and in the Bayuda areas.

Sample 6.9 has Pb-isotopes composition similar to the Hamisana plutons and the intrusions in the Eastern Desert of Egypt (Fig. 68a) (STERN and KRÖNER, 1993; SULTAN et al, 1992). In contrast, Pb-isotopes from granites in Adola Belt of Ethiopia and others from northern Somalia plot in the continental field of the $^{206}Pb/^{204}Pb$ vs. $^{208}Pb/^{204}Pb$ diagram indicating substantial contamination from older (pre-Pan African) crust to the source melt (WORKU and SCHANDELMEIER, 1996; LENOIR et al, 1994). This fact supports the conclusion that magmatism in the southern sector of the Arabian Nubian Shield and in the Mozambique belt had involved larger amount of crustal assimilation than in the Sudanese-Egyptian sector of the Nubian shield.

In the $^{206}Pb/^{204}Pb$ vs. $^{207}Pb/^{204}Pb$ plot the Pb isotopes from the K-feldspars of the post-tectonic pluton (6.9) still plot in the oceanic field (Fig. 68b). This is consistent with the plot in Fig. 68a. On the other hand, the Pb isotopes of the K-feldspars separated from the gneiss (11.13 and 11.14) plot in the continental field (Fig. 68b). They lie to the left of the field occupied by the granitoids from Hamisana and Nakasib area (NE Sudan) (STERN and KRÖNER, 1993). This indicates lower $^{206}Pb/^{204}Pb$ ratios of the Keraf gneiss and hence younger crustal history than the granitoids in the Hamissana and Nakasib area. The three feldspars from the Keraf rocks plot below the 750 Ma line defined by ZARTMAN and DOE (1981) (Fig. 68b). This is conformable with the $^{207}Pb/^{206}Pb$ apparent ages of the gneiss (~730 Ma) and the post-tectonic plutons (~710 Ma).

The Pb isotopic compositions of the feldspars can be further interpreted by the plotting of $^{207}Pb/^{204}Pb$ vs. $^{208}Pb/^{204}Pb$ (Fig. 68c). In this plot Pb isotopes from feldspars

Table 7: Data of the initial Pb-isotopic composition for the feldspars from the KPTA. The feldspars were leached overnight in 1% HF.

Sample	$^{206}Pb/^{204}Pb$	$^{207}Pb/^{204}Pb$	$^{208}Pb/^{204}Pb$	Age/Ma
6.9	18.065	15.562	37.462	711 ± 6
11.13	17.599	15.500	37.107	737 ± 5
11.14	17.516	15.481	37.072	733 ± 18

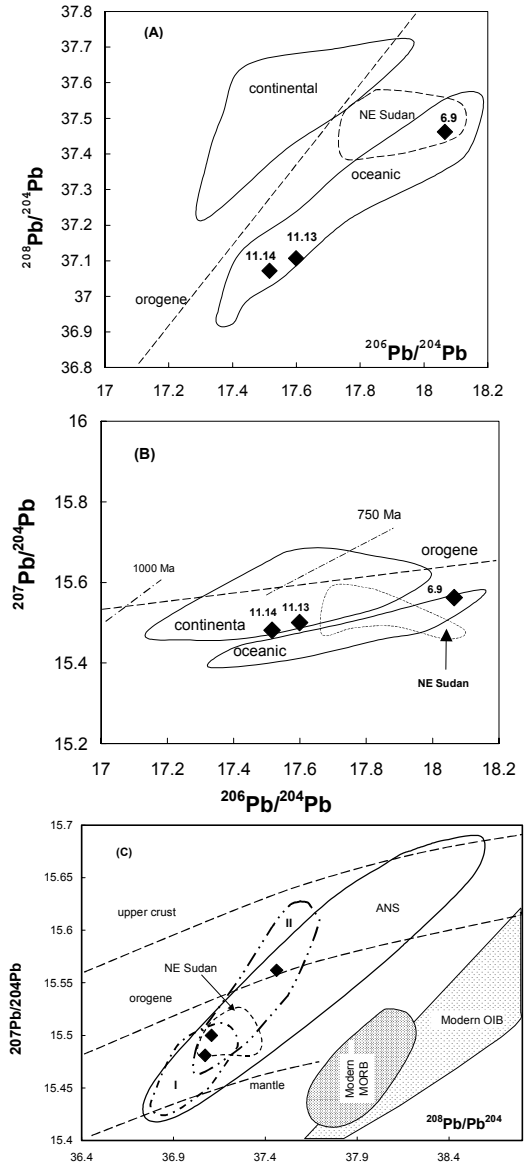

Fig. 68: Pb-isotopic compositions of K-feldspars from high-grad gneiss (11.13 & 11.14) and a pluton (6.9) from the KPTA. In **A** and **B** fields labelled continental and oceanic are after STACEY et al (1980), field labelled NE Sudan is from STERN and KRÖNER (1993) and the trend of the orogene and ages are from ZARTMAN and DOE (1981). **C**: Pb-isotopic composition of the K-feldspars separated from the KPTA compared with data from the Arabian Nubian Shield (ANS). ANS field is after SULTAN et al (1992), NE Sudan is after STERN and KRÖNER (1993), Modern MORB (mid-oceanic ridges) and OIB (ocean island basalt) fields are after HICKEY et al (1986) and the curves labelled upper crust, orogene and mantle are after ZARTMAN and DOE (1981). Fields indicated by **I** and **II** are for oceanic and continental Pb-compositions respectively (STACEY and STOESER, 1983).

of the Keraf gneiss plot in the complex field defined by the overlap of the ANS, continental and oceanic leads. Pb isotopes from NE Sudan (STERN and KRÖNER, 1993) and Eastern Desert of Egypt (SULTAN et al, 1992) plot in the same field.

Pb isotopic compositions of the post-tectonic pluton from the KSZ appear in the continental field (field II) of the $^{208}Pb/^{204}Pb$ vs. $^{207}Pb/^{204}Pb$ plot (Fig. 68c). This position could not be explained in the light of the available data.

Further studies on the Pb isotopic compositions in the Nubian Shield are recommended to understand the extend of the assimilation of the older (Pre-Pan African) crustal material by the Pan African tectonothermal episodes and/or the mantle heterogeneity in NE Africa and Arabia.

8 GENERAL CONCLUSIONS

As originally recognised in the work of Vail (1983 and 1988), Almond and Ahmed (1987), Abdelsalam and Dawoud (1991), Schandelmeier et al (1994) and Stern (1994) that the KSZ is of a particular tectonic significance as it lies between the juvenile ensimatic arc composites of the ANS and the ensialic, isotopically distinguished, older crust of the Nile craton (Fig. 1). The detailed and systematic geological, structural and isotopic investigations of the sheared area could substantially contribute to understand the aspects of the remobilization of the eastern foreland of the Nile craton and the tectonic limitations which had governed the suturing of the Nubian Shield with the Nile craton. This will pave the way for concrete postulations of how and when the Gondwana super-continent was reassembled in the Neoproterozoic.

The dominance of the carbonate-rich and the siliciclastic turbidites and pelagic sediments in the KPTA strongly supports deposition in an aqueous passive margin to the eastern flank of the Nile craton. Most of the sedimentary structures and textures, such as depositional layering and laminations, graded and cross-bedding and oolitic textures, are preserved in these rocks. Rock assemblages with similar characteristics are neither reported in the Gabgaba Terrane to the E nor in the Bayuda Terrane to the W. This confirms that the KPTA is restricted in occurrence to the area of Keraf. The Keraf ophiolitic melange is an additional supporting evidence for the once existence of a basin floored by oceanic lithosphere (Mozambique ocean) (Stern 1994, Abelrahman 1993). The ophiolitic melange occurs as west-verging nappes, that means the position of the Mozambique ocean was somewhere to the east of the present location of the KSZ. Our geochemical investigations show significant variations of the signatures of RRE, TiO_2, MgO and SiO_2 of the Keraf ophiolite compared to those of the Onib ophiolites, immediately to the E (Fig. 1). The mode of occurrence and the rocks associated with the ophiolitic suites are significantly different in the KSZ from those in the Red Sea Hills. Such variations (geochemical and lithological) defy any argument that the Keraf ophiolites were transported from Gabgaba Terrane. The eastern margin of the KPTA is capped by molasse-type sediments. The existence of such suites indicates termination of a tectonic cycle, i.e. accretion of the Nubian Shield against the Nile craton. The high-grade metamorphic rocks are mainly reported in the southern sector of Keraf (Figs. 4 and 5). This indicates either variation in the metamorphic conditions from N to S or the exposed rocks represents different horizons of the crust.

The deformational history and the tectonic evolution of the KSZ manifest Wilson cycle orogeny. The orogeny had started with sedimentation in a passive margin shallow marine basin in the eastern foreland of the Nile craton. This was the situation prior to 710 Ma ago, the zircon age of the early post-tectonic. The initiation of SE-dipping subduction zone (D1), i.e. tectonic activation of the basin, was attributed to the Neoproterozoic enigmatic tectonic changes occurred in the earth crust (DERRY et al, 1992; ASMEROM et al, 1991; HAMBREY and HARLAND, 1985). Subduction had culminated in the collision of the Gabgaba-Gerf Terrane against Bayuda-Wadi Halfa Terrane (D2). D1 and D2 favour SE-NW directed compressional strain which in turn had caused crustal shortening in the same direction and vertical extension (thickening). The compressional strain was partially resolved into N-S directed shear stress, which is preserved as N- and NW-trending left-lateral wrench faults (D4). D4-faults are recognised occupying the planes of the D1 thrusts at the margins of the Keraf ophiolite. D4 faults are well pronounced in the GSZ, where the accumulation of the bulk strain is higher than any where else in the KSZ.

The proposed tectonic model (Fig. 14) ignores any role for D3 phase of deformation. D3 folds are oriented in the same direction of the pre-Keraf structures in the Atmur-Delgo Suture (Fig. 1).

The geometrical shape of the KSZ, i.e. wider (up to 150 km) in the N and narrower (only 30 km) in the S gives a wedge-shaped appearance to the sheared area. Therefore, the distribution of the finite strain within the shear zone is characterised by heterogeneity in a N-S orientation. Consequently, the structural styles and the metamorphic grade may vary in the same orientation. Our field observations as well as the fourier analysis of the D1 folds curvatures indicate that the D1 folds decrease in amplitude southward while D4 faults splay northward. The high grade of metamorphism at the southern sector of the KSZ may indicate greater crustal thickening and stacking than in the N. The variations in the structural styles and in the grade of metamorphism are good basis for the postulation of the geometry of the Neoproterozoic Mozambique ocean.

Geochronology and mineral chemistry data indicate that deformation and high-grade metamorphism in the KSZ occurred at ~730 Ma. Diorite and granodioritic plutons were emplaced at ~710 Ma and the latest thermal event in the KSZ was ~560 Ma. Pb, Sm/Nd and Rb/Sr isotope ratios indicate young crustal residence of rock of the KPTA with no or very little involvement of pre-Pan African continental material in their evolution.

9 REFERENCES

ABDELRAHMAN, E.M. (**1993**). Geochemical and geotectonic controls of the metallogenic evolution of selected ophiolite complexes from the Sudan. Berl. Geowiss. Abh., A **145** (175 pp).

ABDELSALAM, M.G. and DAWOUD, A.S. (**1991**). The Kabus ophiolitic melange Zone, Sudan, and its bearing on the western boundary of the Nubian Shield. J. Geol. Soc. London, **148**: 83-92.

ABDELSALAM, M.G., STERN, R.J., COPELAND, P., ELFAKI, E., ELHUR, B., IBRAHIM, F.M. (**1998**). The Neoproterozoic Keraf suture in NE Sudan: sinistral transpression along the eastern margin of west Gondwana. J. Geol., **106**, 2: 133-148.

ABDELSALAM, M.G., STERN, R.J. (**1996**). Mapping Precambrian structures in the Sahara Desert with SIR-C/X-SAR radar: The Neoproterozoic Keraf Suture, NE Sudan. J. Geophysical Res., **101**, E10: 065-076.

ABDELSALAM, M.G., STERN, R.J., SCHANDELMEIER, H., AND SULTAN, M. (**1995**). Deformational history of the Keraf Zone in NE Sudan, revealed by Shuttle Image Radar. J. Geol., **103**: 475-491.

AHMED, S.A., IDRIS, M.A., ELSIR, M., AND SULIMAN, A. (**1980**). Preliminary geological report on Abu Hamed area (sheet no. 45-c), Northern Sudan. Geol. And Miner. Res. Dept. Khartoum Unpubl. Report, 18.

ALMOND, D.C., AND AHMED, F. (**1987**). Ductile shear zones in the northern Red Sea Hills, Sudan, and their implication for crustal collision. Geol. J., **22**: 175-184.

ALMOND, D.C., DARBYSHIRE, D.P.F. AND AHMED, F. (**1989**). Age limits for major shearing episodes in the Nubian Shield of NE Sudan. J. Afr. Earth Sci., **9**: 489-496, Oxford.

ALSOP, G.I. (**1994**). Relationships between disturbed and localised shear in the tectonic evolution of a Caledonian fold and thrust zone, NW Ireland. Geological Magazine, **131**: 123-136.

ASMEROM, Y., JACOBSEN, S.B., KNOLL, A.H., BUTTERFIELD, N.J., SWETT, K. (**1991**). Strontium isotopic variations of Neoproterozoic seawater: implications for crustal evolution. Geochim. Cosmochim. Acta. **55**: 2883-94.

AYALEW, T., AND PECCERILLO, A. (**1998**). Petrology and geochemistry of the gambella plutonic rocks: implications for magma genesis and the tectonic setting of the Pan African orogenic belt of western Ethiopia. J. of Afr. Earth Sci., **27**,. ¾: 397-416.

BAKHEIT, A.K. (**1991**). Geochemical and tectonic control of sulphide gold mineralisation in Ariab mineral district, Red Sea Hills Sudan. Ph.D. thesis, TU Berlin. **157**.

BARTH, H. and MEINHOLD, D.K. (**1979**). Mineral prospecting in the Bayuda Desert. Unpubl. Technical Report of the Sudanese-German Exploration Project. Bundesanstalt für Geowissenschaften und Rohstoffe, Hanover, A: 1336.

BATCHELOR, R.A. and BOWDEN, P. (**1985**). Petrogenetic interpretation of granitoid rock series using multications parameters. Chem. Geol., **48**: 43-55. Amsterdam.

BERG, S.G. and KARLSTROM, K.E. (**1992**). The Chaparaal shear zone: deformation partitioning and heterogeneous bulk crustal shortening during Proterozoic orogeny in central Arizona. Bull. of the geological society of America, **104**: 329-45.

BERHE, S.M. (**1990**). Ophiolites in NE and E Africa: Implications for Proterozoic crustal growth. J. Geol. Soc. Lond., **147**: 41-57.

BERTRAND, J.M., and CABY, R. (**1978**). Geodynamic evolution of the Pan African orogenic belt: a new interpretation of the Hoggar Shield (Algerian Sahara). Geol. Rundschau, **67**: 357-388.

BEYTH, M., STERN, R.J. AND MATTHEWS, A. (**1997**). Significance of high-grade metasediments from the Neoproterozoic basement of Eritrea. Prec. Res. **86**; 45-58.

BLACK, R., and LIEGEOIS, J.P. (**1993**). Cratons, mobile belts, alkaline rocks and continental lithospheric mantle: the Pan African testimony. J. Geol. Soc. London, **150**: 89-98.

BOKHARI, F.Y. and KRAMERS, J.D. (**1982**). Lead isotopic data from massive sulfide deposits in the Saudi Arabian Shield. Econ. Geol., **77**: 1766-1769.

BOWITZ, J. (**1988**). Mineralogische und geochemische Untersuchungen an Verwitterungsprofilen und kretazisch Paläoböden in Südägypten. Diss. TU Berlin, **D83**, 101 S., Berlin.

BOYNTON, W.V. (**1984**). Geochemistry of rare earth elements: meteoritic studies. In P. Henderson (ed.), rare earth element geochemistry, 63-114, Elsevier, Amsterdam.

CAMP, V.E. (**1984**). Island arcs and their role in the evolution of the western Arabian Shield. Geol. Soc. Am. Bull., **95**: 913-921, Washington.

CARMICHAEL, I.S.E., TURNER, F.J. and VERHOOGEN, J. (**1974**). Igneous petrology. 415pp. New York (McGraw-Hill Co.).

CARRERAS, J. and CASAS, J.M. (**1987**). On folding and shear zone development: a mesoscale structural study on the transition between two different tectonic styles. Tectonophysics, **135**: 87-98.

CAWTHORN, R.G. and COLLERSON, K.D. (**1974**). The recalculations of pyroxene end-member parameters and the estimation of ferrous and ferric iron content from electron microprobe analyses. Am. Mineral., **59**: 1203-1208.

COLEMAN, R.G. (**1977**). Ophiolites ancient oceanic lithospher? 229 pp., Berlin, Springer.

CONDIE, K.C. (**1998**). Plate tectonics and crustal evolution. Butterworth-Heinmann, Oxford OX2 8DP, London, 69 pp.

COX, K.G., BELL, J.D. and PANKHURST, R.J. (**1979**). The interpretation of igneous rocks. George, Allan and Unwin, London.

DAWOUD, A.S. (**1980**). Structural and metamorphic evolution of the area Southwest of Abu Hamed, Nile Province, Sudan. PhD. thesis, Univ. of Khartoum, Sudan.

DEER, W.A., HOWIE, R.A. and ZUSSMAN, J. (**1992**). An introduction to the rock forming minerals. 2nd edition. Longmans Group Ltd., London, England.

DENKLER, T., FRANZ, G. and SCHANDELMEIER, H. (**1994**). Tectonometamorphic evolution of the Neoproterozoic Delgo suture zone, Northern Sudan. Geol. Rundschau, **83**: 578-590.

DERRY, L.A., KAUFMAN, A.J. and JACOBSEN, S.B. (**1992**). Sedimentary cycling and environmental change in the Late Proterozoic: evidence from stable and radiogenic isotopes. Geochem. Cosmochem. Acta. **56**: 1317-29.

DICK, H.J.P. and BULLEN, T. (**1984**). Chromian spinel as a petrogenetic indicator in abyssal and Alpine type peridotites and spatially related lavas. Contr. Miner. Petrol. **86**: 54-76, Heidelberg.

DIXON, T.H. and GOLOMBEK, M.P. (**1988**). Late Precambrian crustal accretion rates in NE Africa and Arabia. J. Geol. **16**: 991-994.

DOOLEY, T.P. and MCCLAY, K.R. (**1996**). J. Geol. Soc. London, **153**: 375-387.

DRURY, S.A. and FIHO, C.R.D.S. (**1998**). Neoproterozoic terrane in Eritrea: review and prospects. J. Afr. Geol. Soc., **27**, ¾, 331-349.

EL RABAA, S.M. (**1972**). Geological setting and structural control of the Rubatab pegmatites, Northern Province, Sudan. Sudan, Res. Rec., **1**: 7-10, Geol. Dept., Univ. Khartoum.

EL RABAA, S.M. (**1976**). The geology of the late Precambrian early Palaeozoic sediments in Sudan. 3rd. Conf. African Geol. Soc., Abs. Khartoum.

EL SHAZLY, A.K. and COLEMAN, R.G. (**1990**). Metamorphism in the Oman mountains in relation to ophiolite emplacement. In: Robertson, A.H.F., Searle, M.P. and Ries, A.C. (eds.). The geology and tectonics of the Oman region. Geol. Soc. Spec. Publ. **49**: 473-493.

EMBLETON, J.C.B., HUGHES, D.J., KLEMENIC, P.M., POOLES,S. and VAIL, J.R. (**1983**). A new approach to the stratigraphy and tectonic evolution of the Red Sea hills, Sudan. Bull. Fac. Earth Sci., **6**: 101-112. King Abdulaziz Univ., Jeddah.

EL SAYED, M.M., FURNES, H. and MOHAMED, F.H. (**1999**). Geochemical constrain on the tectonomagmatic evolution of the late Precambrian Fawakhir ophiolite, Central Eastern Desert. J. of Afric. Earth Sci. **29**,3: 515-533.

ENGEL, A.E.J. and ENGEL, C.G. (**1964**). Composition of basalts from the Mid-Atlantic ridges. Science, 144: 1330-1333, Washington.

EVENSON , N.M., HAMILTON, P.J. AND O'NIONS, R.K. (**1978**). Rare earth abundance in chondritic meteorites. Geochem. Cosmochem. Acte, **42**, 1199-1212.

FERRY, J.M. and SPEAR, F.S. 1978. Experimental calibration of the partitioning of Fe and Mg between biotite and garnet. Contrib. Mineral. and Petrol.,**66**, 113-117, Berlin and Heidelberg.

FITCHES, W.R., GRAHAM, R.H., HUSSEIN, I.M., RIES, A.C., SCHACKLETON, R.M. and PRICE, R.C., (**1983**). The Late Proterozoic ophiolite of Sol Hamid, NE Sudan. Precamb. Res., **19**: 385-411, Amesterdam.

GEORGE, R., ROGERS, N. and KELLY, S. (**1998**). Earliest magmatism in Ethiopia: evidence for two mantle plumes in one flood basalt province. Geology, **26**,10: 923-926.

GILLESPIE, J.G. and DIXON, T.H. (**1983**). Pb isotope systematics of some granitic rocks from the Egyptian shield. Precamb. Res., **20**: 63-77.

GREGORY, R.T. (**1998**). Tectonics of the Arabian margin associated with the formation and exhumation of high-pressure rocks, Sultanate of Oman. Tectonics, **17**, 5: 657-670.

GRIFFITHS, P.S., CURTIS, P.A.S., FADUL, S.E.A. and SCHOLES, P.D. (**1987**). Reconnaissance geological mapping and mineral exploration in Northern Sudan using satellite remote sensing. J. Geol. **22**: 225-249.

HALLBERG, J.A. (**1985**). Geology and mineral deposits of the Leonora-Laverton area. NE Yilgarn block, W Australia. Hespirian Press, Perth, W Australia, 140pp.

HAMBREY, M.J. and HARLAND, W.B. (**1985**). The Late Proterozoic glacial era. Palaeogeogr. Palaeoclimatol. Palaeoecol. **51**:255-72.

HARKER, A. (**1909**). The natural history of igneous rocks. Methuen, London.

Harland, W.B. 1971. Tectonic transpression in Caledonian Spitsbergen. Geological Magazine, **108**: 27-42.

HARMS, U., DARBYSHIRE, D.P.F., DENKLER, T., HENGST, M. and SCHANDELMEIER, H. (**1994**). Evolution of the Neoproterozoic Delgo suture zone and crustal growth in

northern Sudan: geochemical and radiogenic isotope constrains. Geol. Rundschau, **83**: 591-603.

HARMS, U., SCHANDELMEIER, H. and DARBYSHIRE, D.P.F. (**1990**). Pan African reworked early/middle Preoterozoic crust in NE Africa west of the Nile: Sr and Nd isotope evidences. J. Geol. Soc. London, **147**: 859-872.

HARRIS, N.B.W., GASS, I.G.and Hawakesworth, C.J. 1990. A geochemical approach to allochthonous terranes: a Pan African case study. Phil. Trans. Royl. Soc. Lond., A. 331: 533-548.

HARRIS, N.B.W., HAWKESWOTH, C.J. and RIES, A.C. (**1984**). Crustal evolution in NE and E Africa from model Nd ages: Nature, **309**: 773-776.

HAWTHORNE, F. (**1981**). Crystal chemistry of the amphiboles. Mineral. Soc. Am., Reviews in mineral., **9A**: 1-102.

HERRON, M.M. (**1988**). Geochemical classification of terrignous sands and shales from core or log data. J. Sed. Petrol., **58**: 820-829.

HESS, P.C. (**1989**). Origins of igneous rocks. Harvard Univ. Press, Cambridge, Massachusetts, London.

HICKEY, R.L., FREY, F.A., GERLACH, D.C. and LOPEZ-ESCOBAR, L. (**1986**). Multiple sources for basaltic arc rocks from the southern volcanic zone of the Andes (34°-41°S): trace elements and isotopic evidence for contributions from subducted oceanic crust, mantle, and continental crust. J. Geophy. Res., **91**: 5963-5983.

HOLDSWORTH, R.E. and STRACHAN, R.A. (**1991**). Interlinked system of ductile strike-slip and thrusting formed by Caledonian sinistral transpression in northeastern Greenland. Geology **19**: 510-513.

HUDLESTON, P.J. (**1973**). Fold morphology and some implications of theories of fold development. Tectonophysics, **16**: 1-46.

HUDLESTON, P.J. and STEPHANSSON, O. (**1973**). Layer shortening and fold shape development in the buckling of single layers. Tectonophysics, **17**: 299-321.

HUDLESTON, P.J. SCHULTZ-ELA, D., and SOUTHWICK, D.L. (**1988**). Transpression in an Archean greenstone belt, northern Minnesota. Canadian J. of Earth Science **25**: 1060-1068.

IRVINE, T.N. (**1967**). Chromain spinel as a petrogenetic indicator, Part 2: petrologic applications. Can. J. Earth Sci. **4**: 71-103, Ottawa.

IRVINE,T.N. and BARAGAR, W.R.A. (**1971**). A guide to the chemical classification of the common volcanic rocks. Can. J. Earth Sci., **8**: 523-548. Oxford.

KOBER, B. (**1986**). Whole – grain evaporation for $^{207}Pb/^{207}Pb$-age investigation on single zircons using a double filament thermal ion source. Contrib. To Mineral. and Petrol. **93**: 482 – 490.

KOBER, B. (**1987**). Single – zircon evaporation combined with Pb^{+} emitter bedding for $^{207}Pb/^{207}Pb$-age investigations using thermal ion mass spectrometry, and implications to zirconology. Contrib. To Mineral. and Petrol. **96**: 63 – 71.

KRÖNER, A., GREILING, R., REISCHMANN, T., HUSSEIN, I.M., STERN, R.J., DÜRR, S., KRUGER, J., AND ZIMMER, M., (**1987a**). Pan-African crustal evolution in the Nubian segment of the NE Africa, in Kröner, A., (ed.), Proterozoic lithospheric evolution: Am. Geophys. Union Geodynamics series **17**: 235-257.

KRÖNER, A., STERN, R.J., DAWOUD, A.S., COMPSTON, W. AND REICHMANN, T. (**1987b**). The pan African continental margin in NE Africa: evidence from a geochronological study of granulites at Sabaloka, Sudan. Earth Panet. Sci. Lett., **85**: 91-104.

KRÖNER, A., LINNEBACHER, D., STERN, R.J., REISCHMANN, T., MANTON, AND HUSSEIN, I.M. (**1991**). Evolution of Pan African island arc assemblages in the

southern Red Sea Hills, Sudan and southwestern Arabia as exemplified by geochemistry and geochronology. Precamb. Res. **53**: 99-118.

KRÖNER, A. (**1977**). The Precambrian geotectonic evolution of Africa: plate accretion vs. plate destruction. Precamb. Res. **4**: 163-213.

KÜSTER, D. and HARMS, U. (**1998**). Post-collisional potassic granitoids from the southern and northwestern parts of the Late Proterozoic east African Orogeny: a review. LITHOS, **45**: 177-195.

KÜSTER, D. and LIEGEOIS, J.P. (**2000**). Isotopic and geochemical study of high-grade metamorphic lithologies from Bayuda Desert, Sudan: new insights into the Neoproterozoic evolution of the East Sahara Craton. Precamb. Res., accepted.

LECUYER, C., BROUXEL, M. and ALBAREDE, F. (**1990**). Elemental fluxes during hydrothermal alteration of the Trinity ophiolites (California, USA) by Seawater. Chem. Geol. **89**: 87-115.

LE MAITRE, R.W., BATMAN, P., DUDEK, A., KELLER, J., LE BAS, M.J., SABINE, P.A., SCHMIDT, R., SORENSEN, H., STRECKEISEN, A., WOOLLEY, A. and ZANETTIN, B. (**1989**). A classification of igneous rocks and glossary of terms. 193 pp., Blackwell, London.

LENOIR, J.L., KÜSTER, D., LIEGEOIS, J.P., UTKE, A., HAIDER A. and MATHEIS, G. (**1994**). Origin and regional significance of late Precambrian and early Palaeozoic granitoids in the pan African belt of Somalia. Geol. Rundschau, **83**: 624-641, Stuttgard.

LIPPARD, S.J., SHELTON, A.W. AND GASS, I.G. (**1986**). The ophiolite of northern Oman. Mem. Geol. Soc. **11**, 1, 178.

MANIAR, P.D. and PICCOLI, P.M. (**1989**). Tectonic discremination of granitoids. Bull. Geol. Soc. America, **101**: 635-643.

MASUDA, A. and NAGASAWA, S. (**1975**). Rocks with negative Ce anomalies, dredged from Shatsky Rise. Geochem. J., **9**: 227-233.

MEINHOLD, K.D. (**1983**). Summary of the regional and economic geology of the Bayuda Desert, Sudan. Bull. Geol. Miner. Resour. Dept. Sudan, **33**: 45, Khartoum.

MEINHOLD, K.D. (**1979**). The Precambrian basement complex of the Bayuda Desert, Northern Sudan. Rev. Geol. Dynam. Geog. Phys., **21**, 5: 395-401.

MESCHEDE, M. (**1986**). Amethod of discriminating between different types of mid-ocean ridge basalts and continental tholeiites with the Nb-Zr-Y diagram. Chemical geology, **56**: 207-218.

MILLER, D.D. (**1998**). Distributed shear, rotation, and partitioned strain along the San Andreas fault, central California. Geology, **26**, no. 10: 867-870.

MILLSON, J.A., MERCADIER, C.G.L., LIVERA, S.E. and PETERS, J.M. (**1996**). The Lower Palaeozoic of Oman and its context in the evolution of a Gondwana continental margin. J. Geol. Soc. London, **153**: 213-230.

MORIMONTO, N. (**1989**). Nomenclature of pyroxenes. Am. Mineral., **73**: 1123-1133.

MULLEN, E.D. (**1983**). $MnO/TiO_2/P_2O_5$: a minor element discriminant for basaltic rocks of oceanic environments and its implication for petrogenesis. Earth Plant. Sci. Lett., **62**: 53-62, Amsterdam.

NASSEEF, M.O., MCDONALD, R. and GASS, I.G. (**1984**). The Jebel Thurwah upper Proterozoic ophiolite complex, western Saudi Arabia. J. Geol. Soc. London, **141**: 537-546.

NELSON, B.K. and DEPAOLO, D.J. 1985. Rapid production of continental crust 1.7 to 1.9 b.y. ago: Nd isotopic evidence from the basement of N. America mid-continent. Geol. Soc. Am. Bull., 96,746-754.

NESBITT, H.W. and YOUNG, G.M. (**1984**). Early Proterozoic climates and plate mo-

tions inferred from major element chemistry of lutites. Nature, **299**: 715-717.

NESBITT, H.W. and YOUNG, G.M. (**1984**). Prediction of some weathering trends of plutonic and volcanic rocks based upon thermodynamic and kinetic considerations. Geochim. Cosmochim. Acta, **48**: 1523-1534.

NESBITT, H.W. and YOUNG, G.M. (**1989**). Formation and diagenesis of weathering profiles. J. Geol., **97**: 129-147.

PEARCE, T.H. (**1975**). Basalt geochemistry used to investigate past tectonic environments on Cyprus. Tectonophysics, **25**: 41-67.

PEARCE, J.A., HARRIS, N.B.W. and TINDLE, A.G. (**1984**). Trace element discrimination diagrams for the tectonic interpretation of granitic rocks. J. Petrol., **25**: 956-983.

PEARCE, T.H., GORMAN, B.E. and BIRKETT, T.C. (**1977**). The relation between major element chemistry and tectonic environment of basic and intermediate volcanic rocks. Earth and Planetary Sc. Letters, **36**: 121-132.

PECCERLIO, A. and TAYLOR, S.R. (**1976**). Geochemistry of Eocene calc-alkaline rocks from the Kastamonu area, northern Turkey. Contrib. Mineral. Petrol. **58**: 63-81.

POBER, E. and FAUPL, P. (**1988**). The chemistry of detrital chromain spinels and its implication for the geodynamic evolution of the eastern Alps. Geol. Rundschau, **77**: 641-670, Stuttgard.

RAMSAY, J.G. (**1967**). Folding and fracturing of rocks. McGraw-Hill, New York, pp 359.

RAMSAY, J.G. and HUBER, M.I. (**1987**). The techniques of modern structural geology, V2: folds and fractures. Academic press London.

RIES, A.C., SHACKLETON, R.M., and DAWOUD, A. S. (**1985**). Geochronology, geochemistry and tectonics of the NE Bayuda Desert, northern Sudan: implications for the western margin of the late Proterozoic fold belt of NE Africa. Precamb. Res., **30**: 43-62.

ROBINSON, P., SOEAR, F.S., SCHUMACHER, J.C., LAIRD, J., KLEIN, C., EVANS, B.W. and DOOLAN, B.L. (**1981**). Phase relations of metamorphic amphiboles: natural occurrence and theory. Mineral. Soc. Am. Reviews in Mineral., **9B**: 1-228.

ROCCI, G. (**1965**). Essai d' interpretation de mesures geochronologiques. La structure de l`Ouest africain: Sci. Terre. Nancy, **10**: 461-478.

ROLLINSON, H.R. (**1993**). Using geochemical data: evaluation, presentation, interpretation. J. Wiley, New York.

SANDERSON, D.J. and MARCHINI, W.R.D. (**1984**). Transpresison. J. of Structural Geology **6**: 449-458.

SAUNDERS, A.D. and TARNEY, J. (**1984**). Geochemical characteristics of basaltic volcanism within back-arc basins. In B.P. KOKELAAR and M.F. HOWELLS (ed.), Marginal basin geology, Geol. Soc. London, Spec. Publ., **16**: 59-76, London.

SAUNDERS, A.D., TARNEY, J., MARSH, N.G. and WOOD, D.A. (**1980**). Ophiolites as ocean crust or marginal basin crust. A geological approach. Proc. Intern. Ophiol. Symp. Cyprus, 193-204.

SCHANDELMEIER, H., DARBYSHIRE, D.P.E., HARMS, U. AND RICHTER, A. (**1988**). The East Sahara craton: evidence for pre-Pan Africa crust in NE Africa W of the Nile. In El Gaby, S., and Greiling, R.O. eds. The Pan African belts of NE Africa and adjacent areas. Braunschweig, Friedr. Vieweg and Sohn. 69-94.

SCHANDELMEIER, H., WIPFLER, E., KÜSTER, D., SULTAN, M., BECKER, R., STERN, R.J., and ABDELSALAM, M.G. (**1994**). Atmur-Delgo suture: a Neoproterozoic oceanic basin extending into the interior of NE Africa. Geology, **22**: 563-566.

SCHANDELMEIER, H., RICHTER, H., HARMS, U. and ABDELRAHMAN, E.M. (1990). Lithology and structure of the Late Proterozoic Jabel Rahib fold and thrust belt. Berliner Geowiss. Abh. (A) **120**.1: 15-30, Berlin.

SHERVAIS, J.W. (**1982**). Ti-V plots and petrogenesis of modern and ophiolitic lavas. Earth and Planet. Sc. Lett., **59**: 101-118.

SPEAR, F.S. and CHENEY, J.T. (**1989**). A petrogenetic grid for the pelitic schist in the system SiO_2-Al_2O_3-FeO-MgO-K_2O-H_2O. Contrib. To Mineral. and Petrol., **101**: 149-164.

STACEY, J.S., DOE, B.R., ROBERTS, J.R., DE LEVAUX, M.H. and GRAMLICH, J.W. (**1980**). A lead isotopic study of mineralization in the Saudi Arabian Shield. Contrib. Mineral. Petrol., **74**: 175-188, Berlin and Heidelberg.

STACEY, J.S. and STOESER, D.B. (**1983**). Distribution of oceanic and continental leads in the Arabian-Nubian Shield. Cont. Min. and Petrol. **84**: 91-105, Berlin and Heidelberg.

STERN, R.J. (**1994**). Arc assembly and continental collision in the Neoproterozoic East African Orogen: implications for the consolidation of Gondwanaland. Ann. Rev. of Earth and Planetary Sci., **22**: 319-351.

STERN, R. J., ABDELSALAM, M: G., SCHANDELMEIER, H., SULTAN, M., WICKHAM, S. (**1993**). Carbonates of the Keraf zone, NE Sudan: a Neoproterozoic (ca. 750 Ma) passive margin on the eastern flank of west Gondwanaland.Geol. Soc. of America Abs. with Prog. ,v. **25**, No. 6: 49.

STERN, R.J., KRÖNER, A., BENDER, R, T. REISCHMANN, and DAWOUD, A.S. (**1994**). Precambrian basement around Wadi Halfa, Sudan: a new perspective on the evolution of the Eastern Saharan Craton. Geologische Rundschau , v. **83**: 564-577.

STERN, R.J. and KRÖNER, A. (**1983**). Late Precambrian crustal evolution in NE Sudan: Isotopic and geochronologic constrains. J. Geol. **101**: 555-574.

STERN, R.J., KRÖNER, A. and RASHWAN, A.A. (**1991**). A late Precambrian (710 Ma) high volcanicity rift in the Southern Eastern Desert of Egypt. Geol. Rundschau, **80**: 155-170.

STEVENS, R.E. (**1944**). Composition of some chromites of the western hemisphere. Am. Mineralogist, **29**: 1-34.

SULTAN, M., CHAMBERLIN, K.R., BOWRING, S.A., ARVIDSON, R.E., ABUZEID, H. and EL KALIOUBY, B. (**1990**). Geochronological and isotopic evidence for involvement of pre-Pan African crust in the Nubian Shield, Egypt. Geology. **18**: 761-764.

SULTAN, M., BICKFORD, M., E., EL KALIOUBY, B., and ARVIDSON, R.E. (**1992**). Common Pb systematics of Precambrian granitic rocks of the Nubian Shield (Egypt) and tectonic implications. Geol. Soc. America Bull., **104**: 456-470.

SULTAN, M., TUCKER, R.D., EL ALFY, Z., ATTIA, R. and RAGAB, A.I. (**1994**). U-Pb (zircon) ages of the gneissic terrane west of the Nile, southern Egypt. Geol. Rundschau, **83**: 514-522.

SUN, S.S. and MCDONOUGH, W.F. (**1989**). Chemical and isotopic systematics of oceanic basalts: implications for mantle composition processes, in magmatism in the ocean basins. Geological Soc., Special Publ., **42**: 313-345.

TADESSE, T., HOSHINO, M. and SAWADA, Y. (**1990**). Geochemistry of low-grade metavolcanic rocks from the Pan-African of the Axum area, northern Ethiopia. Prec. Res. **99**: 101-124.

TAYLOR, S.R. and MCLENNAN, S.M. (**1985**). The continental crust: its composition and evolution. Blackwell, Oxford, 312 pp.

TSIKOURAS, B. and HATZIPANAGIOTOU, K. (**1998**). Petrogenetic evolution of an

ophiolite fragment in an ensialic marginal basin, northern Aegean (Samothraki Island, Greece). Eur. J. Mineral., **10**: 551-567.

VAIL, J.R. (**1971**). Geological reconnaissance in part of Berber District, Northern Province, Sudan. Bull. Geol. Surv. Sudan, **18**: 76. Khartoum.

VAIL, J.R. (**1979**). Outline of geology and mineralisation of the Nubian Shield east of the Nile Valley, Sudan. In: TAHON, S.A. (ed.) Evolution and mineralisation of the Arabian-Nubian Shield, Proceed. Symp.: **2**, 97-107, Oxford (Pergamon Press).

VAIL, J.R. (**1983**). Pan-African crustal accretion in NE Africa. J. of Afr. Earth Sc., **1** (3-4) :285-294.

VAIL, J.R. (**1985**). Alkaline ring complexes in Sudan. J. Afr. Earth Sc., **3** (1-2), 51-59, Oxford.

VAIL, J.R. (**1988**). Tectonics and evolution of the Proterozoic basement of NE Africa. In: El Gaby, S., and Greiling, R. (eds.), The Pan-African belt of NE Africa and adjacent areas. Earth and Evol. Sc., 192-226, Wiesbaden (Vieweg).

VAIL, J.R. (**1978**). Outline of the geology and mineral deposits of the Democratic Republic of the Sudan and adjacent areas. Overseas Geol. Miner. Resour., 49, 67 pp., London.

WHITEMAN, A.J. **1971**). The geology of the Sudan Republic. 290pp., Oxford (Clarendon Press).

WILSON, M. (**1989**). Igneous petrogenesis: a global tectonic approach. 446 pp., Unwin Hyman, London.

WINCHESTER, J.A. and FLOYD, P.A. (**1977**). Geochemical discrimination of different magma series and their differentiation products using immobile elements. Chemical Geology, **20**: 325-343.

WIPFLER, E.L. (**1994**). Geochemishe, strukturelle und erzmikroskopishe Untersuchungen zur Lagerstättenentwicklung des westlichen Ariab-Nakasib belt, Red Sea Provinz, northeast Sudan. Berl. Geowiss. Abh., **166** (A), 1-206.

WIPFLER, E.L. (**1996**). Transpressve structures in the Neoproterozoic Ariab-Nakasib belt, NE Sudan: evidence for suturing by oblique collision. Journal of African Earth Science, v. 23, no. **3**: 347-362.

WIPKI, M. (**1995**). Eigenschaften, Verteilung und Entstehung von Kaolinlagerstätten im Nordsudan. PhD thesis, TU Berlin, Band **2**, D 83, Berlin.

WOODCOCK, N.H. and SCHUBERT, C. (**1994**). Continental strike slip tectonics. In continental deformation (ed. P.L. Hancock), pp. 251-63. Pergamon Press.

WORELY, B.A. and WILLSON, C.J.L. (**1996**). Deformation partitioning and foliation reactivation during transpressional orogenesis, an example from the Central longmen Shan, China. Journal of structural geology **18**: 395-411.

WORKU, H. and SCHANDELMEIER, H. (**1996**). Tectonic evolution of the Neoproterozoic Adola Belt of southern Ethiopia: evidence for a Wilson Cycle process and implications for oblique plate collision. Precamb. Res., **77**: 179-210.

WUST, H.J., TODT, W., and KRÖNER, A. (**1987**). Conventional and single grain zircon ages for meta-sediments and granitic clasts from the E Desert of Egypt: evidence for active continental margin evolution in Pan African times. Terra Cobnita (abs.). **7**: 333-334.

ZARTMAN, R.E. and DOE, B.R. (**1981**). Plumbotectonics- the model. Tectonophysics, **75**: 135-162, Amsterdam.

ZARTMAN, R.E. and HAINES, S.M. (**1988**). The plumbotectonic model for Pb isotopic systematics among major terrestrial reservoirs – a case for bidirectional transport. Geochem. Cosmochem. Acta, **52**: 1327-1339, New York.

10 APPENDIX

I Petrography of selected samples from the KPTA:

Mafic-Ultramafic sequence:

5.7: Amphibole-plagioclase-chlorite-zoisite-epidote-calcite/dolomite-muscovite-spinel.

5.7b: Talc schist: talc-serpentine-spinel

5.7c: Plagioclase-calcite/dolomite-chlorite-epidote-spinel-silica.

5.7d: Plagioclase-amphibole-chlorite-talc-dolomite-spinel-zoisite.

5.11: Plagioclase-olivine-chlorite-talc-zoisite-amphibole-spinel-silica.

8.8a: Hornblende-chlorite-epidote-spinel

9.4a: Epidote-chlorite-calcite-talc-serpentine-spinel-silica.

9.5a: Chlorite-epidote-calcite-biotite-spinel.

9.5b: Dolomite-serpentine-muscovite-epidote-chlorite-spinel-silica.

9.5d: Chlorite-dolomite-epidote-zoisite-spinel

9.7: Talc-serpentine-dolomite-spinel-muscovite-plagioclase-clinopyroxine?-silica.

10.1a: Serpentine-talc schist: serpentine-talc-epidote-spinel.

10.8b: Talc-serpentine schist: talc-serpentine-calcite-spinel (opaques).

10.8d: Talc-schist: talc-muscovite-epidote-spinel. About 90% of the rock is talc.

10.9a: Hornblende-epidote-plagioclase-chlorite-chloritoid?-spinel-silica.

10.9d: Plagiogranite:plagioclase-quartz-chlorite-hornblende-epidote-zoisite-muscovite

10.11a: Epidote-chlorite-spinel-silica.

11.1c: Clinopyroxine-hornblende-chlorite-epidote-calcite (after plagioclase)-spinel.

11.1b: Hornblende-epidote-calcite-dolomite-chlorite-silica.

11.2: Hornblende-chlorite-epidote-zoisite-calcite.

11.4b:Amphibole-brucite?-chlorite-epidote-serpentine-calcite-biotite-muscovite-plagioclase.

11.8a: Clinopyroxine-olivine-chloritoid-calcite-talc-chlorite-epidote-spinel.

11.8c: Meta-gabbro: plagioclase-amphibole (altered)-chlorite-epidote-spinel-calcite-silica.

Low-grade metasediments:

1.3a: Quartz-K-feldspar-biotite-muscovite-plagioclase-Fe-oxides

2.4.2: quartz-dolomite-calcite-Fe-oxides

2.4.4: Dolomite/calcite-muscovite-quartz-chlorite-opaque minerals.

2.5.1: Dolomite-calcite-quartz-plagioclase-chlorite-Fe-oxides.

3.6: Amphibole-chlorite-dolomite-plagioclase-quartz.

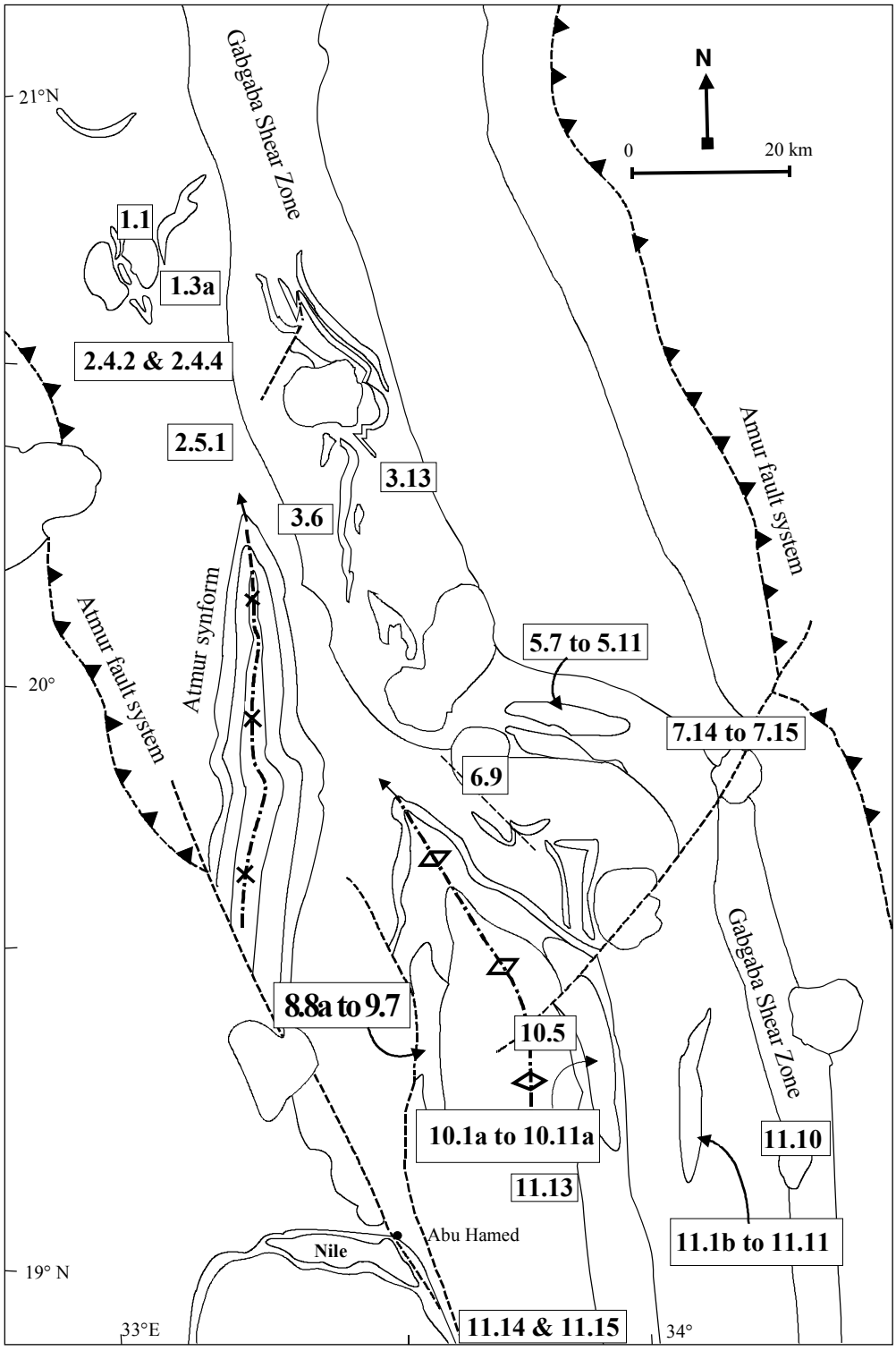

Location map of selected samples used in the petrographic analysis. Samples A26, A43, A45, A52, A55 and A57 were collected from the junction of Dam et Tor with the KSZ.

High-grade metamorphic rocks:

11.13: High-grade gneiss: quartz-plagioclase-biotite-K-feldspars-garnet

11.14: High-grade gneiss: plagioclase-quartz-biotite-muscovite-hornblende-garnet

11.15: Gneiss: plagioclase-quartz-biotite-hornblende-epidote-chlorite.

12.1b: Calc-silicate: calcite/dolomite-diopside-quartz.

A26: Plagioclase-quartz-hornblende-biotite-garnet-opaque minerals.

A43: Schist: quartz-K-feldspar-Fe-oxides-muscovite.

A45: Hornblende-garnet-plagioclase-quartz-epidote-opaque minerals.

A52: Plagioclase-quartz(mirmikit)-hornblende-opaque minerals.

A55: Hornblendite: hornblende-biotite-plagioclase-clinopyroxene-pinkish mineral

Plutons, sills and dykes:

1.1: Diorite: plagioclase-hornblende-quartz-chlorite-epidote-muscovite.

3.13: Diorite: hornblende-biotite-plagioclase-quartz.

6.9: Granodiorite: plagioclase (zoned)-hornblende-K-feldspars-quartz (mirmikit)-muscovite.

7.15: Granodiorite: plagioclase-quartz-hornblende-biotite-epidote-muscovite.

7.14: Gabbro: olivine-pyroxene-plagioclase-hornblende-biotite-calcite-muscovite.

7.14b: Granodiorite: quartz-plagioclase-biotite-hornblende-epidote-chlorite.

10.5: Diorite: hornblende-biotite-plagioclase-muscovite-chlorite-quartz.

11.10: Granite: quartz-K-feldspars-plagioclase-biotite.

11.11: Doleritic sill: hornblende-biotite-epidote-zoisite-calcite-chlorite-silica.

A57: K-feldspar-aegirine-clay minerals.

II Calculation of the fourier coefficients (b_1, b_2,b_3) of a folded layer.

$y_1 = b_1 Sinx_1 + b_3 Sin3x_1 + b_5 Sin5x_1$

$y_2 = b_1 Sinx_2 + b_3 Sin3x_2 + b_5 Sin5x_2$

$y_3 = b_1 Sinx_3 + b_3 Sin3x_3 + b_5 Sin5x_3$

The determinants of the following matrices are calculated:

$$D = \begin{vmatrix} Sinx_1 & Sin3x_1 & Sin5x_1 \\ Sinx_2 & Sin3x_2 & Sin5x_2 \\ Sinx_3 & Sin3x_3 & Sin5x_3 \end{vmatrix}$$

$$D_1 = \begin{vmatrix} y_1 & Sin3x_1 & Sin5x_1 \\ y_2 & Sin3x_2 & Sin5x_2 \\ y_3 & Sin3x_3 & Sin5x_3 \end{vmatrix}$$

$$D_2 = \begin{vmatrix} Sinx_1 & y1 & Sin5x_1 \\ Sinx_2 & y_2 & Sin5x_2 \\ Sinx_3 & y_3 & Sin5x_3 \end{vmatrix}$$

$$D_3 = \begin{vmatrix} \text{Sin}x_1 & \text{Sin}3x_1 & y_1 \\ \text{Sin}x_2 & \text{Sin}3x_2 & y_2 \\ \text{Sin}x_3 & \text{Sin}3x_3 & y_3 \end{vmatrix}$$

$b_1 = D_1/D$, $b_3 = D_2/D$ and $b_5 = D_3/D$

III Calculation of the fourier coefficients (b_1, b_2,b_3) of Atmur synform:

The three points selected have co-ordinates:

(80,12), (67,9) and (55,5)

$$D = \begin{vmatrix} \text{Sin}5 & \text{Sin}15 & \text{Sin}25 \\ \text{Sin}9 & \text{Sin}27 & \text{Sin}45 \\ \text{Sin}12 & \text{Sin}36 & \text{Sin}60 \end{vmatrix}$$

$$D_1 = \begin{vmatrix} 55 & \text{Sin}15 & \text{Sin}25 \\ 67 & \text{Sin}27 & \text{Sin}45 \\ 80 & \text{Sin}36 & \text{Sin}60 \end{vmatrix}$$

$$D_2 = \begin{vmatrix} \text{Sin}5 & 55 & \text{Sin}25 \\ \text{Sin}9 & 67 & \text{Sin}45 \\ \text{Sin}12 & 80 & \text{Sin}80 \end{vmatrix}$$

$$D_3 = \begin{vmatrix} \text{Sin}5 & \text{Sin}15 & 55 \\ \text{Sin}9 & \text{Sin}27 & 67 \\ \text{Sin}12 & \text{Sin}36 & 80 \end{vmatrix}$$

$b_1 = D_1/D$, $b_3 = D_2/D$ and $b_5 = D_3/D$

IV Calculation of the fourier coefficients (b_1, b_2,b_3) of Abu Hamed antiform:

The three points selected have co-ordinates:

(27,16), (16,11) and (6,6)

$$D = \begin{vmatrix} \text{Sin}6 & \text{Sin}18 & \text{Sin}30 \\ \text{Sin}11 & \text{Sin}33 & \text{Sin}55 \\ \text{Sin}16 & \text{Sin}48 & \text{Sin}80 \end{vmatrix}$$

$$D_1 = \begin{vmatrix} 6 & \text{Sin}18 & \text{Sin}30 \\ 16 & \text{Sin}33 & \text{Sin}55 \\ 27 & \text{Sin}48 & \text{Sin}80 \end{vmatrix}$$

$$D_2 = \begin{vmatrix} \text{Sin6} & 6 & \text{Sin30} \\ \text{Sin11} & 16 & \text{Sin55} \\ \text{Sin16} & 27 & \text{Sin80} \end{vmatrix}$$

$$D_3 = \begin{vmatrix} \text{Sin6} & \text{Sin18} & 6 \\ \text{Sin11} & \text{Sin33} & 16 \\ \text{Sin16} & \text{Sin48} & 27 \end{vmatrix}$$

$b_1 = D_1/D$, $b_3 = D_2/D$ and $b_5 = D_3/D$

V Calculation of the fourier coefficients (b_1, b_2,b_3) of a mesoscopic D1 fold:

The three points selected have co-ordinates:

(36,44), (26,29) and (14,14)

$$D = \begin{vmatrix} \text{Sin14} & \text{Sin42} & \text{Sin70} \\ \text{Sin29} & \text{Sin87} & \text{Sin145} \\ \text{Sin44} & \text{Sin132} & \text{Sin220} \end{vmatrix}$$

$$D_1 = \begin{vmatrix} 14 & \text{Sin42} & \text{Sin70} \\ 26 & \text{Sin87} & \text{Sin145} \\ 36 & \text{Sin132} & \text{Sin220} \end{vmatrix}$$

$$D_2 = \begin{vmatrix} \text{Sin14} & 14 & \text{Sin70} \\ \text{Sin29} & 26 & \text{Sin145} \\ \text{Sin44} & 36 & \text{Sin220} \end{vmatrix}$$

$$D_3 = \begin{vmatrix} \text{Sin14} & \text{Sin42} & 55 \\ \text{Sin29} & \text{Sin87} & 67 \\ \text{Sin44} & \text{Sin132} & 80 \end{vmatrix}$$

$b_1 = D_1/D$, $b_3 = D_2/D$ and $b_5 = D_3/D$

Table a.1: XRF of major and trace elements data for the basal tectonites (mental sequence) of the Keraf ophiolites.

Sample	4.5	8.8c	10.8b	8.8b	10.1a	10.1b	10.1	5.9b	9.5b	5.9b	5.8a	9.7
SiO_2	39.98	41.02	40.30	42.67	37.2	37.22	35.95	37.95	38.97	40.80	43.24	36.41
Al_2O_3	0.16	1.08	0.55	0.67	1.53	1.67	1.44	0.10	1.00	0.15	1.73	8.48
Fe_2O_3	5.27	5.53	6.36	6.42	11.79	12.05	11.44	5.23	5.38	4.31	10.37	7.87
MgO	39.20	38.24	37.96	37.71	34.80	33.36	33.75	24.42	23.60	21.79	19.43	17.64
MnO	0.073	0.063	0.051	0.059	0.111	0.134	0.103	0.049	0.080	0.067	0.071	0.080
CaO	2.47	0.10	0.21	0.96	2.04	1.71	2.02	5.41	2.85	4.07	4.40	10.08
Na_2O	b.d.l.	b.d.l.	b.d.l.	0.10	b.d.l.	b.d.l.	b.d.l.	b.d.l.	b.d.l.	b.d.l.	b.d.l.	b.d.l.
K_2O	b.d.l.	b.d.l.	0.02	b.d.l.	b.d.l.	0.02	b.d.l.	b.d.l.	0.02	0.02	b.d.l.	0.02
TiO_2	0.02	0.02	0.02	0.02	0.09	0.08	0.09	0.02	0.02	0.02	0.04	0.34
P_2O_5	0.013	0.02	0.01	0.02	0.01	0.04	0.01	0.04	b.d.l.	b.d.l.	0.027	0.106
SO_3	0.117	0.02	b.d.l.	0.09	0.01	0.06	b.d.l.	0.089	b.d.l.	0.1	0.07	0.01
L.O.I.	13.93	13.60	12.89	11.69	12.7	12.19	13.53	27.34	27.59	28.23	21.78	19.21
Total	101.18	99.94	98.60	100.62	100.52	98.70	98.53	100.54	99.60	99.78	101.20	100.14
As	b.d.l.	b.d.l.	24	b.d.l.	b.d.l.	7	b.d.l.	23	240	33	148	368
Ba	25	20	20	35	41	30	20	20	20	b.d.l.	20	24
Bi	b.d.l.	b.d.l.	3	b.d.l.	3	6.3	3	b.d.l.	8	3	4.70	b.d.l.
Cu	53	b.d.l.	42	b.d.l.	7	b.d.l.	5	22	10	27	245	35
Cr	1510	2244	2340	2805	3582	2839	3387	1973	1658	2186	3131	1557
Ga	3	3	3	6	3	6	4	3	5	5	4	9
Ni	2060	2014	1951	2130	1148	1049	1101	1503	1351	1615	737	592
Pb	10	b.d.l.	10	b.d.l.	10	10	b.d.l.	b.d.l.	b.d.l.	b.d.l.	b.d.l.	b.d.l.
Rb	5	5	5	5	5	5	5	5	10	10	5	5
Sb	14.8	5.3	4.5	3.9	3	3.4	5.6	5.7	11.6	5.7	5.1	4.5
Sr	12	10	10	13	74	41	51	64	39	61	113	353
Th	8	b.d.l.	b.d.l.	b.d.l.	b.d.l.	b.d.l.	b.d.l.	b.d.l.	8	8	b.d.l.	b.d.l.
U	5	b.d.l.	5	5	5	5	b.d.l.	5	5	5	5	5
V	12	30	20	38	50	52	42	12	35	12	88	108
Zn	17	18	22	17	79	84	68	12	27	23	57	52
Zr	10	10	10	10	15	17	14	10	25	25	10	41
Nd	nd	nd	nd	nd	nd	nd	nd	0.1	10	13	nd	nd
Ce	nd	nd	nd	nd	nd	nd	nd	0.2	53	0.4	nd	nd
Hf	nd	nd	nd	nd	nd	nd	nd	1.4	2	3	nd	nd
La	nd	nd	nd	nd	nd	nd	nd	0.5	20	1.3	nd	nd
Mo	nd	nd	nd	nd	nd	nd	nd	nd	3	4	nd	nd
Nb	nd	nd	nd	nd	nd	nd	nd	nd	3	3	nd	nd
Pr	nd	nd	nd	nd	nd	nd	nd	0.3	10	b.d.l.	nd	nd
Sc	nd	nd	nd	nd	nd	nd	nd	nd	10	10	nd	nd
Sm	nd	nd	nd	nd	nd	nd	nd	0.5	4	4	nd	nd
Y	nd	nd	nd	nd	nd	nd	nd	nd	10	10	nd	nd
Yb	nd	nd	nd	nd	nd	nd	nd	0.1	nd	0.1	nd	nd
Gd	nd	nd	nd	nd	nd	nd	nd	0.5	nd	0.4	nd	nd
Ho	nd	nd	nd	nd	nd	nd	nd	0.1	nd	0.1	nd	nd
Er	nd	nd	nd	nd	nd	nd	nd	0.2	nd	0.1	nd	nd
Dy	nd	nd	nd	nd	nd	nd	nd	0.3	nd	0.1	nd	nd
Eu	nd	nd	nd	nd	nd	nd	nd	0.2	nd	0.1	nd	nd
Lu	nd	nd	nd	nd	nd	nd	nd	0.1	nd	0.1	nd	nd

nd: not determined
b.d.l.: below detection limit

Table a.2: XRF of major and trace elements data for the cumulate mafic-ultramafic sequence of the Keraf ophiolites.

Sampl	9.9	7.14	11.4c	6.2	10.7b	11.8c	7.11	6.14	6.1c	3.6	9.4a	10.5	2.4.2	10.7b
SiO_2 %	41.58	48.67	36.81	38.29	35.33	51.10	51.48	51.21	38.10	42.80	37.39	52.90	36.15	33.78
Al_2O_3	9.95	10.40	18.67	13.65	14.03	12.74	10.21	10.88	9.98	13.12	15.76	14.57	8.64	15.52
Fe_2O_3	8.77	8.85	4.74	11.88	2.63	8.21	9.05	8.44	7.69	11.55	4.79	7.20	9.20	2.70
MgO	12.41	14.25	10.58	10.43	9.32	9.62	15.52	15.15	12.65	9.87	9.53	9.91	7.97	5.52
MnO	0.116	0.0863	0.0544	0.106	0.054	0.119	0.129	0.133	0.098	0.146	0.069	0.085	0.139	0.376
CaO	9.29	11.68	12.71	8.70	13.22	5.83	11.85	11.87	14.64	12.01	9.88	6.78	14.40	13.62
Na_2O	<0.10	1.11	1.65	0.58	1.77	2.27	1.08	1.20	b.d.l.	2.03	2.07	2.81	0.41	2.29
K_2O	0.37	0.34	0.49	0.10	0.84	0.25	0.25	0.30	0.02	0.31	0.13	1.99	0.11	0.82
TiO_2	0.65	0.51	0.20	0.56	0.05	0.67	0.42	0.52	0.82	0.63	0.12	0.62	0.68	0.06
P_2O_5	0.152	0.075	0.013	0.145	<0.010	0.323	0.015	0.028	0.854	0.193	0.016	0.144	0.113	0.011
SO_3	<0.01	0.31	<0.01	0.04	b.d.l.	b.d.l.	<0.10	<0.10	<0.01	<0.01	b.d.l.	b.d.l.	0.02	b.d.l.
L.O.I.	16.54	2.92	13.98	14.48	20.09	9.01	0.66	0.70	14.35	8.26	18.97	3.10	20.83	22.23
Total	99.8	99.1	99.4	98.8	99.3	100.2	100.9	100.7	99.0	100.7	98.5	99.9	98.5	99.4
As ppn	670	b.d.l.	<7	30	b.d.l.	<5	b.d.l.	<5	172	b.d.l.	39	21	67	<7
Ba	41	146	72	<20	59	132	84	138	25	58	47	607	73	68
Bi	<3.0	b.d.l.	b.d.l.	<3.0	8	7	9	7	<3.0	b.d.l.	b.d.l.	b.d.l.	<3.0	b.d.l.
Cu	51	33	27	57	221	23	35	29	62	b.d.l.	b.d.l.	67	47	226
Cr	1124	1147	731	875	1062	648	1307	1178	904	600	949	683	510	1478
Ga	12	8	11	17	10	12	12	5	11	11	8	15	7	10
Ni	621	191	135	281	214	181	223	213	610	95	268	256	66	221
Pb	b.d.l.	b.d.l.	<10	b.d.l.	b.d.l.	<10	<10	b.d.l.	13	<10	b.d.l.	<10	b.d.l.	<10
Rb	15	7	12	<5	27	22	<10	<10	<5	8	<5	32	<5	26
Sb	20.2	<3.0	3.2	4.4	5.1	<3	<3	<3	6.8	<3.0	5.8	3.6	3.0	6.2
Sr	181	276	317	83	211	393	341	364	334	144	174	336	410	213
Th	b.d.l.	b.d.l.	<8.0	<8.0	<5	<5	b.d.l.	<5	9.2	b.d.l.	<8.0	<8.0	<8.0	b.d.l.
U	b.d.l.	<5.0	b.d.l.	<5.0	b.d.l.	<5	<5	b.d.l.	<5.0	<5.0	b.d.l.	b.d.l.	b.d.l.	b.d.l.
V	177	140	163	217	75	183	173	175	138	208	87	141	176	79
Zn	66	37	11	84	<10	76	50	49	81	74	20	58	54	<10
Zr	52	39	12	43	<25	73	54	49	154	50	10	69	48	<10
Nd	n.d.	n.d.	n.d.	n.d.	12	32	14	16	n.d.	n.d.	n.d.	n.d.	n.d.	n.d.
Ce	n.d.	n.d.	n.d.	n.d.	30	62	31	<20	n.d.	n.d.	n.d.	n.d.	n.d.	n.d.
Hf	n.d.	n.d.	n.d.	n.d.	2	3	3	3	n.d.	n.d.	n.d.	n.d.	n.d.	n.d.
La	n.d.	n.d.	n.d.	n.d.	<20	18.6	<20	<20	n.d.	n.d.	n.d.	n.d.	n.d.	n.d.
Mo	n.d.	n.d.	n.d.	n.d.	5	5	4	3	n.d.	n.d.	n.d.	n.d.	n.d.	n.d.
Nb	n.d.	n.d.	n.d.	n.d.	<3	27.1	<3	<3	n.d.	n.d.	n.d.	n.d.	n.d.	n.d.
Pr	n.d.	n.d.	n.d.	n.d.	<10	5.8	<10	<10	n.d.	n.d.	n.d.	n.d.	n.d.	n.d.
Sc	n.d.	n.d.	n.d.	n.d.	19	25	41	43	n.d.	n.d.	n.d.	n.d.	n.d.	n.d.
Sm	n.d.	n.d.	n.d.	n.d.	<4	6	<4	5	n.d.	n.d.	n.d.	n.d.	n.d.	n.d.
Y	n.d.	n.d.	n.d.	n.d.	<10	15	14	14	n.d.	n.d.	n.d.	n.d.	n.d.	n.d.
Yb	n.d.	n.d.	n.d.	n.d.	n.d.	1.3	n.d.	n.d.	n.d.	n.d.	n.d.	n.d.	n.d.	n.d.
Gd	n.d.	n.d.	n.d.	n.d.	n.d.	3.7	n.d.	n.d.	n.d.	n.d.	n.d.	n.d.	n.d.	n.d.
Ho	n.d.	n.d.	n.d.	n.d.	n.d.	0.4	n.d.	n.d.	n.d.	n.d.	n.d.	n.d.	n.d.	n.d.
Er	n.d.	n.d.	n.d.	n.d.	n.d.	1.6	n.d.	n.d.	n.d.	n.d.	n.d.	n.d.	n.d.	n.d.
Dy	n.d.	n.d.	n.d.	n.d.	n.d.	2.7	n.d.	n.d.	n.d.	n.d.	n.d.	n.d.	n.d.	n.d.
Eu	n.d.	n.d.	n.d.	n.d.	n.d.	1.8	n.d.	n.d.	n.d.	n.d.	n.d.	n.d.	n.d.	n.d.
Lu	n.d.	n.d.	n.d.	n.d.	n.d.	0.2	n.d.	n.d.	n.d.	n.d.	n.d.	n.d.	n.d.	n.d.
Mg#	0.58	0.61	0.68	0.46	0.77	0.53	0.62	0.63	0.61	0.45	0.66	0.57	0.45	0.66

n.d.: not determined

Table a.3: XRF of major and trace elements data for the mafic and intermediate sequence of the Keraf ophiolites.

Sample	11.8a	11.1a	11.1b	11.2	5.7c	5.11	8.8a	10.9b	10.9c	10.11a	11.8d	10.8d
SiO_2 %	35.22	34.60	38.3	37.87	50.82	45.58	38.88	57.24	50.19	52.6	78.08	33.30
Al_2O_3	16.45	24.58	16.94	19.03	14.30	15.93	22.05	16.76	16.41	14.66	8.48	28.82
Fe_2O_3	12.06	12.59	17.82	16.35	13.57	14.63	13.09	8.64	8.81	9.00	4.48	4.80
MgO	11.10	4.93	5.26	6.71	5.78	9.15	6.46	4.85	7.84	2.73	1.18	16.27
MnO	0.186	0.203	0.278	0.251	0.220	0.211	0.172	0.166	0.141	0.172	0.238	0.034
CaO	9.99	16.85	12.47	14.51	9.20	8.19	9.66	3.76	9.17	12.00	0.77	<0.10
Na_2O	b.d.l.	<0.10	0.96	b.d.l.	3.61	2.31	1.89	0.17	3.55	1.58	2.91	0.22
K_2O	2.89	0.04	0.08	0.05	0.09	0.05	3.26	2.16	0.25	0.03	0.63	3.52
TiO_2	0.44	0.80	1.81	1.42	1.42	0.68	1.43	0.75	1.11	1.38	0.58	0.97
P_2O_5	<0.01	0.085	0.03	0.045	0.128	<0.01	0.217	0.198	0.174	0.27	0.071	0.017
SO_3	b.d.l.	b.d.l.	b.d.l.	b.d.l.	b.d.l.	b.d.l.	b.d.l.	b.d.l.	b.d.l.	b.d.l.	b.d.l.	b.d.l.
L.O.I.	11.43	5.32	6.27	3.56	1.65	3.77	1.45	5.33	2.44	5.03	1.46	8.77
Total	99.9	100.3	100.3	99.8	100.8	100.5	98.8	100.0	100.1	99.5	98.8	98.1
As ppm	b.d.l.	b.d.l.	b.d.l.	b.d.l.	<5	b.d.l.	<5	b.d.l.	b.d.l.	<5	<5	44
Ba	763	<20	39	43	37	b.d.l.	1734	425	178	23	457	>5000
Bi	9	20	10	14	7	9	17	6	8	8	b.d.l.	b.d.l.
Cu	219	33	<10	31	67	172	122	49	26	52	217	b.d.l.
Cr	29	27	26	47	54	94	24	83	140	52	39	65
Ga	10	37	12	15	15	6	16	18	13	23	10	16
Ni	52	<8	<8	23	24	27	12	57	136	17	43	18
Pb	<10	<10	<10	<10	b.d.l.	<10	18	<10	<10	<10	<10	b.d.l.
Rb	75	b.d.l.	b.d.l.	<10	<10	<10	67	43	<10	b.d.l.	10	40
Sb	<3	3	<3	b.d.l.	<3	<3	b.d.l.	4.8	4.2	<3	<3	<3
Sr	571	3124	741	864	308	99	1814	294	464	743	101	154
Th	b.d.l.	b.d.l.	b.d.l.	b.d.l.	<5	<5	b.d.l.	b.d.l.	b.d.l.	b.d.l.	12	12
U	<5	<5	b.d.l.	b.d.l.	b.d.l.	<5	<5	b.d.l.	b.d.l.	b.d.l.	<5	b.d.l.
V	597	401	495	545	392	446	321	148	187	259	52	141
Zn	40	51	121	114	84	74	46	84	75	71	77	33
Zr	<25	149	86	85	81	<25	122	113	98	154	106	238
Nd	<10	17	21	24	13	0.2	<10	22	22	26	16	48
Ce	31	49	29	<20	7.8	0.1	24	43	53	42	45	101.1
Hf	2	1.4	2	3	3	2	<2	3.4	4	4	5	7.4
La	b.d.l.	1.4	<20	<20	2.8	0.2	<20	11	<20	23	<20	53
Mo	3	5	2	3	6	5	6	3	<2	3	2	4
Nb	<3	3	<3	<3	3	<3	3	6	3	3	7	3
Pr	<10	1.1	<10	<10	0.1	0.1	<10	3.1	<10	5.4	<10	13
Sc	37	36	53	59	38	59	53	28	26	34	<10	23
Sm	<4	5	6	5	4	<4	5	4.1	5	5.4	<4	10.5
Y	<10	15	32	27	32	<10	23	29	18	29	22	22
Yb	n.d.	1.4	n.d.	n.d.	3	0.2	n.d.	2.6	n.d.	3.1	n.d.	1.1
Gd	n.d.	1.7	n.d.	n.d.	3.6	0.3	n.d.	4.3	n.d.	5.2	n.d.	6.2
Ho	n.d.	0.4	n.d.	n.d.	0.9	0.1	n.d.	1	n.d.	1	n.d.	0.5
Er	n.d.	1.4	n.d.	n.d.	2.5	0.4	n.d.	2.3	n.d.	3.2	n.d.	1.8
Dy	n.d.	2.1	n.d.	n.d.	4.5	0.2	n.d.	4.4	n.d.	5.4	n.d.	n.d.
Eu	n.d.	0.6	n.d.	n.d.	1.3	0.1	n.d.	1.4	n.d.	1.8	n.d.	4.2
Lu	n.d.	0.2	n.d.	n.d.	0.4	0.1	n.d.	0.4	n.d.	0.4	n.d.	0.2

n.d.: not determined b.d.l.: below detection limit

Table a.4: XRF major and trace elements data for the post-tectonic intrusions of the KPTA.

Sample	**5.9c**	**11.11**	**1.1**	**7.14b**	**3.13**	**3.8**	**7.15**	**7.15a**	**11.10**	**6.9**	**3.10**
SiO_2 %	47.41	47.65	52.00	54.74	56.88	63.16	66.87	66.90	69.51	70.72	71.35
Al_2O_3	11.33	13.61	17.60	13.84	16.68	14.37	15.88	17.16	14.82	15.85	16.13
Fe_2O_3	11.60	14.04	7.13	7.16	7.90	1.87	2.96	3.21	3.57	2.26	1.95
MnO	0.14	0.188	0.118	0.084	0.153	0.027	0.026	0.040	0.067	0.046	0.026
MgO	5.54	6.14	5.93	4.77	4.13	1.01	1.64	1.24	0.51	0.55	0.62
CaO	11.42	12.99	10.41	7.69	7.83	3.15	4.06	4.01	2.39	2.74	2.39
Na_2O	1.71	0.75	2.99	3.06	3.44	4.37	5.09	4.99	3.86	4.17	3.84
K_2O	0.02	0.02	0.62	1.09	0.78	2.14	1.36	1.43	3.49	2.36	1.85
TiO_2	0.74	1.51	1.19	0.96	0.67	0.26	0.46	0.48	0.44	0.36	0.27
P_2O_5	0.104	0.117	0.214	0.420	0.170	0.109	0.176	0.143	0.170	0.118	0.078
L.O.I	9.04	3.32	1.57	4.84	2.36	1.18	0.84	0.79	0.94	0.67	1.32
SUM	98.66	100.36	99.77	98.45	101.05	101.45	100.18	100.42	99.75	99.92	99.82
As ppm	b.d.l.	<5	b.d.l.	<7	<5	<7	14	5	6	7	5
Ba	32	36	157	290	492	711	419	495	780	1080	684
Ce	nd	34	32	nd	<20	nd	56	56	80	94	52
Cr	b.d.l.	132	247	59	94	16	<10	14	12	15	24
Cu	101	101	42	<4	32	9	23	23	11	<10	21
Dy	nd	nd	3.2	nd	nd	nd	1.1	nd	6.7	1.7	0.8
Eu	nd	nd	1.4	nd	nd	nd	0.8	nd	1.8	0.9	0.6
Ga	9	19	15	18	15	18	20	26	24	26	21
Gd	nd	nd	1.6	nd	nd	nd	1.6	nd	6.5	2.6	1.4
Er	nd	nd	1.5	nd	nd	nd	0.6	nd	4.5	0.9	0.4
Hf	b.d.l.	3	4	b.d.l.	3	b.d.l.	3	4	8.1	3.3	2.3
Ho	nd	nd	0.6	nd	nd	nd	0.2	nd	nd	nd	0.1
La	nd	<20	12.5	nd	<20	nd	11.0	nd	32.9	31.4	12.5
Lu	nd	nd	0.2	nd	nd	nd	0.1	0.10	0.6	0.1	0.1
Nb	0	10	5	0	3	0	3	0	6	4	3
Nd	50	18	19	60	15	87	85	<10	44	26	<10
Ni	16	83	89	24	17	<10	<10	9	<8	<8	<8
Pb	<10	b.d.l.	<10	<10	b.d.l.	<10	<10	b.d.l.	<10	<10	b.d.l.
Pr	nd	nd	2.7	nd	nd	nd	2.2	nd	9.3	6	2.4
Rb	5	10	15	21	15	65	24	31	80	58	55
Sb	3.9	<3	<3	4.8	<3	3.6	3.9	5	4.8	4	4.5
Sc	b.d.l.	52	26	b.d.l.	26	b.d.l.	b.d.l.	<10	<10	<10	b.d.l.
Sm	b.d.l.	b.d.l.	3	b.d.l.	b.d.l.	b.d.l.	2.1	b.d.l.	8.4	4.3	2
Sr	87	434	685	490	515	446	643	703	252	568	517
Th	b.d.l.	<5	b.d.l.	b.d.l.	b.d.l.	<8.0	<8.0	b.d.l.	6	<5	b.d.l.
Tl	b.d.l.	b.d.l.	b.d.l.	b.d.l.	b.d.l.	<2.5	<2.5	<2.5	<2.5	<2.5	<2.5
V	284	393	189	158	191	32	55	71	36	43	35
Y	0	29	19	0	17	0	0	10	39	10	10
Yb	nd	nd	1.6	nd	nd	nd	0.6	0.6	4	0.8	0.4
Zn	50	98	54	67	77	37	40	52	77	49	39
Zr	44	100	132	141	89	99	142	161	299	153	115

nd: not determined b.d.l.: below detection limit

Table a.4 cont.

Sample	8.5	8.5a	3.11k	8.4c
SiO_2 %	73.53	74.17	76.77	75.85
Al_2O_3	14.21	13.45	12.83	12.61
Fe_2O_3	1.58	1.52	0.26	1.07
MnO	0.054	0.037	0.010	0.037
MgO	0.20	0.55	0.16	0.40
CaO	1.61	1.65	0.69	1.10
Na_2O	3.77	4.03	5.20	3.70
K_2O	3.73	4.02	3.60	4.74
TiO_2	0.27	0.26	<0.02	0.2
P_2O_5	0.078	0.111	0.028	0.086
L.O.I	0.34	0.13	0.83	0.43
SUM	99.33	99.12	100.51	100.04
As ppm	6	11	17	8
Ba	903	843	62	590
Ce	82	nd	nd	nd
Cr	<10	<10	<10	<10
Cu	11	9	<4	b.d.l.
Dy	nd	nd	nd	nd
Eu	nd	nd	nd	nd
Ga	18	15	36	16
Gd	nd	nd	nd	nd
Er	nd	nd	nd	nd
Hf	4	b.d.l.	b.d.l.	b.d.l.
Ho	nd	nd	nd	nd
La	44.0	44.0	nd	nd
Lu	nd	nd	nd	nd
Nb	0	11	0	0
Nd	29	86	107	99
Ni	<8	<10	<10	<10
Pb	<10	15	37	17
Pr	nd	nd	nd	nd
Rb	43	41	517	88
Sb	3.8	3.8	4.8	5.4
Sc	<10	b.d.l.	b.d.l.	b.d.l.
Sm	b.d.l.	b.d.l.	b.d.l.	b.d.l.
Sr	327	306	18	187
Th	8	10.3	21.9	8.8
Tl	b.d.l.	<2.5	3.4	<2.5
V	26	21	15	17
Y	10	0	0	0
Yb	nd	nd	nd	nd
Zn	33	26	b.d.l.	22
Zr	121	107	92	83

Table a.5: XRF major and trace elements data of the high-grade metamorphic rocks of the KPTA.

Sample	**12.2a**	**12.1c**	**6.8**	**8.9**	**8.11a**	**8.12a**	**11.15**	**12.2b**
SiO2 %	79.95	75.62	73.63	73.20	71.41	71.31	67.13	60.23
Al_2O_3	13.40	13.87	14.27	14.56	15.55	15.48	14.95	13.05
Fe_2O_3	2.73	0.96	0.96	0.93	1.30	1.35	3.60	7.55
MgO	0.55	0.33	0.26	0.36	0.61	0.76	1.93	1.21
MnO	0.0481	0.0079	0.0243	0.0062	0.0096	0.0101	0.0356	0.1264
CaO	1.51	1.61	1.34	2.15	3.02	2.97	4.19	14.86
Na_2O	4.28	4.28	4.35	5.23	5.98	5.59	4.20	0.36
K_2O	4.09	4.30	4.11	2.08	0.98	1.05	1.46	0.03
TiO_2	0.41	0.14	0.12	0.17	0.28	0.30	0.55	1.48
P_2O_5	0.161	0.078	0.041	0.078	0.110	0.152	0.219	0.490
SO_3	0.036	b.d.l.	0.042	<0.010	b.d.l.	b.d.l.	b.d.l.	b.d.l.
L.O.I.	0.65	0.81	0.54	0.54	0.62	0.64	0.76	0.44
Total	101.26	100.48	99.35	99.17	99.70	99.40	98.60	101.12
Ag ppm	<2.0	2.30	<2.0	<2.0	<2.0	<2.0	b.d.l.	<2.0
As	<7	18	<7	10	11	<7	11	9
Ba	1277	806	365	748	307	301	424	110
Br	<4.0	<4.0	<4.0	<4.0	<4.0	<4.0	<4.0	<4.0
Co	101	143	92	118	111	75	88	88
Cu	4	17	b.d.l.	<4	<4	<4	42	9
Cr	<10	15	12	<10	<10	<10	15	b.d.l.
Ga	19	16	20	21	17	20	16	19
Ni	b.d.l.	10	<10	<10	<10	<10	13	<10
Pb	<10	20	14	<10	<10	b.d.l.	b.d.l.	14
Rb	57	52	123	33	22	26	39	<5
Sb	3.9	3.2	3.7	4.5	5.5	5.1	3.5	<3.0
Se	b.d.l.	b.d.l.	b.d.l.	b.d.l.	<3.0	b.d.l.	<3.0	<3.0
Sr	221	494	115	504	658	642	295	1437
Th	30.7	<8.0	<8.0	<8.0	<8.0	<8.0	b.d.l.	<8.0
Tl	<2.5	<2.5	<2.5	<2.5	<2.5	<2.5	<2.5	b.d.l.
U	<5.0	<5.0	<5.0	<5.0	b.d.l.	b.d.l.	b.d.l.	<5.0
V	17	12	10	<10	23	21	64	215
Zn	73	<10	26	33	28	29	39	23
Zr	439	98	55	83	99	121	67	246
CIA	*48.50*	*48. 5*	*50. 8*	*49.*	*48.*	*49.5*	*48.11*	*.0*

b.d.l.: below detection level

Table a.6: XRF major and trace elements data of the metavolcanics from the KPTA.

Sample	**6.3**	**5.1e**	**6.1b**	**5.2**	**5.3**	**5.1c**	**5.1a**	**5.1d**
SiO2	49.33	52.83	50.66	52.60	53.09	57.02	61.50	71.16
Al2O3	11.65	13.78	14.18	15.12	15.41	15.72	16.03	10.82
Fe2O3	13.87	6.12	16.00	4.70	6.87	4.92	3.05	4.41
MnO	0.001	0.001	0.002	0.002	0.002	0.002	0.002	0.001
MgO	9.50	3.28	8.69	2.33	4.30	2.46	1.27	1.81
CaO	9.42	10.54	1.7	11.09	6.26	7.34	6.99	3.13
Na2O	2.35	3.81	1.62	3.65	4.96	4.01	2.69	4.53
K2O	0.06	0.83	0.02	1.24	0.54	1.39	2.53	0.08
TiO2	1.23	0.61	1.54	0.44	0.59	0.54	0.29	0.31
P2O5	0.098	0.408	0.216	0.149	0.174	0.159	0.171	0.096
SO3	b.d.l.	b.d.l.	0.038	0.09	0.016	0.01	b.d.l.	0.073
L.O.I.	2.77	7.14	4.56	7.16	6.21	6.99	4.57	4.48
Total	100.13	99.19	99.22	98.38	98.30	100.42	98.91	100.65
Ag ppm	b.d.l.	2	b.d.l.	b.d.l.	2	2	2	2
As	18	7	14	8	7	7	7	7
Ba	20	241	36	439	726	625	637	27
Bi	4.20	b.d.l.	6.9	b.d.l.	b.d.l.	b.d.l.	b.d.l.	b.d.l.
Br	4	4	4	4	4	4	4	4.4
Cu	161	b.d.l.	176	21	57	26	13	12
Cr	169	90	b.d.l.	10	59	10	10	10
Ga	14	14	19	15	18	15	18	11
Ni	94	65	46	11	31	17	10	10
Pb	b.d.l.	10	b.d.l.	10	10	10	10	b.d.l.
Rb	5	19	5	21	9	28	47	5
Sb	3	3.4	3	3	5.6	4.7	5.3	3.7
Se	3	b.d.l.	3.2	3	b.d.l.	b.d.l.	3	b.d.l.
Sr	161	465	55	650	372	423	620	181
Th	b.d.l.	8	8	b.d.l.	b.d.l.	8	8	b.d.l.
Tl	b.d.l.	b.d.l.	b.d.l.	b.d.l.	2.5	b.d.l.	2.5	b.d.l.
U	5	5	b.d.l.	5	5	5	5	b.d.l.
V	284	77	458	109	151	154	46	30
Zn	79	73	102	45	77	48	31	47
Zr	74	135	109	81	87	99	106	64

b.d.l.: below detection limit

Table a.7: XRF major and trace elements data of the siliciclastic low-grade metasediments of the KPTA.

Sample	**10.2c**	**1.2a**	**10.10b**	**5.10**	**10.10a**	**11.9a**	**10.2a**	**10.3a**	**7.6**	**7.16**	**5.5**
SiO_2 %	75.76	71.38	74.55	71.83	73.31	67.93	71.35	67.30	41.87	63.15	57.39
Al_2O_3	12.49	14.04	12.84	10.92	13.06	13.75	13.59	13.72	11.25	14.19	14.40
Fe_2O_3	1.20	1.38	1.47	4.45	1.73	4.22	1.71	4.07	15.16	8.65	6.66
MgO	0.28	0.37	0.68	1.74	0.52	2.10	0.46	1.40	7.33	5.15	4.94
MnO	0.061	0.031	0.047	0.069	0.083	0.128	0.076	0.121	0.226	0.123	0.095
CaO	0.99	1.05	1.18	3.16	1.34	2.69	1.89	3.66	11.77	0.91	5.19
Na_2O	4.55	4.45	4.66	4.57	4.35	5.16	4.24	5.02	b.d.l.	0.67	4.11
K_2O	4.13	3.21	3.44	0.09	3.64	0.72	2.69	1.68	<0.02	2.39	0.80
TiO_2	0.18	0.19	0.21	0.31	0.25	0.42	0.32	0.63	1.65	1.00	0.71
P_2O_5	0.047	0.084	0.081	0.097	0.101	0.134	0.070	0.215	0.164	0.389	0.190
SO_3	0.034	0.076	0.020	0.074	<0.010	0.016	0.038	0.031	0.013	0.013	0.022
L.O.I.	0.96	4.26	1.36	3.29	1.32	3.49	1.87	1.47	10.80	1.42	6.17
Total	100.50	100.43	100.41	100.28	99.56	100.49	98.22	99.20	99.73	98.27	100.46
Ag (ppm)	b.d.l.	<2.0	<2.0	<2.0	2.10	<2.0	<2.0	<2.0	<2.0	<2.0	<2.0
As	<7	10	<7	<7	9	13	<7	<7	12	<7	b.d.l.
Ba	800	945	555	27	623	144	592	616	<20	481	303
Bi	b.d.l.	b.d.l.	b.d.l.	b.d.l.	b.d.l.	b.d.l.	b.d.l.	b.d.l.	4.4	b.d.l.	b.d.l.
Br	<4.0	<4.0	<4.0	4.4	<4.0	<4.0	<4.0	<4.0	<4.0	<4.0	<4.0
Cu	<4	9	<4	12	4	25	54	<4	131	6	25
Cr	13	16	11	<10	<10	19	<10	<10	19	58	56
Cs	b.d.l.	b.d.l.	b.d.l.	b.d.l.	b.d.l.	b.d.l.	b.d.l.	b.d.l.	b.d.l.	b.d.l.	b.d.l.
Ga	18	15	14	11	16	14	13	18	10	20	15
Ni	<10	<10	<10	<10	<10	<10	<10	<10	74	50	58
Pb	<10	<10	<10	b.d.l.	<10	<10	<10	13	<10	<10	<10
Rb	67	75	63	<5	63	16	42	31	<5	56	16
Sb	4.2	4.5	4.8	3.7	4.9	5.1	4.3	4.5	<3.0	5.0	5.9
Se	b.d.l.	<3.0	b.d.l.	b.d.l.	b.d.l.	<3.0	b.d.l.	b.d.l.	<3.0	<3.0	b.d.l.
Sr	80	236	80	181	<10.0	473	139	328	69	82	114
Th	<8.0	<8.0	<8.0	b.d.l.	<8.0	<8.0	<8.0	<8.0	<8.0	<8.0	<8.0
Tl	<2.5	b.d.l.	b.d.l.	b.d.l.	b.d.l.	<2.5	b.d.l.	b.d.l.	b.d.l.	<2.5	b.d.l.
U	<5.0	<5.0	<5.0	b.d.l.	<5.0	<5.0	<5.0	<5.0	<5.0	<5.0	<5.0
V	11	17	14	30	17	78	25	56	375	165	166
Zn	30	26	28	47	400	47	158	80	94	126	88
Zr	149	123	99	64	36	128	236	251	89	178	114

b.d.l.: below detection limit

Table a.7 Cont.

Sample	**3.11d**	**7.6**	**11.9b**	**3.2**
SiO_2 %	45.96	42.87	60.75	40.56
Al_2O_3	b.d.l.	11.19	16.08	12.90
Fe_2O_3	0.04	15.16	6.62	2.66
MgO	18.07	7.33	3.57	23.65
MnO	0.013	0.226	0.102	1.63
CaO	24.96	11.75	3.35	2.66
Na_2O	b.d.l.	b.d.l.	3.42	0.66
K_2O	<0.02	<0.02	1.36	0.35
TiO_2	0.03	1.65	0.67	0.173
P_2O_5	0.018	0.164	0.214	<0.010
SO_3	0.041	0.013	b.d.l.	<2.0
L.O.I.	11.47	10.80	4.19	14.31
Total	100.22	100.73	99.18	98.64
Ag (ppm)	b.d.l.	<2.0	<2.0	9
As	<7	12	10	261
Ba	<20	<20	306	b.d.l.
Bi	b.d.l.	4.4	<3.0	b.d.l.
Br	b.d.l.	<4.0	<4.0	14
Cu	b.d.l.	131	36	32
Cr	16	19	33	b.d.l.
Cs	b.d.l.	b.d.l.	b.d.l.	10
Ga	b.d.l.	10	18	0.073
Ni	19	74	16	14
Pb	b.d.l.	<10	<10	<10
Rb	<5	<5	30	11
Sb	3.7	<3.0	6.2	3.4
Se	b.d.l.	<3.0	b.d.l.	<3.0
Sr	392	69	445	1100
Th	b.d.l.	<8.0	<8.0	b.d.l.
Tl	b.d.l.	b.d.l.	b.d.l.	b.d.l.
U	<5.0	<5.0	<5.0	b.d.l.
V	<10	375	108	54
Zn	b.d.l.	94	77	24
Zr	11	89	158	66

Table a.8: XRF major and trace elements analysis of the carbonate rich metasediments from the KPTA.

	Marbles										
Sample	**12.2c**	**4.4**	**4.1**	**4.3.2**	**2.2c**	**3.3**	**2.4.3**	**2.6.1**	**12.1**	**4.6**	**2.4.5**
SiO_2 %	0.90	2.15	1.99	1.92	1.34	1.51	3.70	12.62	2.42	3.81	10.71
Al_2O_3	<0.10	0.50	0.58	0.52	<0.10	0.46	1.37	3.25	0.30	1.04	2.74
Fe_2O_3	0.12	0.24	0.27	0.26	0.13	0.17	0.49	1.61	0.20	0.86	1.07
MgO	2.10	0.49	0.66	0.79	2.64	0.60	0.29	1.24	3.62	0.63	0.40
MnO	<0.004	<0.005	<0.006	<0.007	<0.008	<0.009	0.032	0.017	0.01	0.016	0.019
CaO	51.89	50.75	51.19	50.83	49.66	50.65	48.57	43.65	48.36	46.58	44.66
Na_2O	b.d.l.	b.d.l.	b.d.l.	b.d.l.	b.d.l.	b.d.l.	b.d.l.	0.30	b.d.l.	<0.10	0.30
K_2O	<0.02	0.04	0.03	0.05	<0.02	0.03	0.26	0.31	0.06	0.09	0.11
TiO_2	<0.02	0.04	0.03	0.03	<0.02	0.03	0.07	0.19	0.02	0.09	0.11
P_2O_5	0.019	0.030	0.031	0.042	0.056	0.028	0.037	0.110	0.020	0.036	0.078
SO_3	b.d.l.	b.d.l.	b.d.l.	0.014	<0.010	b.d.l.	<0.010	0.040	0.202	0.040	0.018
L.O.I.	44.86	45.06	44.58	45.14	45.80	44.38	44.46	35.41	45.09	43.38	40.23
Total	99.31	98.87	98.88	99.16	99.16	99.27	98.60	98.38	99.78	98.26	99.05
Ag ppm	b.d.l.	b.d.l.	b.d.l.	3.30	b.d.l.	b.d.l.	b.d.l.	2.9	b.d.l.	<2.0	b.d.l.
As	<7	<7	10	<7	<7	9	11	<7	<7	12	15
Ba	61	22	54	32	96	25	178	127	79	79	81
Bi	b.d.l.	b.d.l.	b.d.l.	b.d.l.	b.d.l.	b.d.l.	b.d.l.	b.d.l.	b.d.l.	b.d.l.	b.d.l.
Br	b.d.l.	b.d.l.	<4.0	<4.0	b.d.l.	b.d.l.	<4.0	<4.0	<4.0	<4.0	<4.0
Cu	<4	b.d.l.	b.d.l.	b.d.l.	b.d.l.	b.d.l.	b.d.l.	17	b.d.l.	b.d.l.	4
Cr	11	13	13	<10	34	<10	13	24	16	36	<10
Cs	b.d.l.	b.d.l.	b.d.l.	b.d.l.	5.40	b.d.l.	b.d.l.	b.d.l.	b.d.l.	b.d.l.	b.d.l.
Ga	b.d.l.	b.d.l.	b.d.l.	b.d.l.	b.d.l.	b.d.l.	<3	<3	b.d.l.	<3	<3
Ni	<10	<10	<10	<10	94	b.d.l.	11	14	<10	<10	<10
Pb	b.d.l.	b.d.l.	b.d.l.	b.d.l.	b.d.l.	b.d.l.	b.d.l.	<10	<10	<10	<10
Rb	6	7	5	5	<5	<5	9	12	7	6	6
Sb	b.d.l.	<3.0	3.9	<3.0	<3.0	<3.0	<3.0	<3.0	<3.0	<3.0	<3.0
Se	<3.0	<3.0	<3.0	<3.0	<3.0	<3.0	b.d.l.	<3.0	<3.0	<3.0	<3.0
Sr	1735	2249	2256	2805	2211	2129	757	1011	2390	2260	1370
Th	b.d.l.	b.d.l.	b.d.l.	b.d.l.	b.d.l.	b.d.l.	b.d.l.	<8.0	b.d.l.	b.d.l.	b.d.l.
Tl	b.d.l.	b.d.l.	b.d.l.	b.d.l.	b.d.l.	b.d.l.	b.d.l.	b.d.l.	b.d.l.	b.d.l.	b.d.l.
U	b.d.l.	b.d.l.	b.d.l.	<5.0	b.d.l.	b.d.l.	<5.0	<5.0	b.d.l.	b.d.l.	<5.0
V	<10	14	12	14	<10	17	24	61	<10	23	62
Zn	b.d.l.	b.d.l.	b.d.l.	<10	b.d.l.	b.d.l.	<10	14	b.d.l.	<10	<10
Zr	28	40	38	45	34	35	29	43	37	51	37

b.d.l.= below detection level

	Marbles								Dolomites		
Sample	**2.5.1**	**5.12**	**4.3.1**	**3.13a**	**2.4.4**	**2.4.1**	**3.5**	**3.2**	**3.7**	**3.9c**	**5.6**
SiO_2 %	6.23	7.13	7.71	5.67	14.84	11.61	16.06	38.56	7.65	2.83	0.87
Al_2O_3	1.64	2.57	0.58	1.82	4.35	3.64	5.84	10.09	<0.10	0.26	0.15
Fe_2O_3	1.45	1.57	0.39	1.15	1.93	1.41	5.37	2.66	0.04	0.19	0.05
MgO	0.73	0.56	4.25	0.98	0.54	4.68	3.28	1.63	18.89	18.51	17.43
MnO	0.077	0.0349	0.076	0.03	0.044	0.123	0.285	0.073	<0.004	0.004	<0.004
CaO	47.93	45.69	44.11	46.35	41.49	34.82	35.66	26.65	30.00	30.94	31.83
Na_2O	0.26	0.28	b.d.l.	0.12	0.22	<0.10	0.46	2.66	b.d.l.	b.d.l.	b.d.l.
K_2O	0.08	0.36	0.06	0.18	0.67	0.57	0.25	0.66	<0.02	<0.02	0.02
TiO_2	0.14	0.19	0.04	0.10	0.22	0.11	0.35	0.35	<0.02	<0.02	<0.02
P_2O_5	0.092	0.050	0.034	0.042	0.108	0.135	0.065	0.173	0.047	0.031	0.100
SO_3	<0.010	0.033	b.d.l.	<0.01(	0.097	b.d.l.	<0.010	<0.010	b.d.l.	b.d.l.	b.d.l.
L.O.I.	41.64	40.54	43.54	42.70	35.11	42.46	33.81	15.31	42.88	47.05	50.48
Total	99.75	98.64	100.36	98.77	99.25	99.29	100.91	98.58	99.00	99.20	100.30
Ag ppm	b.d.l.	<2.0	b.d.l.	<2.0	b.d.l.	b.d.l.	b.d.l.	<2.0	b.d.l.	<2.0	b.d.l.
As	10	21	<7	<7	9	28	b.d.l.	9	<7	11	<7
Ba	107	121	39	87	347	144	76	261	<20	<20	28
Bi	b.d.l.	b.d.l.	b.d.l.	b.d.l.	b.d.l.	b.d.l.	b.d.l.	b.d.l.	b.d.l.	b.d.l.	b.d.l.
Br	b.d.l.	<4.0	b.d.l.	<4.0	b.d.l.	b.d.l.	<4.0	b.d.l.	b.d.l.	b.d.l.	<4.0
Cu	7	<4	b.d.l.	7	24	b.d.l.	11	14	b.d.l.	b.d.l.	b.d.l.
Cr	18	25	<10	<10	35	b.d.l.	b.d.l.	32	13	12	<10
Cs	b.d.l.	<2.0	b.d.l.	b.d.l.	b.d.l.	b.d.l.	b.d.l.	b.d.l.	b.d.l.	b.d.l.	b.d.l.
Ga	<3	<3	b.d.l.	b.d.l.	3	4	9	10	<3	b.d.l.	<3
Ni	<10	11	<10	<10	17	15	<10	14	<10	<10	<10
Pb	<10	<10	b.d.l.	<10	b.d.l.	<10	17	<10	<10	b.d.l.	b.d.l.
Rb	<5	14	6	9	15	13	8	11	<5	<5	<5
Sb	<3.0	<3.0	<3.0	<3.0	3.5	<3.0	b.d.l.	3.4	<3.0	3.1	<3.0
Se	b.d.l.	<3.0	<3.0	<3.0	<3.0	<3.0	b.d.l.	<3.0	b.d.l.	b.d.l.	b.d.l.
Sr	173	1556	2940	1490	526	781	233	1100	659	318	340
Th	b.d.l.	b.d.l.	b.d.l.	b.d.l.	<8.0	<8.0	<8.0	b.d.l.	b.d.l.	b.d.l.	b.d.l.
Tl	b.d.l.	b.d.l.	b.d.l.	b.d.l.	b.d.l.	b.d.l.	b.d.l.	b.d.l.	b.d.l.	b.d.l.	b.d.l.
U	<5.0	<5.0	b.d.l.	<5.0	<5.0	b.d.l.	b.d.l.	b.d.l.	<5.0	<5.0	b.d.l.
V	46	38	25	25	152	272	129	54	<10	18	10
Zn	<10	<10	b.d.l.	<10	b.d.l.	34	70	24	b.d.l.	b.d.l.	b.d.l.
Zr	21	60	48	41	57	77	39	66	13	12	10

Table a.8 cont.

Dolomites

Sample	**9.2b**	**1.2b**	**7.7b**	**3.9**	**3.11b**	**3.11a**	**3.9b**	**2.2**
SiO_2 %	1.04	8.38	5.08	7.10	5.96	9.65	7.06	4.45
Al_2O_3	0.14	0.26	0.43	0.18	<0.10	0.14	0.18	1.07
Fe_2O_3	0.06	0.13	0.05	0.04	0.05	0.05	0.04	0.93
MgO	*19.05*	*1 .19*	*19.9*	*18. 4*	*18.59*	19.18	*19.55*	18.74
MnO	0.0048	0.009	<0.004	<0.004	<0.004	<0.004	<0.004	0.0414
CaO	30.70	34.30	29.02	29.93	29.79	29.35	28.73	27.18
Na_2O	b.d.l.	b.d.l.	b.d.l.	b.d.l.	b.d.l.	b.d.l.	b.d.l.	0.21
K_2O	b.d.l.	0.10	<0.02	<0.02	<0.02	<0.02	<0.02	0.07
TiO_2	<0.02	<0.02	<0.02	<0.02	<0.02	<0.02	<0.02	0.06
P_2O_5	0.015	0.022	0.027	0.022	0.036	0.034	0.016	0.142
SO_3	b.d.l.	<0.010	b.d.l.	b.d.l.	b.d.l.	<0.010	b.d.l.	0.067
L.O.I.	48.55	40.78	45.89	43.15	46.08	43.08	44.45	46.33
Total	98.91	99.58	99.96	98.62	99.99	100.90	99.50	98.95
Ag ppm	<2.0	<2.0	b.d.l.	<2.0	<2.0	b.d.l.	b.d.l.	b.d.l.
As	8	b.d.l.	<7	<7	<7	<7	7	10
Ba	<20	<20	<20	<20	<20	<20	<20	32
Bi	b.d.l.	b.d.l.	b.d.l.	b.d.l.	b.d.l.	b.d.l.	b.d.l.	b.d.l.
Br	<4.0	<4.0	<4.0	<4.0	<4.0	b.d.l.	<4.0	<4.0
Cu	b.d.l.	b.d.l.	b.d.l.	b.d.l.	b.d.l.	b.d.l.	b.d.l.	b.d.l.
Cr	12	<10	<10	<10	<10	<10	<10	35
Cs	b.d.l.	b.d.l.	<2.0	b.d.l.	b.d.l.	b.d.l.	b.d.l.	<2.0
Ga	b.d.l.	b.d.l.	<3	b.d.l.	<3	<3	<3	<3
Ni	<10	<10	<10	<10	<10	<10	<10	11
Pb	<10	b.d.l.	b.d.l.	b.d.l.	b.d.l.	b.d.l.	b.d.l.	<10
Rb	<5	9	<5	<5	<5	<5	<5	<5
Sb	4.1	<3.0	4.5	4.7	<3.0	3.5	<3.0	4.0
Se	b.d.l.	b.d.l.	b.d.l.	b.d.l.	b.d.l.	b.d.l.	b.d.l.	b.d.l.
Sr	478	581	596	674	253	261	685	467
Th	<8.0	<8.0	b.d.l.	<8.0	<8.0	<8.0	<8.0	<8.0
Tl	b.d.l.	b.d.l.	b.d.l.	b.d.l.	b.d.l.	b.d.l.	b.d.l.	b.d.l.
U	b.d.l.	b.d.l.	b.d.l.	b.d.l.	<5.0	<5.0	<5.0	b.d.l.
V	<10	<10	<10	<10	42	35	<10	26
Zn	b.d.l.	<10	b.d.l.	b.d.l.	b.d.l.	b.d.l.	b.d.l.	<10
Zr	11	13	14	13	<10	11	14	20

Table a.9: Microprobe analysis data of the amphiboles from the KPTA. Structural formula is calculated on the basis of 23 oxygen.

	Rock: Diorite (sample 1.1)											
Point No.	**#64**	**#65**	**#67**	**#68**	**#69**	**#70**	**#71**	**#72**	**#81**	**#82**	**#83**	**#84**
SiO_2	42.24	49.73	45.06	43.25	46.56	43.23	49.35	46.68	49.47	44.40	42.59	43.13
TiO_2	1.42	1.27	1.90	3.62	2.16	3.19	0.91	1.51	1.01	2.07	3.08	2.64
Al_2O_3	15.81	6.31	9.90	11.37	9.29	11.24	6.44	8.36	6.38	9.56	11.28	11.06
Cr_2O_3	0.06	0.10	0.06	0.08	0.01	0.02	0.08	0.04	0.04	0.05	0.07	0.08
Fe_2O_3	0.00	0.45	0.68	0.82	1.75	1.96	2.33	3.11	2.04	3.06	2.04	2.55
FeO	11.73	11.04	11.88	13.22	11.37	12.44	10.68	10.40	9.22	11.02	11.58	11.22
MnO	0.20	0.29	0.20	0.26	0.11	0.25	0.22	0.22	0.18	0.25	0.22	0.26
MgO	6.06	14.04	12.31	11.54	13.10	11.41	14.25	13.19	15.00	12.32	11.47	11.93
CaO	17.02	11.89	11.55	12.02	11.99	11.62	12.27	11.86	12.08	11.79	11.57	11.98
Na_2O	0.62	0.89	1.64	1.93	1.53	1.92	0.92	1.21	0.88	1.54	1.76	1.40
K_2O	0.24	0.32	0.75	0.53	0.42	0.59	0.49	0.53	0.47	0.50	0.43	0.80
Total	97.88	98.57	97.95	100.94	100.36	100.85	100.0	99.29	99.11	99.03	98.1	99.8
Si	6.365	7.268	6.720	6.351	6.756	6.387	7.144	6.851	7.183	6.607	6.383	6.407
Ti	0.161	0.140	0.214	0.400	0.236	0.354	0.099	0.166	0.110	0.232	0.348	0.295
Al^{IV}	1.635	0.732	1.280	1.649	1.244	1.613	0.856	1.149	0.817	1.393	1.617	1.593
Al^{VI}	1.172	0.355	0.460	0.318	0.345	0.345	0.243	0.296	0.274	0.284	0.374	0.343
Cr	0.007	0.011	0.007	0.010	0.001	0.002	0.009	0.005	0.005	0.006	0.008	0.009
Fe^{3+}	0.000	0.049	0.076	0.091	0.191	0.218	0.254	0.343	0.223	0.343	0.231	0.285
Fe^{2+}	1.478	1.350	1.481	1.624	1.380	1.538	1.293	1.276	1.120	1.371	1.451	1.394
Mn^{2+}	0.026	0.036	0.026	0.032	0.013	0.031	0.026	0.028	0.023	0.031	0.028	0.033
Mg	1.360	3.059	2.737	2.526	2.834	2.512	3.076	2.885	3.246	2.733	2.562	2.641
Ca	2.747	1.862	1.846	1.891	1.863	1.840	1.902	1.864	1.879	1.879	1.858	1.906
Na	0.182	0.253	0.474	0.549	0.431	0.551	0.257	0.345	0.249	0.444	0.510	0.403
K	0.045	0.060	0.143	0.099	0.077	0.111	0.090	0.099	0.088	0.094	0.083	0.152
$Mg^{\#}$	0.479	0.694	0.649	0.609	0.673	0.620	0.704	0.693	0.743	0.666	0.638	0.655
Total	17.180	17.175	17.464	17.539	17.371	17.501	17.249	17.308	17.216	17.418	17.451	17.460

	Table a.9 cont.			*Sample 1.1*							
Point No.	**#86**	**#87**	**#88**	**#89**	**#90**	**#91**	**#92**	**#93**	**#94**	**#95**	**#96**
SiO_2	42.02	42.71	42.49	50.13	54.97	49.84	47.66	49.02	53.08	49.70	54.78
TiO_2	2.70	3.30	3.32	0.87	0.00	1.18	1.22	0.80	0.51	1.20	0.08
Al_2O_3	10.95	11.06	11.13	5.68	1.74	6.28	7.87	6.77	3.43	6.30	1.89
Cr_2O_3	0.03	0.12	0.06	0.05	0.00	0.03	0.10	0.09	0.02	0.07	0.09
Fe_2O_3	1.67	1.80	2.80	2.59	0.00	2.41	2.76	1.86	0.07	1.89	0.00
FeO	13.13	12.60	11.26	9.36	11.19	9.99	10.20	10.33	10.20	10.30	10.78
MnO	0.24	0.30	0.23	0.32	0.14	0.18	0.24	0.20	0.23	0.31	0.24
MgO	10.87	11.19	11.39	15.05	16.21	14.50	13.87	14.45	15.98	14.37	16.28
CaO	11.92	11.76	11.53	12.13	12.92	11.76	12.03	12.32	12.53	11.94	12.85
Na_2O	1.43	1.76	1.58	0.84	0.15	1.06	1.18	0.92	0.32	1.02	0.14
K_2O	0.87	0.45	0.47	0.46	0.04	0.52	0.71	0.55	0.11	0.38	0.04
Total	97.83	99.19	98.32	99.81	99.82	100.23	100.69	99.37	98.54	100.5	100.24
Si	6.381	6.372	6.361	7.242	7.870	7.192	6.930	7.126	7.658	7.195	7.849
Ti	0.308	0.370	0.373	0.094	0.000	0.128	0.133	0.087	0.055	0.131	0.009
Al^{IV}	1.619	1.628	1.639	0.758	0.130	0.808	1.070	0.874	0.342	0.805	0.151
Al^{VI}	0.340	0.316	0.325	0.208	0.163	0.259	0.279	0.287	0.241	0.270	0.168
Cr	0.004	0.014	0.007	0.006	0.000	0.003	0.011	0.010	0.002	0.008	0.010
Fe^{3+}	0.191	0.202	0.315	0.282	0.000	0.262	0.302	0.204	0.007	0.206	0.000
Fe^{2+}	1.668	1.572	1.410	1.130	1.339	1.206	1.240	1.256	1.231	1.247	1.291
Mn^{2+}	0.030	0.037	0.029	0.039	0.016	0.022	0.029	0.025	0.028	0.038	0.029
Mg	2.459	2.488	2.541	3.241	3.458	3.120	3.005	3.132	3.436	3.101	3.476
Ca	1.939	1.880	1.849	1.878	1.981	1.818	1.874	1.919	1.937	1.852	1.972
Na	0.422	0.509	0.458	0.234	0.042	0.297	0.333	0.259	0.089	0.286	0.040
K	0.168	0.085	0.090	0.084	0.008	0.096	0.131	0.102	0.020	0.070	0.008
$Mg^{\#}$	0.596	0.613	0.643	0.741	0.721	0.721	0.708	0.714	0.736	0.713	0.729
Total	17.530	17.475	17.397	17.196	17.009	17.210	17.337	17.280	17.046	17.208	17.002

Table a.9 cont. ***Rock:Amphibolite (Sample A55)***

Point No.	#139	#140	#141	#147	#148	#149	#150	#151	#152	#153	#156	#157
SiO_2	49.47	48.26	49.28	49.37	49.28	49.44	48.69	48.85	51.22	49.04	48.11	49.03
TiO_2	0.43	0.40	0.43	0.29	0.41	0.37	0.53	0.47	0.33	0.38	0.50	0.49
Al_2O_3	9.22	10.19	9.63	9.30	9.58	9.55	10.06	10.15	7.23	10.15	10.20	9.80
Cr_2O_3	0.15	0.23	0.18	0.21	0.17	0.19	0.16	0.16	0.12	0.12	0.43	0.24
Fe_2O_3	1.49	1.69	0.89	0.18	0.86	0.97	1.02	1.00	0.18	0.15	0.31	0.76
FeO	8.70	8.47	9.40	10.02	9.29	9.29	9.54	9.32	9.18	9.89	10.16	9.37
MnO	0.20	0.17	0.20	0.12	0.22	0.15	0.23	0.10	0.10	0.20	0.11	0.22
MgO	14.52	13.89	14.47	14.49	14.62	14.51	14.07	14.22	15.47	14.25	13.90	14.30
CaO	12.13	11.79	12.46	12.70	12.59	12.40	12.33	12.36	12.35	12.52	12.57	12.41
Na_2O	1.09	1.21	1.18	1.06	1.15	1.17	1.25	1.14	0.91	1.24	1.21	1.13
K_2O	0.15	0.14	0.16	0.14	0.13	0.14	0.16	0.17	0.10	0.16	0.16	0.14
Total	99.65	99.82	100.4	100.17	101.34	100.28	100.27	100.06	99.37	100.4	99.75	99.98
Si	7.068	6.975	7.011	7.058	7.008	7.034	6.957	6.969	7.314	6.992	6.920	7.001
Ti	0.047	0.043	0.047	0.032	0.044	0.040	0.057	0.051	0.036	0.041	0.054	0.052
Al^{IV}	0.932	1.025	0.989	0.942	0.992	0.966	1.043	1.031	0.686	1.008	1.080	0.999
Al^{VI}	0.620	0.710	0.626	0.625	0.614	0.635	0.651	0.676	0.531	0.697	0.648	0.650
Cr	0.017	0.026	0.020	0.024	0.019	0.021	0.018	0.018	0.013	0.014	0.049	0.028
Fe^{3+}	0.160	0.184	0.096	0.020	0.092	0.104	0.110	0.107	0.019	0.016	0.033	0.082
Fe^{2+}	1.040	1.024	1.118	1.198	1.104	1.105	1.140	1.112	1.096	1.179	1.222	1.119
Mn^{2+}	0.024	0.021	0.024	0.014	0.027	0.018	0.028	0.012	0.012	0.024	0.013	0.026
Mg	3.092	2.992	3.068	3.087	3.100	3.077	2.996	3.023	3.293	3.029	2.981	3.043
Ca	1.856	1.826	1.899	1.945	1.919	1.890	1.887	1.890	1.890	1.913	1.937	1.898
Na	0.302	0.340	0.325	0.294	0.318	0.322	0.345	0.316	0.253	0.343	0.338	0.314
$Mg^{\#}$	0.748	0.745	0.733	0.720	0.737	0.736	0.724	0.731	0.750	0.720	0.709	0.731
K	0.027	0.026	0.030	0.025	0.023	0.025	0.030	0.031	0.019	0.029	0.029	0.025
Total	17.184	17.192	17.254	17.265	17.260	17.237	17.263	17.237	17.162	17.285	17.305	17.236

Table a.9 cont.

	Sample A55				***Rock: Metasediment (Sample A45)***						
Point No.	#158	#159	#160	#161	#164	#165	#166	#168	#169	#170	#186
SiO_2	48.75	49.23	48.47	49.06	43.42	43.89	43.94	44.54	44.62	45.69	43.86
TiO_2	0.50	0.51	0.40	0.45	0.47	0.53	0.56	0.50	0.42	0.55	0.45
Al_2O_3	10.14	10.16	10.11	9.92	14.52	14.16	14.30	13.78	14.10	13.44	14.61
Cr_2O_3	0.26	0.09	0.10	0.11	0.02	0.00	0.05	0.08	0.06	0.03	0.03
Fe_2O_3	0.00	1.01	0.31	0.00	9.07	8.68	8.68	8.53	8.45	11.78	9.10
FeO	10.38	9.39	10.02	9.93	6.43	7.00	6.66	7.21	7.33	4.45	6.72
MnO	0.10	0.18	0.14	0.11	0.21	0.15	0.18	0.21	0.23	0.26	0.24
MgO	14.07	14.34	14.05	13.94	10.67	10.96	10.94	10.99	10.65	11.02	10.74
CaO	12.63	12.39	12.44	12.32	10.03	10.26	10.19	10.06	9.94	9.11	10.16
Na_2O	1.23	1.24	1.30	1.21	2.07	2.15	2.05	2.30	2.21	1.85	2.15
K_2O	0.19	0.19	0.15	0.17	0.16	0.20	0.17	0.18	0.19	0.19	0.17
Total	100.9	100.86	99.59	99.31	99.42	100.5	100.41	101.61	101.7	102.57	100.95
Si	6.961	6.971	6.968	7.046	6.329	6.352	6.360	6.418	6.434	6.513	6.328
Ti	0.054	0.054	0.043	0.048	0.052	0.058	0.061	0.054	0.046	0.059	0.049
Al^{IV}	1.039	1.029	1.032	0.954	1.671	1.648	1.640	1.582	1.566	1.487	1.672
Al^{VI}	0.667	0.667	0.681	0.727	0.823	0.767	0.800	0.757	0.830	0.772	0.811
Cr	0.029	0.010	0.012	0.013	0.002	0.000	0.005	0.009	0.007	0.003	0.004
Fe^{3+}	0.000	0.108	0.033	0.000	0.995	0.945	0.945	0.925	0.916	1.264	0.988
Fe^{2+}	1.240	1.112	1.204	1.193	0.784	0.848	0.806	0.869	0.884	0.531	0.810
Mn^{2+}	0.012	0.022	0.017	0.013	0.026	0.018	0.022	0.025	0.028	0.031	0.029
Mg	2.994	3.027	3.010	2.985	2.318	2.365	2.360	2.361	2.289	2.341	2.309
Ca	1.933	1.880	1.915	1.897	1.566	1.590	1.579	1.554	1.535	1.392	1.570
Na	0.339	0.341	0.362	0.336	0.585	0.602	0.576	0.643	0.616	0.511	0.601
$Mg^{\#}$	0.707	0.731	0.714	0.714	0.747	0.736	0.745	0.731	0.721	0.815	0.740
K	0.035	0.035	0.027	0.031	0.030	0.038	0.032	0.033	0.036	0.035	0.031
Total	17.304	17.256	17.305	17.243	17.181	17.230	17.187	17.230	17.187	16.938	17.202

Table a.9 cont.

	Sample A45								*Metasediment (A26)*		
Point No.	**#187**	**#188**	**#189**	**#190**	**#202**	**#212**	**#213**	**#214**	**#46**	**#47**	**#48**
SiO_2	43.35	42.83	43.36	43.68	43.68	44.48	43.63	44.69	41.01	40.95	40.78
TiO_2	0.38	0.34	0.51	0.51	0.49	0.57	0.45	0.66	0.87	0.79	0.77
Al_2O_3	15.02	15.51	14.88	14.83	13.65	13.25	12.39	13.71	15.32	15.05	15.24
Cr_2O_3	0.01	0.05	0.03	0.00	0.04	0.05	0.00	0.10	0.00	0.00	0.05
Fe_2O_3	9.36	9.60	8.24	7.90	9.59	7.40	7.02	8.41	6.01	5.27	4.54
FeO	6.19	6.28	7.02	7.51	6.23	8.13	8.68	6.87	12.61	13.26	13.91
MnO	0.32	0.20	0.23	0.12	0.24	0.25	0.21	0.21	0.17	0.11	0.21
MgO	10.56	10.52	10.57	10.64	10.90	10.96	10.62	11.01	7.81	7.75	7.36
CaO	10.02	10.12	10.16	10.23	9.85	10.32	10.13	10.03	10.98	11.05	11.09
Na_2O	2.10	2.25	2.14	2.20	2.16	2.18	2.21	2.01	1.39	1.35	1.43
K_2O	0.19	0.21	0.20	0.23	0.22	0.20	0.18	0.21	0.83	0.93	0.75
Total	101.57	99.98	100.5	101.21	99.36	101.73	98.30	101.32	99.68	98.62	98.10
Si	6.292	6.206	6.311	6.329	6.377	6.463	6.510	6.449	6.158	6.191	6.196
Ti	0.041	0.037	0.056	0.056	0.054	0.062	0.050	0.072	0.098	0.090	0.088
Al^{IV}	1.708	1.794	1.689	1.671	1.623	1.537	1.490	1.551	1.842	1.809	1.804
Al^{VI}	0.861	0.854	0.863	0.861	0.725	0.732	0.689	0.780	0.869	0.873	0.926
Cr	0.001	0.005	0.003	0.000	0.005	0.005	0.000	0.012	0.000	0.000	0.006
Fe^{3+}	1.022	1.046	0.902	0.861	1.053	0.809	0.788	0.913	0.679	0.599	0.519
Fe^{2+}	0.752	0.762	0.854	0.910	0.760	0.988	1.083	0.829	1.583	1.676	1.767
Mn^{2+}	0.040	0.024	0.028	0.015	0.030	0.031	0.027	0.025	0.022	0.014	0.026
Mg	2.284	2.271	2.294	2.298	2.372	2.373	2.362	2.369	1.748	1.747	1.667
Ca	1.559	1.571	1.584	1.589	1.541	1.607	1.619	1.550	1.766	1.790	1.805
Na	0.590	0.633	0.603	0.618	0.610	0.615	0.639	0.562	0.405	0.396	0.420
$Mg^{\#}$	0.015	0.015	0.015	0.015	0.016	0.016	0.016	0.016	0.012	0.012	0.011
K	0.034	0.040	0.038	0.042	0.041	0.038	0.034	0.039	0.159	0.179	0.146
Total	17.183	17.243	17.225	17.249	17.192	17.260	17.293	17.152	17.331	17.366	17.371

Table a.10: Microprobe analysis data of the feldspars from the KPTA. Structural formula is calculated on the basis of 32 oxygen.

Mineral: Feldspars

	Metavolcanic (Sample A57)			*Metasediments (Sample No. A26)*						
Point	**#12**	**#13**	**#18**	**#22**	**#23**	**#24**	**#38**	**#39**	**#49**	**#50**
SiO_2	62.47	64.38	65.19	57.93	58.68	58.34	58.47	57.69	60.75	60.22
TiO_2	0.03	0.03	0.02	0.01	0.00	0.02	0.00	0.00	0.00	0.01
Al_2O_3	18.45	16.70	17.80	25.60	26.56	25.95	26.47	27.08	25.30	24.87
Fe_2O_3	0.69	1.33	0.06	0.13	0.11	0.13	0.10	0.10	0.14	0.10
MgO	0.02	0.03	0.00	0.00	0.00	0.00	0.00	0.00	0.00	0.00
CaO	0.03	0.19	0.01	7.97	8.10	8.29	8.46	8.65	6.45	6.15
Na2O	4.14	0.44	0.68	6.63	6.86	7.04	6.48	6.60	8.06	7.85
K2O	12.42	15.63	16.02	0.12	0.12	0.05	0.08	0.08	0.07	0.08
Total	98.2	98.7	99.8	98.4	100.4	99.8	100.1	100.2	100.8	99.3
Si	2.934	3.021	3.017	2.628	2.610	2.615	2.610	2.577	2.683	2.695
Ti	0.001	0.001	0.001	0.000	0.000	0.001	0.000	0.000	0.000	0.000
Al^{IV}	1.021	0.923	0.971	1.369	1.392	1.371	1.392	1.425	1.317	1.312
Fe^{3+}	0.024	0.047	0.002	0.004	0.004	0.005	0.003	0.003	0.005	0.003
Mg	0.001	0.002	0.000	0.000	0.000	0.000	0.000	0.000	0.000	0.000
Ca	0.002	0.010	0.000	0.388	0.386	0.398	0.405	0.414	0.305	0.295
Na	0.377	0.040	0.061	0.583	0.592	0.612	0.560	0.572	0.690	0.681
K	0.744	0.936	0.946	0.007	0.007	0.003	0.004	0.004	0.004	0.005
Total	5.103	4.981	4.999	4.98	4.991	5.004	4.975	4.996	5.004	4.99
Ab	34	4	6	60	60	60	58	58	69	69
An	0	1	0	40	39	39	42	42	31	30
Or	66	95	94	1	1	0	0	0	0	0

Table a.10 cont.

	Diorite (sample 1.1)											
Point	**#57**	**#58**	**#59**	**#60**	**#61**	**#62**	**#73**	**#74**	**#75**	**#80**	**#97**	**#98**
SiO_2	60.74	60.17	54.85	55.13	53.62	61.27	61.90	66.53	66.66	64.82	64.64	64.00
TiO_2	0.01	0.03	0.02	0.07	0.03	0.03	0.00	0.03	0.00	0.00	0.00	0.03
Al_2O_3	25.17	25.50	27.08	29.18	29.55	25.14	24.70	21.69	21.61	22.38	21.15	23.23
Fe_2O_3	0.22	0.20	0.15	0.20	0.13	0.16	0.22	0.06	0.09	0.09	0.02	0.07
MgO	0.00	0.00	0.00	0.00	0.00	0.00	0.00	0.00	0.00	0.00	0.00	0.00
CaO	6.85	7.45	11.10	11.15	11.66	6.12	5.84	2.65	2.76	3.37	3.40	4.20
Na2O	7.50	7.24	5.24	5.20	4.86	8.02	7.97	10.03	10.04	9.84	9.93	9.07
K2O	0.22	0.19	0.04	0.06	0.09	0.13	0.03	0.00	0.05	0.08	0.04	0.02
Total	100.7	100.8	98.5	101.0	100.0	100.9	100.7	101.0	101.2	100.6	99.2	100.6
Si	2.685	2.662	2.511	2.461	2.424	2.699	2.725	2.892	2.893	2.841	2.873	2.806
Ti	0.000	0.001	0.001	0.002	0.001	0.001	0.000	0.001	0.000	0.000	0.000	0.001
Al^{IV}	1.311	1.330	1.461	1.535	1.575	1.305	1.281	1.111	1.105	1.156	1.108	1.200
Fe^{3+}	0.007	0.007	0.005	0.007	0.004	0.005	0.007	0.002	0.003	0.003	0.001	0.002
Mg	0.000	0.000	0.000	0.000	0.000	0.000	0.000	0.000	0.000	0.000	0.000	0.000
Ca	0.324	0.353	0.544	0.533	0.565	0.289	0.275	0.124	0.128	0.158	0.162	0.197
Na	0.642	0.621	0.465	0.450	0.426	0.685	0.680	0.845	0.845	0.836	0.855	0.771
K	0.012	0.011	0.002	0.004	0.005	0.007	0.002	0.000	0.003	0.004	0.002	0.001
Total	4.983	4.985	4.989	4.992	5.001	4.991	4.971	4.974	4.977	4.999	5.001	4.978
Ab	66	63	46	46	43	70	71	87	87	84	84	79
An	33	36	54	54	57	29	29	13	13	16	16	20
Or	1	1	0	0	1	1	0	0	0	0	0	0

Table a.10 cont.

	Granodiorite (sample 6.9)							*Gneiss (sample 11.13)*					
Point	**#103**	**#105**	**#106**	**#112**	**#113**	**#114**	**#115**	**#130**	**#131**	**#133**	**#134**	**#135**	**#136**
SiO_2	64.54	63.06	63.46	64.32	62.13	62.49	71.24	63.35	63.31	63.24	63.16	63.57	63.58
TiO_2	0.01	0.01	0.00	0.02	0.03	0.02	0.01	0.00	0.00	0.01	0.00	0.00	0.00
Al_2O_3	23.70	23.89	23.86	23.41	23.98	24.19	19.15	22.46	23.99	22.10	23.42	24.16	23.86
Fe_2O_3	0.17	0.03	0.01	0.17	0.04	0.02	0.00	0.23	0.05	0.06	0.08	0.02	0.01
MgO	0.00	0.01	0.00	0.00	0.00	0.00	0.00	0.00	0.00	0.00	0.00	0.00	0.00
CaO	5.12	4.84	4.87	4.17	5.74	5.49	3.78	4.90	4.92	4.88	4.98	4.95	4.96
Na2O	4.96	8.23	8.61	9.33	8.22	8.42	7.08	8.69	8.99	8.89	9.01	8.86	8.65
K2O	0.09	0.27	0.25	0.18	0.24	0.18	0.06	0.16	0.19	0.22	0.26	0.22	0.16
Total	98.6	100.3	101.1	101.6	100.4	100.8	101.3	99.8	101.5	99.4	100.9	101.8	101.2
Si	2.844	2.776	2.777	2.798	2.746	2.748	3.043	2.809	2.764	2.817	2.775	2.765	2.777
Ti	0.000	0.000	0.000	0.001	0.001	0.001	0.000	0.000	0.000	0.000	0.000	0.000	0.000
Al ^{IV}	1.231	1.239	1.230	1.201	1.249	1.254	0.964	1.173	1.235	1.160	1.213	1.239	1.228
Fe^{3+}	0.006	0.001	0.000	0.006	0.001	0.001	0.000	0.008	0.002	0.002	0.003	0.001	0.000
Mg	0.000	0.000	0.000	0.000	0.000	0.000	0.000	0.000	0.000	0.000	0.000	0.000	0.000
Ca	0.242	0.228	0.228	0.194	0.272	0.258	0.173	0.233	0.230	0.233	0.235	0.231	0.232
Na	0.424	0.702	0.730	0.787	0.704	0.718	0.586	0.747	0.761	0.768	0.768	0.747	0.733
K	0.005	0.015	0.014	0.010	0.013	0.010	0.003	0.009	0.011	0.012	0.015	0.012	0.009
Total	4.752	4.963	4.98	4.997	4.987	4.989	4.77	4.979	5.003	4.992	5.008	4.994	4.98
Ab	63	74	75	79	71	73	77	76	76	76	75	75	75
An	36	24	23	20	27	26	23	24	23	23	23	23	24
Or	1	2	1	1	1	1	0	1	1	1	1	1	1

Table a.10 cont.

	Gneiss	*Rock: Metasediment (sample A45)*											
Point	**#138**	**#167**	**#172**	**#174**	**#192**	**#193**	**#194**	**#203**	**#206**	**#208**	**#209**	**#211**	**#215**
SiO_2	62.27	64.19	63.69	63.72	63.63	62.38	63.13	63.05	64.78	63.34	62.83	62.91	62.30
TiO_2	0.03	0.05	0.00	0.00	0.00	0.00	0.00	0.02	0.00	0.04	0.02	0.03	0.03
Al_2O_3	23.72	23.38	23.81	23.51	23.19	22.58	23.52	23.75	23.24	23.50	22.15	23.93	24.36
Fe_2O_3	0.05	0.17	0.05	0.15	0.10	0.04	0.08	0.24	0.13	0.05	0.23	0.08	0.19
MgO	0.00	0.00	0.00	0.01	0.00	0.00	0.00	0.00	0.00	0.00	0.03	0.00	0.01
CaO	4.99	4.14	4.81	4.39	4.44	4.45	4.26	4.74	3.93	4.45	4.24	4.77	5.51
Na2O	8.64	9.59	8.93	9.36	9.30	8.93	9.29	8.89	8.51	9.09	9.69	8.86	8.54
K2O	0.27	0.06	0.04	0.06	0.05	0.05	0.06	0.03	0.05	0.05	0.05	0.03	0.03
Total	100.0	101.6	101.3	101.2	100.7	98.4	100.3	100.7	100.7	100.5	99.2	100.6	101.0
Si	2.760	2.795	2.779	2.786	2.794	2.801	2.782	2.770	2.827	2.785	2.806	2.766	2.736
Ti	0.001	0.002	0.000	0.000	0.000	0.000	0.000	0.001	0.000	0.001	0.001	0.001	0.001
Al ^{IV}	1.239	1.200	1.224	1.211	1.200	1.195	1.222	1.230	1.196	1.218	1.166	1.240	1.261
Fe^{3+}	0.002	0.006	0.002	0.005	0.003	0.001	0.003	0.008	0.004	0.002	0.008	0.003	0.006
Mg	0.000	0.000	0.000	0.001	0.000	0.000	0.000	0.000	0.000	0.000	0.002	0.000	0.001
Ca	0.237	0.193	0.225	0.206	0.209	0.214	0.201	0.223	0.184	0.209	0.203	0.225	0.259
Na	0.743	0.809	0.755	0.793	0.792	0.778	0.794	0.757	0.720	0.775	0.839	0.755	0.727
K	0.015	0.004	0.002	0.004	0.003	0.003	0.003	0.001	0.003	0.003	0.003	0.002	0.002
Total	4.997	5.008	4.987	5.005	5.001	4.991	5.004	4.99	4.934	4.993	5.027	4.991	4.994
Ab	75	80	77	79	79	78	80	77	79	79	80	77	74
An	24	19	23	21	21	22	20	23	20	21	19	23	26
Or	2	0	0	0	0	0	0	0	0	0	0	0	0

Table a.11: Microprobe analysis data of the garnets from the KPTA. Structural formula is calculated on the basis of 24 oxygen.

	Metasediment (sample A26)											
Point	**#25**	**#27**	**#28**	**#29**	**#30**	**#31**	**#32**	**#33**	**#35**	**#40**	**#41**	**#42**
SiO_2	37.97	38.29	38.27	38.19	38.33	37.9	38.1	38.29	38.05	38.49	38.58	38.23
TiO_2	0.03	0.02	0.01	0.12	0.10	0.08	0.10	0.10	0.07	0.03	0.02	0.15
Al_2O_3	20.26	20.27	20.53	21.2	20.8	20.91	21.04	20.33	21.02	20.8	20.99	20.76
FeO	26.51	25.72	25.74	25.68	26.29	25.96	25.8	26.39	26.3	26.17	26.63	26.13
MnO	3.06	3.00	3.18	3.30	3.32	3.40	3.53	3.29	3.46	3.25	3.14	3.29
MgO	2.86	3.36	3.34	3.26	3.29	3.37	3.28	3.26	3.33	2.78	3.23	3.25
CaO	7.75	8.10	7.93	8.03	7.96	7.75	7.99	7.91	7.68	8.01	8.16	8.00
Total	98.49	98.81	99.01	99.77	100.1	99.37	99.86	99.57	100.09	99.54	100.75	99.81
Si	3.054	3.058	3.051	3.02	3.029	3.016	3.016	3.046	3.01	3.055	3.03	3.029
Ti	0.002	0.001	0.001	0.007	0.006	0.005	0.006	0.006	0.004	0.002	0.001	0.009
Al^{VI}	1.921	1.909	1.929	1.976	1.938	1.961	1.963	1.905	1.96	1.946	1.943	1.938
Fe^{2+}	1.783	1.718	1.716	1.698	1.738	1.728	1.708	1.756	1.74	1.737	1.749	1.731
Mn^{2+}	0.208	0.203	0.214	0.221	0.223	0.229	0.236	0.222	0.232	0.218	0.209	0.221
Mg	0.343	0.4	0.396	0.384	0.388	0.4	0.387	0.387	0.392	0.329	0.379	0.384
Ca	0.668	0.694	0.677	0.680	0.674	0.661	0.677	0.674	0.651	0.682	0.687	0.679
Total	7.982	7.985	7.984	7.985	7.996	7.999	7.996	7.995	8.000	7.970	7.997	7.992
Pyp	11	13	13	13	13	13	13	13	13	11	13	13
Alm	59	57	57	57	57	57	57	58	58	59	58	57
Spess	7	7	7	7	7	8	8	7	8	7	7	7
Gross	22	23	23	23	22	22	22	22	21	23	23	23

Table a.11 cont.

	Metasediment (sample A26)						*Gneiss (sample 11.13)*				
Point	**#43**	**#44**	**#45**	**#54**	**#55**	**#56**	**#116**	**#117**	**#118**	**#119**	**#120**
SiO_2	38.27	38.01	38.04	37.88	37.56	38.07	37.07	37.33	37.94	37.79	38.11
TiO_2	0.12	0.12	0.12	0.09	0.14	0.15	0.00	0.00	0.00	0.01	0.04
Al_2O_3	20.81	20.6	20.93	21.13	20.67	20.93	21.02	20.85	21.32	20.84	20.82
FeO	26.03	25.39	25.15	25.81	25.04	25.5	25.72	26.22	26.85	27.66	27.34
MnO	3.38	3.36	3.54	3.55	3.36	3.35	10.46	9.69	9.70	9.55	9.03
MgO	3.09	3.11	3.14	3.15	3.16	3.20	2.55	2.77	2.79	2.82	2.88
CaO	7.99	8.56	8.39	8.02	8.57	8.21	2.19	2.45	2.19	2.20	2.23
Total	99.71	99.16	99.33	99.63	99.41	99.44	99.07	99.32	100.79	100.93	100.48
Si	3.035	3.031	3.024	3.008	2.993	3.023	3.008	3.018	3.02	3.018	3.043
Ti	0.007	0.007	0.007	0.006	0.009	0.009	0.000	0.000	0.000	0.000	0.003
Al^{VI}	1.945	1.935	1.96	1.977	1.935	1.959	2.01	1.987	2	1.961	1.959
Fe^{2+}	1.726	1.693	1.672	1.714	1.669	1.693	1.745	1.773	1.788	1.847	1.825
Mn^{2+}	0.227	0.227	0.238	0.239	0.227	0.225	0.719	0.664	0.654	0.646	0.611
Mg	0.366	0.37	0.372	0.373	0.375	0.378	0.309	0.334	0.331	0.335	0.342
Ca	0.679	0.731	0.715	0.682	0.731	0.698	0.191	0.212	0.187	0.188	0.191
Total	7.985	7.994	7.989	7.998	8.000	7.988	7.985	7.988	7.980	7.999	7.975
Pyp	12	12	12	12	13	13	10	11	11	11	12
Alm	58	56	56	57	56	57	59	59	60	61	61
Spess	8	8	8	8	8	8	24	22	22	21	21
Gross	23	24	24	23	22	23	6	7	6	6	6

Table a.11 cont.

	11.13	*Metasediment (sample A45)*									
Point	**#121**	**#175**	**#176**	**#177**	**#178**	**#179**	**#180**	**#181**	**#182**	**#184**	**#185**
SiO_2	38.11	38.41	38.43	38.42	38.62	38.55	38.93	38.57	38.53	38.98	38.64
TiO_2	0.00	0.00	0.04	0.06	0.01	0.08	0.09	0.01	0.03	0.08	0.11
Al_2O_3	21.41	21	21.29	21.34	21.12	19.84	20.84	21.47	20.91	21.45	21.15
FeO	27.1	28.97	28.59	29.08	28.86	28.47	28.72	29.41	29.22	29.13	28.48
MnO	9.40	2.58	3.03	2.84	2.94	2.79	2.72	2.73	2.70	2.91	2.73
MgO	2.80	4.65	4.85	4.82	4.85	4.70	4.72	4.63	4.51	4.52	4.79
CaO	2.22	4.06	3.92	4.13	3.97	4.40	4.74	4.02	4.19	4.57	4.89
Total	101.05	99.69	100.2	100.7	100.4	98.86	100.8	100.85	100.13	101.65	100.79
Si	3.024	3.039	3.024	3.013	3.035	3.08	3.047	3.021	3.041	3.028	3.024
Ti	0.000	0.000	0.002	0.004	0.000	0.005	0.005	0.000	0.002	0.005	0.006
Al^{VI}	2.002	1.958	1.975	1.972	1.956	1.868	1.922	1.982	1.945	1.964	1.951
Fe^{2+}	1.798	1.917	1.881	1.908	1.896	1.902	1.88	1.926	1.929	1.893	1.864
Mn^{2+}	0.632	0.173	0.202	0.188	0.195	0.189	0.180	0.181	0.181	0.191	0.181
Mg	0.331	0.549	0.568	0.563	0.568	0.56	0.551	0.54	0.53	0.523	0.559
Ca	0.189	0.345	0.331	0.347	0.334	0.376	0.398	0.337	0.354	0.380	0.410
Total	7.975	7.982	7.985	7.996	7.986	7.981	7.985	7.988	7.984	7.985	7.995
Pyp	11	18	19	19	19	18	18	18	18	18	19
Alm	61	64	63	63	63	63	62	65	64	63	62
Spess	21	6	7	6	7	6	6	6	6	6	6
Gross	6	12	11	11	11	12	13	11	12	13	14

Table a.11 cont.

	Metasediment (sample A45)			
Point	**#197**	**#198**	**#199**	**#200**
SiO_2	38.6	38.3	38.19	38.9
TiO_2	0.00	0.10	0.13	0.03
Al_2O_3	21.62	21.31	21.47	20.06
FeO	29.17	27.65	28.11	28.15
MnO	3.18	3.10	3.26	3.08
MgO	4.43	4.35	4.43	4.36
CaO	3.65	4.96	4.60	4.84
Total	100.64	99.77	100.2	99.49
Si	3.027	3.024	3.008	3.087
Ti	0.000	0.006	0.007	0.002
Al^{VI}	1.998	1.983	1.994	1.876
Fe^{2+}	1.913	1.826	1.852	1.868
Mn^{2+}	0.211	0.207	0.218	0.207
Mg	0.518	0.512	0.52	0.516
Ca	0.307	0.420	0.388	0.412
Total	7.974	7.978	7.987	7.971
Pyp	18	17	17	17
Alm	65	62	62	62
Spess	7	7	7	7
Gross	10	14	13	13

Table a.12: Microprobe analysis data of the pyroxenes from the KPTA. Structural formula is calculated on the basis of 6 oxygen.

	Rock: Amphibolite (sample A55)			*Rock: Metavolcanic (sample A57)*								
Point	**#142**	**#144**	**#146**	**#1**	**#2**	**#3**	**#4**	**#5**	**#6**	**#7**	**#8**	**#9**
SiO_2	53.51	52.88	54.41	52.86	52.91	52.56	52.64	52.42	52.89	52.54	52.62	53.47
TiO_2	0.07	0.16	0.04	0.20	0.21	0.22	0.28	0.23	0.20	0.22	0.19	0.11
Al_2O_3	1.87	3.33	0.95	1.96	1.98	1.37	1.59	1.14	1.17	1.24	1.44	2.48
Cr_2O_3	0.11	0.21	0.02	0.02	0.03	0.00	0.00	0.00	0.00	0.01	0.00	0.00
Fe_2O_3	0.00	0.00	0.16	27.47	28.27	27.17	25.13	27.19	26.48	24.60	28.25	28.90
FeO	6.57	7.31	6.06	3.04	2.36	3.33	5.15	2.82	3.31	5.04	2.01	1.33
MnO	0.30	0.21	0.18	0.29	0.17	0.25	0.34	0.36	0.39	0.34	0.39	0.16
MgO	14.45	14.35	14.47	0.02	0.05	0.02	0.01	0.02	0.01	0.00	0.02	0.01
CaO	22.67	20.08	24.75	1.66	1.47	2.49	2.71	2.30	2.20	2.42	2.18	0.89
Na_2O	0.37	0.49	0.28	12.47	12.70	12.13	11.70	12.22	12.24	11.75	12.47	13.23
K_2O	0.03	0.03	0.02	0.02	0.02	0.00	0.00	0.02	0.04	0.01	0.02	0.01
Total	99.9	99.1	101.3	100.0	100.2	99.5	99.5	98.7	98.9	98.2	99.6	100.6
Si	1.976	1.961	1.986	2.017	2.013	2.022	2.028	2.030	2.042	2.049	2.018	2.016
Ti	0.002	0.004	0.001	0.006	0.006	0.006	0.008	0.007	0.006	0.006	0.006	0.003
Al^{IV}	0.024	0.039	0.014	0.000	0.000	0.000	0.000	0.000	0.000	0.000	0.000	0.000
Al^{VI}	0.057	0.106	0.027	0.088	0.089	0.062	0.072	0.052	0.053	0.057	0.065	0.110
Cr	0.003	0.006	0.001	0.000	0.001	0.000	0.000	0.000	0.000	0.000	0.000	0.000
Fe^{3+}	0.000	0.000	0.004	0.789	0.810	0.786	0.729	0.793	0.770	0.722	0.815	0.820
Fe^{2+}	0.203	0.227	0.185	0.097	0.075	0.107	0.166	0.091	0.107	0.164	0.065	0.042
Mn^{2+}	0.009	0.007	0.005	0.010	0.006	0.008	0.011	0.012	0.013	0.011	0.013	0.005
Mg	0.795	0.793	0.787	0.001	0.003	0.001	0.001	0.001	0.000	0.000	0.001	0.000
Ca	0.897	0.798	0.968	0.068	0.060	0.103	0.112	0.096	0.091	0.101	0.089	0.036
Na	0.026	0.035	0.020	0.923	0.937	0.905	0.874	0.918	0.917	0.889	0.927	0.967
K	0.001	0.001	0.001	0.001	0.001	0.000	0.000	0.001	0.002	0.000	0.001	0.000
Total	3.994	3.978	4.000	4.000	4.000	4.000	4.000	4.000	4.000	4.000	4.000	4.000
Wo	47	44	50	41	44	49	40	51	46	38	58	46
En	42	44	41	1	2	0	0	0	0	0	1	1
Fs	11	12	10	59	55	51	60	49	54	62	42	54

Table a.13: Microprobe analysis data of the biotite from the KPTA. Structural formula is calculated on the basis of 24 oxygen.

Mineral: Biotite

	Rock: Granodiorite (sample 6.9)					*Rock: Gneiss (sample 11.13)*						
Point	**#107**	**#108**	**#109**	**#110**	**#111**	**#123**	**#124**	**#125**	**#126**	**#127**	**#128**	**#129**
SiO_2	35.68	36.79	36.26	36.72	37.04	35.96	35.81	35.78	34.77	34.39	35.46	32.68
TiO_2	2.30	1.96	2.41	2.74	2.69	1.17	1.53	1.32	0.44	0.64	1.20	0.61
Al_2O_3	16.00	16.61	15.98	15.57	16.67	17.25	14.69	16.37	18.53	17.12	17.74	18.26
Cr_2O_3	0.00	0.00	0.01	0.01	0.00	0.00	0.00	0.02	0.00	0.00	0.02	0.00
FeO	19.98	21.21	21.53	20.85	20.65	19.61	19.12	19.31	18.42	18.82	18.23	20.43
MnO	0.32	0.41	0.39	0.38	0.23	0.73	0.64	0.66	0.64	0.71	0.71	0.96
MgO	8.74	9.28	9.04	8.89	8.86	10.02	9.60	9.74	10.48	11.27	10.65	10.80
CaO	0.08	0.16	0.02	0.00	0.03	0.33	0.43	0.26	1.39	0.68	0.21	0.53
Na2O	0.39	0.06	0.03	0.06	0.02	0.05	0.05	0.05	0.09	0.04	0.06	0.03
K2O	9.64	9.36	9.80	9.80	9.99	8.45	8.29	8.75	6.66	6.38	8.68	4.20
F	2.81	2.48	2.05	2.08	1.91	1.61	1.06	0.29	2.27	1.00	1.69	0.65
H2O	3.60	3.74	3.73	3.73	3.80	3.75	3.64	3.78	3.65	3.69	3.74	3.65
Total	99.4	101.9	101.1	100.7	101.8	98.8	94.8	96.3	97.2	94.7	98.3	92.8
Si	5.618	5.620	5.598	5.673	5.632	5.574	5.770	5.637	5.451	5.482	5.507	5.293
Ti	0.272	0.225	0.28	0.318	0.307	0.136	0.186	0.156	0.052	0.077	0.14	0.075
Al IV	2.382	2.380	2.402	2.327	2.368	2.426	2.230	2.363	2.549	2.518	2.493	2.707
Al VI	0.588	0.611	0.505	0.507	0.62	0.726	0.56	0.676	0.874	0.699	0.755	0.778
Cr	0.000	0.000	0.002	0.001	0.001	0.001	0.001	0.002	0.000	0.000	0.003	0.000
Fe^{2+}	2.631	2.71	2.779	2.693	2.626	2.542	2.577	2.545	2.415	2.509	2.367	2.767
Mn^{2+}	0.043	0.054	0.05	0.05	0.029	0.096	0.088	0.089	0.084	0.096	0.094	0.131
Mg	2.052	2.113	2.079	2.047	2.008	2.316	2.305	2.288	2.448	2.679	2.465	2.609
Ca	0.013	0.027	0.003	0.000	0.004	0.055	0.074	0.045	0.233	0.116	0.035	0.091
Na	0.118	0.017	0.010	0.018	0.006	0.014	0.014	0.015	0.028	0.013	0.019	0.010
K	1.935	1.825	1.93	1.931	1.938	1.672	1.703	1.758	1.332	1.298	1.719	0.868
F	0.221	0.189	0.158	0.160	0.145	0.125	0.085	0.023	0.178	0.080	0.131	0.053
OH	3.779	3.811	3.842	3.840	3.855	3.875	3.915	3.977	3.822	3.920	3.869	3.947
Total	19.651	19.581	19.64	19.57	19.54	19.56	19.508	19.57	19.47	19.49	19.6	19.33

Table a.14: Microprobe analysis data of the chlorite, epidote and ilmenite from the KPTA. Structural formulas are calculated on the basis of 36 and 12.5 oxygen for chlorite and epidote respectively.

	Mineral chlorite		
	Metasediment (A26)		
Point	#51	#52	#53
SiO_2	25.73	25.71	25.2
TiO_2	0.08	0.1	0.1
Al_2O_3	22.65	21.89	21.1
Cr_2O_3	0	0	0
FeO	22.87	22.57	22.87
MnO	0.07	0.19	0.05
MgO	15.79	16	15.51
CaO	0.06	0.04	0.04
Na_2O	0	0.02	0.02
K_2O	0.02	0.01	0.01
H_2O	11.52	11.41	11.16
Total	98.79	97.95	96.06
Si	5.359	5.404	5.419
Ti	0.013	0.016	0.016
Al^{IV}	2.641	2.596	2.581
Al^{VI}	2.92	2.826	2.767
Cr	0	0	0
Fe^{2+}	3.984	3.966	4.113
Mn^{2+}	0.013	0.034	0.01
Mg	4.901	5.012	4.972
Ca	0.014	0.009	0.01
Na	0	0.008	0.007
K	0.005	0.004	0.002
Total	35.85	35.875	35.9

	Mineral epidote					
	Diorite (11)					
Point	#77	#78	#79	#100	#101	#102
SiO_2	38.8	38.6	38.8	38.1	38	38.4
TiO_2	0.22	0.08	0.67	0.31	0.32	0.34
Al_2O_3	27.5	25.8	27.2	25.5	25.9	26.8
Cr_2O_3	0	0.01	0	0.02	0.01	0.04
Fe_2O_3	8.06	8.69	6.18	9.8	9.73	8.76
Mn_2O_3	0.25	0.09	0.2	0.51	0.54	0.39
MgO	0	0	0.07	0.04	0.03	0.04
CaO	23.1	23.8	23.3	22.8	22.4	22.5
F	0	0.21	0.51	0	0	0
H_2O	1.93	1.88	1.87	1.89	1.89	1.91
Total	99.8	99.0	98.8	98.9	98.9	99.3
Si	3.02	3.05	3.05	3.02	3.01	3.02
Ti	0.01	0	0.04	0.02	0.02	0.02
Al^{IV}	0	0	0	0	0	0
Al^{VI}	2.52	2.4	2.52	2.38	2.42	2.48
Cr	0	0	0	0	0	0
Fe^{3+}	0.47	0.52	0.37	0.58	0.58	0.52
Mn^{3+}	0.02	0.01	0.01	0.03	0.03	0.02
Mg	0	0	0.01	0.01	0	0.01
Ca	1.92	2.01	1.96	1.93	1.9	1.89
F	0	0.01	0.02	0	0	0
Total	9.0	9.0	9.0	9.0	9.0	9.0

	Ilmenite	
	Metasediment (A45)	
Point	#216	#217
SiO_2	0.06	0.05
TiO_2	49.10	49.66
Al_2O_3	0.03	0.00
Cr_2O_3	0.02	0.01
Fe_2O_3	5.37	5.59
FeO	41.13	39.56
MnO	2.85	4.94
MgO	0.09	0.07
CaO	0.03	0.03
Total	98.67	99.91
Si	0.001	0.001
Ti	0.946	0.945
Fe^{3+}	0.103	0.106
Fe^{2+}	0.881	0.838
Mn^{2+}	0.062	0.106
Mg	0.003	0.002
Ca	0.001	0.001
Total	2.000	2.000
Ilmen.	88	84
Geikiel.	1	0
Pyroph	6	11
Hemat.	5	5

11 PLATES

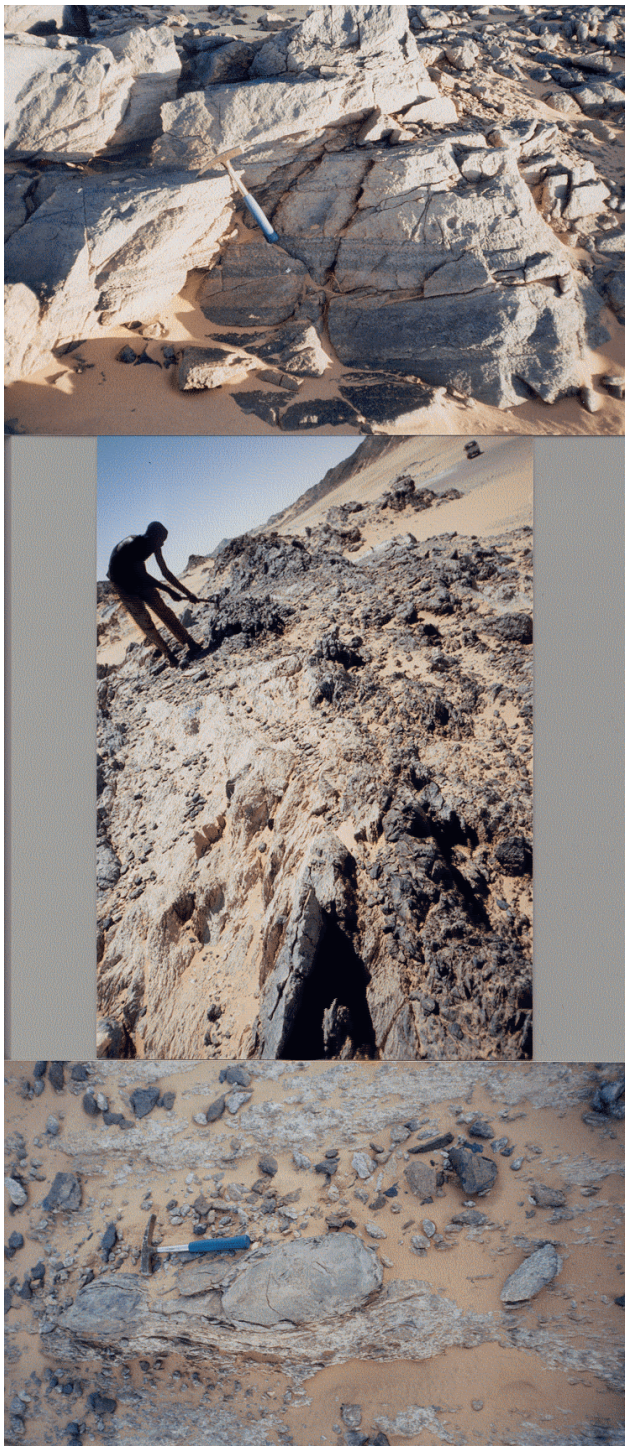

Plate 1: **A**) Layered gabbro from ridge 2 of the Keraf ophiolites. **B**) Ophiolitic melange zone from ridge 3, dark patches are pyroxenite and light one are talc-serpentine schist. **C**) Boudin structures from ridge 1 of the Keraf ophiolites. The compentent layers are pyroxenite and dunite while the less competent layers are serpentinites (for ridge 1 location see Fig. 5).

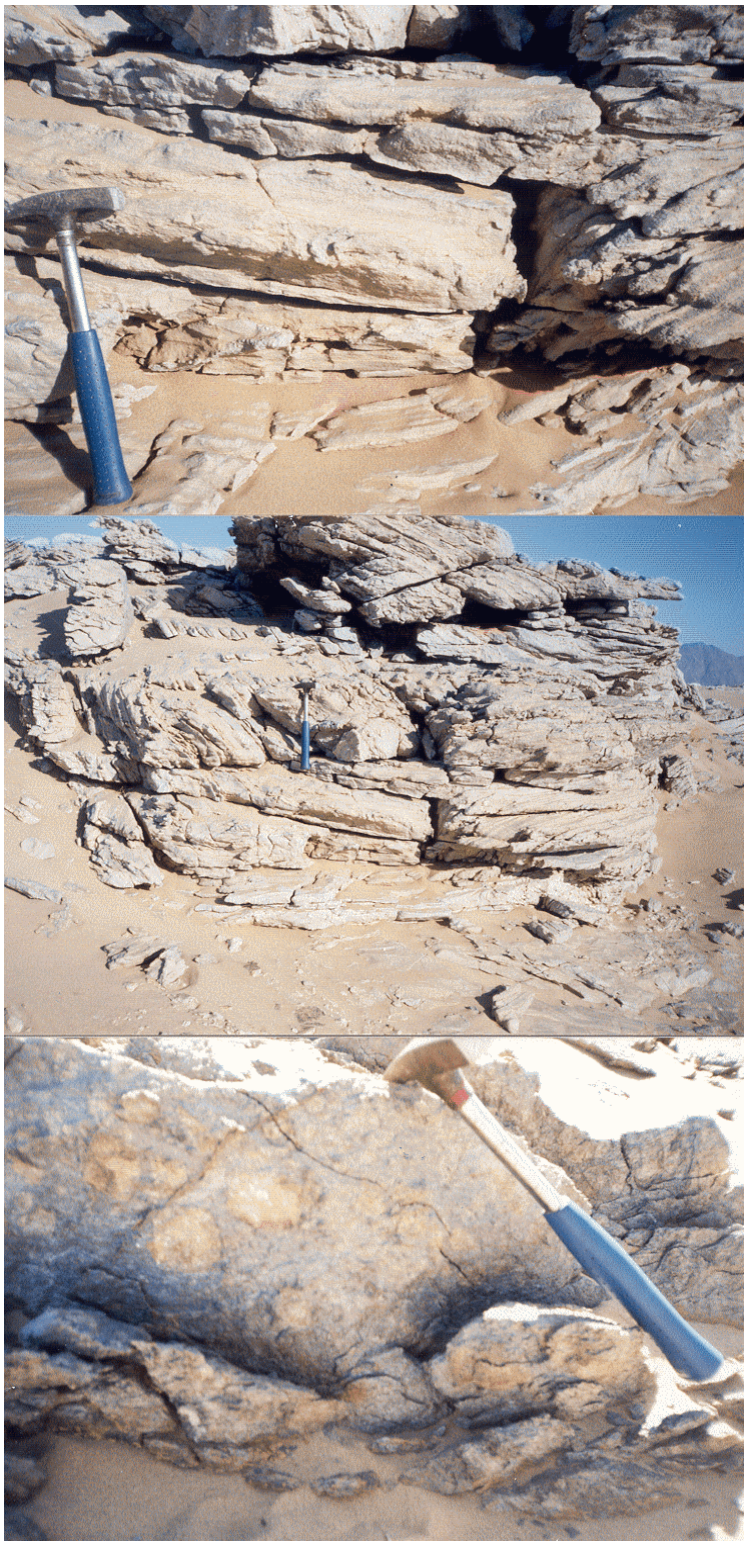

Plate 2: Primary structures in the low-grade metasediments of the KPTA. **A**) Graded bedding and sedimentary laminations. **B**) Cross bedding in sandstones. **C**) Conglomerate with rounded dioritic cobbles.

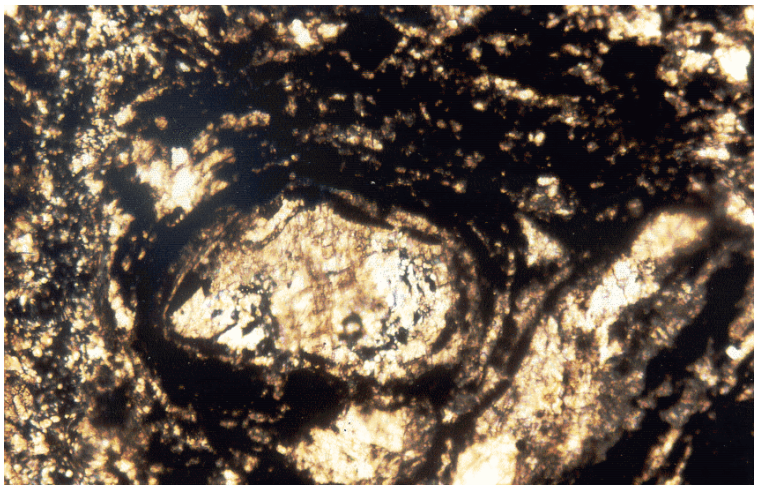

Plate 3: Oolite from limestone of the KPTA (magnification is 50*).

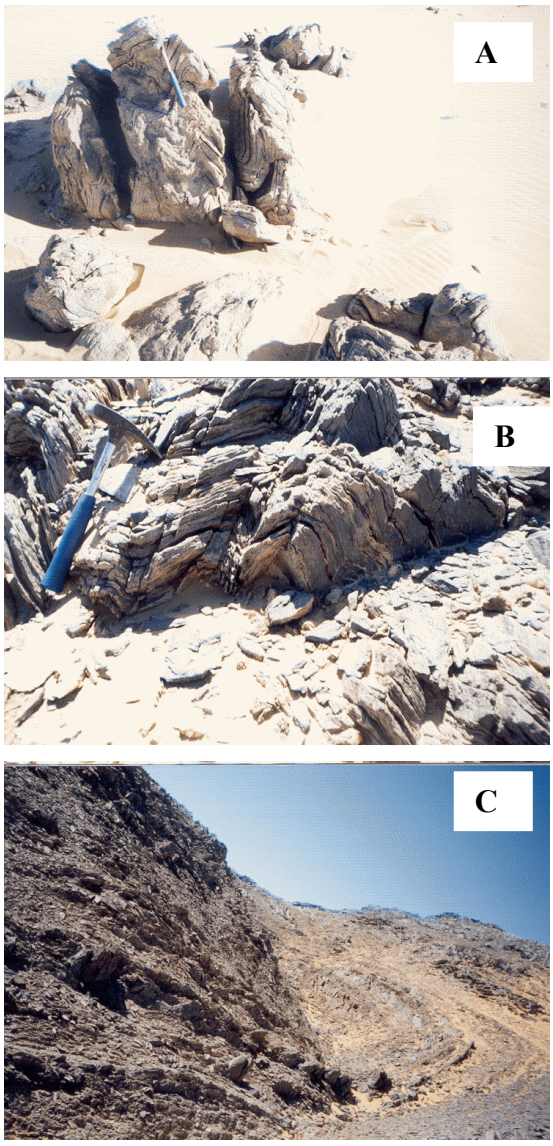

Plate 4: D1 folds from the high-grade gneiss (**A**), from the Keraf ophiolites (**B**) and from the low-grade metasediments (**C**).

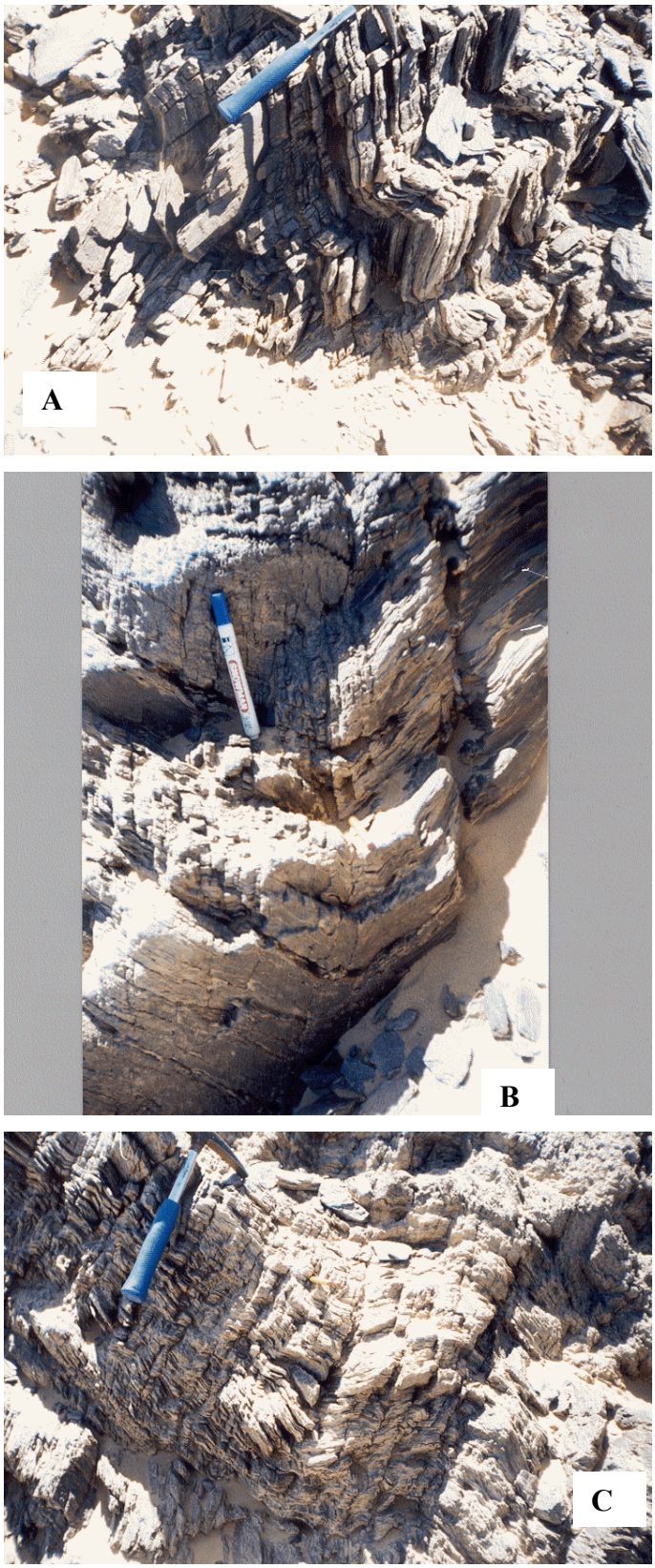

Plate 5: D2 folds from the Keraf ophiolites and the low-grade metasediments. A) Mesoscopic D2 fold with widely spaced S2 foliations which transect S1 foliations. B) Upright asymmetrical D2 fold. C) S2 foliations crenulate S1 foliations.

Plate 6: Kink-bands in upright limb of a D2 fold.

Plate 7: D3 folding styles from the low-grade metasediments. Note the rounded hinges and the faint S3 foliations.

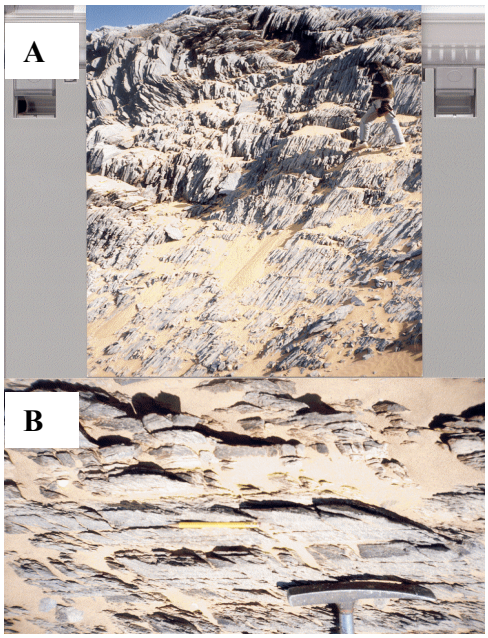

Plate 8: S4 shear foliations in the low-grade metamorphism. **A**) N-S trending vertical foliations. **B**) S4 trensect and displace S1 foliations in the gabgaba Shear Zone.

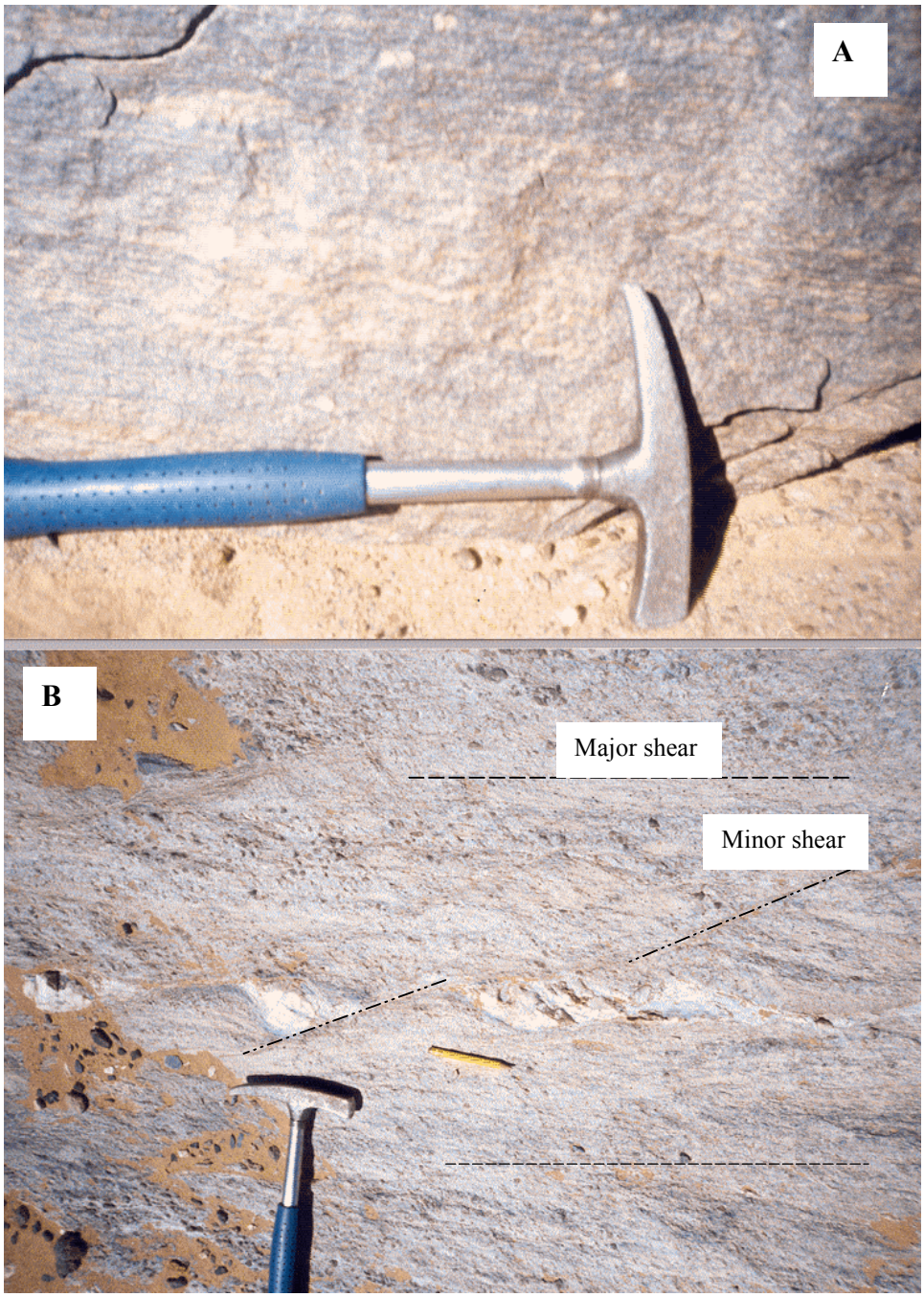

Plate: 9: D4 shear indicators. **A)** Vertical N-S trending mylonitic bands with horizontal stretched grains of K–feldspar and quartz (rock is post-tectonic granite). **B**) N-S trending D4 shear planes with minor NW trending shear bands in an angle of 30° with the major shear trend.